**UNIVERSITY OF SOUTHAMPTON**

Faculty of Earth and Life Sciences
School of Ocean and Earth Science

# The Frequency, Magnitude and Timing of Sediment Transport in Submarine Canyons

*by*

**Lewis P. Bailey**
MSci

*A thesis for the degree of*
*Doctor of Philosophy*

December 2021

University of Southampton

Abstract

Faculty of Earth and Life Sciences
School of Ocean and Earth Science

Doctor of Philosophy

**The Frequency, Magnitude and Timing of Sediment Transport in Submarine Canyons**

by Lewis P. Bailey

Submarine canyons globally incise 11 % of the seafloor on continental slopes, and provide conduits for sediment and associated particle transport from the shallow marine realm to the deep-sea. Turbidity currents are thought to be the primary mechanism of sediment transport. An individual turbidity current can transport more than ten times the annual sediment for all the world's rivers at speeds of up to 20 $ms^{-1}$. These fast flow velocities coupled with high sediment concentration mean turbidity currents can be destructive; posing a threat to subsea infrastructure. Understanding the frequency, timing and magnitude of turbidity currents (and other mechanisms of sediment transport) is therefore integral to developing our knowledge of particle flux to the deep sea, as well as for geohazard assessments. Despite this, very few measurements of turbidity currents exist, and only over the past decade have technological advancements, such as the use of acoustic Doppler current profilers (ADCPs), been deployed to directly monitor flows in detail. However, deployments are typically of short duration (a few months), use instruments that record at low temporal resolution, or are located distal to the flow source, therefore missing parts of an annual or longer cycles of turbidity current activity. To quantify the frequency and timing of sediment transport in submarine canyons this thesis focuses on unprecedented temporally and spatially extensive geophysical monitoring datasets, specifically using ADCPs in physiographically-diverse settings to show that: (1) Turbidity current activity is primarily controlled by sediment supply. Once sediment is available only minor triggering mechanism are required to initiate a flow; (2) Periods of enhanced turbidity current activity can be anticipated and flow probability is predictable where both sediment supply and triggering mechanism can be quantified; and (3) Even in systems of turbidity current inactivity, the focusing of bottom currents and internal submarine canyon tides are capable of transporting particles to the deep-sea. These findings highlight the highly active and complex nature of sediment transport in submarine canyons.

# Contents

# List of Figures

# List of Tables

# Declaration of Authorship

I declare that this thesis and the work presented in it is my own and has been generated by me as the result of my own original research.

I confirm that:

1. This work was done wholly or mainly while in candidature for a research degree at this University;
2. Where any part of this thesis has previously been submitted for a degree or any other qualification at this University or any other institution, this has been clearly stated;
3. Where I have consulted the published work of others, this is always clearly attributed;
4. Where I have quoted from the work of others, the source is always given. With the exception of such quotations, this thesis is entirely my own work;
5. I have acknowledged all main sources of help;
6. Where the thesis is based on work done by myself jointly with others, I have made clear exactly what was done by others and what I have contributed myself;
7. Parts of this work have been published as: (see 'Publications')

Signed:..... Date:.....

# Publications

Lewis P. Bailey, Michael A. Clare, Kurt J. Rosenberger, Matthieu J. B. Cartigny, Peter J. Talling, Charles K. Paull, Roberto Gwiazda, Daniel R. Parsons, Stephen M. Simmons, Jingping Xu, Ivan D. Haigh, Katherine L. Maier, Mary McGann, Eve Lundsten and the Monterey CCE Team (2021). Preconditioning by Sediment Accumulation Can Produce Powerful Turbidity Currents without Major External Triggers. *Earth and Planetary Science Letters*, 562, 116845. DOI: 10.1016/j.epsl.2021.116845 (see Chapter 2)

Catharina J. Heerema, Peter J. Talling, Matthieu J. B. Cartigny, Charles K. Paull, Lewis P. Bailey, Stephen M. Simmons, Daniel R. Parsons, Michael A. Clare, Roberto Gwiazda, Krystal Anderson, Katherine L. Maier, Jingping P. Xu, Esther J. Sumner, Kurt J. Rosenberger, Jenny Gales, Mary McGann, Lionel Carter, Edward Pope and the Monterey Coordinated Canyon Experiment (CCE) Team (2020). What Determines the Downstream Evolution of Turbidity Currents? *Earth and Planetary Science Letters*, 532, 116023. DOI: 10.1016/j.epsl.2019.116023 (see Appendix A)

## Submitted Manuscripts

Maarten S. Heijnen, Michael A. Clare, Matthieu J.B. Cartigny, Peter J. Talling, Sophie Hage, Ed L. Pope, Lewis Bailey, Esther Sumner, D. Gwyn Lintern, Cooper Stacey, Daniel R. Parsons, Stephen M. Simmons, Ye Chen, Stephen M. Hubbard, Joris T. Eggenhuisen, Ian Kane, and John E. Hughes Clarke. How is sediment carried through submarine channels to build lobes? Submitted to *Earth and Planetary Science Letters*.

Ed L. Pope, Matthieu J. B. Cartigny, Michael A. Clare, Peter J. Talling, D. Gwyn Lintern, Age Vellinga, Sophie Hage, Sanem Açikalin, Lewis Bailey, Natasha Chapplow, Ye Chen, Joris T. Eggenhuisen, Alison Hendry, Catharina J. Heerema, Maarten Heijnen, Stephen M. Hubbard, James E. Hunt, Claire McGhee, Daniel R. Parsons, Stephen M. Simmons, Cooper D. Stacey and Daniela Vendettuoli. First Source-to-sink Monitoring shows Dense Head Controls Sediment Flux and Runout in Turbidity Currents. Submitted to *Science Advances*.

Daniela Vendettuoli, Michael A. Clare, Esther J. Sumner, Matthieu J.B. Cartigny, Peter J. Talling, John Wood, Lewis P. Bailey, Maria Azpiroz-Zabala, Charles K. Paull6, Roberto Gwiazda, Jingping Xu, Cooper Stacey, D. Gwyn Lintern, Stephen M. Simmons, Ed L. Pope and Sophie Hage. Global Monitoring Data shows Grain Size Controls Turbidity Current Structure. Submitted to *Geophysical Research Letters*.

# Authorship Contributions

Preconditioning by Sediment Accumulation Can Produce Powerful Turbidity Currents without Major External Triggers (Chapter 2). LB: methodology, analysis, validation, visualisation, writing original draft. MC: analysis, conceptualisation, validation, editing original draft, supervision. KC: analysis, conceptualisation, investigation, editing original draft. MJBC: analysis, editing original draft. PT: analysis, conceptualisation, editing original draft, funding acquisition. CP: conceptualisation, investigation, review, funding acquisition. RG: investigation, review. DP: conceptualisation, investigation, review, funding acquisition. SS: investigation, review. JX: conceptualisation, review, funding acquisition. IH: review, supervision. KM: investigation, review. MM: investigation, review. EL: investigation, data curation, review.

A Predictive Model to Forecast Turbidity Current Activity Offshore from River Deltas. (Chapter 3) LB: conceptualisation, methodology, analysis, investigation, validation, visualisation, writing original draft, editing original draft. MC: conceptualisation, methodology, analysis, writing original draft, editing original draft, supervision, funding acquisition. EP: analysis, editing original draft. IH: conceptualisation, methodology, editing original draft, supervision. MJBC: editing original draft, funding acquisition. PT: editing original draft, funding acquisition. GL: editing original draft, funding acquisition. SH: editing original draft. MH: editing original draft.

Spatiotemporal Unsteadiness of Bottom Currents Revealed from Direct Monitoring across a Mixed Depositional System (Chapter 4) LB: conceptualisation, methodology, analysis, investigation, validation, visualisation, writing original draft, editing original draft. MC: conceptualisation, investigation, analysis, editing original draft, supervision, funding acquisition. JH: analysis, investigation, editing original draft, supervision. EM: analysis, editing original draft. IK: editing original draft. IH: editing original draft, supervision. MF: review. RA: review. GM: review. RW: review.

# Acknowledgements

Thank you to everyone who has been part of my PhD throughout the past four years. I have been lucky to travel around the world, visiting amazing places and collaborate with so many incredible people. This list of names that have supported this project or have been part of my life as a PhD student would go on forever, so I'd like to think know who you are instead! But many thanks to all of you! A special thanks, firstly goes to Mike. I could not have asked for a better lead supervisor. You have shaped me as a scientist and prepared me for a future in research. I appreciate all the endless feedback, guidance and time you gave me and I look forward to continue working with you over the next few years. Secondly, thank you to Kerri. You have supported me from sending in project applications to thesis submission, and now know a surprising amount about turbidity currents! You have given me confidence to go outside my comfort zone on endless occasions and encouraged me to take on so many opportunities. But mostly, thank you for helping me become the person I am today.

# Chapter 1

# Introduction

## 1.1 Rationale

Submarine canyons are recessed topographic features that globally incise 11% of the seafloor on continental slopes worldwide, including both active and passive margins, in total spanning an estimated length of >250,000 km (Fig. 1.1; Twichell & Roberts, 1982; Harris & Whiteway, 2011; Huang et al., 2014). These are sculpted by the erosive effects of mass wasting events (e.g. submarine landslides) and sediment density flows (e.g. turbidity currents; Shepard, 1972, 1981), often extending beyond the continental slope. In some cases, submarines canyons, and the linked channel-lobe systems that extend further into the deep sea, can be >400 km in length; rivalling or exceeding the scale of rivers on land (Normark et al., 2003).

The morphology and dynamics of submarine canyons and channels act as preferential transport routes for sediment (e.g. Nittrouer & Wright, 1994), organic matter (e.g. Galy et al., 2007; Lee et al., 2019; Hage et al., 2020), and pollutants, such as microplastics (e.g. Kane & Clare, 2019; Pohl et al., 2020) and marine litter (e.g. Mordecai et al., 2011; Tubau et al., 2015; van den Beld et al., 2017; Pierdomenico et al., 2019; Zhong & Peng, 2021) from the terrestrial and shallow marine zone to the deep sea. As such, some of the most extensive sediment (and associated particulate matter) accumulations globally are located in depositional lobes located at the terminus of submarine canyon-channel systems (Talling et al., 2013; Hessler & Fildani, 2019), with many of the largest hydrocarbon reserves hosted in their ancient deposits (Nilsen et al., 2007). Elevated transfer of particles such as organic carbon and nutrients also enhance primary productivity and ecological diversity. For example, submarine canyons support fisheries (Yoklavich et al., 2000) and other marine habitats, including vulnerable marine ecosystems such as

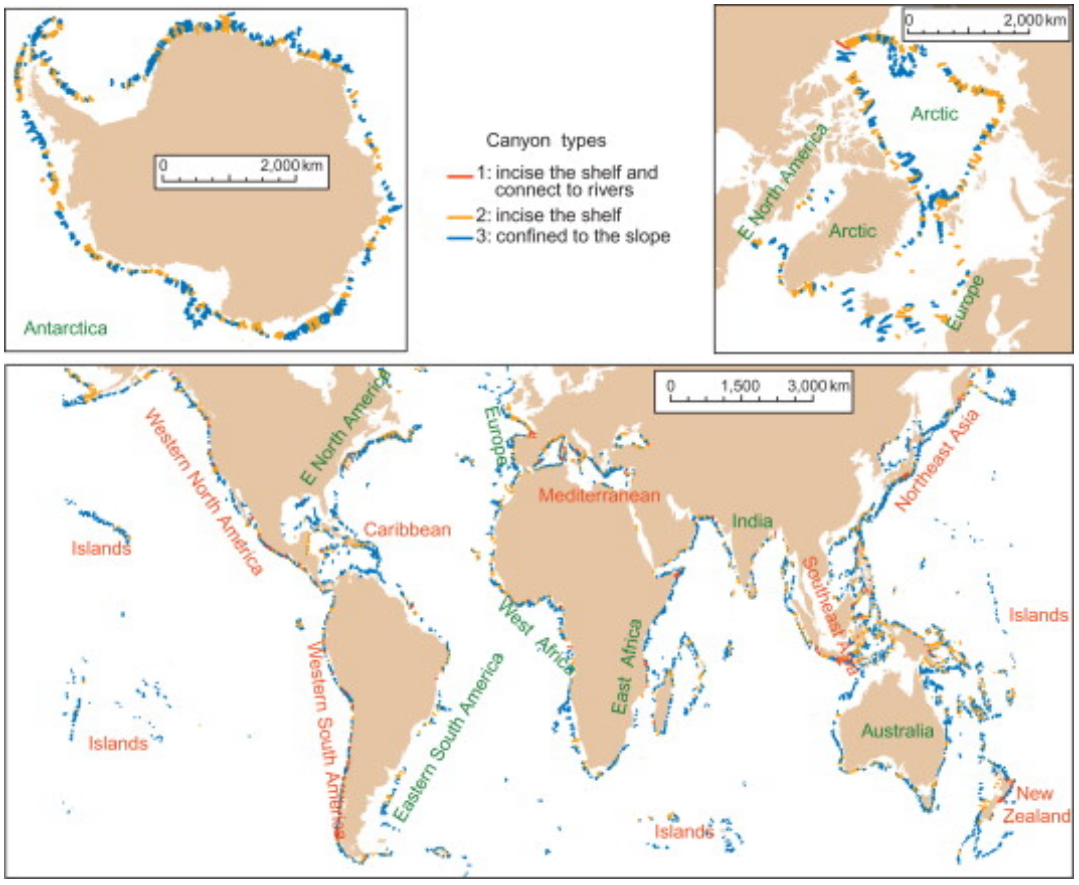


**Figure 1.1:** Global distribution of large submarine canyons, as classified by Harris & Whiteway (2011). Canyons are described as (1) shelf-incising and river associated; (2) shelf-incising; and (3) confined to the slope, or blind. Active continental margins labelled in red, passive in green. From Harris (2012).

cold-water corals and sponge fields (Schlacher et al., 2007; Huvenne et al., 2011; Davies et al., 2014). However, enhanced particle transport through submarine canyons can also complicate the routing and engineering of subsea infrastructure, as the sediment flows that occur within canyons can damage seafloor telecommunications cables (which today carry over 99% of intercontinental data traffic; Carter et al., 2014), and oil and gas pipelines (e.g. Syahnur et al., 2015; Sequeiros et al., 2019). While cable and pipeline routes are typically chosen to avoid crossing submarine channels, it is not always possible, particularly in locations where canyons extend beyond the continental shelf and 100s-1000s of km into the deep sea (e.g. Carter et al., 2014; Pope et al., 2017a,b; Talling et al., 2021).

Despite their importance, the processes that control particle transport in submarine canyons and channels remain poorly understood in comparison to rivers, which geomorphologically share many similarities (Shepard, 1981; McGregor et al., 1982; Mitchell, 2005, 2006; Straub et al., 2007; Amblas et al., 2018). Unlike fluvial systems, very few direct measurements of sediment transport processes exist in submarine canyons, and even fewer record at multiple locations within a submarine canyon system (e.g. Paull

et al., 2018). Additionally, many of these studies measure events distal from the original source (e.g. Cooper et al., 2013; Azpiroz-Zabala et al., 2017; Zhang et al., 2018), at low resolution, or for short time intervals (e.g. days to months), therefore missing annual or longer cycles (e.g. Puig et al., 2004). To develop our understanding of the processes that govern the frequency, magnitude and timing of sediment transport we require high temporal resolution of events from coastal source to deep sea sinks over long (>years) timescales. This is integral for our knowledge of global sediment dynamics, the ultimate fate of organic matter and pollutants, assessing geohazards and informing ecological conservation.

## 1.2 Thesis Aims, Objectives and Structure

The overall aim of this thesis is to quantify the frequency and timing of turbidity currents and other sediment transport events in and proximal submarine canyons, and to what extent the mechanisms that initiate, precondition and trigger these sediment transport events relate to their magnitude (i.e. velocity and runout). To address this aim, there are three key research questions as follows:

**Question 1: What is the controlling factor in turbidity current activity and timing – system preconditioning or external triggers? (Chapter 2)**

**Question 2: How do preconditioning and triggering mechanisms combine to enhance turbidity current activity? (Chapter 3)**

**Question 3: What controls sediment transport in submarine canyons during sustained periods of turbidity current inactivity? (Chapter 4)**

This thesis focuses on three physiograpically diverse localities that feature unusually detailed and temporally-extensive (18 months to 5 years) monitoring data: (1) Monterey Canyon, offshore California, USA; (2) Bute Inlet, British Columbia, Canada; and (3) offshore North Mozambique, East Africa. See Section 1.7 for more detail on each of these study sites with an overview of each of the research questions.

The structure of the thesis is as follows: This first chapter (Chapter 1) outlines the research drivers (Sections 1.1 and 1.2), provides context for the research questions that are addressed in this thesis (Sections 1.3 to 1.6), and briefly introduces the study areas, with explanation of why the sites were chosen (Section 1.7). Chapters 2 and 3 aims to identify the drivers of turbidity current activity in submarine canyons and channels where sediment supply is high. Specifically, Chapter 2 seeks to understand the controls on turbidity current activity; is it large external triggers such as earthquakes, storms, or river floods, or the factors that precondition the system for turbidity current generation? Chapter 3 then builds on this, and explores how preconditioning and triggering

mechanisms combine to increase turbidity current likelihood. Chapter 4 then identifies the mechanisms that control sediment transport in submarine canyons, where sediment supply, and therefore turbidity current activity, is greatly reduced. Finally, Chapter 5 revisits the original research questions, providing answers and discussing and synthesising key findings, and outlines future directions for research that have arisen from this study.

## 1.3 Sediment Transport Mechanisms in Submarine Canyons

The mechanisms that transport and deposit sediment through submarine canyons and on the continental slope fall between a continuum of down-slope, episodic, and gravity driven sediment flows (e.g. turbidity currents), to along-slope, semi-permanent and density driven contour currents (e.g. thermohaline circulation). This thesis focuses on the role of turbidity currents and internal currents within submarine canyons as mechanisms of sediment transport, and how these processes interact with ocean bottom current circulation.

### 1.3.1 Turbidity Currents

Turbidity currents are sediment-laden density flows that may include a dense ($\gg$10% volume) near-bed layer, overlain by clouds of more dilute suspended sediment (Fig. 1.2 Bagnold, 1954; Eggenhuisen et al., 2017; Paull et al., 2018; Wang et al., 2020). These submarine flows are considered the dominant process of transporting sediment through submarine canyons and channels (e.g. Twichell & Roberts, 1982; Shanmugam, 2000; Paull et al., 2011; Talling et al., 2012; Talling, 2014). For example, an individual turbidity current can transport more than ten times the annual sediment for all the world's rivers (Milliman & Syvitski, 1992; Talling, 2014, and references therein), be more than 200 km wide (Talling et al., 2007) and runout >100s-1000s of km (Piper et al., 1999; Carter et al., 2012; Talling et al., 2021). Previous studies that reported sequential seafloor cable breaks, inferred velocities of up to 20 $ms^{-1}$ (e.g. Gaoping Canyon, offshore Taiwan; Hsu et al., 2008) and, in some locations, detailed monitoring has revealed that individual flows can last for several days (e.g. Congo Canyon, offshore Angola; Azpiroz-Zabala et al., 2017).

Recent work by Paull et al. (2018) has described the anatomy of turbidity currents in the Monterey Submarine Canyon, offshore California (Fig. 1.2). Here turbidity currents are interpretted to first initiate following failure of the loosely packed sand in the canyon axis or flanks (Fig. 1.2c) forming a dense fast-moving layer that accelerates down-slope (Figs. 1.2b, c: Stages 1, 2). Shear between the dense remobilized layer and overlying

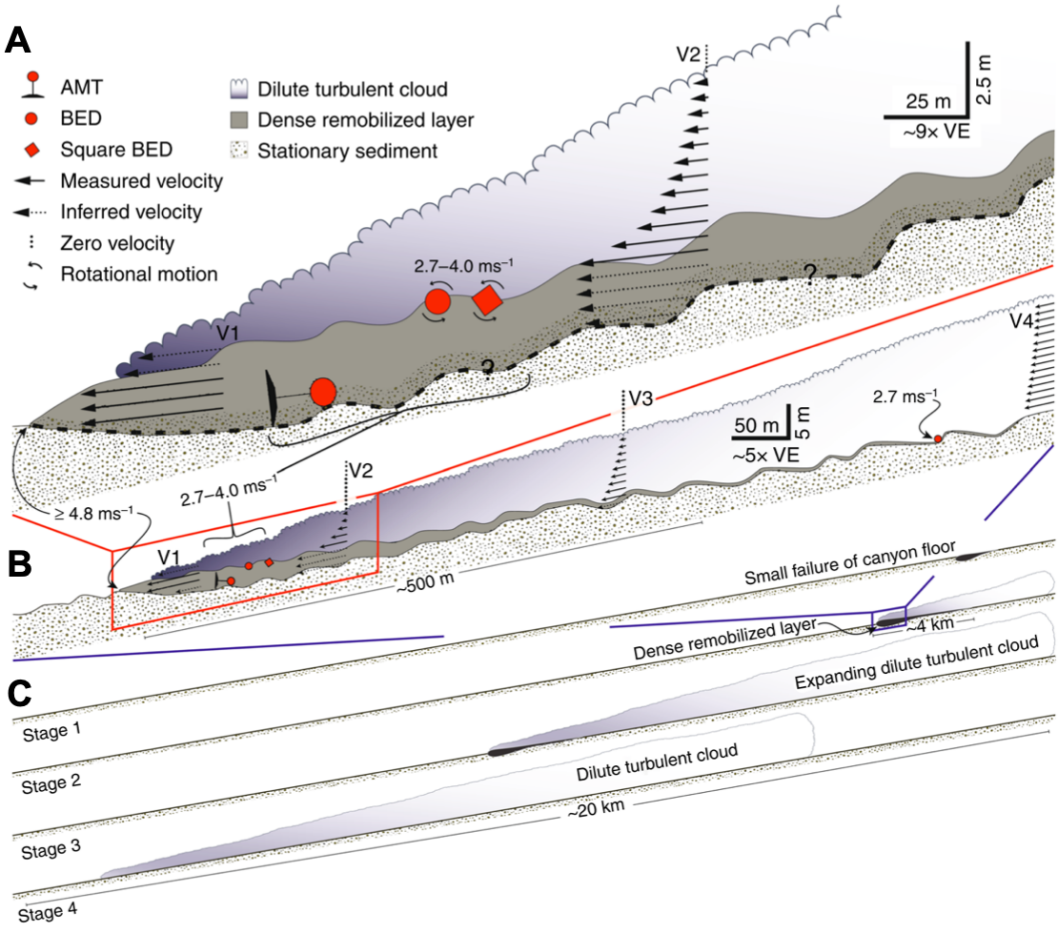


**Figure 1.2:** Conceptual structure and evolution of a turbidity current in Monterey Canyon, offshore California adapted from Paull et al. (2018). (A) The highest velocities, labelled as V1 occur in a dense remobilised sediment layer near the front of the turbidity current. (B) The velocity of the remobilised layer decreases coincident with increased water column turbidity. (C) The evolution of a turbidity current as it moves down-canyon. Stage 1, slope failure (NB. Turbidity current do not always initiate through slope failure (see Section 1.4); stage 2, failed sediment propagates down-canyon as remobilised layer; stage 3, fast flow progressively generates an expanding dilute turbulent cloud which; stage 4, continues as a turbidity current. BED refers to benthic event detector, this is a motion sensor encased in boulder-sized housing that was initially buried in the seafloor and then carried down-canyon with turbidity currents. The AMT (Acoustic Monitoring Transponder) is an 850-kg frame which also holds a BED.

water causes mixing (Figs. 1.2b, c: Stages 2, 3) that generates an overlying dilute, turbulent sediment-suspension (Fig. 1.2a: V1, V2). Following the initial passing of the dense turbidity current head, the tail consists of a more turbulent sediment that can last for several hours (Figs. 1.2b, c: Stage 4).

The high sediment concentration coupled with the high velocities of turbidity currents mean such flows can be very powerful. Turbidity currents in Monterey Canyon, offshore California, were shown to be capable of carrying exceptionally heavy (800 kg) objects at speeds of $>4$ ms$^{-1}$ for many kilometres (Paull et al., 2018). These powerful

turbidity currents pose a significant hazard to subsea infrastructure. The role of turbidity currents as a geohazard was first recognised following a series of seafloor cable breaks in the mouth of the Congo River and shallow regions of the connected Congo Canyon, offshore Angola, in the early 1900s (Heezen et al., 1964), and as a result of a series of sequential seafloor cable breaks that occurred over a distance of 700 km offshore from Newfoundland, East Canada, in 1929 (Heezen & Ewing, 1952; Piper et al., 1999). In both cases, the breaks were linked to turbidity currents. Despite our knowledge of these instances of damage by turbidity currents, fibre-optic cables breakages still occur in submarine canyons. For example, broken or damaged cables following inferred turbidity current activity are common in the Gaoping Canyon, offshore Taiwan. There, cable breaks were recorded during 2006, 2009, 2010 and 2015 (Hsu et al., 2008; Carter et al., 2012; Liu et al., 2012; Gavey et al., 2017; Pope et al., 2017a,b). Similarly, a turbidity current was recorded >1,000 km offshore in the Congo Canyon resulting in cable breaks and slowing regional data traffic during the early stages of the COVID-19 pandemic (Talling et al., 2021). We increasingly rely on these seafloor connections to provide stable internet connections, for financial trading and for data transfer; hence there is a compelling need to understand the factors that control turbidity current activity, and assess when and where they are likely to occur.

### 1.3.2 Internal Canyon Tidal Currents

Submarine canyons can be efficient generators of internal tides (i.e. internal gravity waves with tidal frequencies) through topographic influence on barotropic tides (Bell Jr, 1975; Baines, 1982), or trapping and channelling energy towards the canyon head (Gordon & Marshall, 1976; Hotchkiss & Wunsch, 1982). Current energy tends to be elevated near-bed, where strong (>1 $ms^{-1}$) tidal currents are capable of resuspending and transporting sediment between turbidity currents, or dominate sediment transport in systems with little or no turbidity current activity (Shepard, 1976; Petruncio et al., 1998; Lee et al., 2009; Martín et al., 2011; Shanmugam, 2013; Aslam et al., 2018; Maier et al., 2019b). Where particularly strong currents exist, the tidal influence has also been observed on the shelf adjacent to canyons (Stow et al., 2013). The net direction of sediment transport through internal currents can be highly variable. Observations of net down-canyon sediment fluxes in Whittard Canyon, offshore Ireland, and Monterey and Eel Canyons, offshore California have been attributed to the reflection of internal waves when hitting steep bathymetry in canyon heads (Petruncio et al., 1998; Zhao et al., 2012; Hall et al., 2014, 2017; Waterhouse et al., 2017; Maier et al., 2019b). However, measurements from the Lisbon-Setúbal and Cascais Canyons, offshore Portugal, demonstrated net up-canyon sediment transport (de Stigter et al., 2011). Understanding the dynamic and spatial variation of internal currents is therefore key to our knowledge of sediment transport and deposition in submarine canyons.

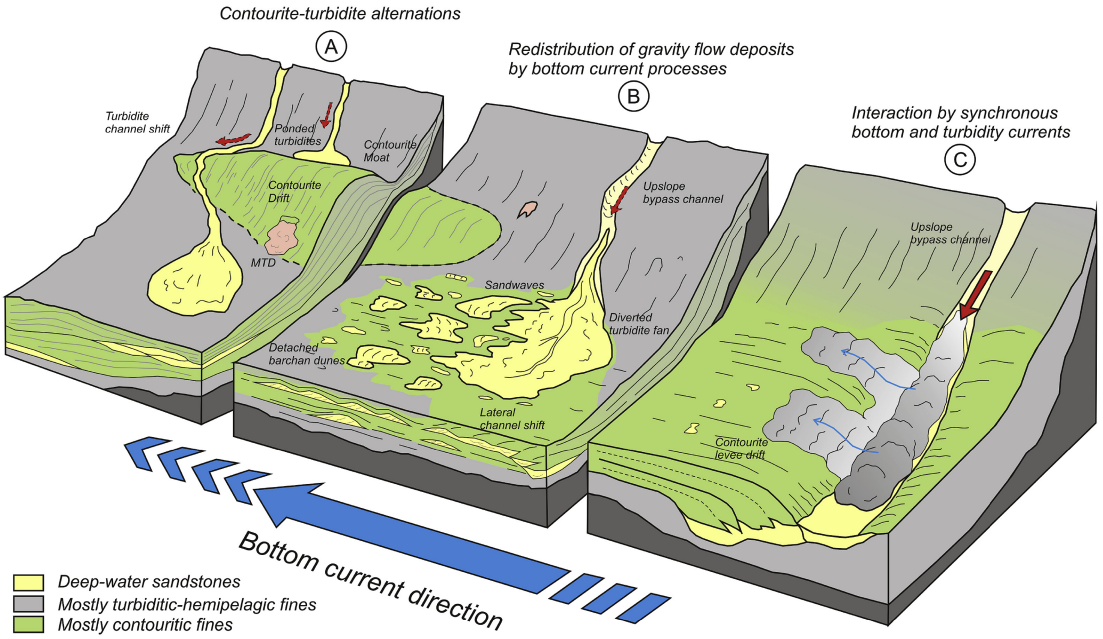


**Figure 1.3:** Conceptual deep-water depositional processes for the interaction of sediment gravity flows and bottom currents from Fonnesu et al. (2020). (A) Contourite-turbidite alternations where contourite drifts and moats influence the pathway of turbiditic channels. (B) Redistribution of gravity flow deposits by contour-current processes. (C) Synchronous interaction where along-slope contour current deflects a down-slope turbidity current. The red arrows indicate gravity flow pathways, blue arrows indicate the direction and effect of bottom currents.

### 1.3.3 Contour Current Interaction

A contour current refers to a density-driven current which flows along slope, subparallel to bathymetric contours on a semi-permanent basis. While these currents move at much slower velocities than turbidity currents (typically much less than 1 $ms^{-1}$; Rebesco et al., 2014, and references therein), their persistence over many millions of years can rework and deposit sediment to form extensive (100s km long) and thick (up to kms) sediment drift deposits (e.g. contourites; Faugères & Stow, 2008; Rebesco et al., 2014). These deposits are important for palaeoclimate reconstructions (e.g. Camerlenghi et al., 1997; Sagnotti et al., 2001; Lucchi et al., 2002a,b; Grützner et al., 2003, 2005; Villa et al., 2003; Amblas et al., 2006), hydrocarbon exploration (e.g. Viana et al., 2007; Brackenridge et al., 2013; Shanmugam, 2013; Stow et al., 2013) and geological hazard assessments (Laberg & Camerlenghi, 2008).

It is increasingly being recognised that contour currents and turbidity currents rarely operate in isolation, and that mixed depositional systems may be the norm; wherein down- and along-slope processes interact. These interactions are most pronounced where along-slope contour currents orthogonally intersect down-slope oriented submarine canyons or channels, either directly deflecting sediment suspended by gravity

flows, or shaping the morphology during periods when gravity flows are not operational (e.g. Mulder et al., 2008; Hernández-Molina et al., 2017; Sansom, 2018; Miramontes et al., 2019; Fonnesu et al., 2020; Fuhrmann et al., 2020, 2021; Pandolpho et al., 2021; Rodrigues et al., 2021, Fig. 1.3). These dynamic interactions can modify sediment transport regimes, controlling the distribution and fate of sediments, organic carbon, nutrients, and anthropogenic particles such as microplastics (Viana et al., 2007; Maier et al., 2019b; Kane et al., 2020). However, in comparison to turbidity currents, contour current and contourite research is still in its infancy and very few detailed measurements of near-bed contour currents exist (Rebesco et al., 2014; McCave et al., 2017).

## 1.4 Mechanisms of Turbidity Current Initiation

While internal canyon currents and contour currents are semi-permanent, turbidity currents are episodic events. The mechanisms of turbidity current initiation are variable, and are typically presumed to be a function of physiographic setting (i.e. river-connected or -disconnected submarine canyons; Fig. 1.4). In this thesis, *initiation* mechanism refer to the process(es) whereby a turbidity current is generated (unlike a *trigger*, see Section 1.5, which is a short-lived event which instantaneously results in turbidity current initiation). The main mechanisms of initiation are outlined below:

### 1.4.1 Hyperpycnal Flow

River plumes that are denser than seawater (>40 kg $m^{-3}$ of sediment) are theoretically able to initiate turbidity currents though direct (hyperpycnal) plunging. However, such an initiation mechanism is rare in marine settings due to the density contrast between seawater and freshwater. For example, in a study of 150 rivers by Mulder & Syvitski (1995), only 6 % had a sediment concentration sufficient to enable direct plunging. Turbidity currents initiating through hyperpycnal flows have only been monitored in two submarine canyons, the Var Canyon, Mediterranean Sea (Khripounoff et al., 2009, 2012), and the Gaoping Canyon, offshore Taiwan (Carter et al., 2012; Liu et al., 2012, 2013). In both settings turbidity currents occurred during river flood peaks.

### 1.4.2 Convective River Plume Sediment Settling

Experiments have shown that turbidity currents can initiate from a more dilute river plume (as low as 1 kg $m^{-3}$ of sediment) if suspended sediment concentrations locally become denser than seawater (Parsons et al., 2001). Sediment concentrations in ~40 % of rivers in the Mulder & Syvitski (1995) database have the potential to produce

sediment plumes above this threshold, most commonly at small mountainous river deltas (Mulder & Syvitski, 1995; Mulder et al., 2003).

### 1.4.3 Sediment Release from Turbidity Maximum Zone

Very dilute river plumes can generate turbidity currents where suspended sediment accumulates to form a turbidity maximum zone. For example, direct monitoring of the Squamish River plume, British Columbia, Canada by Hage et al. (2019) revealed sediment plume concentrations were highest at low water during spring tides in the interface between fresh river water and saline fjord water (i.e. the turbidity maximum). A combination of elevated river discharge and low tide then forces the turbidity maximum away from the delta lip and onto the steeper part of the delta where a turbidity current may initiate and be maintained as a result of erosion and incorporation of unconsolidated sediment on the delta slope.

### 1.4.4 Slope Failure

Submarine slope failures can occur either abruptly as a result of slope oversteepening (e.g. Prior et al., 1981), gradually by retrogressive breaching (e.g. Mastbergen & Van den Berg, 2003), due to external loading (e.g. earthquake, storm waves, human activities; Prior & Bornhold, 1989; Piper & Savoye, 1993; Mulder et al., 1997; Wright & Rathje, 2003), or through generation of excess pore pressures in the subsurface (e.g. Masson et al., 2010; Dugan & Sheahan, 2012; Talling et al., 2014). The mixing of sediment with seawater during the down-slope runout of submarine landslides can result in the sediment body disintegrating, therefore enabling turbulence to suspend sediment and turbidity current generation (Felix & Peakall, 2006). The runout of a turbidity current initiated through slope failure is typically far greater than the toe of the submarine landslide deposit (Hizzett et al., 2018) and may extend for many 100s of km (e.g. Piper et al., 1999; Talling et al., 2007).

### 1.4.5 Sediment Resuspension

Sediment may be resuspended following storms, strong internal currents, or human activity (see Sections 1.5.2 and 1.5.4). Such processes can produce shelf sediment plumes or result in sediment becoming trapped within nepheloid layers near the canyon head. Recent monitoring has shown that both cases may generate turbidity currents, even in sediment starved systems (e.g. Normandeau et al., 2020). These flows can last for several days but are usually very dilute ($<$0.001 vol.% sediment density) and relatively slow moving (0.5 $ms^{-1}$). However, in some cases much faster turbidity currents (2 $ms^{-1}$) have been recorded where heavy ($\sim$200 kg) instrument blocks were transported

down canyon (Inman et al., 1976; de Stigter et al., 2007; Martín et al., 2011; Normandeau et al., 2020).

## 1.5 Mechanisms of Turbidity Current Triggering

A *trigger* is described as a short-lived event which can instantaneously result in turbidity current initiation. This section outlines mechanisms that have previously been attributed to trigger flows:

### 1.5.1 River Delta Processes

As outlined in Section 1.4 sediment discharge from rivers can directly initiate turbidity currents through a hyperpycnal flow, sediment settling from the river plume or sediment release from a turbidity maximum. Turbidity current timing at river deltas has also been linked to low tide (Figs. 1.4a). For example, tidal unloading on seabed sediments increases the susceptibility of the slope to fail (see Section 1.5.5; Ayranci et al., 2012; Hughes Clarke et al., 2014; Clare et al., 2016; Lintern et al., 2016), especially following gas bubble expansion in organic rich sediments (Christian et al., 1997). Furthermore, the shear stress on the delta lip may be amplified at low tide resulting in flushing of sediment from the delta top increasing sediment concentration in the river surface plume or turbidity maximum zone, thereby increasing the likelihood of a turbidity current (Clare et al., 2016; Hughes Clarke, 2016; Hage et al., 2019).

### 1.5.2 Oceanographic Processes

Oceanographic and river delta processes can combine when submarine canyons and channels are river-connected (Fig. 1.4b). However, >97 % of all submarine canyon systems globally have no direct connection to rivers (Fig. 1.1; Harris & Whiteway, 2011). In such systems the following processes are the likely dominant mechanisms of turbidity current triggering:

#### 1.5.2.1 Storms

Storms can trigger turbidity currents either through (1) dynamic wave loading, or; (2) sediment resuspension as a result of wave action (Fig. 1.4c). Dynamic wave loading alters pore pressures where wave crests increase pore pressures while troughs generate seepage pressures (Seed & Rahman, 1978). Where pore pressures are able to build over time this can promote liquefaction of the sediment, therefore triggering a slope failure

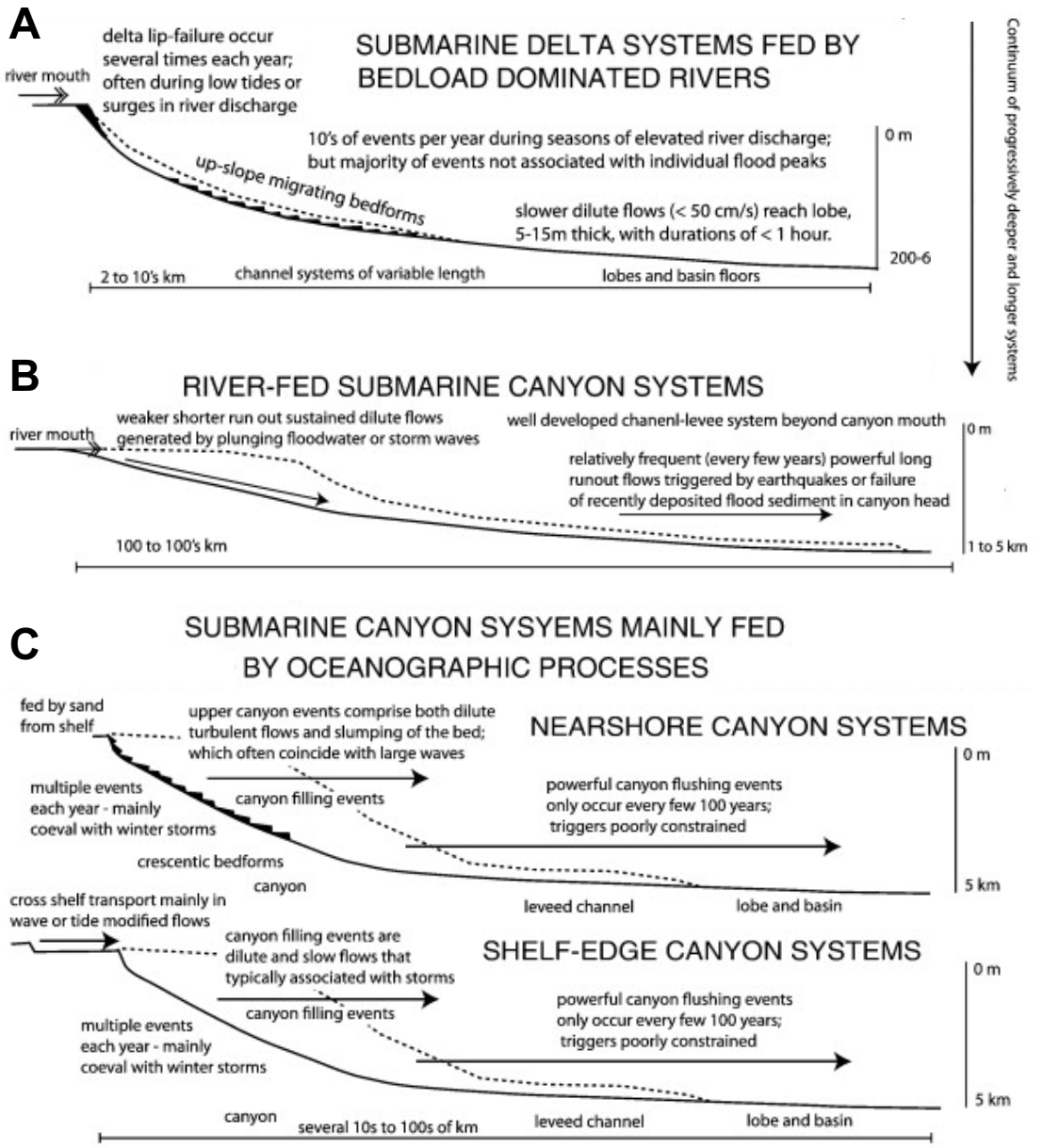


**Figure 1.4:** Generalised models of flow types, frequency, triggering mechanisms and runout distances in different physiographic settings adapted from Talling (2014). (A) Submarine delta systems associated with bedload dominated rivers where suspended sediment concentration is too low to form hyperpycnal flows. (B) River-fed submarine canyon systems where the canyon head is connected to a major river mouth. (C) Submarine canyon system fed by oceanographic processes. Canyon head may be close to shore to intercept littoral cells or located near the shelf edge.

(e.g. Chamberlain, 1964; Prior & Bornhold, 1989; Puig et al., 2008). Increased wave energy during storms also results in enhanced near-bed suspension of sediment, which then has the potential to initiate a turbidity current. This can occur in the head of a canyon (e.g. Inman et al., 1976; Puig et al., 2004), or result in transport of sediment up-canyon (e.g. Normandeau et al., 2020), or from the surrounding shelf to the canyon head (e.g. Carson et al., 1986).

#### 1.5.2.2 Dense-Water Cascading

Cascades of dense water can resuspend and transport sediments. This meteorologically-driven oceanographic phenomenon occurs following the formation of dense shelf water either by cooling, evaporation or freezing. The density contrast results in a gravity driven current which flows down the continental shelf (Killworth, 1983; Ivanov et al., 2004). Submarine canyons channelise cascades of dense water, and sediment transport events as a consequence of this phenomenon have been recorded in multiple canyons located within the Gulf of Lions, Mediterranean Sea (Canals et al., 2006, 2009; Ogston et al., 2008; Palanques et al., 2008, 2011; Puig et al., 2008) and West Halibut Canyon, offshore Newfoundland (Puig et al., 2013a).

#### 1.5.2.3 Internal Canyon Currents

Strong internal canyon currents and periodic internal wave sediment resuspensions have been recorded in a number of canyons in physiographically diverse settings (Fig 1.4). This includes river-connected submarine canyons such as the Gaoping Canyon, offshore Taiwan (Liu et al., 2010), the river-disconnected Monterey (Xu et al., 2002; Maier et al., 2019b) and Mugu (Xu et al., 2010) Canyons, offshore California and shelf-separated systems such as the Halibut Canyon, offshore Newfoundland (Puig et al., 2013a). Such resuspensions may trigger turbidity currents (see Section 1.4.5; de Stigter et al., 2007; Martín et al., 2011).

### 1.5.3 Large External Triggers

Previous studies on turbidity current triggering commonly infer that flows are caused by major external triggers such as earthquakes, tropical cyclones and floods. However, while there are a number of examples where large events have triggered turbidity currents, these are not always a prerequisite.

#### 1.5.3.1 Earthquakes

Earthquake shaking can trigger turbidity currents via slope failures. This was most famously shown by the 1929 Grand Banks event, where a 7.2 $M_W$ earthquake-triggered a turbidity current was recorded by sequential cable breaks extending up to 720 km offshore (Heezen & Ewing, 1952; Piper et al., 1999). More recently, the 2016 7.8 $M_W$ Kaikōura earthquake, offshore New Zealand, triggered a turbidity current with a runout of >680 km through the Hikurangi submarine channel (Mountjoy et al., 2018). Furthermore, cable breaks have been detected in the Goaping Canyon, offshore Taiwan in 2006 and 2010 (Fig. 1.5a; Hsu et al., 2008; Carter et al., 2012, 2014; Gavey et al., 2017; Pope

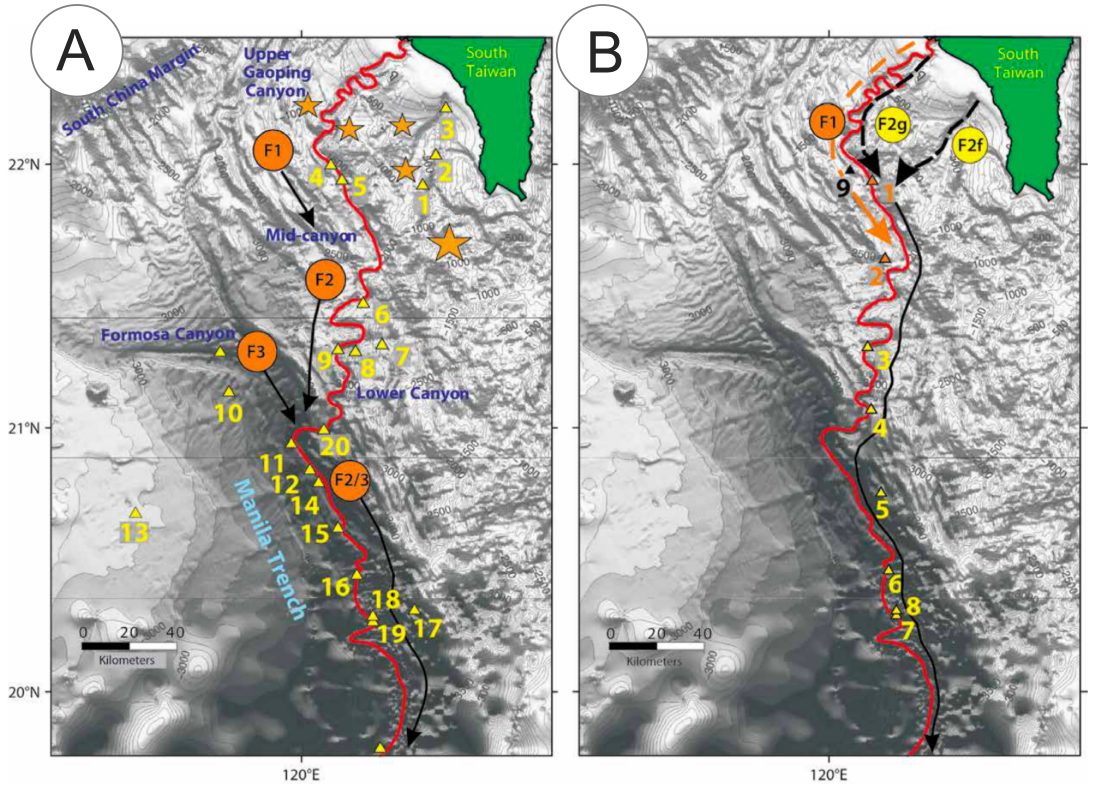


**Figure 1.5:** Cable breaks in the Gaoping Canyon, offshore Taiwan, from Carter et al. (2014). Following (A) the 2006 Pingtung earthquake (epicenters of main and aftershocks = stars) when landslides and at least three sediment density flows (F1–3) were formed and damaged 22 cables crossing the Gaoping/Manila Trench system; and (B) Typhoon Morakot when two flows formed, F1 during a phase of hyperpycnal conditions associated with river flood discharge, and F2 three days later, potentially through the failure of sediment deposits in either Gaoping (F2g) or Fangliao (F2f) Canyons. Triangles are the cable breaks numbered in sequence of timing, where time data was available.

et al., 2017a), offshore Japan (Pope et al., 2017a) and offshore Algeria (Cattaneo et al., 2012) following large (6.4-9.0 $M_W$) earthquakes. As such, the deposits of turbidity currents (turbidites) are becoming increasingly used as a tool to reconstruct past records of earthquakes, capable of extending beyond instrumental or historical archives (Goldfinger, 2011; Howarth et al., 2021).

Insights from a global database of fibre-optic cable breaks have, however, shown that not all >7 $M_W$ earthquakes generate damaging turbidity currents (Pope et al., 2017a). In addition, some of the largest recent earthquakes have not produced widespread turbidites. This includes the 2004 (9.1 $M_W$) and 2005 (8.7 $M_W$) Sumatran earthquakes (Sumner et al., 2013) and the 2010 8.8 $M_W$ earthquake offshore Chile which also resulted in no failure of the slope (Völker et al., 2011). It is possible this is a consequence of repeated ground shaking resulting in consolidation and strengthening of seafloor sediments (Lee et al., 1996; Sultan et al., 2004; Vanoudheusden et al., 2004; Völker et al., 2011; Sumner et al., 2013). In some cases, small (3.0-4.0 $M_W$) magnitude earthquakes are capable of triggering cable breaking turbidity currents. As such, the susceptibility

of a slope to failure is more dependent on sediment availability and the mechanical properties of sediment rather than earthquake magnitude (Pope et al., 2017a).

#### 1.5.3.2 Tropical Cyclones

Tropical cyclones have been shown to trigger turbidity currents at a number of localities worldwide (e.g. Bea et al., 1983; Dengler et al., 1984; Carter et al., 2012; Liu et al., 2012, 2013; Pope et al., 2017b; Zhang et al., 2018; Sequeiros et al., 2019; Kawagucci et al., 2020). Tropical cyclones can result in extreme winds, torrential rains and subsequent river floods, large waves and storm surges. As such, turbidity currents may be triggered; (1) synchronous to their passage as a consequence of dynamic loading from storm waves, currents and surges. However, synchronous triggering of turbidity currents is dependent on a number of factors. For example, storm waves must be close enough, and have the ability, to load or resuspend sediment in the canyon head. Additionally, the approach direction of the tropical cyclone can either induce currents that are synchronous with waves (i.e. wave energy is increased), or, if approach is opposite to wave direction, reduce wave energy (Sequeiros et al., 2019). Damaging turbidity currents are more commonly triggered with (2) near-synchronous timing to their passage, as a consequence of peak flood discharges, or (3) indirect or delayed triggering (Fig. 1.5b; Pope et al., 2017b, see Section 1.5.5).

#### 1.5.3.3 Extreme Floods

Modern extreme flooding events are less well monitored than earthquakes and tropical cyclones, but large amounts of sediment can be transported to the ocean during glacial lake outburst floods (GLOFs). For example, a jökulhlaup (GLOF triggered by geothermal heating) from Vatnajökull, Iceland in 1996 transported $\sim$0.07 km$^3$ of sediment offshore during a $\sim$42-hour period (Maria et al., 2000), though it is unclear if this event generated a long runout turbidity current. More recently, in 2020, a GLOF resulted in a turbidity current within a submarine channel in Bute Inlet, a fjord in British Columbia, Canada. This flow had an inferred runout beyond the depositional lobe of the system ($\sim$60 km). The turbidity of the river flowing into Bute Inlet remains elevated at the time of thesis submission and it has been suggested that such events may result in long lasting (decades) increases in sediment delivery (Giesbrecht et al., 2021; Tilston et al., 2021).

### 1.5.4 Anthropogenic Processes

Human activity has previously been shown to result in turbidity current triggering. For example, land reclamation to extend the Nice Airport runway resulted in overloading

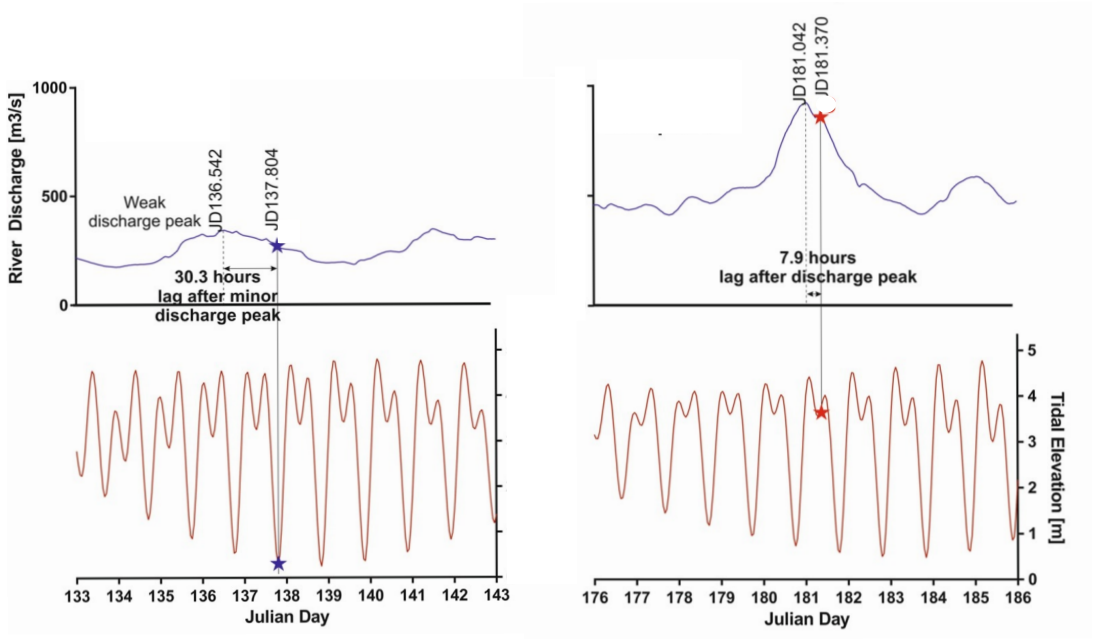


**Figure 1.6:** Time series Squamish River discharge and tidal elevation during two delta-lip failure events during 2011 at the Squamish Delta, British Columbia, Canada, adapted from Clare et al. (2016). Both examples demonstrate a lag period where slope failure (marked with a star) occurs hours after peak Squamish River discharge during a slack water tidal minimum.

of the slope, initiating failure (Piper & Savoye, 1993; Mulder et al., 1997). Bottom trawling is another example of anthropogenic impacts on turbidity current activity. This is a non-selective commercial fishing technique where heavy nets are dragged along the seafloor. Bottom trawling can generate dilute, slow-moving turbidity currents following sediment resuspension (Palanques et al., 2006; Martín et al., 2008; Puig et al., 2012, 2013b; Paradis et al., 2017; Arjona-Camas et al., 2019). Turbidity currents have also been suggested to be triggered following dumping of dredged material (Xu et al., 2004) and the release of mine tailings into the ocean (Normark, 1989; Hay, 1987; Iatrou et al., 2007).

### 1.5.5 Preconditioning

Where turbidity currents initiate through slope failure, *preconditioning factors* are often cited as a factor in flow timing. For example, the development of excess pore pressures will promote failure of the slope (e.g. Masson et al., 2010; Dugan & Sheahan, 2012; Talling et al., 2014), especially where sedimentation is rapid, and pore fluid can be trapped by less permeable 'weak layers' (e.g. Özener et al., 2009; Locat et al., 2014; Gatter et al., 2021). These pore pressures may remain elevated for periods after initial sedimentation (from hours to $\gg$years depending on sediment grain size and hydraulic conductivity; Bennett & Faris, 1979; Major & Iverson, 1999; Iverson, 2005; Fleckenstein et al., 2006; Özener et al., 2009). Such preconditioning has been attributed to delays

between initial sediment input to a system and turbidity current timing in submarine canyons and channels. For example, at the Squamish Delta, British Columbia, Canada (a fjord-head delta), slope failure and subsequent turbidity current lagged peaks of rapid sediment input (i.e. peaks in Squamish River discharge) by hours to days, until ultimate failure at low tide (Fig. 1.6; Hughes Clarke et al., 2014; Clare et al., 2016).

## 1.6 Methods of Monitoring Sediment Transport

### 1.6.1 Conventional Deposit Analysis

Turbidity current activity and sediment transport through submarine canyons has long been assessed based on their resultant deposits and the seascapes that they sculpt: either through seafloor mapping (e.g. sidescan sonar, bathymetry and backscatter; label 1 in Fig. 1.7), subsurface surveys (label 2 in Fig. 1.7) and sediment core sampling and dating (label 3 in Fig. 1.7). However, uncertainty arises when relying on the depositional record, as erosion and complete-reworking of deposits in submarine canyons and channels can occur on daily to monthly timescales (Smith et al., 2005, 2007; Paull et al., 2018; Vendettuoli et al., 2019; Guiastrennec-Faugas et al., 2020; Heijnen et al., 2020), thus providing underestimates of transport activity. Additionally, identifying turbidity current triggers requires measuring the timing of flows and external events with precision. For example, over days to hours, a storm may generate both large wave heights at its peak, and river flooding following its passage (e.g. Pope et al., 2017b). Only in rare occasions (e.g. Ikehara et al., 2014) can deposits be dated to sufficiently high resolution, with dating uncertainties typically too great for robust correlations to potential triggering mechanisms in most instances (Urlaub et al., 2013; Pope et al., 2015).

The properties of the flow are not always obvious from the deposit left behind. For example, submarine channel drift deposits, relating to the interaction of turbidity currents and contour currents, have competing models of formation arising from apparently similar channel geometries and stratigraphic architecture (e.g. Rebesco et al., 2014; Sansom, 2018; Fonnesu et al., 2020; Fuhrmann et al., 2020; Miramontes et al., 2020). Scaled-down laboratory models can be used to link deposits to processes (e.g. Miramontes et al., 2020), however, there are many uncertainties in such models due to a lack of field-scale validation (Talling et al., 2013, 2015).

### 1.6.2 Emerging Techniques and In-situ Measurements

In-situ measurements of turbidity currents has historically relied on breaks in the seafloor network of fibre-optic cables to determine the flow paths, velocities and timing (e.g. Heezen & Ewing, 1952; Heezen et al., 1964, 1966, 1969; Krause et al., 1970; Piper

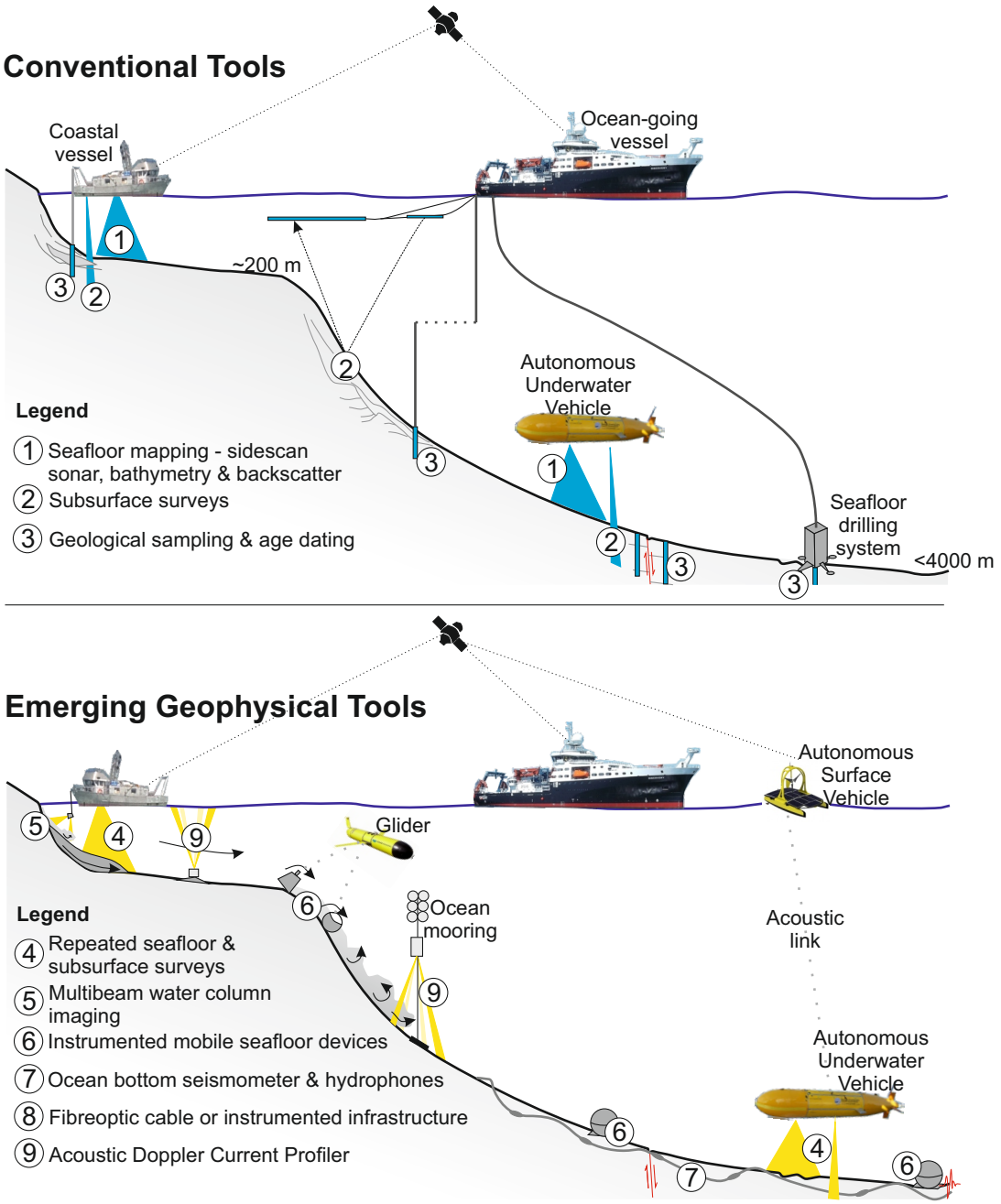


**Figure 1.7:** An overview of conventional tools for monitoring deposits of sediment transport processes and emerging geophysical tools to directly monitor offshore sediment transport. Adapted from Clare et al. (2017).

et al., 1999; Hsu et al., 2008; Carter et al., 2009, 2012, 2014; Cattaneo et al., 2012; Gavey et al., 2017; Pope et al., 2017a,b; Talling et al., 2021). However, cable breaks will not record less powerful (i.e. lower velocity and sediment concentration) turbidity currents, nor other internal or thermohaline currents that interact with, but do not damage a cable. Furthermore, transit velocities derived from cable breaks (i.e. based on the distance between breaks and their relative timings) assume the front of a turbidity current is responsible for the break, which is not always the case (e.g. Sumner & Paull, 2014).

Direct measurements of flow properties in submarine canyons were first made using fixed-point current meters that recorded at a single elevation above the seafloor. Early studies (e.g. Inman et al., 1976; Prior et al., 1987) measured internal canyon currents along with episodic down-canyon pulses (up to 3 $ms^{-1}$) capable of transporting coarse sediment. While many more recent studies have continued to deployed point-current meters (e.g. Khripounoff et al., 2003; Puig et al., 2004; Xu et al., 2010; Martín et al., 2011), technological advancements in direct flow monitoring over the past two decades have led to a step change in our understanding of turbidity current behaviour. This includes the use of: (i) high resolution repeat seafloor surveys to capture turbidity current initiation or the resultant erosion and deposition on the seafloor (label 4 in Fig. 1.7; e.g. Smith et al., 2005, 2007; Hughes Clarke et al., 2012, 2014; Clare et al., 2016; Hughes Clarke, 2016; Mastbergen et al., 2016; Hizzett et al., 2018; Mountjoy et al., 2018; Paull et al., 2018; Sequeiros et al., 2019; Vendettuoli et al., 2019; Guiastrennec-Faugas et al., 2020; Heijnen et al., 2020; Normandeau et al., 2020); (ii) water column imaging to actively view turbidity current interaction with the seafloor (label 5 in Fig. 1.7; Hughes Clarke, 2016; Hage et al., 2019); (iii) weighted mobile sensors which are incorporated in the flow to record velocity and movement (label 6 in Fig. 1.7; Paull et al., 2010, 2018; Hughes Clarke et al., 2014); (iv) networks of hydrophones or ocean bottom seismometers to passively record passing flows (label 7 in Fig. 1.7; Caplan-Auerbach et al., 2014; Lintern et al., 2016) and; (v) instrumented seafloor infrastructure or cables to measure near-bed currents, slope instability and seafloor displacement (label 8 in Fig. 1.7; Lintern & Hill, 2010; Delaney & Kelley, 2015; Lintern et al., 2016, 2019; Hill & Lintern, 2021; Zhan et al., 2021).

### 1.6.3 Acoustic Doppler Current Profilers

This thesis focuses on measurements recorded by acoustic Doppler current profilers (ADCPs; label 9 in Fig. 1.7) to monitor the frequency, magnitude and timing of sediment transport processes in submarine canyons (see Section 1.7.2). The number of submarine canyon ADCP deployments globally is increasingly dramatically (as of 2021 ADCP measurements are known in <10 submarine canyons and channels). Previous work has used ADCPs to identify the types, properties and triggers of sediment transport mechanism in submarine canyons (e.g. Xu et al., 2004, 2014; Khripounoff et al., 2012; Cooper et al., 2013; Clare et al., 2016; Azpiroz-Zabala et al., 2017; Paull et al., 2018; Guiastrennec-Faugas et al., 2019; Maier et al., 2019b; Heerema et al., 2020; Normandeau et al., 2020).

The ADCPs used throughout this thesis include four transducers each mounted at a 20-degree angle (relative to vertical) on the instrument to emit and then receive sound pulses, or pings, along four beams (Fig. 1.8a). Current measurements over a specified depth range are recorded in a series of interval bins (Fig. 1.8a) based on changes in the Doppler shift intensity of the backscattered acoustic signal (Griffiths & Flatt, 1987).

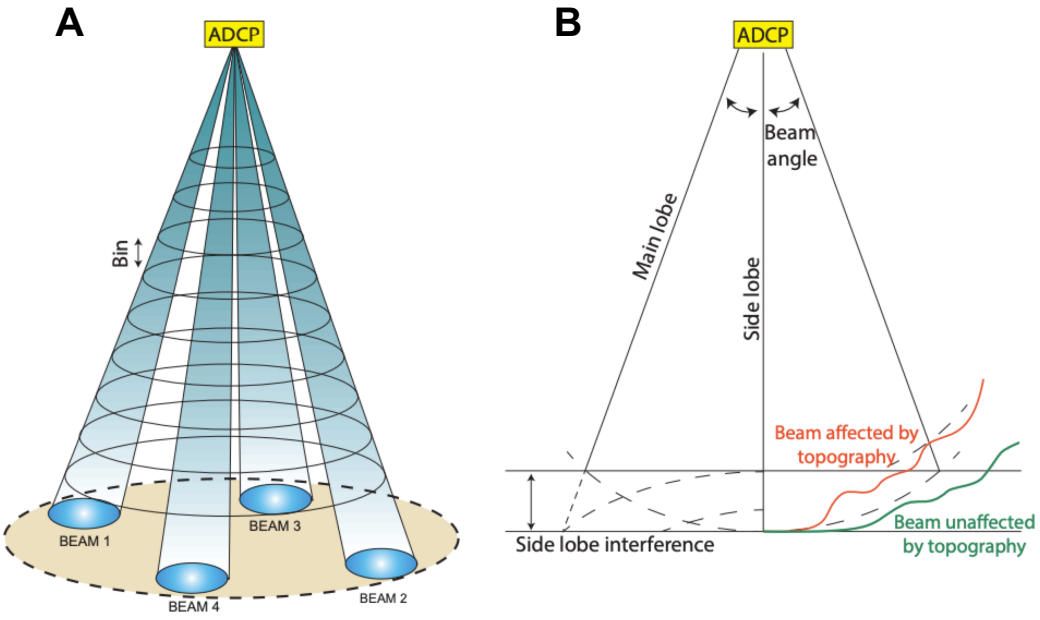


**Figure 1.8:** Basic working principles of an acoustic Doppler current profiler (ADCP) modified from Clare et al. (2020) and Heerema (2021). (A) Diagram to show configuration of the four ADCP beams where velocity and echo intensity are calculated for set binned intervals. (B) A schematic to show how beam interaction with a topographically variable seafloor may reduce data quality.

Three of the ADCP beams allow for measurements of the three-dimensional velocity field for each bin (i.e. north, east and up velocity), with the fourth beam allowing for an estimate of measurement error. The size of each measurement bin is governed by the instrument frequency; a higher frequency will result in more detail, though this will decrease the range as energy will dissipate more quickly. The echo intensity (i.e. strength of signal return) provides a qualitative proxy for sediment concentration, where higher echoes represent greater concentration. More robust estimates for suspended sediment concentration can be calculated if the echo intensity is corrected for acoustic attenuation and a single grain size is assumed (Azpiroz-Zabala et al., 2017; Simmons et al., 2020).

ADCPs can be installed either so the beams face upwards or point down towards the seafloor. Upward facing instruments deployed from a seabed frame have yielded valuable direct measurements of sediment transport (e.g. Paull et al., 2018; Eidam et al., 2019). While such a configuration is useful for measuring ocean currents or dilute turbidity currents, it can leave the instrument susceptible to damage from passing turbidity currents with higher sediment concentrations or dense near-bed layers (e.g. Paull et al., 2018; Wang et al., 2020). Turbidity current monitoring studies therefore, more typically, configure down-looking ADCPs moored to the seafloor with heavy anchor weights and wire rope to connect to a high buoyancy float (e.g. Xu et al., 2010; Xu, 2011; Cooper et al., 2013; Xu et al., 2014, 2013; Azpiroz-Zabala et al., 2017; Paull et al.,

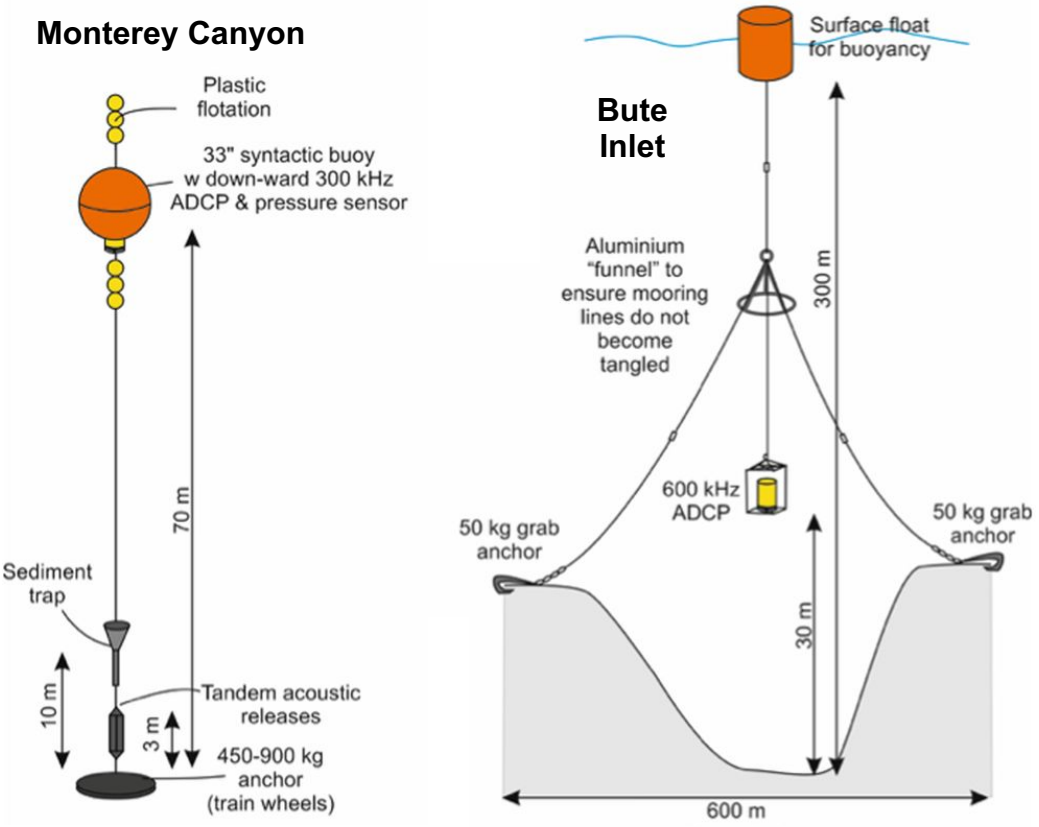


**Figure 1.9:** Comparison of subsurface single-point moorings deployed in Monterey Canyon, offshore California (Paull et al., 2018) and two-point mooring supported by a surface buoy in Bute Inlet, British Columbia, Canada. Modified from Clare et al. (2020).

2018; Talling et al., 2021, Fig. 1.9). While the instrument is positioned above any turbidity current passing below, there have been occasions where a flow will tilt or move the mooring array down-canyon, or in some cases result in the instrument breaking free (e.g. Symons et al., 2017; Paull et al., 2018; Talling et al., 2021). To avoid this ADCPs can be deployed as a surface buoy suspended system with two or more anchors (Fig. 1.9; Clare et al., 2020). This method is typically more practical in shallow water (<500 m) fjord or lake systems, though a two-anchor mooring has previously been successfully deployed in >1200 m water depth in the Var Canyon, Mediterranean Sea (Khripounoff et al., 2012). Other limitations of using downward-looking ADCPs is a 'blanking' zone which occurs if near-bed the flow is too dense or side-lobe interference (i.e. where local bathymetry, such as a canyon wall, protrudes into the beam resulting in an overpowering echo) which typically affects ~6 % of the instrument height above the seafloor (Fig. 1.8b; Sumner & Paull, 2014; Clare et al., 2020).

## 1.7 Study Sites and Research Questions

This thesis will focus on detailed geophysical monitoring datasets, specifically using ADCPs for precise measurements of transport event timing. As outlined above, multiple processes of sediment transport occur in submarine canyons and channels, and mechanisms of turbidity current initiation and triggering are highly variable in different physiographic settings (Fig. 1.4). This thesis focuses on three localities that feature unusually detailed and temporally-extensive monitoring data, that each typify a distinct setting, featuring different mechanisms of sediment supply (Fig. 1.10). These include the oceanographically-fed Monterey Canyon, offshore California and a river-fed submarine channel in Bute Inlet fjord, British Columbia, both of which have high sediment supply, and feature frequent (sub-annual) turbidity currents. In contrast, while the northern Mozambique continental slope is incised by numerous submarine canyons, it is sediment-starved. This sediment-poor system is chosen to understand what controls contemporary sediment transport dynamics in the absence of regular turbidity currents. Understanding the factors that controls sediment transport frequency, timing and magnitude in each of these diverse settings aims to better our understanding of the continuum of particulate transport mechaimsms through subaminre canyons globally.

### 1.7.1 Study Sites

#### 1.7.1.1 Monterey Canyon

Monterey Canyon, located offshore California, USA (Fig. 1.10a), is one of largest submarine canyons on the Pacific Coast of North America (Greene et al., 2002) and perhaps one of the best studied systems on the planet. The head of Monterey Canyon lies within 100 m of the coastline in Monterey Bay, before extending over 300 km offshore to water depths in excess of 4 km (Smith et al., 2005). The Salinas, Pajaro and San Lorenzo Rivers all flow into Monterey Bay, but all three are detached from the head of Monterey Canyon, and therefore provide minor direct sediment input. Instead, sand is supplied through two littoral cells (the Santa Cruz cell to the north, and South Monterey Bay cell to the south) which each terminate at the canyon head (Eittreim et al., 2002; Willis & Griggs, 2003; Farnsworth & Warrick, 2007; Thornton, 2016). Sediment transport to the head of Monterey Canyon is highest during the winter, as the most energetic waves approach from the north-west, diminishing during summer when swells from the south prevail (Patsch & Griggs, 2006).

Recent monitoring has demonstrated that the canyon morphology is capable of generating strong (up to 1 $ms^{-1}$) internal currents which can transport fine-grained sediment and organic matter (Petruncio et al., 1998; Zhao et al., 2012; Hall et al., 2014; Maier

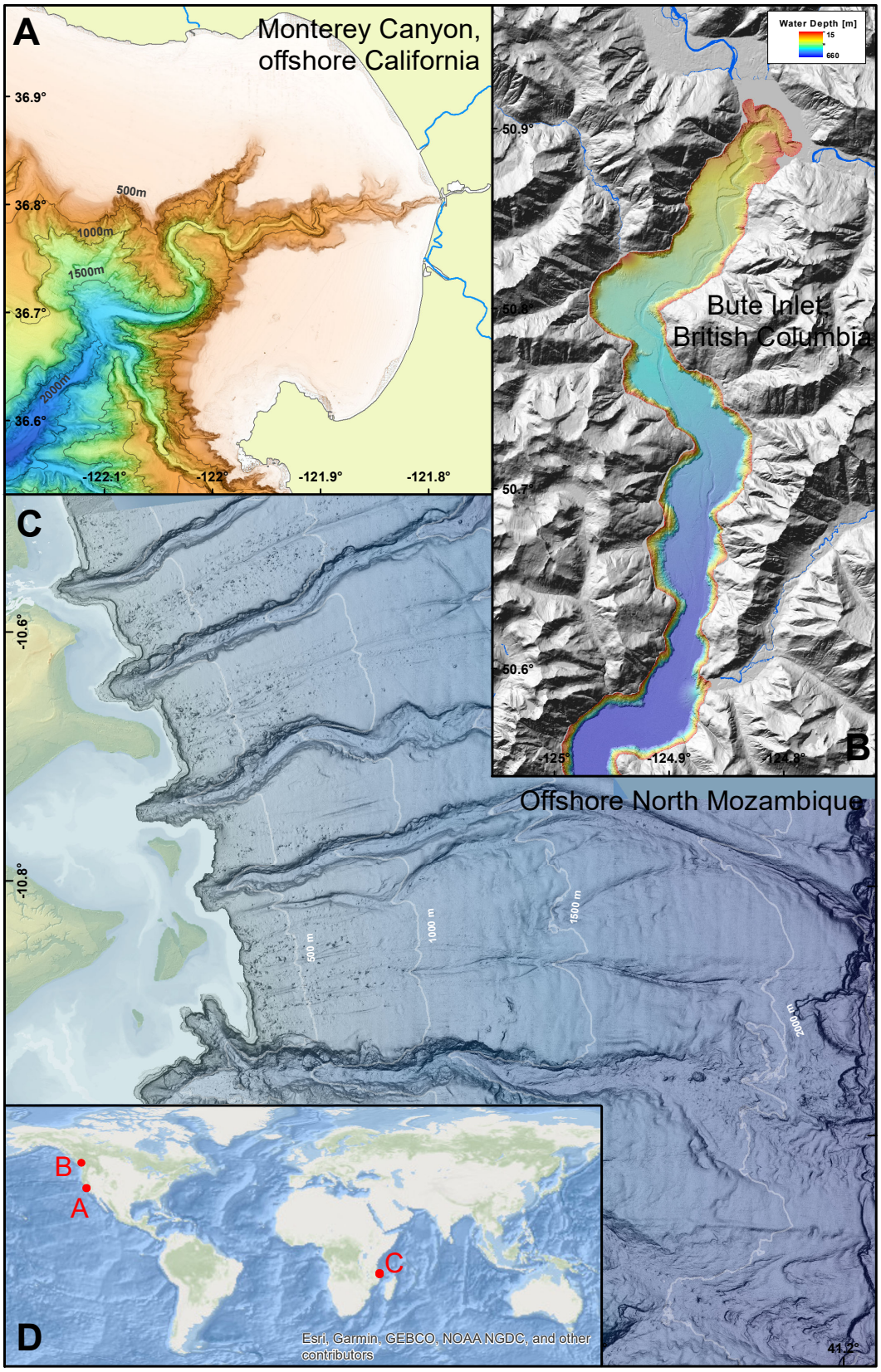


**Figure 1.10:** Direct monitoring study sites used in this thesis to investigate the frequency, timing and magnitude of sediment transport in submarine canyons. (A) Monterey Canyon, offfore California, USA; (B) Bute Inlet, British Columbia, Canada; and, (C) the continental shelf offshore North Mozambiuqe. (D) The global location of each site.

et al., 2019b). However, within the upper 50 km from the head of Monterey Canyon, sediment is dominantly transported down-canyon by frequent (sub-annual) turbidity currents (Paull et al., 2003, 2005, 2010, 2018; Smith et al., 2005, 2007; Xu et al., 2004). Turbidity currents have been recorded with velocities of up to 7.2 $ms^{-1}$ and capable of transporting 1,000 kg instrumented blocks >1 km down-canyon (Paull et al., 2003, 2010, 2018). A number of mechanisms have previously been suggested to trigger turbidity currents. The majority of flow activity has been attributed to storms, yet not all turbidity currents are associated with large wave heights (Inman et al., 1976; Paull et al., 2003, 2010, 2018; Piper & Normark, 2009; Xu et al., 2004, 2014), and other turbidity currents have been linked to river flooding (Parsons et al., 2001), earthquakes (Garfield et al., 1994) and human activity (Xu et al., 2004). Despite the activity in the upper reaches of Monterey Canyon, very few turbidity currents are preserved in water depths beyond 2,800 m where turbidite recurrence is 150-300 years (Fildani et al., 2006; Stevens et al., 2014; Nieminski et al., 2019).

#### 1.7.1.2 Bute Inlet

Bute Inlet is a fjord located within the Pacific Ranges of the Coast Mountains of British Columbia, Canada (Fig. 1.10b). The region is macrotidal, predominantly semidiurnal, with a range of 5 m. Mountains exceeding elevations of 3000 m are common, with many maintaining small ice caps and valley glaciers (Holland, 1976) within the drainage basins of the Homathko and Southgate Rivers, which provide 75% and 19% of the freshwater entering the fjord respectively (Farrow et al., 1983). The flood hydrographs of both the Homathko and Southgate Rivers display a broad peak through May-August associated with enhanced glacial melting during the freshet where discharge can increase by an order of magnitude (e.g. Homathko River, <100 $m^3s^{-1}$ to >1,000 $m^3s^{-1}$). Large, short duration (days) annual river floods are then common during October and November, associated with periods of intense rainfall. The Homathko and Southgate Rivers are the predominant mechanism of sediment input to the fjord, combining to supply 1.6 x $10^6$ $m^3$ of sediment each year (Syvitski & Farrow, 1983).

The delta fronts of the Homathko and Southgate Rivers are characterised by a series of subaqueous channels, which converge into two well-developed channels entering the fjord from opposite sides. These two channels join to form a single sand-rich submarine channel (Prior et al., 1986; Zeng et al., 1991) that continues down-fjord for 40 km to a water depth of 660 m where the channel transitions to a depositional lobe (Conway et al., 2012). Repeat bathymetric mapping of the submarine channel over the past decade has demonstrated its rapid evolution. For example, 5-to-30 m high knickpoints migrate 100-450 m up-channel annually (Gales et al., 2019; Heijnen et al., 2020). Such rapid evolution has been attributed to turbidity current activity. Here, many 10s of

turbidity current occur annually, concentrated during the freshet with almost no flows recorded during the winter (Bornhold et al., 1994).

#### 1.7.1.3 Offshore Northern Mozambique

The present-day northern Mozambique slope lies offshore from a narrow (10-20 km) mixed carbonate-siliciclastic shelf bounded on the seaward edge by a barrier island system and a steep shelf break. A sequence of east-west trending submarine canyons occurs along the continental slope, cutting into the shelf break, and incising up to 200 m vertically (Fig. 1.10c). The morphology of individual canyons is variable, but all terminate at or prior to intersection with the Davie Fracture Zone ~70 km offshore (Franke et al., 2015). The development of the East African Rift System during the Cenozoic strongly modified continental drainage patterns (Roberts et al., 2012; Stagna et al., 2021). As such, present day sediment supply to the canyon heads is very low (Maselli et al., 2020).

Ocean currents offshore Mozambique are complex and can be highly energetic. Surface circulation is strongly influenced southward-bound Mozambique Current which forms part of the Agulhas Current system, the strongest western boundary current in the southern hemisphere (Lutjeharms, 2006). The deeper-water regime (>800 m water depth) is dominated by the north-flowing Mozambique Undercurrent (de Ruijter et al., 2002). The entire water column can also be affected by the formation of mesoscale (>300 km diameter) southward-bound anticyclonic eddies (de Ruijter et al., 2002; Schouten et al., 2003; Ullgren et al., 2016) that can alter the bottom current regime (Miramontes et al., 2019) and may have the potential to resuspend sediment (Zhang et al., 2014).

### 1.7.2 Key Questions

At the core of this thesis are three fundamental science questions relating to the frequency, timing and magnitude of sediment transport events within, and proximal to, submarine canyons or channels. As outlined below, each of these questions will use uniquely detailed direct monitoring datasets from the case study sites to further our understanding in the flux and ultimate fate of sediment, and associated particulate matter, as well as assessing seafloor geohazards and risks to critical subsea infrastructure. Each question has formed the bases of a research publication.

**Question 1: What is the controlling factor in turbidity current activity and timing – system preconditioning or external triggers?**

The timing, frequency and magnitude of turbidity currents is governed by the mechanisms leading to flow initiation and triggering. Testing models for how turbidity currents are triggered requires measuring the timing of turbidity currents and potential triggers with precision. For example, over days to hours, a storm may generate both large wave heights at its peak, and river flooding following its passage (Pope et al., 2017b). Precise timing can be provided by seafloor cable breaks or direct monitoring of turbidity currents; however, cable breaks fail to measure weaker events that leave cables intact, and breakages may not occur at the timing of flow impact (e.g. Sumner & Paull, 2014). ADCP measurements provide an accurate method to record the precise timing of a passing turbidity current. However, previous studies using ADCPs have either collected data at low temporal resolution, or involved instruments located far away from where flows originate (e.g. Cooper et al., 2013; Azpiroz-Zabala et al., 2017; Zhang et al., 2018). Moreover, monitoring instruments have typically been deployed for only a few months, missing parts of annual or longer cycles (e.g Puig et al., 2004). This means that the controls on turbidity currents activity remain poorly tested.

To understand the factors that control turbidity current activity, Chapter 2 investigates the timing of turbidity currents from Monterey Canyon, the site of the most detailed direct monitoring dataset in a deep-sea submarine canyon (Paull et al., 2018). A variety of competing triggering mechanisms (storms, river floods, earthquakes and human activity) make Monterey Canyon an ideal test site to identify common factors in flow timing. Data were collected during the 18-month-long Coordinated Canyon Experiment (CCE) including six moored high-resolution (300 kHz) ADCPs moored ~65 m above the seafloor along the upper 50 km of the canyon axis, along with a dense network of novel equipment (Paull et al., 2018). This uniquely detailed monitoring dataset is used to demonstrate that no consistent triggering mechanism is present for turbidity currents in Monterey Canyon. Instead preconditioning and sediment supply is the controlling factor on flow timing and frequency. Furthermore, comparisons with turbidity current timing in a mud-dominated river-connected system (Congo Canyon, offshore Angola) and a sandy submarine channel connected to a fjord-delta (Howe Sound, British Columbia, Canada) demonstrate that sediment supply is the common driver of turbidity current activity across different physiographic sites.

**Question 2: How do preconditioning and triggering mechanisms combine to enhance turbidity current activity?**

Analysis in Chapter 2 shows that the common driver of turbidity current activity is sediment supply. Such elevations in sediment supply to submarine canyon and channel heads are often highly predictable; for example, during peaks in a river flood hydrograph, or when longshore sediment transport rate is elevated during storm seasons. Therefore, on an annual cycle, periods of enhanced turbidity current activity may be similarly predictable. To build on this, Chapter 3 uses a novel multivariate statistical

approach to combine preconditioning and triggering factors to predict the likelihood of turbidity current occurrence for given environmental conditions.

For a system such as Monterey Canyon, where numerous potential triggering mechanisms exist, the relationship between preconditioning and triggering factors is complex. However, the mechanisms for turbidity current generation are better constrained offshore from river deltas. Here, the combination of increased river discharge preconditioning the system and low tides ultimately triggering flows has previously been described (Ayranci et al., 2012; Hughes Clarke et al., 2012; Clare et al., 2016; Lintern et al., 2016; Hage et al., 2019; Hill & Lintern, 2021). Despite this, the number ($N > 22$) of precisely timed turbidity current field measurements has limited previous work to univariate statistical analysis. Such methods test the significance of individual parameters (i.e. river discharge and tide) in isolation, but so far have not allowed us to investigate multiple coincident environmental factors that combine (often in a non-linear manner or with threshold behaviours) to generate turbidity currents. As such, it has not been possible to develop a model to assess the relative importance of these trigger to predict turbidity current timing.

Chapter 3 analyses the most extensive number ($N = 113$) of field-monitored turbidity currents from source-to-sink in Bute Inlet. Precise (1-hour resolution) turbidity current timing was recorded using six Acoustic Doppler Current Profilers (ADCPs) from the Homathko River Delta to the deep-water channel-lobe over two separate deployment campaigns during 2016 and 2018. These measurements, along with Homathko River discharge and tidal elevation at the time of flow generation, are used to develop an innovative multivariate statistical approach for predicting turbidity current timing at Bute Inlet. The strong predictive power of this model is shown by hindcasting turbidity current activity in Bute Inlet as well as similar physiographic sites (Howe Sound, another fjord-head delta; and the Fraser River, the largest river in western Canada, both British Columbia). This chapter concludes by discussing the application of the predictive model to other submarine canyon systems and its use in assessing geohazard risk to critical seafloor infrastructure.

**Question 3: What controls sediment transport in submarine canyons during sustained periods of turbidity current inactivity?**

Near-bed currents are capable of shaping seafloor morphology during periods when turbidity currents are not operational (e.g. Mulder et al., 2008; Hernández-Molina et al., 2017; Fonnesu et al., 2020; Fuhrmann et al., 2020, 2021) to modify sediment transport regimes, and control the distribution and fate of sediments, organic carbon, nutrients, and anthropogenic particles such as microplastics (Viana et al., 2007; Maier et al., 2019b; Kane et al., 2020). Despite this, our understanding of such interactions, and hence robust reconstruction of past oceanographic regimes, palaeo-climates and modern transport pathways, is hindered by a paucity of direct near-seafloor measurements. While

the number of sites where turbidity currents have been directly monitored using ADCPs over the past decade has increased (e.g. Xu et al., 2004; Cooper et al., 2013; Talling et al., 2015, 2021; Hughes Clarke, 2016; Lintern et al., 2016; Azpiroz-Zabala et al., 2017; Paull et al., 2018; Hage et al., 2019; Miramontes et al., 2019; Normandeau et al., 2020), very few measurements of near-bed contour currents exist (e.g. Rebesco et al., 2014; McCave et al., 2017). Additionally, these previous attempts to monitor such currents using ADCPs have not truly characterised the near-bed regime or spatial footprint of near bed variability. For example, measurements have used low frequency instruments, recorded too far from the seafloor or for short time periods, or only at a single location (e.g. Zhang et al., 2014; Zhao et al., 2015; Steinmann et al., 2020; Wilckens et al., 2021). To fill key gaps in our understanding of deep-sea particulate transport, to calibrate numerical models, and enable robust palaeoceanographic and climatic reconstructions, there is a compelling need to acquire field-scale current measurements as close to the seafloor as possible in contourite-modified mixed systems to determine how magnitude varies: (1) across large spatial areas; (2) in response to variable seafloor relief; (3) over differing timescales (e.g. tidal to seasonal).

Chapter 4 integrates new high-resolution multibeam bathymetric data acquired over a mixed canyon-contourite system offshore Mozambique, where turbidity currents are rare (recurrence time of 100 years), therefore permitting an investigation on the spatial and temporal variation of near-bed currents. This study site spans an area of 65 x 50 km, with direct measurements of near-bed currents made at 35 deep-sea mooring locations over a five-year period. The unusually large number of moorings and extensive seafloor surveying enables the first quantitative characterisation of near-bed currents across the diverse geomorphology of a mixed deep-sea depositional system study area, including within and adjacent to submarine canyons, within linear gullies, and unconfined areas of open slope. In this Chapter direct measurements are used to determine: (1) the net direction and velocity of near-bed currents across the study area; (2) temporal fluctuations in current direction and velocity in; (3) the cumulative effects of near-bed currents on particle transport; and (4) the influence of topography on bottom currents within canyons and smaller gullies.

# Chapter 2

# Preconditioning by Sediment Accumulation Can Produce Powerful Turbidity Currents without Major External Triggers

**This chapter is a reproduction of text published in**
***Earth and Planetary Science Letters***

Lewis P. Bailey, Michael A. Clare, Kurt J. Rosenberger, Matthieu J. B. Cartigny, Peter J. Talling, Charles K. Paull, Roberto Gwiazda, Daniel R. Parsons, Stephen M. Simmons, Jingping Xu, Ivan D. Haigh, Katherine L. Maier, Mary McGann, Eve Lundsten and the Monterey CCE Team (2021). Preconditioning by Sediment Accumulation Can Produce Powerful Turbidity Currents without Major External Triggers. Earth and Planetary Science Letters, 562, 116845. DOI: 10.1016/j.epsl.2021.116845

The research question was conceptualised by MC, KR, PT, CP and JX. Data were collected and processed by KR, CP, RG, KM, MM and EL. LB led data analysis, data visualisation and developed statistical methods with assistance from MC and IH. LB wrote the original manuscript with feedback from MC, KR, MJBC and PT with the original draft being reviewed and edited by all co-authors.

Turbidity currents dominate sediment transfer into the deep ocean, and can damage critical seabed infrastructure. It is commonly inferred that powerful turbidity currents are triggered by major external events, such as storms, river floods, or earthquakes. However, basic models for turbidity current triggering remain poorly tested, with few studies accurately recording precise flow timing. Here, we analyse the most detailed series of measurements yet made of powerful (up to 7.2 $ms^{-1}$) turbidity currents, within

Monterey Canyon, offshore California. During 18-months of instrument deployment, fourteen turbidity currents were directly monitored. No consistent triggering mechanism was observed, though flows did cluster around enhanced seasonal sediment supply. We compare turbidity current timing at Monterey Canyon (a sandy canyon-head fed by longshore drift) to the only other systems where numerous (>10-100) flows has been measured precisely via direct monitoring; the Squamish Delta (a sandy fjord-head delta), and the Congo Canyon (connected to the mud-dominated mouth of the Congo River). A common seasonal pattern emerges, leading to a new model for preconditioning and triggering of turbidity currents initiating through slope failure in areas of sediment accumulation, such as canyon heads or river mouths. In this model, rapid or sustained sediment supply alone can produce elevated pore pressures, which may persist, thereby predisposing slopes to fail. Once preconditioned, a range of minor external perturbations, such as moderate storm-waves, result in local pore pressure variation, and thus become effective triggers. Major external triggers are therefore not always a prerequisite for triggering of powerful turbidity currents.

## 2.1 Introduction

Turbidity currents are one of the most important processes for moving sediment across our planet, dominating transport from continental shelves to the deep sea, and play a key role in the transport and burial of organic carbon (Galy et al., 2007) and pollutants (Mordecai et al., 2011). These submarine flows can reach velocities of up to 20 $ms^{-1}$ (Hsu et al., 2008) and runout for hundreds of kilometres (Piper et al., 1999). Powerful turbidity currents can break important seafloor infrastructure, such as telecommunication cables that today carry over 95% of transoceanic data traffic (e.g. Heezen & Ewing, 1952; Heezen et al., 1964; Hsu et al., 2008; Piper et al., 1999; Hsu et al., 2008; Carter et al., 2009, 2012; Gavey et al., 2017; Pope et al., 2017b).

Given their role in global sediment transport, and their potential for damaging critical infrastructure, it is important to understand what controls turbidity current activity. Previous studies commonly infer that turbidity currents are caused by major external events, such as storms, river floods or major earthquakes (Table 2.1). Turbidity current deposits ('turbidites') may then provide valuable records of such events that can be extended beyond historical or instrumental archives (e.g. Mulder et al., 2001; Goldfinger, 2011). To interpret the turbidite record, it is thus important to understand whether turbidity currents can sometimes be triggered without a major external trigger, and whether the nature or magnitude of trigger can be linked to flow velocity or runout distance.

This contribution seeks to understand the roles of preconditioning and triggering factors and how these control turbidity current activity, timing and frequency. Previous

**Table 2.1:** Summary of previous studies of how turbidity currents are triggered in submarine canyons and channels with different types of sediment supply, based on precise timings of flow events measured via direct monitoring.

| Sediment Supply | Site | Flows | Period | Triggers | Reference |
|---|---|---|---|---|---|
| River-fed fjords | Knight Inlet, Canada<br>Bute Inlet, Canada | 39<br>35 | 17 months<br>13 months | Elevation in freshet river discharge. | Bornhold et al. (1994) |
| | Squamish Prodelta, Canada | 106 | 147 days | System active during river discharge $> 300$ m$^3$s$^{-1}$. Tidal drawdown or rapid sedimentation trigger. | Hughes Clarke et al. (2014); Clare et al. (2016); Hizzett et al. (2018) |
| River-fed canyons | Congo Canyon, offshore Angola | 6 | 4 months | Elevated river discharge but not flood peaks. | Heezen et al. (1964); Azpiroz-Zabala et al. (2017) |
| | Gaoping Canyon, offshore Taiwan | 23 | 3.5 years | Flows initiate following typhoon elevation of river discharge. | Zhang et al. (2018). |
| | | 2 | 2 months | Typhoon-triggered hyperpycnal. flows | Liu et al. (2012) |
| | | Cable Breaks | | River flooding, tropical cyclones and earthquakes. | Hsu et al. (2008); Pope et al. (2017b) |
| | Gulf of Lions canyon system, Mediterranean | 6 | 4 months | Dense shelf water cascading, storms, river flooding and trawling. | Canals et al. (2006) |
| | Var Canyon, Mediterranean | 8 | 2 years | Hyperpycnal flows during river flooding and some local storms. | Khripounoff et al. (2009) |
| Littoral-drift fed canyons | Eel River Shelf and Canyon, offshore California | 11 | 83 days | Storms, not directly linked to river floods. | Puig et al. (2004) |
| | Hueneme & Mugu Canyons, offshore California | 6 | 6 months | Same storm capable of triggering flows in both canyons simultaneously. | Xu et al. (2010) |
| | Monterey Canyon, offshore California | 4<br>10 | 11 months<br>16 & 26 months | Coincident with elevation in storm activity. | Xu et al. (2004)<br>Paull et al. (2003, 2010) |
| | Nazaré Canyon, offshore Portugal | 3 | 22 months | Predominately storm waves, minor contribution from flooding. | Martín et al. (2011) |
| Sediment starved canyon | Gulf of St. Lawrence, East Canada | 4 | 27 months | Sustained storms resuspend sediment the canyon heads. | Normandeau et al. (2020) |

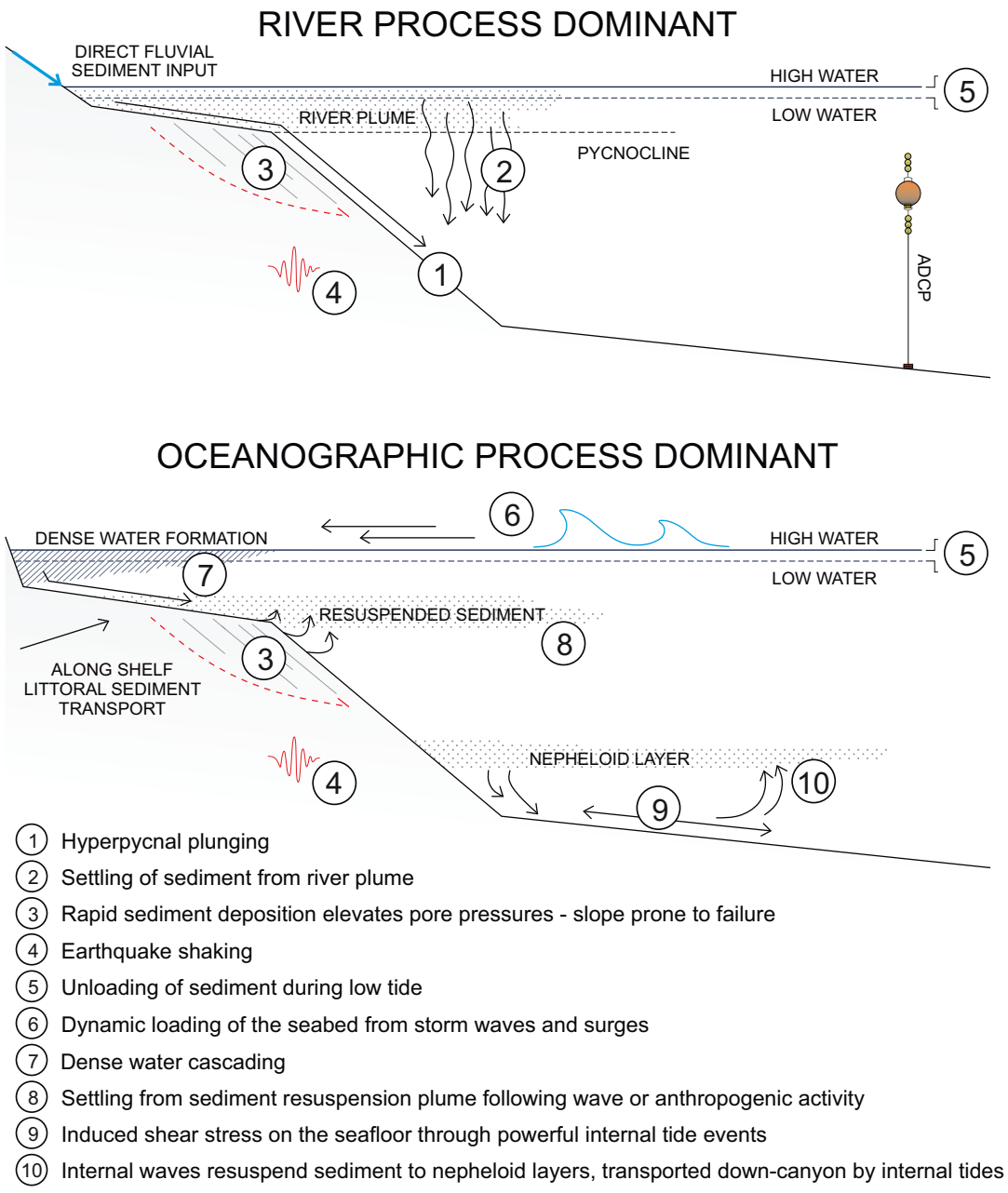


**Figure 2.1:** Previous hypotheses for initiation, preconditioning and triggering mechanisms of turbidity currents in submarine canyons.

work demonstrates multiple mechanisms are capable of generating turbidity currents (Table 2.1; Talling, 2014). Mechanisms of initiation vary across different settings. For example, where submarine canyons have direct fluvial input, plunging of (hyperpycnal) river floodwater can produce turbidity currents, if the floodwater contains sufficient sediment to be denser than seawater (label 1 in Fig. 2.1; Mulder & Syvitski, 1995; Johnson et al., 2001; Khripounoff et al., 2009). Rivers with lower sediment concentrations generate surface (homopycnal) plumes. Sediment settling from surface plumes can also generate turbidity currents, including via sediment trapping due to convergent near-bed flow, and episodic remobilisation on the bed (label 2 in Fig. 2.1; Hage et al.,

2019). Flows can also form via disintegration of submarine slope failures (label 3 in Fig. 2.1; Piper et al., 1999). Initiation through slope failure is typically a result of preconditioning factors, especially development of high excess pore pressures (e.g. Masson et al., 2010; Dugan & Sheahan, 2012; Talling et al., 2014). Such excess pore pressures are favoured in locations where sedimentation is rapid, and pore fluid can be trapped by less permeable layers (Özener et al., 2009). Short period events that instantaneously initiate the flow are referred to as triggers. These include earthquake shaking (label 4 in Fig. 2.1; Piper et al., 1999; Mountjoy et al., 2018), low tides unloading seabed sediment (label 5 in Fig. 2.1; Hughes Clarke et al., 2014; Clare et al., 2016), and cyclic loading as a result of storm waves or surges (label 6 in Fig. 2.1; Chamberlain, 1964; Puig et al., 2004). Sediment may also be resuspended as shelf sediment plumes during storms (label 7 in Fig. 2.1; Inman et al., 1976; Normandeau et al., 2020), following trawling (Puig et al., 2012) or due to cascading of dense water (label 8 in Fig. 2.1; Canals et al., 2006; Puig et al., 2013a). Internal tides (label 9 in Fig. 2.1) may also cause resuspension of sediment, triggering dilute flows (label 10 in Fig. 2.1; Martín et al., 2011).

Testing models for how turbidity currents are triggered requires measuring the timing of turbidity currents and potential triggers with precision. For example, over days to hours, a storm may generate both large wave heights (causing cyclic loading of the seafloor) at its peak, and river flooding (initiating a plunging hyperpycnal flow) following its passage (Pope et al., 2017b). The precise start time of a turbidity current is needed to distinguish between these different triggers. Only in rare cases (e.g. Ikehara et al., 2014) can deposits be dated at sufficiently high resolution to directly isolate such external triggers, therefore more robust constraints on flow timing are needed. Precise timing can be provided by seafloor cable breaks or direct monitoring of turbidity currents; however, cable breaks fail to measure weaker events that leave cables intact, and breakages may not occur at the timing of flow impact. The accuracy of instruments used in direct flow monitoring, such as Acoustic Doppler current profilers (ADCPs), is a function of data resolution and distance from source. Previous studies using ADCPs have either collected data at low temporal resolution, or involved instruments located far away from where flows originate. Moreover, monitoring instruments were typically deployed for a few months, missing parts of annual or longer cycles. This results in the controls on turbidity currents activity remaining poorly tested (Table 2.1).

Here, we analyse the most detailed measurements yet of oceanic turbidity currents (Paull et al., 2018). Data were collected during the 18-month-long Coordinated Canyon Experiment (CCE) in Monterey Canyon, offshore California (Fig. 2.2). No previous direct monitoring has deployed such a dense network of novel equipment to record high-resolution measurements of turbidity currents at multiple locations along their path. The longevity of the monitoring period also allows investigation of seasonal patterns in turbidity current activity. Our objective is to understand the roles of preconditioning

and triggering mechanisms on the timing of turbidity currents. We address the following specific aims. First, using the uniquely detailed CCE flow monitoring dataset, how do turbidity currents initiate in Monterey Canyon? Then, how are these flows related to major external events, and what is the control on turbidity current activity in Monterey Canyon? Finally, we then we compare results across different settings, scales and grain sizes of turbidity current systems to propose a new model for preconditioning and flow triggering which can be tested by future studies. We conclude by discussing the wider implications of this new model for offshore geohazard assessments.

## 2.2 Background

Monterey Canyon is located offshore California on the tectonically active North American and Pacific Plate Boundary (Greene, 1990). The head of Monterey Canyon lies within 100 m of the coast and extends over 300 km offshore to water depths in excess of 4,000 m (Fig. 2.2; Smith et al., 2005). The Salinas, Pajaro and San Lorenzo Rivers flow into Monterey Bay (Fig. 2.2). These subaerial fluvial drainage pathways were formed during rapid uplift of the Coast Ranges in southern Monterey Bay and coastal central California (Dupre, 1990; Page et al., 1998; Ducea et al., 2003) combined with the onset of large-scale (>100 m) eustatic sea-level and climatic variations in the Pleistocene. These variations were transposed onto local tectonics around Monterey Bay such that the shoreline (e.g. Waelbroeck et al., 2002; Stanford et al., 2011), and therefore river systems (e.g. Nagel et al., 1986), moved westward to the shelf edge during the Last Glacial Maximum (LGM). Throughout this period numerous canyons in the greater Monterey system, offshore central California, likely were active and fed sediment to the Monterey Fan (e.g. Normark, 1970; Normark & Hess, 1980; Greene & Hicks, 1990; Fildani & Normark, 2004). Rapid sea-level rise associated with a post-LGM Pleistocene transgression correlates with a continued shoreward incision of Monterey Canyon head (Paull et al., 2005).

In present day, the Pajaro and San Lorenzo Rivers are detached from the head of Monterey Canyon, providing minor direct sediment input (Fig. 2.2). The Salinas River is engineered to enter Monterey Canyon directly under low flow conditions, and discharges ~130,000 $m^3yr^{-1}$ of suspended sand. However, the majority of sediment transport occurs during elevated river discharge (Gray et al., 2015). As a result, 95% of Salinas River sediment discharge enters Monterey Bay 6.7 km to the south of the canyon head (Casagrande & Watson, 2003; Watson et al., 2003). Sediment from the Salinas, Pajaro and San Lorenzo Rivers instead feeds littoral cells entering Monterey Canyon through longshore drift (Farnsworth & Warrick, 2007). The Santa Cruz cell provides >200,000 $m^3yr^{-1}$ (Fig. 2.2: Eittreim et al., 2002) of sand, with an additional 300,000-800,000 $m^3yr^{-1}$ of sand from the South Monterey Bay cell (Fig. 2.2; Willis & Griggs,

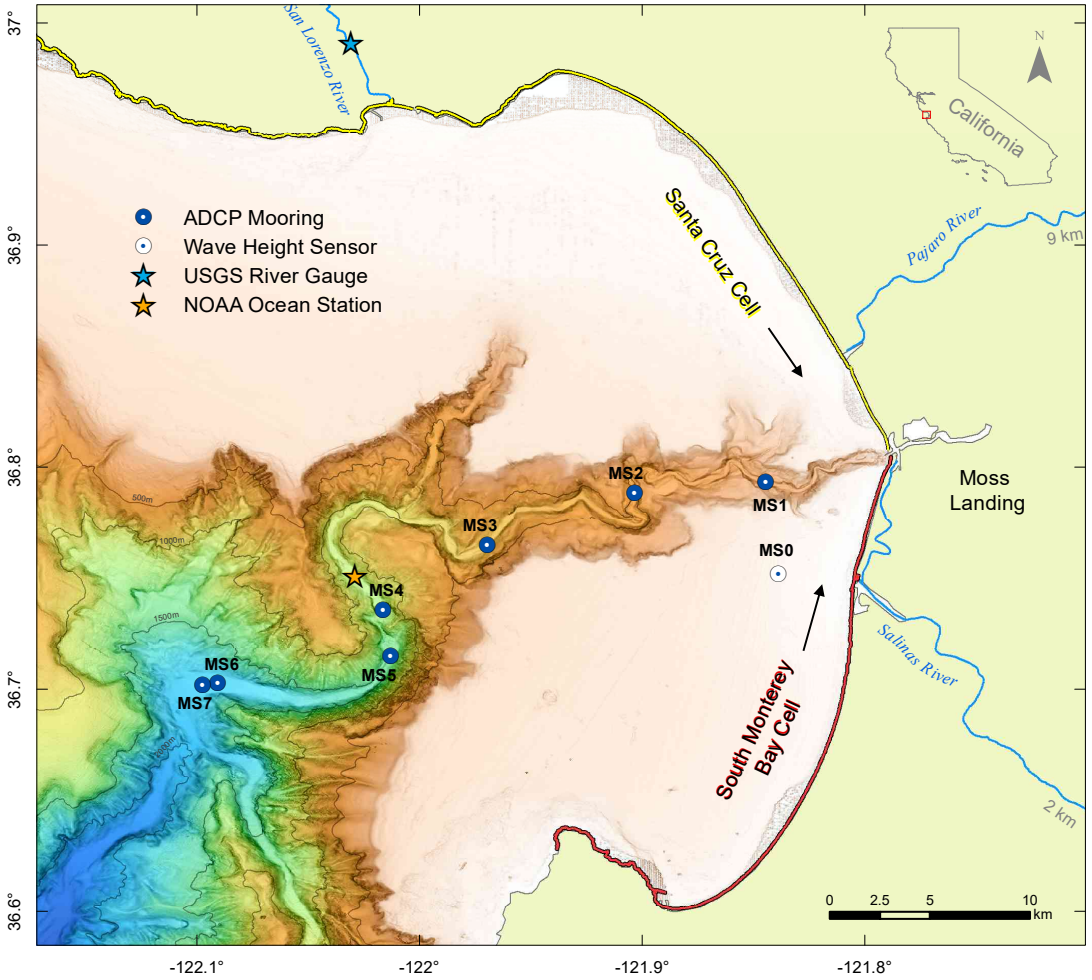


**Figure 2.2:** Monterey Canyon situated offshore California, USA. Map shows mooring locations (MS1-7) and the wave height sensor (MS0) deployed during the CCE. The locations of NOAA metocean buoy and USGS river gauges also shown for San Lorenzo River. Distance labels on Pajaro and Salinas Rivers refer to distance upstream to gauging station beyond the edge of the map. Locations of the Santa Cruz (yellow) and South Monterey Bay Cells (red) are labelled to show littoral transport pathways to the head of Monterey Canyon.

2003; Thornton, 2016). Sediment transport is highest during the winter, as the most energetic waves approach from the north-west, diminishing during summer when swells from the south prevail (Patsch & Griggs, 2006).

Direct monitoring and deposit analysis show sediment is primarily transported down-canyon by frequent turbidity currents. Multiple turbidity currents each year runout through the upper 52 km of the canyon, from 300 m to 1850 m water depth (Paull et al., 2003, 2005, 2010, 2018; Xu et al., 2004). Longer runout flows are much less frequent, with flows only reaching a water depth of ~2800-3500 m every 150-200 years (Stevens et al., 2014). Strong (20-80 $cm.s^{-1}$) internal tidal flows also transport fine-grained sediment between turbidity current events (Maier et al., 2019b).

Several possible triggering mechanisms have been proposed for turbidity currents monitored in Monterey Canyon. Johnson et al. (2001) detected four muddy turbid-water

underflows over a 12-year period using a conductivity, temperature and depth (CTD) probe and transmissometer located 7 km from the head of Monterey Canyon. These underflow events correlated with peak discharge of the Salinas River (Fig. 2.2) and were interpreted as hyperpycnal flows. Turbidity current activity was also determined from the down-canyon movement of 1,000 kg instrument frames in the canyon axis (Paull et al., 2003, 2010). Four transport events occurred in a 16-month period in 2001-2002, with six further events recorded during a 26-month period in 2007-2009. Some events occurred during periods of large surface waves, but others coincided with only moderate sea conditions. In December 2002, Xu et al. (2004) detected two turbidity currents using ADCPs, with durations of 6 hours. These turbidity currents corresponded to the highest sea swells observed during a yearlong deployment. However, this same experiment detected two other flows with similar velocities in March and November 2003, which did not coincide with storms, or earthquakes or floods. The relative importance of external triggering mechanisms, and the nature of the resultant turbidity currents, therefore remains poorly understood due to the limited number of events monitored.

## 2.3 Data and Methods

### 2.3.1 The Coordinated Canyon Experiment

Here we report results from the Coordinated Canyon Experiment that included an array of moorings (labelled MS0 to MS7 in Figs. 2.2, 2.3) and other instruments, deployed during an 18-month period from October 2015 to April 2017. Instruments were placed within the upper 52 km of Monterey Canyon in water depths of up to 1,850 m (Fig. 2.2; Paull et al., 2018). Moorings MS1-to-MS5 and MS7 each held a downward-looking 300 kHz ADCP located ~65 m above the seafloor (Fig. 2.3). ADCPs measured profiles of water column velocity and backscatter (proxy for suspended sediment) at 1 m vertical intervals at 30-second resolution. No ADCP measurements were made at MS1 from 15$^{th}$ January 2016 until redeployment on 1$^{st}$ April 2016, as the MS1 mooring broke loose during a powerful turbidity current (Paull et al., 2018). The ADCP at MS4 failed between April-October 2016. Moorings MS1-3 and MS5 included temperature and pressure sensors to record water depth (Fig. 2.3). A wave height and direction sensor (MS0) was moored outside the canyon to record surface ocean conditions. Small boulder-sized packages with inertial navigation sensors (benthic event detectors, BEDs) were deployed in the upper canyon (Fig. 2.3) to measure movement within turbidity currents (Paull et al., 2018).

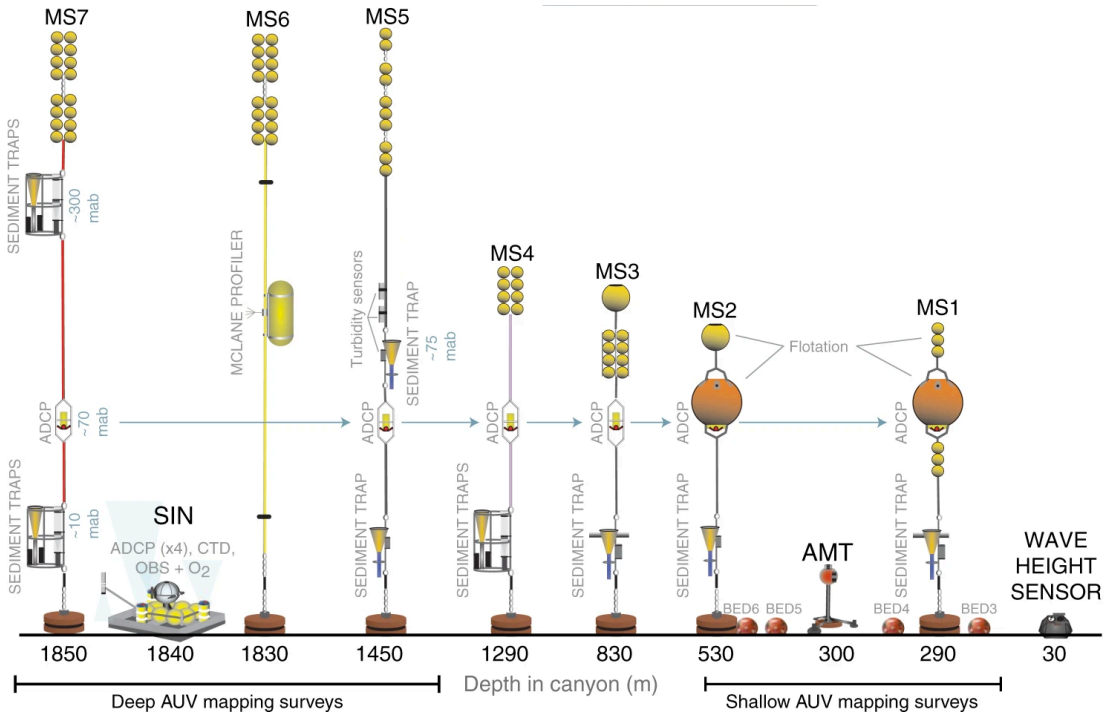


**Figure 2.3:** Schematic drawing (not to scale) of the monitoring instrument array deployed within Monterey Canyon during the Coordinated Canyon Experiment. Adapted from Paull et al. (2018)

.

### 2.3.2 Turbidity Current Timing and Runout

A turbidity current is defined here as an event which results in an abrupt increase in ADCP backscatter and down-canyon velocity. The arrival of a turbidity current at each mooring was also accompanied by an increase in pressure as the mooring is tilted towards the seabed. Movement of the mooring during an event separates turbidity currents from powerful internal tides, which can also show sudden increase in ADCP backscatter and (up and down-canyon) velocity. Minimum flow runout is calculated through successive detection at moorings along the canyon thalweg. The movement of BEDs within the channel axis were used to calculate the initiation time of turbidity currents in the 77 days during which mooring MS1 was out of the canyon. During that time, the sequential movement of BEDs in the upper canyon is interpreted as recording a turbidity current (Paull et al., 2018).

### 2.3.3 Measuring Potential Triggering Mechanisms

We analyse the role of the following variables in triggering turbidity currents: earthquakes, wave energy and direction, storm surges, river discharge, and surface and internal tides (10 m above bed). The timing and magnitude of earthquakes are from U.S. Geological Survey (USGS) Earthquake Hazards Program (https://earthquake.usgs.gov

/earthquakes). Wave height, period and direction, and sea surface height are recorded at MS0 every two hours. Here we calculate an indication of wave energy as,

$$\text{Wave Energy} = \frac{1}{8}\rho g H^2 L, \tag{2.1}$$

where $\rho$ is water density, $g$ is acceleration by gravity. $H$ refers to significant wave height and $L$ is mean wavelength derived from wave period through the wave dispersion relation (Dalrymple & Dean, 1991) recorded at MS0. The longshore component of wave energy is directly proportional to the longshore transport rate of sand (Komar & Inman, 1970). Internal tide signals are obtained from mooring data at MS1 with 30-second resolution. Data were binned and averaged over 10-minute intervals, with measurements related to turbidity currents removed. The bin prior to turbidity current detection was taken as the conditions during the event. Hourly air pressure measurements at National Oceanic and Atmospheric Administration (NOAA) Station 46092 (https://www.ndbc.noaa.gov) provide an indication of potential storm surges. USGS stream gauges 11152500, 1159000 and 11161000 provide daily average discharge for the Salinas, Pajaro and San Lorenzo rivers (Fig. 2.2; https://waterdata.usgs.gov). Suspended sediment concentrations were estimated for the Salinas, Pajaro and San Lorenzo rivers using established rating curves (Johnson et al., 2001).

The time of turbidity current detection at MS1 (or initial BED transport) is taken as the point of flow initiation for comparison to potential triggering variables. As a result, there is some uncertainty in the exact timing of flow initiation. Most flows were first detected at MS1 ($\sim$300 m water depth), therefore flows may have originated anywhere between MS1 and the canyon head. Assuming turbidity current velocity is $>$2 ms$^{-1}$ following initiation to detection at MS1 (or shallowest BED), the transit time from any point in the canyon head will be $<$1 hour and therefore above the resolution of wave energy and direction, storm surges, river discharge, and surface tide measurements. Greater uncertainty arises when comparing event initiation to internal tide velocity.

### 2.3.4 Statistical Comparison of Triggering Variables

The following criteria are used to analyse variation between event and non-event conditions to assess the influence of individual triggers throughout the CCE. We calculate the difference between medians (DBM) as a percentage of overall visual spread (OVS), where OVS is the range from the lowest to highest interquartile (25$^{\text{th}}$ and 75$^{\text{th}}$ percentile) range (e.g. Rao & Liu, 2017). The number of events in this study (N = 14) is insufficient for complex statistical analysis; however, calculating DMB as a percentage of OVS provides a quantification of distribution offset between event and non-event conditions for each of the hypothesised explanatory variables.

**Table 2.2:** Summary of previous direct monitoring at the Squamish Prodelta and Congo Canyon used as comparative studies to Monterey Canyon. Information provided on the settings of each site, deployment periods and how data were collected.

| Site | Setting | Period | Monitoring Methods | Reference |
|---|---|---|---|---|
| Squamish Prodelta, Canada | The Squamish River is heavily influenced by seasonal meltwater. Winter river discharge of $\sim$100 $m^3s^{-1}$ increases in the freshet to $>$500 $m^3s^{-1}$, with peaks of up to 1000 $m^3s^{-1}$ in the summer. Spring tidal reaches 5 m whereas neap tides have a range of$\sim$3 m. At low tide river discharge is focussed within a sub-tidal channel of 1 m depth and 200 m width where it reaches the delta-lip. Seaward of the delta-lip, three main channels are found on the prodelta slope. At a distance of 2 km from the delta-lip, these channels open out and flows become unconfined. | Survey: 29 Mar to 25 Aug 2011<br><br>ADCP: 30 Jun to 20 Jul 2011 | 93 repeat surveys performed in 2011 enable the production of difference maps to observe daily changes in seafloor morphology. Turbidity current activity relates to (i) $>$20,000 $m^3$ evacuations on the delta-lip, or (ii) migration of channel bedforms. This provides 24-hour resolution of turbidity current activity. An upwrad-looking 600 kHz ADCP was also installed in the most northern of the three channels. The ADCP recorded arrival times of turbidity currents to 30 seconds, except when buried from 30/6/11 to 20/7/11. Hourly River Homathko discharge data were obtained 12 km upstream at Brackendale Environmental Canada station 08GA022. | Hughes Clarke et al. (2014); Clare et al. (2016) |
| Congo Canyon, offshore Angola | The Congo Canyon is situated at the mouth of the Congo River, the second largest river globally by discharge. The Congo River hydrograph has two distinct peaks in December and June where river discharge exceeds 38,000 $ms^{-1}$. The canyon extends 760 km offshore to the abyssal plain and covers an area of 300,000 $km^2$ (Khripounoff et al., 2003). The Congo submarine fan still accumulates sediment through turbidity currents to the present day (Van Weering & Van Iperen, 1984). | 1893 to 1932<br><br>ADCP: 2 Dec 2009 to 24 Mar 2010 | Flow timing derived from cable breaks. A cable crossed the canyon 110 km from the mouth of the Congo River from 1893-1897. Due to frequent breakages, this cable was diverted closer to the Congo River mouth to make repairs easier from 1897-1937.<br>A 300 kHz ADCP was suspended in a water depth of $\sim$2,000 m, 85 m above the floor of the Congo Canyon thalweg from a fixed mooring. Acoustic backscatter and velocity were measured every 5 seconds to constrain turbidity current timing. Daily discharge data is from the Kinshasa gauging station located $\sim$450 km upstream from the mouth of the Congo River. | Heezen et al. (1964)<br><br>Azpiroz-Zabala et al. (2017) |

### 2.3.5 Comparative Datasets from River-Fed Systems

We compare our results from Monterey Canyon with previously published observations from two other well-monitored submarine systems for which we provide further details in Table 2.2. As far as we are aware, these are the only other sites where the timing of numerous turbidity currents (>10-100) have been measured precisely via direct monitoring. However, in each case the duration of direct monitoring is <18 months, such that more infrequent events may not be well captured.

The first location is Squamish Delta in Howe Sound, British Columbia, which is fed by a sand-dominated and relatively small (200-1,000 $m^3s^{-1}$) discharge river. At this location, 106 turbidity currents were recorded in 2011 from repeat seafloor surveys and ADCP measurements (Hughes Clarke et al., 2014; Clare et al., 2016). The second location is the upper mud-dominated Congo Canyon, offshore West Africa. This system is fed by the Congo River, the second largest (40,000-60,000 $m^3s^{-1}$) discharge river on Earth (Milliman & Meade, 1983). The timing of turbidity currents in the Congo Canyon was measured using two methods. Especially powerful flows were recorded by cable breaks between 1893 and 1932 (N = 23), close to the coast (Heezen et al., 1964). ADCP moorings at sites ∼150 km from the coast record sufficiently long runout flows (N = 10 Azpiroz-Zabala et al., 2017; Simmons et al., 2020). Data from these two comparative sites allow us to compare patterns of flow timing in diverse physiographic settings with different sediment delivery mechanisms and grain sizes.

## 2.4 Results

### 2.4.1 Source, Number and Character of Events in Monterey Canyon

During the 18-month monitoring period, fourteen flows initiated in upper Monterey Canyon in water depths of <300 m (Fig. 2.4a). Eleven turbidity currents were detected using MS1 and three based on movement of BEDs. Turbidity currents detected during the CCE have frontal (transit) velocities of up to 7.2 $ms^{-1}$. Three flows ran out through the entire instrument array, for at least 52 km along the canyon thalweg (Paull et al., 2018).

### 2.4.2 Correlating Environmental Variables with Turbidity Current Timing in Monterey Canyon

We now consider the relationships between the 14 turbidity currents that initiated in upper Monterey Canyon, and factors that may have triggered the flows. We first determine the potential triggering mechanisms (Fig. 2.1) that occurred during the period

**Table 2.3:** Statistical metrics to compare the distribution variation of potential triggering mechanism conditions with background conditions observed during the CCE. We calculate the difference between medians (DBM) as a percentage of overall visual spread (OVS), where OVS is the range from the lowest to highest interquartile range (Rao & Liu, 2017). Results are ranked in order of their statistical importance for triggering flows.

| Triggering variable | Event median | Background median | Difference between medians | Overall visual spread | DBM/ OVS [%] |
|---|---|---|---|---|---|
| Wave Energy [x$10^4$ $Jm^{-2}$] | 4.2 | 1.6 | 2.6 | 6.2 | 41.9 |
| Air Pressue [mbar] | 1012.5 | 1017.3 | 4.8 | 14.4 | 33.7 |
| Water Level [m from mean] | 0.1 | 0.0 | 0.1 | 0.9 | 17.2 |
| Combined River Discharge [$m^3s^{-1}$] | 25.6 | 2.2 | 23.4 | 202.3 | 11.6 |
| Internal Tide Velocity [$ms^{-1}$] | -3.4 | -2.6 | 0.8 | 23.8 | 3.2 |
| Salinas River Discharge [$m^3s^{-1}$] | 0.0 | 0.0 | 0.0 | 0.6 | 0.0 |

of instrument deployment in Monterey Canyon. Of the triggering mechanisms present we analyse how each correlates to turbidity current timing.

#### 2.4.2.1 Earthquakes

Several small earthquakes, with magnitudes of up to 4.2 $M_W$, and epicentres within 100 km of the canyon head, were detected during the CCE. However, these earthquakes did not coincide with any turbidity currents (Fig. 2.4a). Therefore, small earthquakes did not trigger any flows in Monterey Canyon during the deployment period.

#### 2.4.2.2 Storms – Large Waves and Storm Surges

A storm is defined as a period of large, high-energy waves, low air pressures and strong winds. The compound effect of these factors may also result in a storm surge. Wave energy and air pressure (+42% and -34% DBM/OVS respectively; Table 2.3) were the triggering variables with the largest offset between event and background conditions. Only 35% of turbidity currents occur when wave energy was below the $70^{th}$ percentile of its annual range (Figs. 2.4c). The five largest depressions in air pressure also all correspond to times of turbidity current activity (Fig. 2.4d). However, not all periods of high wave energy and significant wave height correspond to a turbidity current. Periods with some of the highest wave energy (up to 4.2x$10^5$ $Jm^{-2}$), significant wave heights and periods (up to 6 m and 13 seconds) did not include any turbidity current activity (Figs. 2.4c). Similarly, not all turbidity currents occurred during depressions (Fig. 2.4d). Turbidity currents were typically detected at the onset of storms, when wave energy starts increasing rather than at individual peaks (Fig. 2.5). Wave direction measured at MS0 was almost exclusively from the north-west during the CCE, even during summer. Two turbidity currents were detected on rare days of south-west approaching storm waves (Fig. 2.4b).

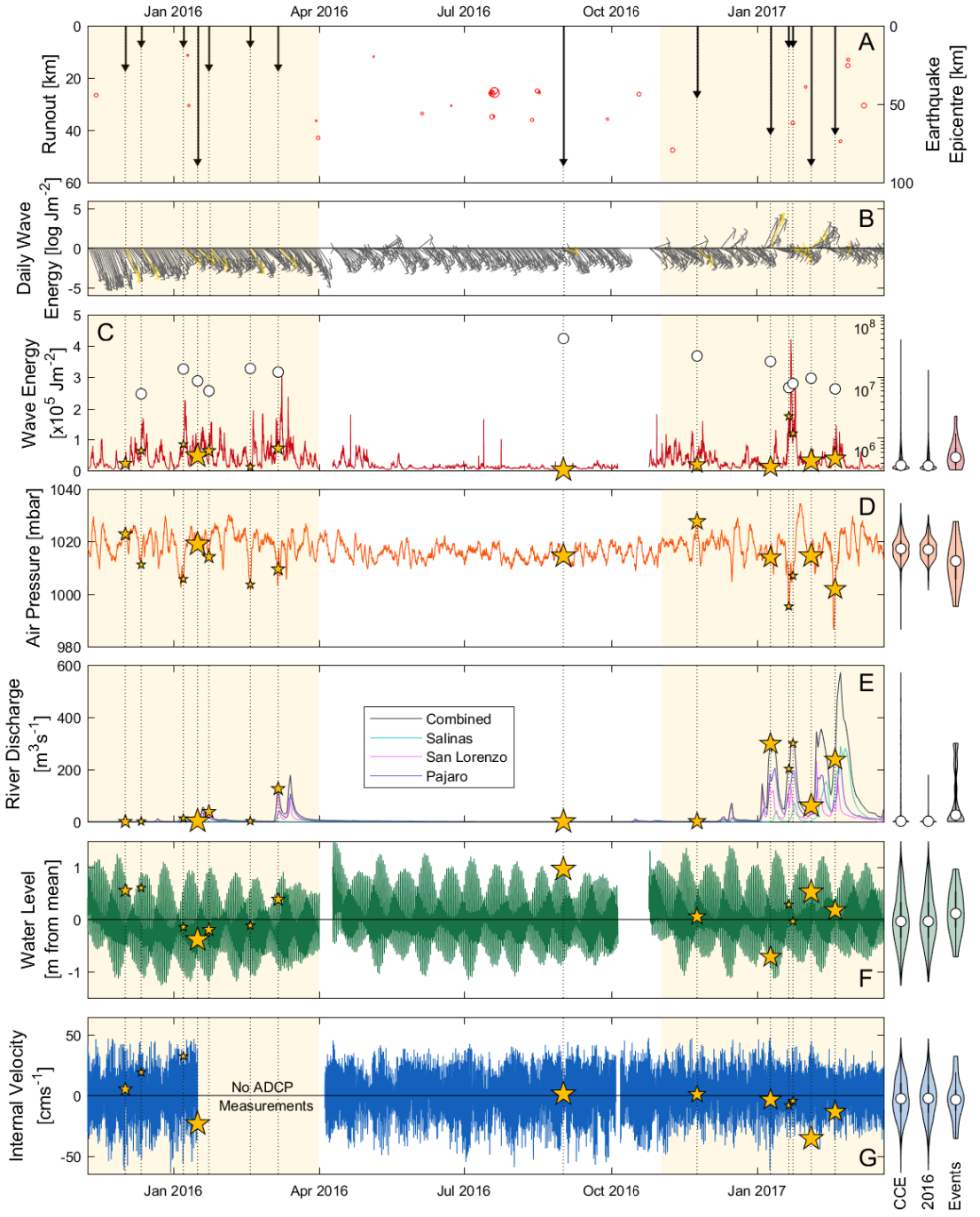


**Figure 2.4:** Time series during CCE of event occurrence and triggering variables discussed. Dotted lines in all panels indicate when turbidity currents occur. (A) The timing of detected turbidity currents and runout distance down-canyon (left); and the timing of earthquakes with epicentres within 100 km of Moss Landing, data point size relative to magnitude (right). (B) Mean daily wave direction measured by wave height sensor, yellow arrows display conditions on days with events. Arrow heads point to direction of wave motion. (C) Red line shows wave energy and white-filled circles indicate the cumulative wave energy since the previous flow. Yellow stars in C-G show the conditions of each variable during events, the size of star

*(continued)*

**Figure 2.4:** *(cont.)* is relative to flow runout. (D) Air pressure measured from NOAA Buoy 46092 located 54 km offshore from Moss Landing, California. (E) River discharge from USGS gauges closest to the mouths of the San Lorenzo, Pajaro and Salinas Rivers, with combined flow. (F) Deviation of water level from mean during CCE measured from wave height sensor. (G) Internal tide velocity measured at MS1 10 m above bed. Data were binned and averaged over 10-minute intervals, with measurements related to turbidity currents removed. Shaded area in A-G shows period of turbidity current clustering in the November-March winter storm season. Violin plots adjacent to C-G show the distribution and range of conditions of each triggering variable throughout the CCE, 2016 and during events. White filled circle shows mean value for each data set and the thick central black line represents the interquartile range. Gaps in wave, water level and internal velocity data are a result of instrument turnover.

#### 2.4.2.3 River Floods

The combined discharge from the Salinas, Pajaro and San Lorenzo Rivers remained below 10 $m^3s^{-1}$ for 80% of the deployment period. In fact, six turbidity currents were detected during a period when the combined river flow was $<3$ $m^3s^{-1}$ (Figs. 2.4e). There is a trend to higher combined discharge during events (+12% DBM/OVS; Table 2.3), but this is skewed by the elevated discharge during January-February 2017. During this period the Salinas, Pajaro and San Lorenzo discharge is the highest observed during the CCE with an abnormal transition from being almost completely dry to moderate discharge (Figs. 2.4e). However, the Salinas River shows no change in median value between events and background conditions (Table 2.3). Elevated river discharges also correlated strongly with storms that caused greater wave energy, or larger wave heights. Turbidity current timing usually preceded peak river flooding. This is most visible when compared to Salinas River discharge. Here, seven events occur within a five-day window of discharge elevation, yet only three turbidity currents are preceded by any substantial river discharge (Figs. 2.4, 2.5).

#### 2.4.2.4 Sea Surface and Internal Tides

Sea surface water level conditions during events show a minor trend to high waters (+17% DBM/OVS; Table 2.3). However, turbidity currents are detected at all stages in the tidal cycle (Figs. 2.4f). Measurements of internal tide velocities were recorded for 11 events, and seven of these coincide with down-canyon flowing internal tides immediately preceding the event (Figs. 2.4g). The distribution of internal tide velocity concurrent with turbidity currents, however, shows almost no variation (3% DBM/OVS; Table 2.3) with measurements throughout the CCE.

### 2.4.3 Clustering of Turbidity Current Activity in Monterey Canyon

Increases in wave energy and decreases in air pressure during storms display the greatest offset in event to background measurements. However, changes in these variables

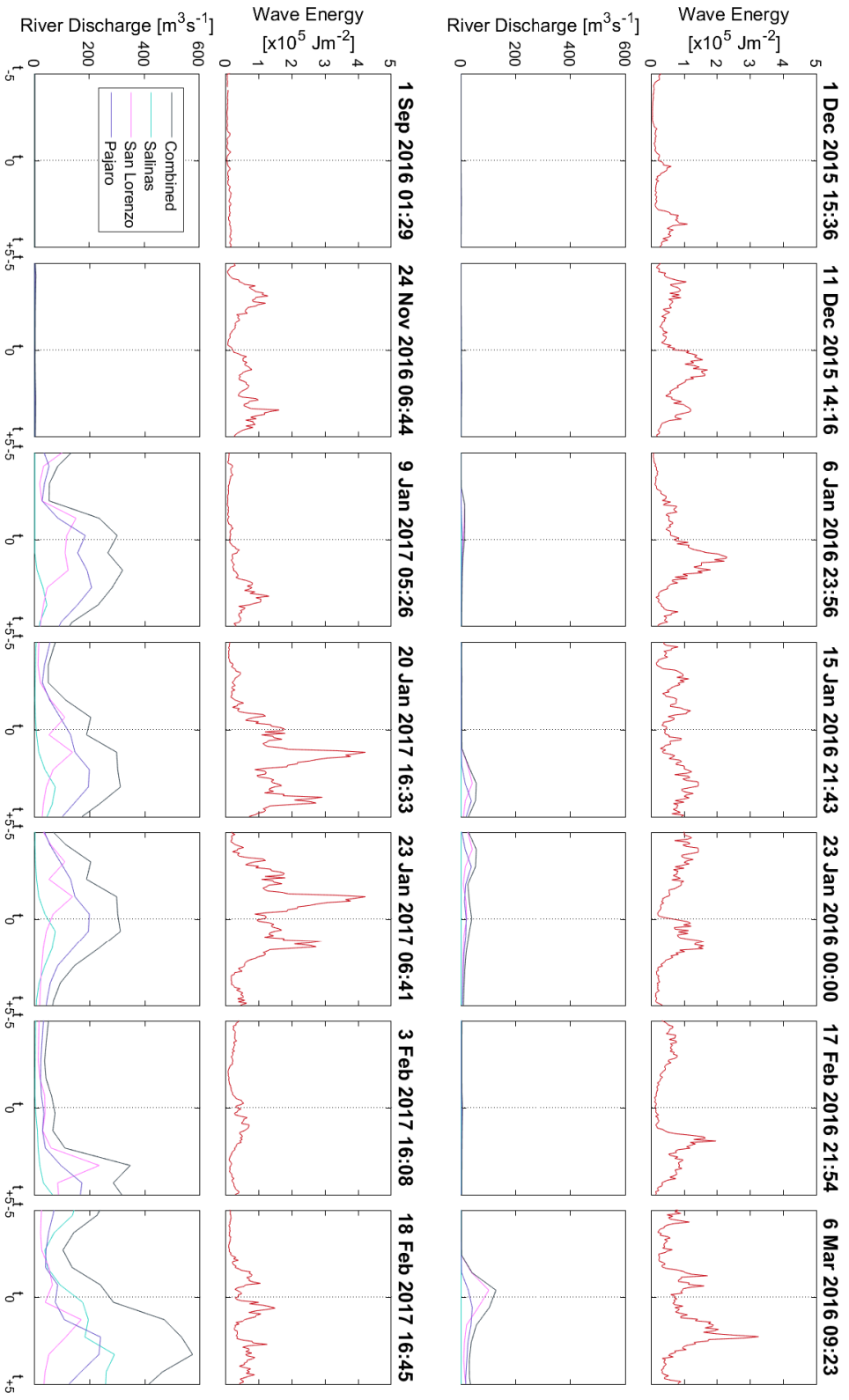


**Figure 2.5:** Measurements of wave energy (red) and San Lorenzo, Pajaro and Salinas Rivers discharge (blue shades), with combined flow (grey) five days prior and following turbidity currents initiating in the upper canyon during the CCE. Central dotted line in each plot indicate first detection of turbidity current.

are not robust predictors of turbidity current activity. What is clear, however, is that turbidity currents are most frequent during the winter months (13 of 14 events; shaded region Fig. 2.4). Throughout the winter, wave energy (a proxy for sediment supply to the canyon head) is also highest. Using the DBM/OVS method, wave energy during 2016 shows a 47% increase during November-March from April-October.

The cumulative wave energy between events (black circles; Fig. 2.4c) is consistent, with each of the 13 events triggered during the winter occurring within an order of magnitude (mean 9.8x$10^6$ $Jm^{-2}$, standard deviation 4.7x$10^6$ $Jm^{-2}$). The single event initiating outside the winter (1$^{st}$ September 2016) occurred after cumulative wave energy of 3.9x$10^7$ $Jm^{-2}$, which is four times higher than the mean value between winter events.

## 2.5 Discussion

This section now discusses how preconditioning and triggering mechanisms relate to turbidity current activity. First, how flows initiate in Monterey Canyon. Then, we assess the role of antecedent conditions prior to events recorded during the CCE, i.e. preconditioning factors, and how these are linked to turbidity current timing and triggering. Finally, we compare results from Monterey Canyon to directly monitored turbidity currents in other systems, and propose a model for the preconditioning and triggering of flows.

### 2.5.1 How do Turbidity Currents Initiate in Monterey Canyon?

Initiation of the observed turbidity currents by plunging (hyperpycnal) river floods, or relating to surface plumes is inconsistent with data from Monterey Canyon. During our study period, the nearby rivers did not exceed the water discharge threshold of 300 $m^3s^{-1}$ (Fig. 2.4e) predicted to generate hyperpycnal flow (Johnson et al., 2001). Moreover, the long distance from the canyon head to the mouths of the Pajaro (5 km) and San Lorenzo Rivers (26 km) does not favour initiation through sediment settling from river plumes (e.g. Parsons et al., 2001), and sediment would likely be dispersed by along-shelf currents (Rosenberger et al., 2016) and waves before settling in the canyon head. Additionally, it is improbable that the turbidity maximum will reach the canyon head 100 m offshore, therefore tidally controlled flow initiation (Hage et al., 2019) is unlikely to apply here. Thus, variations in river discharge are unlikely triggers for the observed turbidity currents.

The head rim of Monterey Canyon progrades and fails on a sub-annual cycle, with an estimated 140,000 $m^3$ of sediment evacuated annually from the rim of the canyon head

and re-deposited locally along the canyon axis (Smith et al., 2005, 2007). Repeat mapping by Smith et al. (2005, 2007) showed a minimum (i.e. Vendettuoli et al., 2019) sediment volume of ∼260,000 $m^3$ accumulated over six months (September 2002 to March 2003). This included a sediment wedge (∼70,000 $m^3$) located near the Moss Landing Harbour mouth resulting in 10 m seaward propagation and >2 m aggradation of the canyon head-rim. This sediment wedge then failed between September 2003 and September 2004, when a total of 230,000 $m^3$ of sediment was evacuated. This period of sediment loss coincided with a turbidity current recorded using ADCPs at 1450 m water depth in November 2003 (Xu et al., 2004). It is likely that some or all of this reported sediment loss in the canyon head is the source of this monitored turbidity current. Therefore, it is conceivable that other turbidity currents, such as those observed during the CCE, are related to the disintegration of sediment failures along the rim of the canyon head.

### 2.5.2 What Preconditions and Triggers Slope Failure in Monterey Canyon?

During our study period no single obvious triggering mechanism was observed to cause flow initiation at Monterey Canyon. Turbidity currents during the CCE did not coincide with earthquakes, though it is important to note that all earthquakes that occurred during instrument deployment were of small (<4.2 $M_W$) magnitude. Our observations show that higher wave energy (+42% DBM/OVS) and lower air pressure (-34% DBM/OVS; Fig. 2.4; Table 2.3) increase the likelihood of turbidity currents. However, the most energetic waves during our study, and previous Monterey Canyon monitoring (e.g. Paull et al., 2003; Xu et al., 2004), did not always generate turbidity currents. Moreover, some turbidity currents initiated during periods of only moderate wave energy (Figs. 2.4, 2.5). Increased discharge of the Salinas River also shows no significant correlation with turbidity currents (Table 2.3). Additionally, the three turbidity currents that coincided with Salinas River discharge >1 $m^3s^{-1}$, all preceded peak river discharge (Fig. 2.5). Turbidity current initiation at all points of sea surface and internal tides (Fig. 2.4) show that tides are also not a consistent triggering mechanism during the CCE.

A seasonality in turbidity current activity is apparent though, with flows clustering during the winter (13 of 14 events; shaded region Fig. 2.4). Throughout the winter sediment supply to littoral cells from rivers is elevated (Fig. 2.4e) and more energetic waves then result in increased longshore transport (Fig. 2.4c), thereby trapping and depositing sediment within the canyon head (Smith et al., 2005, 2007). The volume of sediment entering the canyon head can be estimated using wave energy as a proxy for littoral sand transport (Komar & Inman, 1970). Notably consistent values of cumulative wave energy are observed between these winter turbidity currents (Fig. 2.4c), suggesting a similar volume of sediment enters the canyon head between events. Such

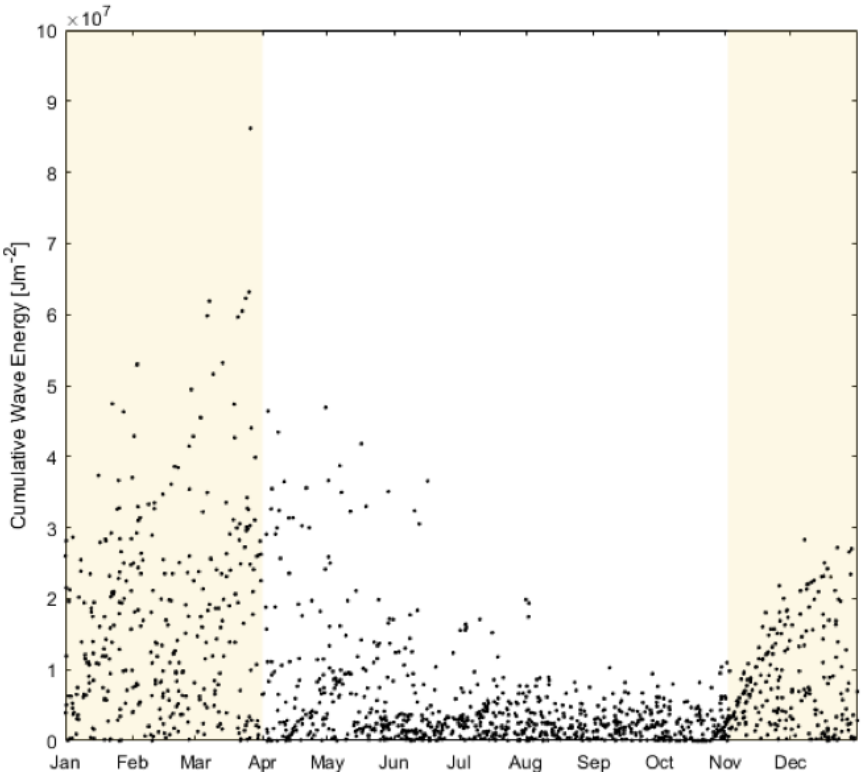


**Figure 2.6:** 100 simulations of randomly generating 14 turbidity currents during throughout 2016. Calculations of cumulative wave energy between each flow made using the wave energy observed through 2016. Bimodal observations in cumulative wave energy from the summer to winter months. Shaded area shows period of turbidity current clustering in the timing of turbidity currents during the CCE aligning with the November-March winter storm season.

consistent cumulative sediment volumes cannot be reproduced by randomly generating the timing of turbidity currents throughout the monitoring period (Fig. 2.6).

The increased rate of sediment supply and accumulation in head of Monterey Canyon during the winter favours turbidity current activity. Submarine slope failures have been linked to periods of enhanced sediment deposition and failure from either slope over-steepening and retrogressive failure known as 'breaching' (Van den Berg et al., 2002; Mastbergen & Van den Berg, 2003) or the development of high excess pore pressures and liquefaction (e.g. Christian et al., 1997; Flemings et al., 2008). Both failure mechanisms are capable of producing turbidity currents, however breaching usually produces more sustained flows (Van den Berg et al., 2002) than those observed during the CCE (Paull et al., 2018).

Direct measurements of pore pressure were not made during the CCE, or in any other sand-rich submarine canyon to date. However, we propose that rapid accumulation of sediment along the head-rim of Monterey Canyon during the winter led to elevated pore pressures, thereby preconditioning failure. Excess pore pressures arise where pore fluid cannot dissipate quickly enough due to low permeability along drainage

paths, which in turn undermines the shear strength and slope stability. Rapid deposition and thicker volumes of sediment therefore favour slope failure (e.g. Dugan & Sheahan, 2012). We note that development of excess pore pressures can also depend on factors other than the total sediment volume supplied. The time-scale over which excess pore pressures are sustained (therefore the period a slope remains preconditioned) or dissipate is controlled strongly by the sediment grain-sizes and hydraulic conductivity. Consolidation coefficients ($c_v$) vary over multiple orders of magnitude depending on small changes in fine-mud fraction, as well as density changes between granular layers of equivalent grain size (Fig. 2.7; Major & Iverson, 1999; Iverson, 2005; Özener et al., 2009). For instance, an additional loading of 10 m sediment thickness will require weeks for pore pressures to dissipate in clean sandy systems (e.g. $c_v \approx 10^{-4}$). However, excess pore pressures may persist for several months when mud is added ($c_v \approx 10^{-5}$), or last for several years in a muddy delta system ($c_v \approx 10^{-6}$; Fig. 2.7; Bennett & Faris, 1979), and may be exacerbated by other effects such as tidal loading-unloading cycles (Christian et al., 1997) or where a hydraulic link exists between onshore and offshore aquifers (e.g. Stegmann et al., 2011). The presence of organic material (that may degrade to release biogenic gases) can also result in elevated pore fluid pressures (e.g. Christian et al., 1997). Deposition of organic debris including macroalgae occurs throughout the year in Monterey Canyon, becoming most abundant during spring/ summer (Okey, 1997; Harrold et al., 1998). While this is the period when turbidity currents are least frequent in Monterey Canyon (Fig. 2.4), degradation of that organic debris will take months (de Bettignies et al., 2020). Thus, there is a balance between build-up of excess pore pressure during periods of more rapid sediment supply, gradual pore pressure dissipation between pulses of storm induced sediment input, and other influences on subsurface pore pressures such as biogenic gas formation. The exact location of sediment deposition is also unknown as we lack repeat seabed surveys over short enough timescales, including along the canyon head-rim; time-lapse surveys from Autonomous Underwater Vehicles were undertaken along the canyon axial channel during the CCE, but only every $\sim$6 months (Paull et al., 2018).

Only one turbidity current initiated outside the winter months (1$^{st}$ September 2016) when average littoral transport rates to the head of Monterey Canyon were lower (Fig. 2.4c). The event was initially relatively weak (velocity of 3 ms$^{-1}$ and $<$10 m thick), but the flow became much more prolonged and faster mid-canyon. Between MS3 and MS5 (Fig. 2.2) the turbidity current thickened to $>$20 m and accelerated to $>$4 ms$^{-1}$ before running out through the entire CCE instrument array (Heerema et al., 2020). Similar to turbidity currents initiating in the winter, no exceptional external mechanism is apparent during, or immediately preceding, this anomalous event (Fig. 2.4). However, this flow did occur following the greatest cumulative build-up in wave energy of all recorded events, over four times higher than the mean between winter turbidity currents (Fig. 2.4c). This represents the highest volume of estimated sediment accumulation in the canyon head prior to turbidity current initiating during the CCE. Such large

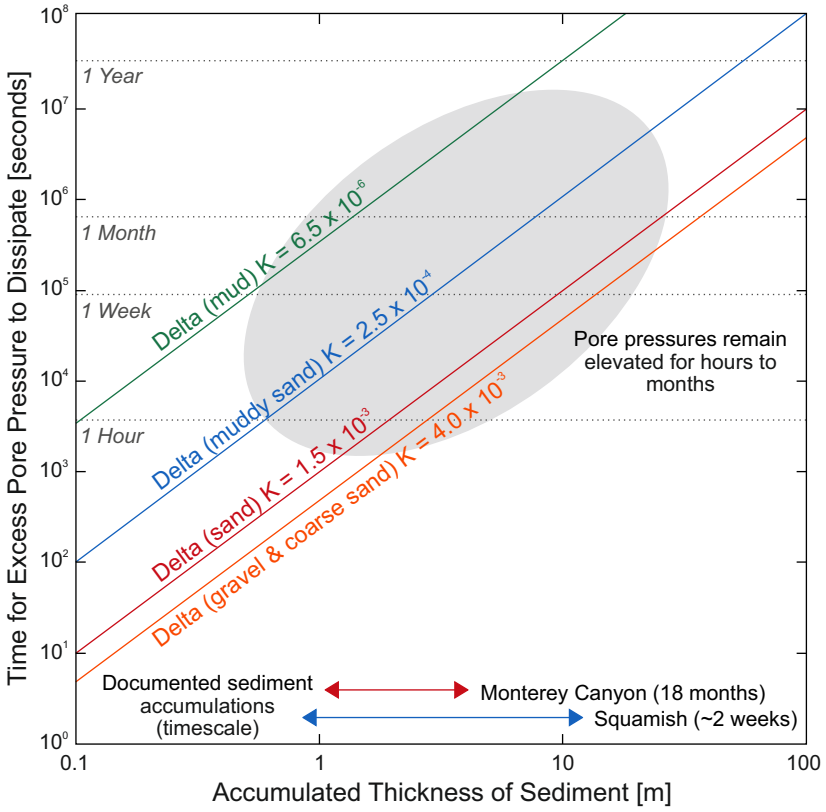


**Figure 2.7:** The role of grain size and sediment supply on the period of system preconditioning demonstrated by hydraulic conductivities in a range of delta systems from Fleckenstein et al. (2006) demonstrating the time for excess pore pressures to dissipate to 1/E (37% of initial value). Clare et al. (2016) show up to 12 m aggradation within 1 week on the delta lip at Squamish, Smith et al. (2005, 2007) show a 8 m aggradation at the head of Monterey Canyon over months.

volumes of sediment are capable of generating excess pore pressures. The rate of pore pressure dissipation is also likely reduced outside the winter through densification and the deposition of a surficial mud layer (Paull et al., 2013; Heerema et al., 2020) resulting in vertical sediment heterogeneity (Özener et al., 2009).

In the absence of a consistent external variable correlating with the timing of flows, turbidity current activity during the CCE is better related to preconditioning factors, rather than an individual instantaneous trigger. We propose a window of enhanced turbidity current activity is set up during the winter storm season, following an increased rate of sediment supply to the head of Monterey Canyon (shaded region Fig. 2.4). Here rapid sediment deposition generates excess pore fluid pressures preconditioning slope failure. Where excess pore pressures cannot fully dissipate, the canyon head can remain preconditioned for several days or weeks. As such it is possible for

delays to exist from initial peaks of sediment input and the timing of a turbidity current. Diminished sediment transport rates outside the winter reduces the build-up of pore pressures, therefore periods where the slope is preconditioned are rarer. However, sufficiently large volumes of sediment deposition (as observed prior to the 1$^{st}$ September 2016 event) can still generate excess pore pressures to precondition failure outside the window of enhanced turbidity current frequency. In both cases, once the slope is preconditioned a large external triggering mechanism is not a requirement for turbidity current initiation. Rather minor perturbations in antecedent conditions, most likely local pore pressure variation as a result of wave loading, are capable of triggering failure.

### 2.5.3 A Common Pattern of Seasonal Increases in Turbidity Current Activity

A common pattern of seasonal increases in turbidity current activity emerges in systems where numerous (>10-100) flows have been precisely measured through direct monitoring. Turbidity currents in Monterey Canyon (a sandy canyon-head system fed by littoral drift), the Squamish Delta (a sandy river-fed fjord-delta) and the Congo Canyon (a muddy system fed by an exceptionally large river) are all most frequent when sediment supply is highest, regardless of setting, grain size or delivery mechanism (Fig. 2.8).

In sand-rich littoral-fed canyons, such as Monterey Canyon and other systems along the Californian Margin (Inman et al., 1976; Paull et al., 2003, 2010, 2018; Xu et al., 2004, 2010; Puig et al., 2004), Nazaré Canyon, offshore Portugal (Martín et al., 2011) and canyons in the Gulf of Lions, Mediterranean (Canals et al., 2006), turbidity current activity is focused in the winter storm seasons, where sediment transport to canyon heads is highest. Turbidity currents still occur outside this period, but are much less common (Fig. 2.8a).

Systems where rivers directly supply sediment are most active during periods of elevated river discharge. For example, turbidity current activity is strongly seasonal at Squamish Delta, with intense activity switching on during periods when river discharge exceeds ~300 $m^3s^{-1}$ (Fig. 2.8b; Hughes Clarke et al., 2014; Clare et al., 2016). Here single monitoring campaigns have recorded >100 individual flows, which primarily occur within the spring/summer freshet season when glacial melting increases river discharge for ~4 months (Fig. 2.8b). Turbidity currents rarely correlate with peaks in river discharge. Instead 25% of flows initiate through slope failure following hours to days delays after rapid deposition on the delta-top, typically at low tide. The remainder of turbidity currents are linked to settling of surface plumes (Clare et al., 2016; Hizzett et al., 2018; Hage et al., 2019). Historical cable breakages related to turbidity currents offshore from the mouths of the Congo and Magdalena Rivers and within the Gulf of Corinth are also most frequent during periods of elevated river discharge (Heezen

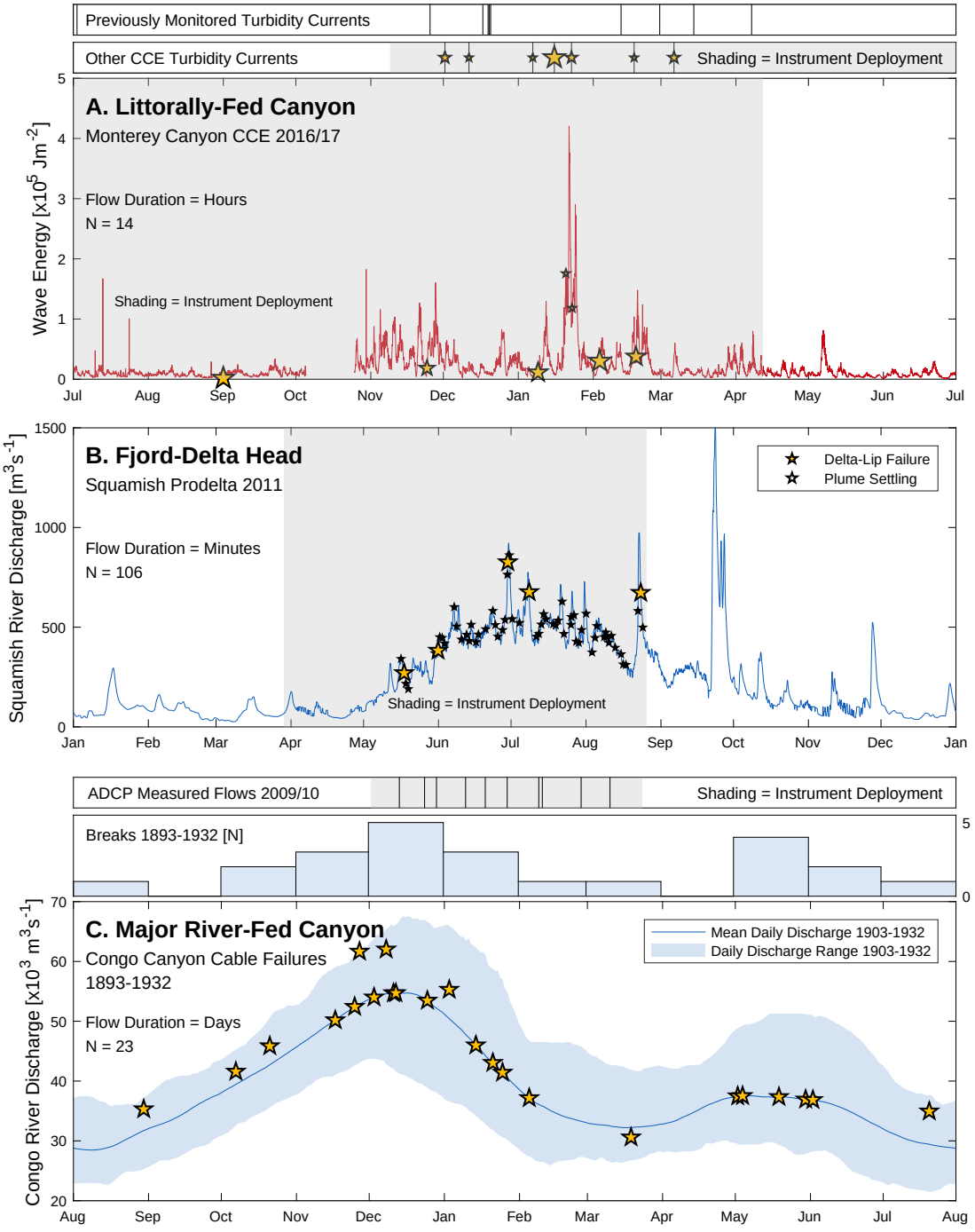


**Figure 2.8:** Comparison of annual turbidity current timing in different physiographic settings and sediment delivery mechanisms. (A) Monterey Canyon as an example of a littoral-fed canyon showing events from July 2016 to June 2017 during the CCE. Stave above plot shows the day and month of previously measured flows by Paull et al. (2003, 2010) and Xu et al. (2004) and other flows recorded during the CCE. (B) Squamish Prodelta, British Columbia, Canada as an example of a submarine channel system connected to a fjord-delta head. Timing and flow initiation shown during 2011 from direct monitoring by Clare et al. (2016). (C) Congo Canyon as an example of a major river-fed canyon. Day and month of historical cable breaks

*(continued)*

et al., 1964, 1966). However, in very large river systems with complex catchments, turbidity currents may show less clustering. For example, the Congo River hydrograph comprises of two broad discharge peaks where turbidity current activity is increased (Fig. 2.8c; Heezen et al., 1964; Azpiroz-Zabala et al., 2017; Simmons et al., 2020).

### 2.5.4 New Model for Preconditioning and Triggering of Turbidity Currents via Slope Failure

We combine insights from Monterey Canyon and these other field sites (Fig. 2.8) into a generalised model for turbidity current activity in areas of sustained sediment accumulation, such as canyon-heads or river mouths. The model assumes that initiation occurs via slope failure, and it is thus not applicable where turbidity currents are triggered primarily in other ways, including hyperpycnal or surface river plumes (Fig. 2.1). The model explains why some flows do not coincide with major external triggers, or variable time delays occur between flows and those major external triggers, as well as seasonal increases in flow activity that follow fluctuations in sediment supply. It is hoped that future work can then test the model more rigorously, including its basic assumptions regarding triggering via slope failure, and persistence of excess pore pressures long after peak sedimentation rates. Unfortunately, at present, there are no suitable time series of excess pore pressure available for such a purpose.

In this model, rapid or sustained sediment deposition causes elevated excess pore pressure in the subsurface. Pore pressures can be further elevated when links exist between onshore and offshore aquifers (e.g. Stegmann et al., 2011), tidal loading-unloading cycles or the presence of organic matter (Christian et al., 1997). The generation of these excess pore pressures precondition slopes such that they are close to failure (Fig. 2.9a). Here, small final perturbations can thus increase pore pressures above a critical value to trigger slope failure and a subsequent turbidity current (Fig. 2.9b). For example, this may arise from further changes in the pore pressure regime due to cyclic wave loading, tidal variations, elevated bed shear stresses arising from dense water cascading and internal tides or a combination of these factors (Fig. 2.1). Large sediment accumulations in the system head and upper reaches may also be entrained within a flow, whereby an initial relatively small event may ignite into a much greater volume, and longer runout flow (e.g. Piper & Savoye, 1993; Hizzett et al., 2018; Heerema et al., 2020). A broad

**Figure 2.8:** *(cont.)* between 1893 and 1932 documented by Heezen et al. (1964). Staves above shows day and month of measured turbidity currents between August 2009 and September 2010 directly monitored by Azpiroz-Zabala et al. (2017) and Simmons et al. (2020) and the number of cable breaks detected by month between 1893 and 1932. Yellow stars in panels show conditions recorded during events. Size of star for turbidity currents during the Monterey CCE relative to runout. For Congo Canyon cable breaks earlier than 1903 stars placed on average Congo River discharge, records prior to 1903 were not available.

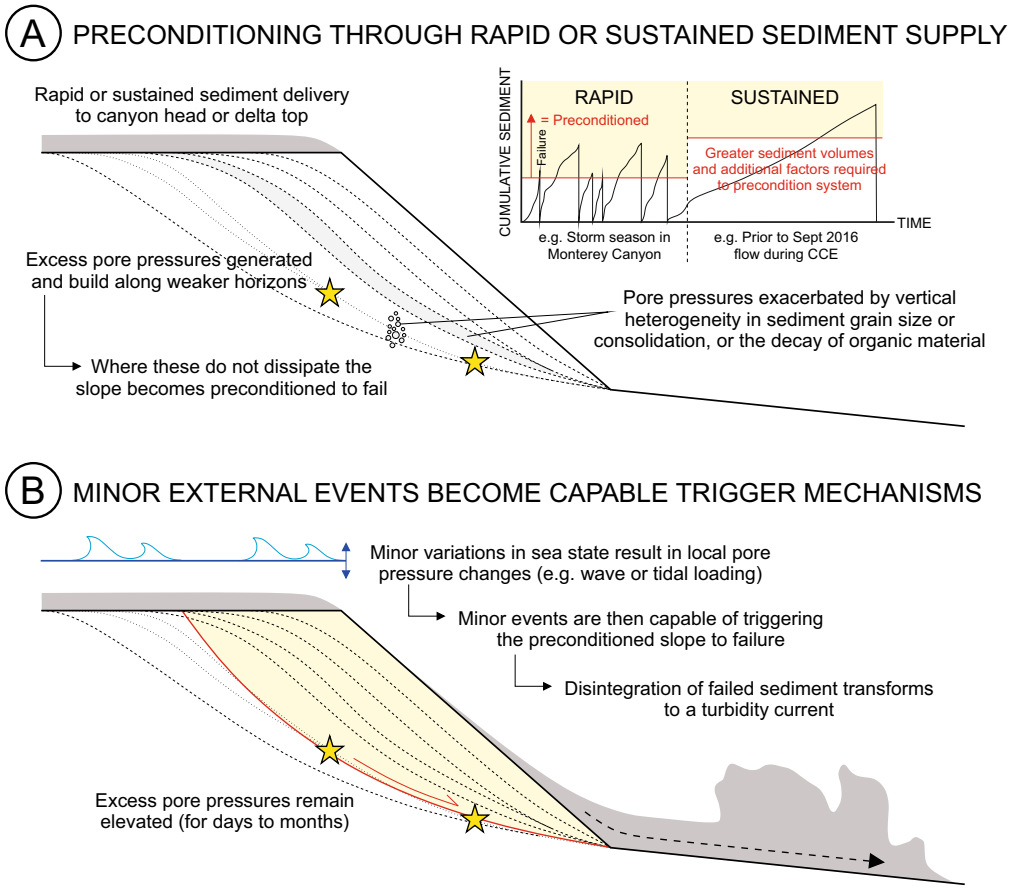


**Figure 2.9:** A new model for turbidity current activity in areas of sustained sediment accumulation, such as canyon-heads or river mouths, where initiation occurs via slope failure. Here (A), rapid or sustained sediment deposition in the system head generates excess pore pressures preconditioning the slope to failure. Where pore pressures cannot fully dissipate the slope will remain preconditioned to failure. (B) This allows minor external events to become capable triggering slope failure and a subsequent turbidity current by through further changes to local pore pressure.

analogy may be drawn with snow avalanches, which can be triggered by progressive snow accumulation, without a major external trigger, although there are also significant differences between snow pack and sediment structures.

The model implies that excess pore pressures take time to accumulate and build along weaker horizons, or eventually dissipate. This can result in time-delays between individual peaks in sediment supply and the timing of slope failure and initiation of turbidity currents. Most commonly, time delays are short (hours to weeks), such that turbidity current activity occurs primarily during specific seasons with elevated sediment supply. However, longer delays can sometimes also occur, as pore pressures persist for longer, or a cumulative sediment supply volume is reached to precondition slopes. In these cases, powerful and long runout turbidity currents occur during periods of low sediment supply, as occurred on 1$^{st}$ September 2016 in Monterey Canyon.

### 2.5.5 Wider Implications for Geohazard Assessment

Although not observed during our study of Monterey Canyon, turbidity currents can clearly be caused by major external triggers, including major earthquakes, typhoons and river floods. This was famously shown by the 1929 Grand Banks event, where a 7.2 $M_W$ earthquake-triggered a turbidity current, recorded by sequential cable breaks extending up to 720 km offshore (Heezen & Ewing, 1952; Piper et al., 1999). More recently, the 2016 7.8 $M_W$ Kaikōura earthquake, New Zealand, triggered a turbidity current with a runout of >680 km through the Hikurangi submarine channel (Mountjoy et al., 2018). Furthermore, cable-breaking flows in the Gaoping Canyon, offshore Taiwan, in 2006, 2009 and 2010 appear to be triggered by either large ($M_L$ >7) earthquakes, tropical cyclones or river floods (Hsu et al., 2008; Carter et al., 2009; Gavey et al., 2017; Pope et al., 2017b).

However, our results show that relatively powerful (up to 7.2 $ms^{-1}$ and long runout >52 km) turbidity currents, can sometimes initiate through slope failure without a major external trigger such as storms, floods or earthquakes. Flows triggered by small external perturbations can move 800 kg objects, and thus could damage cables and seabed infrastructure. Most commonly, increased turbidity current activity occurs during periods of high relative sediment supply, although the precise timing of turbidity currents may not coincide with individual floods or large storm waves. At least in these types of systems, predicting the exact timing of turbidity currents is challenging. However, where sediment supply is seasonal, we can anticipate windows of increased turbidity current likelihood, for geohazard assessments and the routing or maintenance of critical seafloor infrastructure.

## 2.6 Conclusions

This study presents some of the most detailed measurements yet for the timing of turbidity currents and environmental conditions that may trigger flows. No consistent trigger was observed for the fourteen flows that were recorded in Monterey Canyon, but turbidity currents were more frequent in the winter storm season. During this winter, heightened wave energy increases sediment transport to the canyon head and similar volumes of sediment were estimated to enter the canyon head between flows. A single powerful (up to 4.8 $ms^{-1}$ and >52 km runout) event was observed outside the winter, when sediment supply rate is reduced. However, the total sediment volume entering the canyon head was approximately four times higher than the mean between winter events. We therefore propose that turbidity current activity is better related to sediment supply and slope preconditioning rather than individual triggers.

We combine insights from Monterey Canyon and other sites of direct monitoring to produce a model for preconditioning and triggering of turbidity currents via slope failure, in locations of sustained sediment accumulation such as canyon heads and river deltas. In this model, rapid or sustained sediment supply alone can produce elevated pore pressures, which may persist, thereby predisposing slopes to fail for hours to months (or potentially even longer in muddy systems) after initial sediment deposition. Small perturbations in antecedent conditions resulting in local pore pressure variation then become capable triggers, demonstrating that major external events such as earthquakes, storms or river floods are not a prerequisite for turbidity current activity.

# Chapter 3

# Predicting Turbidity Current Activity Offshore from River Deltas: A Novel Statistical Approach

**This chapter is an altered version of text planned for submission to**
***Earth and Planetary Science Letters***

Lewis P. Bailey, Michael A. Clare, Ed L. Pope, Ivan D. Haigh, Matthieu J.B. Cartigny, Peter J. Talling, D. Gwyn Lintern, Sophie Hage, and Maarten Heijnen

LB, MC, and IH conceptualised the research question. LB, MC, EP, MJBC, PT, GL and MH were part of the research fieldwork team. EP analysed ADCP data to calculate the timing of turbidity currents. LB developed the statistical methods, analysed data and led on data visualisation. LB led the writing of the original manuscript with MC, which all other co-authors then reviewed and edited.

Turbidity currents dominate the transfer of sediment and particulate matter from land to the deep sea, and pose a risk to subsea infrastructure such as seafloor telecommunications cables. Numerous mechanisms are capable of triggering turbidity currents, even within a single system. However, due to the limited number of turbidity currents ($N < 22$) recorded by field-scale monitoring campaigns, statistical analysis of their recurrence and potential triggers have been limited to univariate statistical methods (i.e. only allowing for investigation of an individual trigger for each flow). As such, we are yet to quantitatively determine if, and how, multiple coincident triggers may combine to generate turbidity currents, and their relative importance. Here, we analyse the most extensive number ($N = 113$) of directly-monitored turbidity currents within a submarine channel from two field campaigns (freshets of 2016 and 2018) in Bute Inlet, a river-fed fjord located in British Columbia, Canada. We demonstrate the statistical

significance of both river discharge and water level on turbidity current occurrence. Using logistic regression on the timing of turbidity currents during 2018 we statistically determine the relative roles of river discharge and water level, which combine to enhance turbidity current likelihood. Based on this relationship we build a model capable of calculating turbidity current probability for any given input of river discharge and water level; successfully predicting 86% of turbidity current activity (i.e. turbidity currents and non-events) during 2018. Validation of this predictive model on the 2016 Bute Inlet monitoring dataset and other similar sites (the Squamish and Fraser Rivers, both British Columbia, Canada) yield >84% successful hindcasts of turbidity current activity (despite being built on an independent dataset). The model therefore appears to have strong predictive power for systems where sediment supply is seasonal and turbidity currents are principally triggered at low tide. We suggest that our model may be further extended to river deltas where sediment flux is either river- or tidally-controlled, which collectively account for 87% of the global sediment flux from river deltas to the ocean. This predictive model may therefore improve risk assessments for important seafloor infrastructure, and enhance our understanding of land to sea fluxes of sediment, carbon and pollutants at a large number of offshore river deltas.

## 3.1 Introduction

Submarine sediment gravity flows, known as turbidity currents, sculpt the deepest canyons (Shepard, 1972; Harris & Whiteway, 2011) and form some of the largest sediment accumulations on our planet (Talling, 2014). Turbidity currents dominate the transport of terrestrial derived sediments (Talling, 2014), organic matter (Dai et al., 2012; Galy et al., 2007; Hage et al., 2020; Lee et al., 2019), and pollutants, such as litter (Pierdomenico et al., 2019; Zhong & Peng, 2021) and plastics (Lebreton et al., 2017; Pohl et al., 2020), to deep ocean basins. These flows pose a significant hazard to seafloor infrastructure such as telecommunications cables, as a result of their high velocities (up to 20 $ms^{-1}$; Hsu et al., 2008) and long runout distances (Heezen & Ewing, 1952; Piper et al., 1999; Carter et al., 2012, 2014; Gavey et al., 2017). Numerous mechanisms are capable of triggering turbidity currents, even within a single system (Canals et al., 2006; Khripounoff et al., 2009; Carter et al., 2012; Gavey et al., 2017; Bailey et al., 2021). However, field measurements to date have been insufficient for robust statistical analysis of turbidity current triggering and no measurements from source-to-sink exist. As such, we are yet to quantify: (1) how multiple coincident triggers can combine to generate turbidity currents; (2) the relative importance of different triggers where multiple mechanisms may be responsible in a single system, and; (3) whether turbidity current runout is controlled by the type of trigger, or a combination of multiple triggers. Statistical analysis of a large number of turbidity currents measured at high-temporal

resolution, and from source-to-sink, is critical to address these outstanding issues. Robust statistical analysis is needed to advance our ability to predict turbidity current frequency, magnitude and timing to assess the threats posed to seafloor infrastructure, and to quantify the temporally-variable fluxes of sediment and associated particulate matter to the deep sea.

The mechanisms for turbidity current initiation are best constrained offshore from river deltas. These mechanisms include: (1) Delta slope failures generate submarine landslides that can evolve downslope to turbidity currents (Prior et al., 1981; Clare et al., 2016; Hizzett et al., 2018); (2) Plunging of a sediment-laden river flood water can directly form a turbidity current if the suspended sediment concentration exceeds the density of seawater (>40 kg $m^{-3}$; Mulder & Syvitski, 1995; Khripounoff et al., 2009, 2012; Carter et al., 2012; Liu et al., 2012, 2013); (3) Indirectly, from sediment settling-driven convection from a more dilute plume (sediment concentrations as low as 1 kg $m^{-3}$; Parsons et al., 2001); (4) Turbidity currents can also initiate from exceptionally dilute river plumes (<1 kg $m^{-3}$) when sediment accumulating in the tidal turbidity maximum is released at low tide (Hage et al., 2019).

Recent field scale flow monitoring offshore river mouths has advanced our understanding of the controls of turbidity current activity; recognising the combined effect of elevated river discharge and tidal drawdown on flow generation without a need for a large external trigger (Ayranci et al., 2012; Hughes Clarke et al., 2012; Clare et al., 2016; Lintern et al., 2016; Hage et al., 2019; Hill & Lintern, 2021). For example, elevated river discharge may rapidly deposit sediment on the delta-lip, thus preconditioning the delta slope to failure. The likelihood of failure is subsequently heightened at low tide when hydrostatic pore pressures decrease, due to the expansion of gas bubbles (Christian et al., 1997). Similarly, high river discharge can increase suspended sediment in the turbidity maximum; this turbidity maximum is also driven further away from the delta-lip by the promotion of faster flow at lower tides. Similarly, amplification of river flow velocity at low tide, especially during spring cycles, will also increase river bed shear stress resulting in enhanced erosion and flushing sediment from the delta top (Clare et al., 2016; Eidam et al., 2016, 2019). The mechanisms involved may vary, but the common theme is that the triggering of turbidity currents offshore from river deltas appears to be strongly controlled by a combination of both river discharge and tidal fluctuations. However, the number of precisely timed turbidity current field measurements in a single site ($N < 22$) has limited statistical approaches to univariate analysis. Such methods test the significance of individual triggering parameters (i.e. river discharge and tide) in isolation, but so far have not allowed the investigation of multiple coincident environmental factors that combine (often in a non-linear manner or with threshold behaviours) to trigger flows. As such, it has not been possible to develop a model to assess the relative importance of these triggers to predict turbidity current timing.

Here, we analyse the most extensive number (N = 113) of field-monitored turbidity currents in a submarine channel from source-to-sink, in Bute Inlet, a glacial meltwater-fed fjord located in British Columbia, Canada (Fig. 3.1). Precise (up to 4 second-resolution) turbidity current timing was recorded using six Acoustic Doppler Current Profilers (ADCPs) from the Homathko River Delta to the channel-lobe over two separate deployment campaigns during 2016 and 2018 (Table 3.1). These flow timings, along with monitoring of the river discharge and tidal elevation at the time of flow generation, are used to quantify both the individual and combined effects of triggering parameters on turbidity current activity and assess whether this corresponds to flow runout distance. From this, we develop a novel multivariate statistical framework for predicting turbidity current timing at Bute Inlet. We validate our model, and demonstrate its predictive power, by hindcasting turbidity current activity (i.e. timing of turbidity currents and periods without turbidity currents) in Bute Inlet and on similar, but unrelated, systems (Fraser River and Squamish Deltas). Given the fact that the fluvial-marine sediment flux at 87% of deltas worldwide are dominantly controlled by river discharge or tides (Nienhuis et al., 2020), we finally discuss how our statistical approach can provides a basis to predict the timing of turbidity current activity at other river deltas, and its application to assess geohazard risk to critical seafloor infrastructure.

## 3.2 Geographic Setting

Bute Inlet lies within the Pacific Ranges of the Coast Mountains of British Columbia, Canada. The coastal environment of the region is macrotidal, predominantly semidiurnal, with a range of 5 m. Mountains exceeding elevations of 3000 m are common, with many maintaining small ice caps and valley glaciers (Holland, 1976) within the drainage basins of the Homathko and Southgate Rivers, which provide 75% and 19% of the freshwater entering the fjord, respectively (Farrow et al., 1983). The Homathko River has an average discharge of 250 $m^3s^{-1}$, but often exceeds daily discharge maxima of 1000 $m^3s^{-1}$, during the May to August freshet season due to summer glacial melt, decreasing to $\sim$50 $m^3s^{-1}$ in January to February. Peaks in discharge typically also occur in late October to November following periods of intense rainfall. Estimates of maximum suspended sediment concentrations for the Homathko River are 0.5-0.7 kg $m^{-3}$; such concentrations are not sufficient for wholescale plunging of (hyperpycnal) river floodwater (Bornhold et al., 1994; Mulder & Syvitski, 1995). The Southgate River has only been gauged since June 2021, and has a discharge approximately 50 % of the Homathko River. The delta fronts of the Homathko and Southgate Rivers are characterised by a series of subaqueous channels, which converge into two well-developed channels entering the fjord from opposite sides (Fig. 3.1). These two channels join forming a single submarine channel that continues down-fjord for 40 km to a water depth of 660 m where the channel transitions to a depositional lobe (Conway et al.,

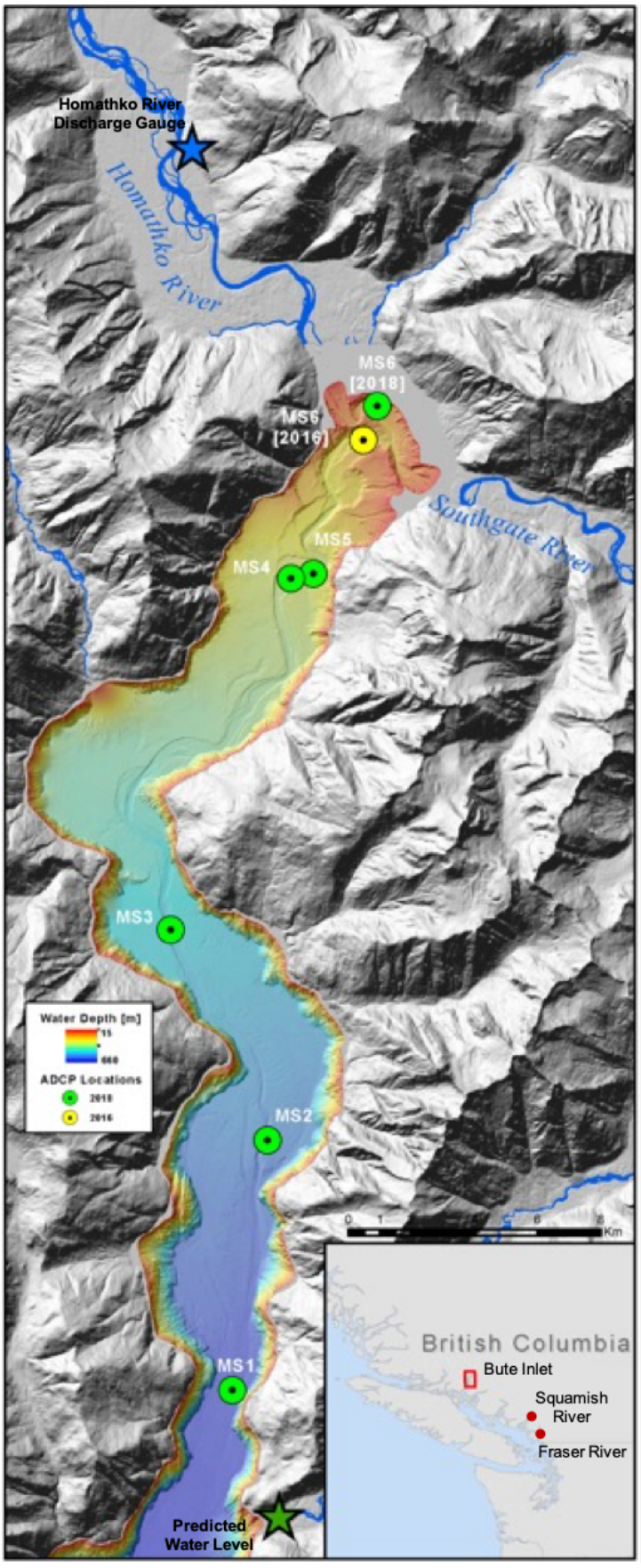


**Figure 3.1:** Bathymetric map of the submarine channel in Bute Inlet, showing the locations of instrument moorings (labelled MS6 to MS1), Homathko River gauge and location of predicted tides in Orford Bay.

2012). This submarine channel is highly active with 10s of turbidity currents frequently occurring in the upper channel during the freshet (Prior et al., 1981; Zeng et al., 1991; Bornhold et al., 1994).

## 3.3 Methods

### 3.3.1 Instrument Deployment

Turbidity current monitoring data were acquired from two separate field campaigns in Bute Inlet during the freshet seasons of 2016 (11$^{th}$ June to 10$^{th}$ October) and 2018 (15$^{th}$ May to 25$^{th}$ September). Six moorings holding downward looking ADCPs were deployed in each monitoring campaign, the positions of which were consistent apart from the uppermost mooring (MS6) which was located ~2.5 km closer to the Homathko River Delta in 2018 (Fig. 3.1; Table 3.1). Measurements of water column velocity and backscatter were made at 4 or 6-second resolution in 0.5-1.0 m vertical intervals (Table 3.1). In 2016, velocity data was only recorded at MS4, while MS6 only made measurements for the first 50 days (~40 %) of deployment. Water damage to MS5 during the 2018 deployment also resulted in no measurements.

### 3.3.2 Measuring Turbidity Currents and Potential Triggers

A turbidity current is defined here as an event which results in an abrupt increase in ADCP backscatter (i.e. increased suspended sediment) and a down-channel increase in velocity. Sequential increases of each of these parameters at each mooring down-channel then provides a minimum runout distance. The detection time at MS6 (the shallowest mooring) is taken as the timing of turbidity current initiation to compare to potential triggering mechanisms. River discharge and tidal drawdown has previously been recognised as the drivers in turbidity current activity offshore from rivers deltas (e.g. Ayranci et al., 2012; Hughes Clarke et al., 2012; Clare et al., 2016; Lintern et al., 2016; Hage et al., 2019; Hill & Lintern, 2021). We therefore compare the timing of turbidity currents to: (1) Hourly discharge data of the Homathko River obtained from Environmental and Natural Resource Canada Station 08GD004 (https://wateroffice.ec.gc.ca), located 10 km upstream from the Homathko Delta. The Southgate River was not gauged during the period of the study so therefore could not be analysed. (2) Water level estimates using tidal predictions (water level measurements were not available for 2018) for peak high and low tides at Orford Bay (http://tides.gc.ca). A time series was produced by fitting a cubic interpretation to splice data into hourly measurement.

**Table 3.1:** Specifications and location information for the moorings and instruments deployed in Bute Inlet during 2016 and 2018.

| | Distance from Delta [m] | | ADCP Frequency [kHz] | | Temporal Resolution [s] | | Bin Size [m] | |
|---|---|---|---|---|---|---|---|---|
| Mooring | 2016 | 2018 | 2016 | 2018 | 2016 | 2018 | 2016 | 2018 |
| MS6 | 5230 | 2880 | 600 | 300 | 2.5 | 6.0 | 1.0 | 1.0 |
| MS5 | 11930 | 11420 | 600 | 600 | 2.5 | 6.0 | 1.0 | 0.5 |
| MS4 | 12479 | 12080 | 600 | 600 | 2.5 | 6.0 | 1.0 | 0.5 |
| MS3 | 28845 | 27870 | 600 | 300 | 10.0 | 6.0 | 1.0 | 0.5 |
| MS2 | 35815 | 35690 | 300 | 600 | 2.5 | 6.0 | 2.0 | 1.0 |
| MS1 | 44295 | 43800 | 300 | 600 | 2.5 | 4.0 | 2.0 | 1.0 |

### 3.3.3 Univariate Statistical Analysis

Non-parametric Mann-Whitney-Wilcoxon and Kolmogorov-Smirnov tests are used to determine whether the distribution of Homathko River discharge and tidal elevation are significantly different at the time of turbidity currents to periods of non-events. The turbidity current sample sizes for both 2016 and 2018 tests are suitable for these statistical tests, both of which have the advantage of not requiring the distribution of data a priori. The Kolmogorov-Smirnov test is sensitive to any differences (i.e. shape, spread or median) in the two distributions whereas the Mann-Whitney-Wilcoxon test is sensitive to changes in the median. Statistically significant differences are defined when $p < 0.05$ at the 5% significance level.

### 3.3.4 Logistic Regression Probability Model

To quantify the relative contribution of Homathko River discharge and tidal elevations for the generation of turbidity currents we use logistic regression. This method is well suited to testing the relationship between a categorical outcome (i.e. the triggering of a turbidity current, $Y = 1$; or not, $Y = 0$), with one or more predictor variables (i.e. Homathko River discharge and tidal elevation). Such analysis of a dichotomous outcome is difficult to describe with ordinary least squares regression due to: firstly, the extremes in predictors not following linear trends; and secondly, errors are neither normally distributed nor constant across the entire data range. Logistic regression solves these problems by applying the logit transformation to the dependent variable. In essence, the logistic model predicts the logit of $Y$ (outcome variable) from $X$ (predictor variables). The logit is the natural logarithm (ln) of odds for $Y$, where the odds are ratios of probabilities of $Y$ happening ($p$) to the probabilities of $Y$ not happening ($1 - p$). The natural logarithm of the odds ratio is, in turn, equivalent to a linear function of the predictor variables. The simple logistic model has the form:

$$\text{logit}(Y) = \ln(odds) = \ln\left(\frac{p}{1-p}\right) = \alpha + \beta x + \beta_n x_n ... \tag{3.1}$$

An estimated regression equation for the probability of the outcome of interest occurring can therefore be derived by taking the antilog of Equation 3.1:

$$\hat{p} = \frac{e^{\alpha+\beta x+\beta_n x_n ...}}{1 + e^{\alpha+\beta x+\beta_n x_n ...}}, \tag{3.2}$$

where, $p$ is the probability for the outcome event occurring $\hat{p}$ is an estimate of probability for the outcome event occurring, $\alpha$ (or y-intercept) and the $\beta$s are regression coefficients and the $x$s are specific values from the n number of categorical or continuous predictor variables. The null hypothesis underlying the overall model states that all regression coefficients equal zero. A rejection of this null hypothesis implies that at least one regression coefficient does not equal zero, therefore the logistic regression equation predicts the probability of the outcome more accurately than the mean of the dependent variable.

### 3.3.5 Data Preparation and Application of Logistic Regression

To estimate turbidity current likelihood, we use Homathko River discharge and position in the tidal cycle as predictor variables. Turbidity current activity in Bute Inlet does not always align with peaks in Homathko River discharge (see Section 3.4.1; Bornhold et al., 1994). Instead, turbidity current activity 'switches on' above a minimum discharge threshold (e.g. Clare et al., 2016). To ensure our model does not overestimate turbidity current likelihood based on discharge peaks, the Homathko River discharge component of the model uses raw discharge normalised to a percentile from 20 years of recorded measurements (1999-2018). This normalisation further allows the model to be applied to other turbidity current systems (i.e. normalisation exaggerates the onset of the freshet when systems are 'switched on' for turbidity current activity; see Section 3.5.2 for application to the Squamish and Fraser Deltas). Turbidity current activity is most favourable at low (spring) tide (e.g. Clare et al., 2016; Hage et al., 2019); however, water level in isolation is a poor predictor of turbidity current activity (see Section 3.4.1). For example, the same measurement of water level for different days may represent different positions in the tidal cycle. We therefore classify water level in a series of tidal zones for low ($L$), high ($H$), high-low ($hL$) and low-high ($lH$) positions in the semidiurnal tidal cycle. Each of these zones is defined as a 4-hour period centred on slack water. To make certain these windows do not overlap $L$ and $H$ zones take priority, with $hL$ and $lH$ zones shortened. Where $hL$ and $lH$ zones preference is taken to the closest tidal peak, and removed from the other window. Dummy coding is applied to each water level measurement to produce a categorical model input (i.e. if hourly

measurement is within the low tide window $L = 1$, and all other zones $H$, $hL$, $lH = 0$). This is then multiplied by the corresponding tidal range (i.e. the distance between the closest neighbouring low and high-water levels) such that a higher value with signify spring tides. We use these variables to apply a five-predictor logistic model, such that:

$$\hat{p}(\mathrm{TC}) = \frac{e^{\alpha+\beta_1 Q+\beta_2 L+\beta_3 H+\beta_4 hL+\beta_5 lH}}{1+e^{\alpha+\beta_1 Q+\beta_2 L+\beta_3 H+\beta_4 hL+\beta_5 lH}} \tag{3.3}$$

where, $\hat{p}$(TC) is the estimate of turbidity current occurrence probability, again $\alpha$ (or y-intercept) and the $\beta$s are regression coefficients, $Q$ is the percentile normalised Homathko River discharge, and $L$, $H$, $hL$ and $lH$ each refer to the tidal zones. Equation 3.3 is effectively a two-predictor logistic model, as only one of the tidal zones will have a non-zero value for a given measurement of water level.

Estimations of the $\alpha$ and $\beta$ constants are calculated using the timing of turbidity currents recorded at MS6 (Fig. 3.1) during 2018. Here, each corresponding hourly measurement throughout 2018 of percentile normalised Homathko River discharge and categorical tidal zones were assigned a value of $p$(TC) = 1, where a turbidity current occurred within that hour, or $p$(TC) = 0, when a turbidity current did not occur. As turbidity current activity is reduced, or switched off entirely, outside of the freshet (Bornhold et al., 1994), and the instrument deployment period aligned with the elevation of Homathko River discharge (Fig. 3.2b), we assume that no turbidity currents occurred outside the monitoring window. The maximum likelihood method, which is designed to maximise the likelihood of reproducing the data (Peng et al., 2002), is then used to calculate $\alpha$ and $\beta$ estimates. Once calculated, the probability of a turbidity current occurring can be estimated for any measurement of percentile of the normalised Homathko River discharge and categorical tidal zone.

### 3.3.6 Evaluation of Logistic Model

We evaluate the logistic model by using a series of statistical tests of individual predictors and the overall model (i.e. the model including all predictor coefficients). Predicted probabilities are then compared to the precise timings of turbidity currents recorded in Bute Inlet during 2018 to determine the quality of model calibration and the ability to discriminate between prediction of turbidity currents and non-events.

#### 3.3.6.1 Statistical Tests of Individual Predictors

The statistical significance of individual regression coefficients (i.e. $\alpha$ and $\beta$ constants) are tested using the Wald chi-squared ($\chi^2$) statistic. The Wald test on individual predictors tests the null hypothesis that each parameter is equal to zero. If the model fails to

reject the null hypothesis the variable can be removed without decreasing the overall model fit. The null hypothesis is rejected and parameters are statistically significant if $p < 0.05$ and $\chi^2 > 3.84$ (critical $\chi^2$ value for a single degree of freedom at the 5 % significance level).

#### 3.3.6.2 Overall Model Evaluation

A logistic model is said to provide a better fit to the data if it demonstrates an improvement over the null (intercept, or $\alpha$-only) model. An improvement over this baseline is assessed using the likelihood ratio and Wald tests (Fox, 1997; Peng et al., 2002). These tests compare the fit of the logistic model (i.e. including predictor variables) to the null model using the log-likelihood function. If the difference is statistically significant the less restrictive model (i.e. model with predictors) is said to fit the data significantly better than the more restrictive model. The likelihood ratio test compares the offset in the log-likelihood value of the logistic model (the maximum likelihood estimate) with the log-likelihood value of the null model (i.e. the vertical offset), whereas the Wald test compares the horizontal offset between these two values. For both tests the model is then said to be statistically significant if the null hypothesis is rejected. In both tests the statistical significance of the logistic model is determined when $p < 0.05$ and $\chi^2 > 11.1$ (the critical $\chi^2$ value for a logistic model with five – the number of predictor variables – degrees of freedom at the 5% significance level).

#### 3.3.6.3 Model Calibration

Model calibration refers to the fit of the model to the actual outcome. The quality of model calibration is assessed through comparison of estimated probabilities of turbidity current occurrence with the actual timing of flows during the 2018 monitoring campaign in Bute Inlet. We measure the fit of the logistic model using the Hosmer-Lemeshow test. The Hosmer-Lemeshow statistic is a Pearson $\chi^2$ statistic calculated based on observed and predicted expected frequencies to assess the model calibration (Lemeshow & Hosmer Jr, 1982). Data are sorted and split into 10 groups according to the probability of turbidity current occurrence. The mean probability in each group is then used to calculate the number of expected turbidity currents. For example, if the mean probability of a group is 0.2, then the expected number of turbidity currents is 19 (i.e. 20% of the 95 detected flows). The expected number of flows is then compared to the actual number of turbidity currents for each group. If the Hosmer-Lemeshow test yields a $\chi^2(8) < 15.5$ (critical $\chi^2$ value for 8 – the number of groups minus two – degrees of freedom at the 5% significance level) and is statistically insignificant ($p > 0.05$ at the 5% significance level; Lemeshow & Hosmer Jr, 1982) the model is said to be well calibrated. Model calibration is then supplemented using the pseudo-$R^2$ ($R^2_{McF}$) index

defined by McFadden (McFadden, 1974). $R^2_{McF}$ values above 0.2 indicate extremely good model fit with good predictive power (Domencich & McFadden, 1975; Louviere et al., 2000).

#### 3.3.6.4 Model Discrimination

Model discrimination assesses the predictive power of the logistic model. The model must have the ability to discriminate between events and non-events. For example, observations of turbidity currents ($Y$ = 1) should be associated with high predicted probabilities and periods of no turbidity currents ($Y$ = 0) with low predicted probabilities. The use of the logit function in logistic regression will not classify observations as positive (i.e. the occurrence of a turbidity current) or negative (i.e. non-events). We therefore choose a cut point ($c$), and classify calculated probabilities above c as 'positive' and below as 'negative'. The value of $c$ is determined by model sensitivity and specificity are equal, where sensitivity is the probability of predicting an observation as 'positive' given that $Y$ = 1, and specificity is the probability of the model predicting a 'negative' given the actual outcome was $Y$ = 0. In choosing a cut-point there is an intrinsic trade-off between sensitivity and specificity. Increasing $c$ results in fewer observations where $Y$ = 1 will be predicted as 'positive' reducing sensitivity, but more $Y$ = 0 observations will be predicted as 'negative', increasing specificity. We therefore choose a value of $c$ where model sensitivity and specificity are equal. We use this c value to assess the overall predictive power of the logistic model i.e. the ability to correctly predict the monitored timing of actual turbidity currents, or absence of flows as 'positive' or negative' events.

The ability for the logistic model to discriminate between the timing of turbidity currents and non-events is further quantified using the concordance (or c-)statistic (Peng et al., 2002). The c-statistic here represents the probability of a randomly selected timing of a turbidity having a higher predicted probability than a randomly selected non-event. The c-statistic is equal to the area under the receiver operating characteristic (ROC) curve (see Section 3.4.2; Bamber, 1975; Hanley & McNeil, 1982). We define the ROC curve as a plot of sensitivity against one minus specificity as c is increased from 0 through to 1 at intervals of 0.001 (see Section 3.4.2). A c-statistic value greater than 0.9 is used to demonstrate a very strong predictive power of a logistic model (Hosmer Jr et al., 2013).

### 3.3.7 Comparison of Univariate and Multivariate Analysis for Predicting Turbidity Currents

Turbidity currents were predicted using the logistic model (see Section 3.4.2; Equation 3.4), as well as using the Homathko River discharge and water level in isolation. To

compare predicted results with the actual timing of turbidity currents, 95 (the number of turbidity currents during 2018) points were randomly selected from the top 10th percentile of results from the logistic model, Homathko River Discharge and lowest 10th percentile of water level. The non-parametric Mann-Whitney-Wilcoxon and Kolmogorov-Smirnov tests (see Section 4.3.3) are used to assess the difference in distribution of Homathko River discharge and water level during both the annual 2018 range and during recorded turbidity currents with each of the predicted outcomes from Homathko River discharge, water level and the logistic model. Here, a good prediction would be expected to show a statistically significant difference ($p < 0.05$ at the 5% significance level) to the annual range of measurements (as shown in Section 3.4.1) and no statistically significant difference ($p > 0.05$ at the 5% significance level) when compared to the measurements of Homathko River discharge and water level recorded during actual monitored turbidity currents. Offsets in distribution are further quantified as the difference between medians (DBM) as a percentage of overall visual spread (OVS), where OVS is the range from the lowest to highest interquartile ($25^{th}$ and $75^{th}$ percentile) range (e.g. Bailey et al., 2021).

### 3.3.8 Testing the Logistic Model on Other Datasets

To validate our model we first apply the logistic equation built using the 2018 dataset in Bute Inlet (see Section 3.4.2, Equation 3.4) to Homathko River discharge, tidal elevation and turbidity current timing recorded during 2016. We then assess the application of the predictive model to other sites using previous direct monitoring datasets from the Squamish River, Howe Sound during 2011 and the Fraser River during 2008, both British Columbia, Canada (Fig. 3.1 insert). Previous work has demonstrated that turbidity current activity at these locations is similarly focused during the freshet, with preferential triggering at low tide (Ayranci et al., 2012; Hughes Clarke et al., 2012; Clare et al., 2016; Lintern et al., 2016; Hage et al., 2019; Hill & Lintern, 2021). Howe Sound is located ~180 km southeast of Bute Inlet with the Squamish and Homathko Rivers having comparable discharge, and grain sizes present on the delta fronts (Hickin, 1989). Three channels incise the Squamish delta front, which extend seaward for ~2 km where each then terminates in a broader depositional lobe. A 600 kHz ADCP measuring at a 30 second temporal resolution, moored at the termination of the northern-most channel recorded precise timings of 22 turbidity currents during a 147 day deployment from March to August of 2011 (Clare et al., 2016). The Fraser River is the largest river in western Canada, with a river discharge is an order of magnitude greater than the Homathko and Squamish Rivers. An instrumented platform, located 250 m seaward of the Fraser Delta, was deployed adjacent to the main submarine channel from January to October 2008. Three turbidity currents were directly monitored using a 150 kHz ADCP along with temperature, pressure, salinity and turbidity sensors during this period (Ayranci et al., 2012).

## 3.4 Results

### 3.4.1 Turbidity Current Activity in Bute Inlet

A total of 113 turbidity currents were directly monitored in Bute Inlet using ADCPs during the Spring and Summer freshet of 2016 (N = 18) and 2018 (N = 95). Most turbidity currents had short down-channel runouts of between 3.1-12.2 km, with only 22% of turbidity currents recorded beyond this, and only two (one per campaign) detected at the final mooring located 44.1 km down-channel (Figs. 3.2a; 3.3a). During instrument deployment, all flows occurred during the freshet when Homathko River discharge was elevated above 230 $m^3$ $s^{-1}$ (Southgate River was not gauged during instrument deployment). Large peaks in the flood hydrograph (>1500 $m^3$ $s^{-1}$ in 2016) were observed between October and November, relating to seasonal periods of intense rainfall (Figs. 3.2b; 3.3b). However, ADCPs were not deployed during this interval, and thus turbidity current activity relating to this seasonal rainfall remains unknown. While there is a link between river discharge and turbidity current activity, individual peaks in the Homathko River discharge during the freshet did not always correlate with turbidity currents (Figs. 3.2b; 3.3b). Turbidity current timing also shows a strong correlation with tides; 68% of flows occur at peak low tide and 60% when tidal range is increased relating to neap-to-spring tidal cycles (Figs. 3.2c; 3.3c). Univariate analysis further quantifies the role of Homathko River discharge and water level on turbidity current timing. Both variables show a significant statistical difference between conditions during turbidity currents and periods where turbidity currents were absent (i.e. p value $< 0.05$ in non-parametric statistical tests; see Section 3.3.3). However, there was no apparent correlation between minimum turbidity current runout and water level, Homathko River discharge, and the cumulative river discharge (i.e. considering this as a proxy for sediment supply) between detected events (Fig. 3.4a-f).

### 3.4.2 Building a Predictive Model with Statistical Significance

To examine the combined effect of Homathko River discharge and tides on turbidity current timing we fit a logistic regression model (Equation. 3.3) to turbidity currents recorded in Bute Inlet during 2018. This model quantifies the roles of the Homathko River discharge (percentile normalised to 20 years of river discharge measurements;) and tides (position in the tidal cycle and tidal range; Table 3.2) such that:

$$\hat{p}(\mathrm{TC}) = \frac{e^{0.09Q+0.36L-0.52H-0.23hL-0.25lH-11.1}}{1+e^{0.09Q+0.36L-0.52H-0.23hL-0.25lH-11.1}}, \tag{3.4}$$

where, $\hat{p}$(TC) is the estimate of turbidity current occurrence probability, $Q$ is the percentile normalised Homathko River discharge, and $L$, $H$, $hL$ and $lH$ each refer to the

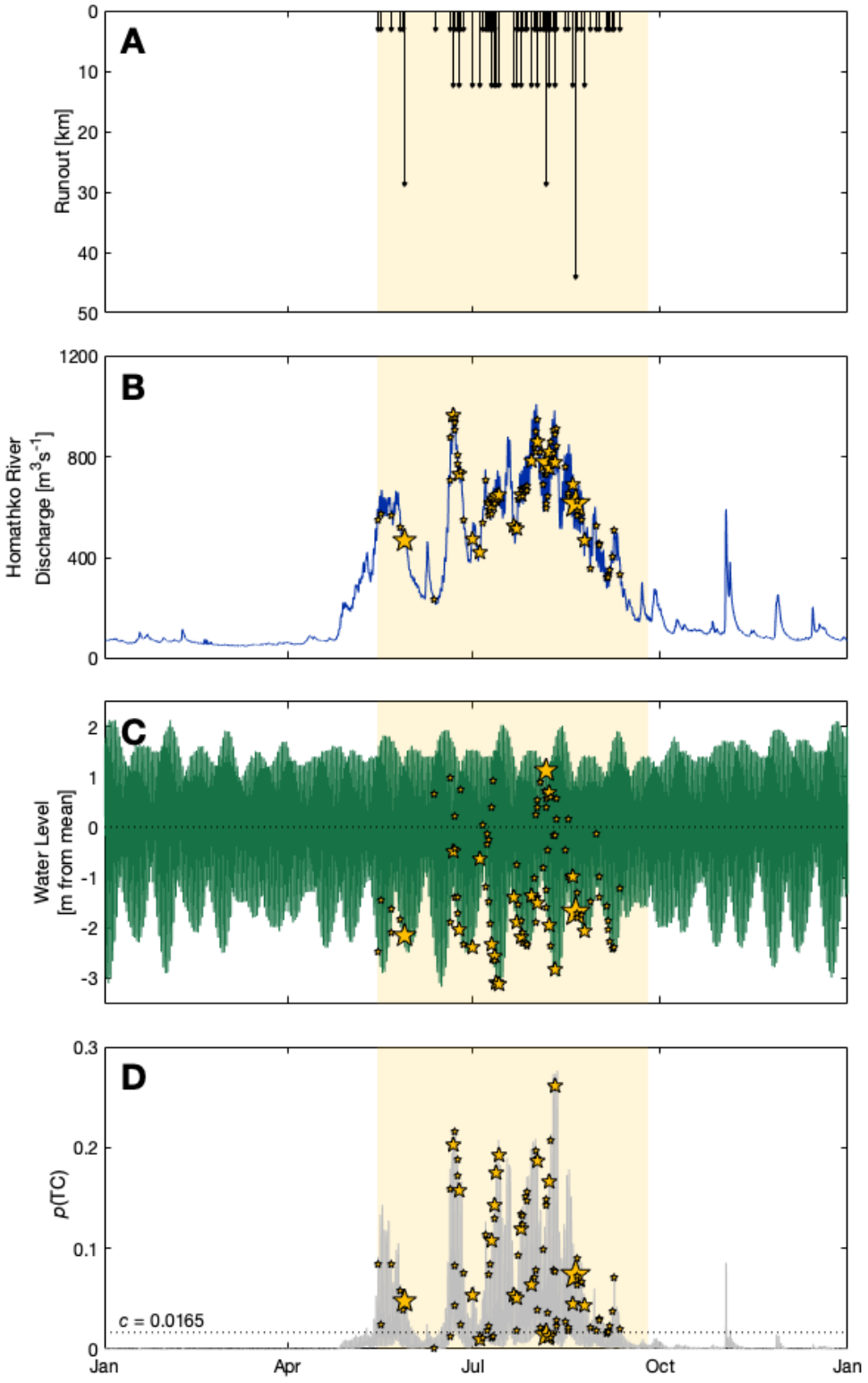


**Figure 3.2:** Time series of recorded and calculated measurements during 2018 at Bute Inlet. (A) The timing of detected turbidity currents with minimum channel runout. (B) Homathko River discharge. (C) Deviation of water level from mean. (D) Estimates for predicted probability of turbidity current occurrence from Eq. iv using Homathko River discharge and water level recorded during 2018. Yellow stars in B-D show the value of each variable during measured turbidity currents, the size of star is relative to minimum flow runout. Highlighted area denotes the period of instrument deployment.

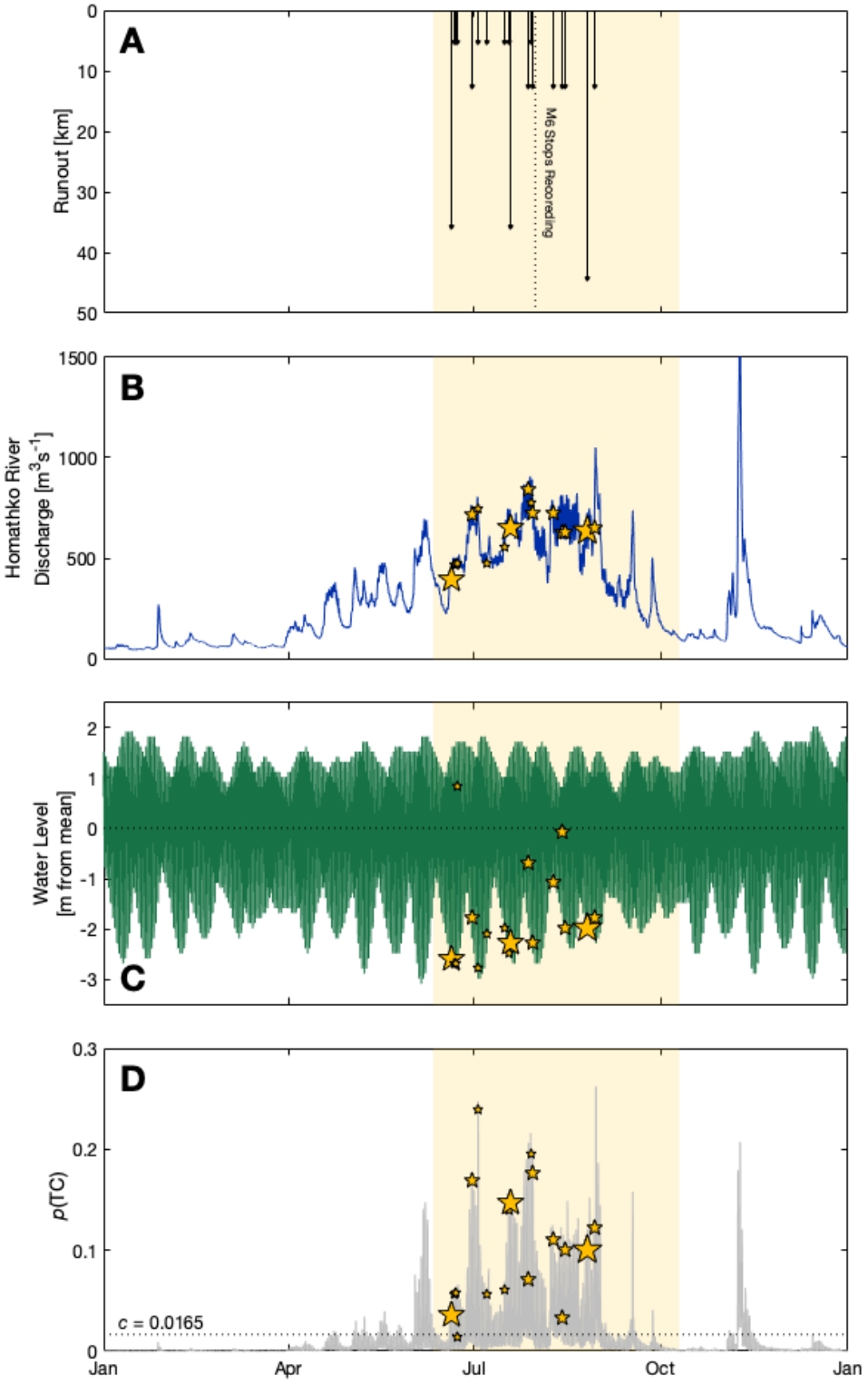


**Figure 3.3:** Time series of recorded and calculated measurements during 2016 at Bute Inlet. (A) The timing of detected turbidity currents with minimum channel runout. (B) Homathko River discharge. (C) Deviation of water level from mean. (D) Estimates for predicted probability of turbidity current occurrence from Eq. iv (built using the 2018 Bute Inlet dataset) using Homathko River discharge and water level recorded during 2016. Yellow stars in B-D show the value of each variable during measured turbidity currents, the size of star is relative to minimum flow runout. Highlighted area denotes the period of instrument deployment. Note most proximal mooring (MS6) stopped recording 50 days into monitoring.

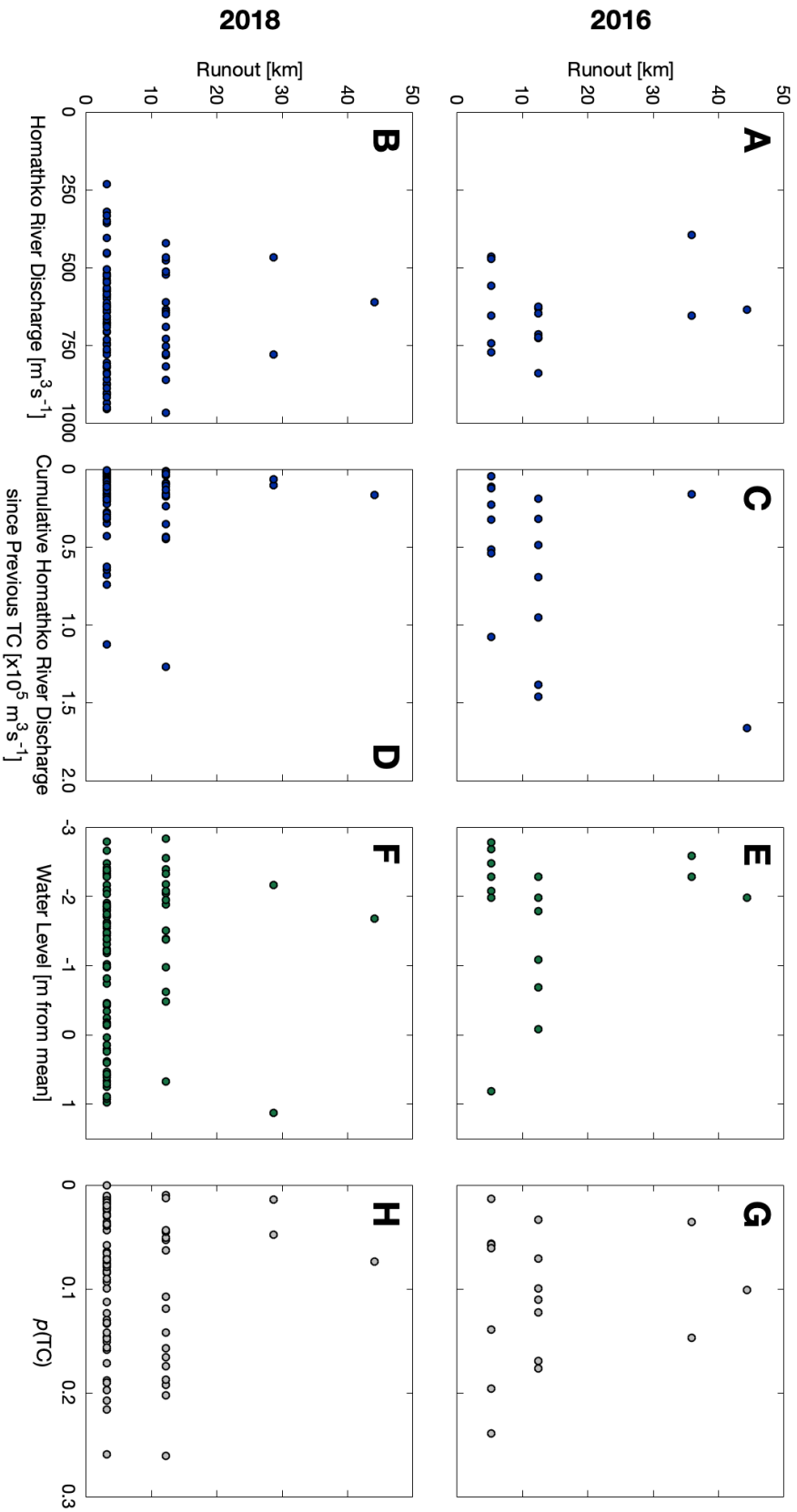


**Figure 3.4:** Cross-plots to show the relationship between turbidity current runout and Homathko River discharge during (A) 2016 and (B) 2018; cumulative river discharge since the previous turbidity current during (C) 2016 and (D) 2018; water level during (E) 2016 and (F) 2018; and predicted probabilities from Equation 3.4 during (G) 2016 and (H) 2018.

tidal zones. Our logistic analysis clearly reveals the controls played by both river discharge and tidal elevation. For example, turbidity current occurrence is at least 1.8 times more likely at low tide than any other position in the cycle for a given tidal range; and for every percentile increase in Homathko River discharge, the likelihood of a turbidity current increases by 9%.

By quantifying the roles of river discharge and tides on turbidity current generation it is possible to predict the likelihood of turbidity current occurrence for any given measurement of Homathko River discharge and position within the tidal cycle when combined with tidal range (Equation 3.4). Visual comparisons between predicted probabilities derived from Equation 3.4 using Homathko River discharge and water level measurements during 2018 with the timing of ADCP observed turbidity currents for 2018 demonstrates the good predictive performance of the logistic model. For example, ADCP monitored turbidity currents generally coincide with higher predicted probabilities while periods of low predicted probabilities feature an absence of observed turbidity currents (Fig. 3.2d). The statistical significance of the overall model and each regression coefficient was assessed by comparing the output from Equation 3.4, and the null model output (see Sections 3.3.6.1 and 3.3.6.2) for Homathko River discharge and tidal cycle measurements for 2018 with the actual 95 ADCP measured turbidity currents during 2018. Values of $p < 0.05$ and $\chi^2 > 11.1$ (the critical $\chi^2$ value; Table 3.2) for both the likelihood ratio and Wald tests demonstrated the output of the logistic model had a stronger predictive power than random chance. Similarly, the Wald test showed the significance of each individual predictor variable with all having values of $p < 0.05$ and $\chi^2 > 3.84$ (the critical $\chi^2$ value for a single variable; Table 3.2). The overall predictive power of the logistic model was assessed by comparing the frequency and timing between predicted turbidity current probabilities and actual monitored turbidity currents during 2018. The Hosmer-Lemeshow statistic ($p > 0.05$ and $\chi^2(8)$ below the critical value) and McFadden pseudo-$R^2$ ($R^2_{McF}$) value above 0.2 (see Section 3.3.6.3; Table 3.2) indicate the overall predicted turbidity current frequencies were well calibrated to the actual monitored outcome, with the model showing good predictive power (Domencich & McFadden, 1975; Louviere et al., 2000).

Predicted probability outputs from the logistic model (Equation 3.4) will range between 0 and 1 and therefore not classify predictions as 'positive' (the occurrence of a turbidity current), or 'negative' (the absence of a turbidity current). We therefore assessed the ability of the predictive model to discriminate between 'positive' and 'negative' events using a cut point ($c$), where model sensitivity and specificity are equal (see Section 3.3.6.4). Above this cut point the logistic model predicts the occurrence of a turbidity current, below the absence of a flow. Using the logistic model output with timing of ADCP monitored turbidity currents for 2018, the probability value where sensitivity and specificity are equal was $c = 0.0165$ (Fig. 3.5). A cut-point of $c = 0.0165$ was able to successfully predict 81 of the 95 ADCP recorded turbidity currents during 2018 as

**Table 3.2:** Results of logistic regression analysis for turbidity current occurrence in Bute Inlet during 2018 with statistical analysis of individual predictors and the overall model. The calculated values for the constant ($\alpha$) and each predictor ($\beta$) coefficient along with standard error ($SE$), Wald's $\chi^2$, degrees of freedom ($df$), $p$-value and odds ratio ($e^{\beta}$). Results of the likelihood ratio, Wald and Hosmer and Lemeshow model evaluations and the McFadden pseudo-$R^2$ ($R^2_{McF}$) displayed.

| Predictor | Coefficient | $SE$ | Wald's $\chi^2$ | $df$ | p | $e^{\beta}$ |
|---|---|---|---|---|---|---|
| Constant ($\alpha$) | -11.1050 | 0.8394 | 175.0056 | 1 | $< 0.0001$ | N/A |
| Homathko River ($Q$) | 0.0880 | 0.0093 | 89.6649 | 1 | $< 0.0001$ | 1.0920 |
| Low Tide ($L$) | 0.3582 | 0.0696 | 26.4898 | 1 | $< 0.0001$ | 1.4308 |
| High Tide ($hL$) | -0.5224 | 0.1720 | 9.2214 | 1 | 0.0024 | 0.5931 |
| High-low Tide ($hL$) | -0.2279 | 0.1159 | 3.8687 | 1 | 0.0492 | 0.7792 |
| Low-high Tide ($lH$) | -0.2538 | 0.1295 | 3.8430 | 1 | 0.0499 | 0.7759 |
| Test | | | $\chi^2$ | $df$ | p | |
| Likelihood Ratio | | | 360.1719 | 5 | $< 0.0001$ | |
| Wald | | | 155.0093 | 5 | $< 0.0001$ | |
| Hosmer & Lemeshow | | | 7.0204 | 8 | 0.5344 | |

$R^2_{McF} = 0.2945$

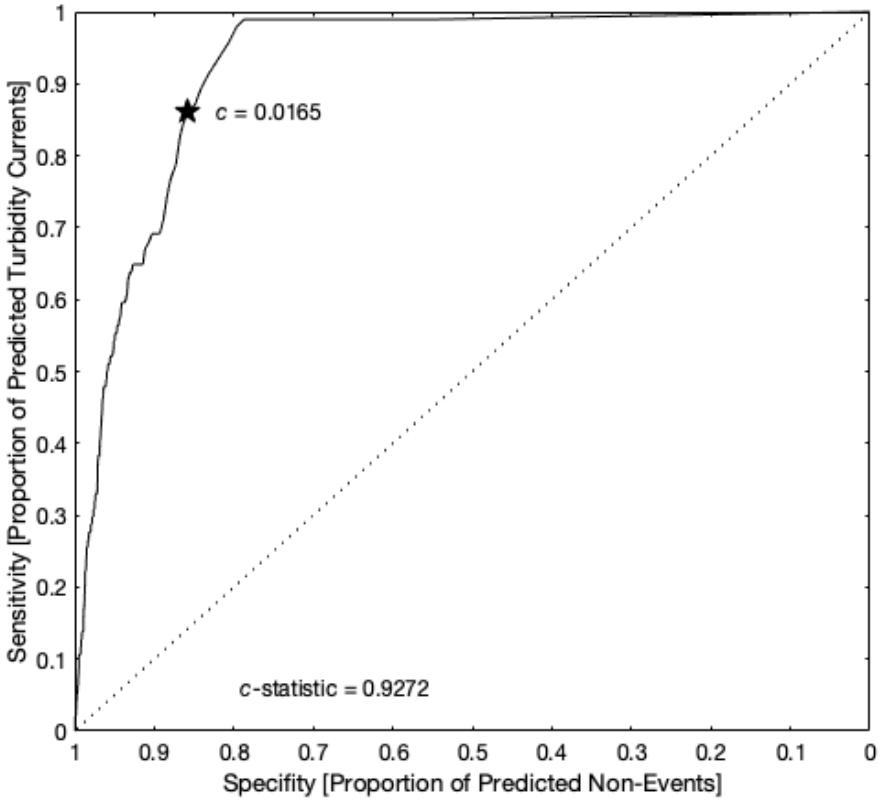


**Figure 3.5:** Receiver Operating Characteristic (ROC) plot for the sensitivity and specificity for the logistic model built using turbidity current timing in Bute Inlet during 2018. Area under line is equivalent to the c-statistic. Position of cut point ($c$) shown. Dotted diagonal line denotes plane of random chance.

**Table 3.3:** Predictive power of the logistic model showing overall accuracy of turbidity current prediction of using cut point $c = 0.0165$ for training dataset (Bute Inlet 2018) and other test datasets. Sensitivity is the probability of predicting an observation as 'positive' given that a turbidity current was detected, and specificity is the probability of the model predicting a 'negative' given the actual outcome was no turbidity current detection. Overall accuracy calculated as the mean of sensitivity and specificity. TCs refer to turbidity currents.

| Dataset | TCs [n] | Predicted TCs [n where $c > 0.0165$] | Sensitivity [%] | Specificity [%] | Overall Model [%] |
|---|---|---|---|---|---|
| Bute Inlet 2018 | 94 | 81 | 86.2 | 85.8 | 86.0 |
| Bute Inlet 2016 | 18 | 17 | 94.4 | 85.4 | 89.9 |
| Squamish Delta 2011 | 22 | 19 | 86.4 | 83.3 | 92.1 |
| Fraser Delta 2008 | 3 | 3 | 100.0 | 84.2 | 92.1 |

'positive' events (i.e. the predicted probability for these turbidity currents was greater than $c$), with an overall model accuracy – for predicting events and non-events – of 86% (Fig. 3.2d; Table 3.3) for a year of Homathko River discharge and water level measurement inputs during 2018.

### 3.4.3 Model Validation: 2016 Bute Inlet Monitoring

The logistic model, which was based on the observed turbidity currents that were recorded in 2018, was then used to predict the probability of turbidity current occurrence in Bute Inlet throughout 2016. Using the predetermined regression coefficients from Equation 3.4, measurements of Homathko River discharge and water level for 2016 were used to calculate turbidity current probabilities, which could then be compared to the timing of ADCP monitored turbidity currents recorded during the 2016 instrument deployment campaign in Bute Inlet. Using the same predetermined cut-point ($c = 0.0165$), 17 of the 18 turbidity currents recorded during the 2016 instrument deployment were correctly predicted as positive. Overall the logistic model was able to successfully predict whether a turbidity current would occur, or not, with 90% accuracy throughout 2016 despite being trained on a separate dataset (Fig 3.3d; Table 3.3).

### 3.4.4 Predictive Power of Univariate vs. Multivariate Analysis

The predictions from the logistic model were then compared to predictions from more simple univariate models made using either the Homathko River discharge or water level measurements in isolation to determine whether the multivariate approach is significantly more powerful. For this, the logistic model (Equation 3.4), Homathko River discharge and water level were each used to predict the timing of 95 turbidity currents during 2018 (see Section 3.3.7). The distribution of Homathko River discharge and

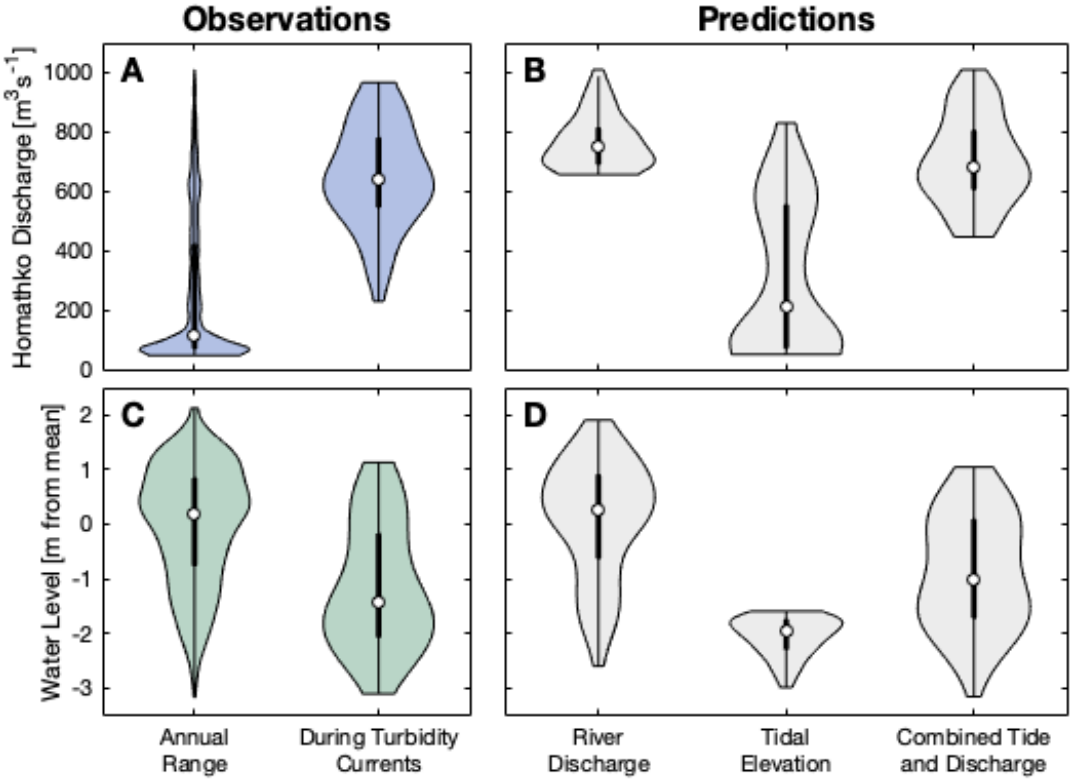


**Figure 3.6:** Violin plots to compare the distribution of background forcing mechanisms with conditions during recorded turbidity currents, and different methods of prediction the occurrence of turbidity current activity at Bute Inlet during 2018. White filled circle shows median value for each data set and the thick central line represents the interquartile range. (A) The distribution of river discharge observations during 2018 with conditions during turbidity currents and (B) the distribution of conditions after predicting the timing of turbidity currents. (C) The distribution of water level observations during 2018 with conditions during turbidity currents and (D) the distribution of conditions after predicting the timing of turbidity currents. Predictions are made by taking 95 random points in above the $90^{th}$ percentile in river discharge, tidal drawdown and the predictive model. The corresponding distribution plots (B and D) for each of the prediction methods represents the river discharge and water level measurements for the same 95 predicted turbidity currents. Statistical difference between violins are quantified in Table 3.4.

water level for each of these three predictions were then compared the actual distribution of triggering variables for the 95 turbidity currents recorded during 2018 as well as the annual range of discharge and tide conditions for 2018 (Fig. 3.6). In isolation, river discharge and tidal water level are found to be poor predictors of turbidity current activity (Fig. 3.6). For example, when using Homathko River discharge alone to predict turbidity currents, a univariate model cannot predict the increased likelihood of a flow occurring at low tide; and hence misses a key mechanistic driver for flow triggering. In this case, the distribution of water level for turbidity currents predicted using Homathko River discharge alone showed no statistical difference ($p > 0.05$) to the annual distribution of water level measurements (Fig. 3.6; Table 3). Similarly, when water level alone was used to predict turbidity current timing, the model omitted the enhanced frequency of flows during short windows of elevated river discharge, and

**Table 3.4:** Statistical tests to compare the difference between Homathko River discharge and water level for all of 2018 and then during turbidity currents with Homathko River discharge and water level measurements for 95 predicted turbidity currents using the logistic model (Equation 3.4) and Homathko River discharge and water level in isolation (see Section 3.3.7), as shown visible in the violin plots in Fig. 3.6. MWW refers to the Mann-Whitney-Wilcoxon test, KS to the Kolmogorov-Smirnov test and DBM/OVS denotes the difference between the distribution of median values as a percentage of the overall visual spread (see Section 3.3.7).

| Difference between Annual Range in Variables with | MWW | KS | DBM/OVS |
|---|---|---|---|
| (1) Homathko River Discharge | | | |
| Recorded Events | $< 0.01$ | $< 0.01$ | 74.1 |
| Homathko River Discharge Predicted | $< 0.01$ | $< 0.01$ | 83.4 |
| Water Level Predicted | 0.45 | 0.37 | 11.7 |
| Logistic Model Predicted | $< 0.01$ | $< 0.01$ | 77.9 |
| (2) Water Level | | | |
| Recorded Events | $< 0.01$ | $< 0.01$ | 55.0 |
| Homathko River Discharge Predicted | 0.45 | 0.45 | 7.4 |
| Water Level Predicted | $< 0.01$ | $< 0.01$ | 69.8 |
| Logistic Model Predicted | $< 0.01$ | $< 0.01$ | 49.5 |
| Difference between Variables during Turbidity Currents with | MWW | KS | DBM/OVS |
| (1) Homathko River Discharge | | | |
| Homathko River Discharge Predicted | $< 0.01$ | $< 0.01$ | 39.0 |
| Water Level Predicted | $< 0.01$ | $< 0.01$ | 67.2 |
| Logistic Model Predicted | 0.30 | 0.40 | 13.7 |
| (2) Water Level | | | |
| Homathko River Discharge Predicted | $< 0.01$ | $< 0.01$ | 39.0 |
| Water Level Predicted | $< 0.01$ | $< 0.01$ | 67.2 |
| Logistic Model Predicted | 0.33 | 0.27 | 13.7 |

yielded no statistical different to the annual range of river discharge ($p > 0.05$; Fig. 3.6; Table 3.4). However, the Homathko River discharge and water level during the 95 predicted turbidity currents using the logistic model showed no statistical difference ($p < 0.05$) to the actual Homathko River discharge and water level measurements during the ADCP recorded turbidity currents (Fig. 3.6; Table 3.4). Therefore, the logistic model, which incorporates both river discharge and tidal elevation, has a far stronger predictive power than univariate predictions that consider those variables in isolation.

## 3.5 Discussion

### 3.5.1 What explains the mismatches between reality and prediction?

Statistically, the logistic model shows strong predictive power for turbidity current occurrence; however, the predicted:observed performance is not fully perfect. For example, a number of turbidity currents detected (one in 2016 and 13 in 2018) during the

field deployments were not predicted as positive events by the multivariate model (i.e. predicted probability $> c$). We therefore now discuss why the model may not always correctly predict a turbidity current. We suggest that at least two potential mechanisms could lead to timing of a monitored turbidity current not being predicted as positive by the logistic model. First, a lag period may occur between elevated river discharge and delta-lip failure, such that an event may occur following a peak, when discharge levels are relatively low. Sediment can rapidly accumulate to prograde the delta-lip, or oversteepen the prodelta slope, during a short-lived period of elevated discharge, but not necessarily lead to immediate collapse. Instead these geometric effects or the generation of excess pore pressures in the subsurface may precondition the delta-lip to failure, with collapse occurring several hours to days later (Carter et al., 2012; Clare et al., 2016). During this lag phase river discharge can drop off, resulting in reduced predicted probabilities of turbidity current occurrence. Second, there may be a disconnect between river discharge and sediment input to the submarine channel head. Homathko River discharge is used as a proxy for sediment delivery to the delta-lip. When river discharge is elevated, the logistic model predicts increased likelihood of turbidity current activity (Equation 3.4; Figs. 3.2; 3.3). However, bedload and/or suspended sediment flux is not linear with discharge (Hickin, 1989). Additionally, the mouth bar located at the top of the delta can store volumes of sediment which accumulates outside the freshet (Wright, 1977). Thus, the greater sediment availability at the onset of the freshet will increase the likelihood of a turbidity current (i.e. Bailey et al., 2021) and may also contribute the long runout ($> 40$ km) turbidity currents recorded on the rising limb of the freshet hydrograph in both 2016 and 2018 (Figs. 3.2b; 3.3b). As such, the use of Homathko River discharge in the predictive model will result in underestimates in turbidity current probabilities during the onset of the freshet. Similar predicted probability inaccuracies may also occur in late Autumn. Here, storm related river flooding can discharge 10% of the annual suspended sediment load in a single day (Hickin, 1989, as observed in November 2016; Fig. 3.3b). However, instruments were not deployed during this period so such a link cannot be tested with the available data.

The model also predicted turbidity currents during some periods in which no turbidity current was recorded. The logistic model predicts a likelihood value for a turbidity current with at least 2.8 km runout (i.e. runout to the most proximal mooring in 2018). However, there is no observable correlation between minimum turbidity current runout and predicted probability or any triggering variable (Fig. 3.4). Furthermore, observations of turbidity currents increase exponentially with proximity to the Homathko Delta (Figs. 3.2a; 3.3a). For example, up to seven individual turbidity currents were recorded during a single low tide period at the Squamish Delta-lip (Hughes Clarke, 2016). It is therefore plausible that turbidity currents did occur in the most proximal part of the channel (or on the prodelta itself) when predicted by the model, but did not runout sufficiently for detection by our ADCP moorings. Additionally, despite high

predicted probabilities, not every low tide during the deployment phase resulted in turbidity current generation (Figs. 3.2c,d; 3.3c,d). It has been proposed that low tide sediment release from a turbidity maximum may also require the presence of sufficient erodible, unconsolidated sediment layer on the seafloor to generate a turbidity current. This layer may be removed following a turbidity current, inhibiting flow initiation at the following low tide (Hage et al., 2019). Our predictive model does not account for previous turbidity current occurrence and assesses flow likelihood independently based on triggering variables. As such, in our current model predicted probability will remain elevated, even in the hours following a detected turbidity current.

### 3.5.2 Testing the Predictive Model at other Deltas: Squamish and Fraser Deltas

In the absence of major external triggers (e.g. earthquakes or large storms), we are able to build a logistic model using variables linked to system preconditioning and flow initiation (river discharge and tidal state) to successfully predict $> 86\%$ (Table 3.3) of turbidity current activity at Bute Inlet. Our model may also have strong predictive power in other settings where mechanisms of turbidity current generation are similar. We therefore now test the efficiency of our statistical model at two other river-fed systems where direct measurements of turbidity currents have been made by previous studies: the Squamish River in Howe Sound and the Fraser River prodelta, both in British Columbia (Fig. 3.1 insert; Ayranci et al., 2012; Hughes Clarke et al., 2012, 2014; Hughes Clarke, 2016; Clare et al., 2016; Lintern et al., 2016; Hizzett et al., 2018; Hage et al., 2019; Vendettuoli et al., 2019).

Previous univariate statistical analysis demonstrated that Squamish River discharge and water level had a significant control on turbidity current timing and rate; however, not all peaks in river discharge or low tide resulted in a turbidity current (Clare et al., 2016). We test the application of our logistic model (Equation 3.4) at Howe Sound by using Squamish River discharge and water level measurements recorded during 2011 (prepared as outlined in Section 3.3.8) to predict turbidity current likelihood and compare to actual timing of the 22 ADCP measured turbidity currents. Using the same predetermined cut-point calculated from the 2018 Bute Inlet dataset ($c$ = 0.0165), the model correctly predicted 19 of the 22 turbidity currents as positive, with an overall model accuracy of 85% (assuming no turbidity currents occurred outside instrument deployment; Fig. 3.7; Table 3.3). Similarly, Fraser River discharge and water level measurements (again prepared as outlined in Section 3.3.8) for 2008 were compared to the timing of three monitored turbidity currents during the same year. On this occasion all three turbidity currents were successfully hindcast as 'positive' (Table 3.3). The logistic model shows good predictive power in, and can be applied to, systems where sediment supply is seasonal and turbidity currents are principally triggered at low tide.

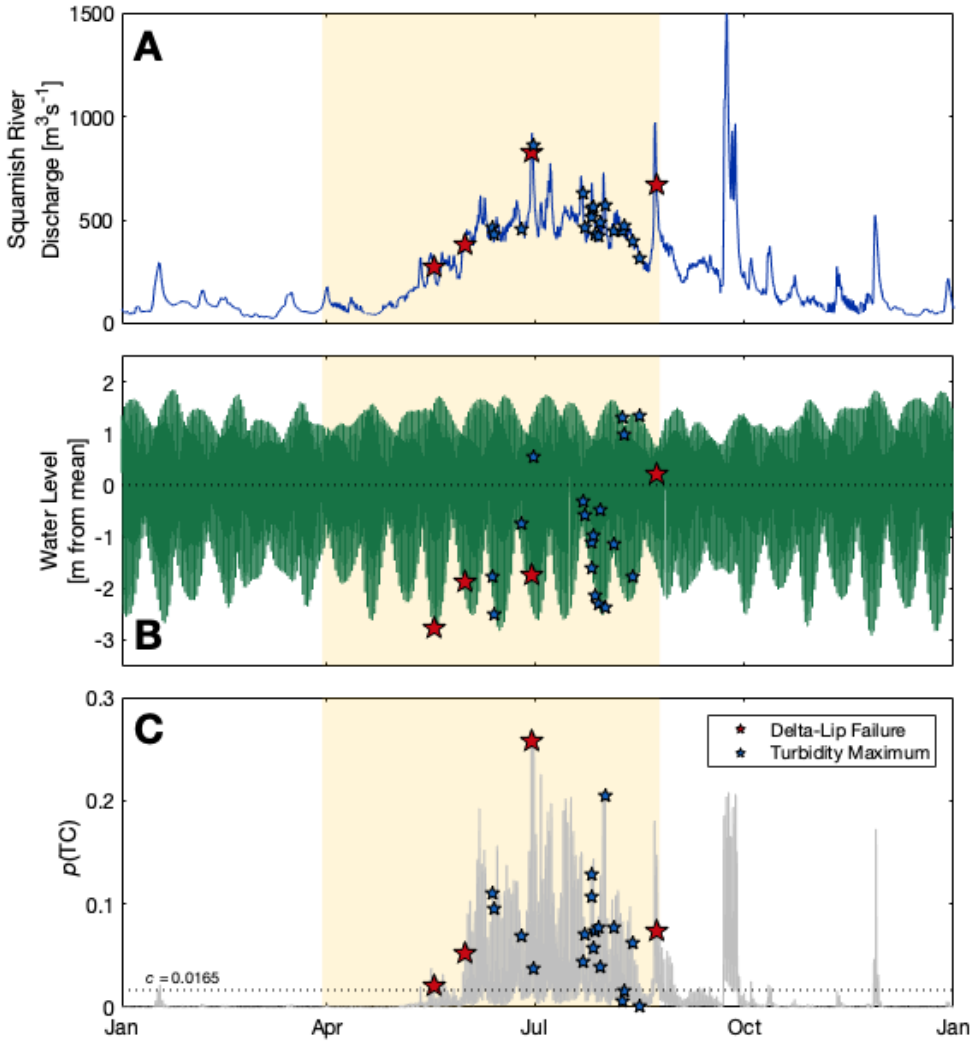


**Figure 3.7:** Time series of recorded and calculated measurements at the Squamish Delta during 2011 (Hughes Clarke et al., 2012; Clare et al., 2016). (A) Squamish River discharge. (B) Deviations of water level from annual mean. (C) Estimates for predicted probability of turbidity current occurrence from Equation 3.4 using measurements of Squamish River discharge and water level recorded during 2011. Stars in A-C denote the timing of ADCP measured turbidity currents, size and colour show mechanism of initiation, with instrument deployment period shown by highlighted zone.

Furthermore, the ability to correctly hindcast turbidity current activity at the Fraser Delta demonstrates the model is not necessarily limited to small bedload-dominant river systems.

### 3.5.3 Wider Application: Is it Feasible to Predict Turbidity Current Activity at other River Deltas Worldwide?

While river-discharge and tidally-dominated deltas only account for 21% of delta systems worldwide, a global analysis of river deltas has shown that these systems dominate the flux of sediment to the ocean (Nienhuis et al., 2020). River- and tide-controlled

deltas – which include some of the largest fluvial systems on Earth such as the Amazon, Congo, Ganges-Brahmaputra and Yellow Rivers – account for 87% of the global sediment flux from river deltas to the ocean (Nienhuis et al., 2020). Direct monitoring of turbidity currents at the Congo Canyon, offshore Angola – fed by the Congo River; the second largest (40,000-60,000 $m^3s^{-1}$) discharge river on Earth (Milliman & Meade, 1983) – has recorded flows most commonly during elevated periods of the Congo River flood hydrograph with a recurrence period correlating with spring tide intervals (Heezen et al., 1964; Khripounoff et al., 2003; Vangriesheim et al., 2009; Azpiroz-Zabala et al., 2017; Talling et al., 2021). As we have shown how combinations of river- and tidal-elevation can explain the generation of turbidity currents, we suggest it is plausible that our logistic model, may be more widely applicable in other systems; potentially including some of the largest systems on the planet.

A number of challenges still exist to scale our logistic model to larger river-fed systems. For example, while previous direct monitoring in the Congo Canyon has identified a link to elevated river discharge and tides, the most proximal mooring was positioned at least 300 km from the head of the canyon. As such, precise flow timing, and therefore position in the tidal cycle, are poorly constrained meaning our logistic model cannot be tested. Furthermore, our logistic model was built using Bute Inlet, a location sheltered from oceanographic processes that affect continental margins that border open oceans. Submarine canyons directly fed by large river systems have the further complication of additional sediment supply through littoral cells or oceanographic turbidity current triggers (e.g. waves, internal currents or dense-water cascading; Puig et al., 2013b). To understand the role of these additional forcing mechanisms, as well as exact position within the tidal cycle during turbidity currents there is a compelling need to monitor the timing of turbidity currents proximal to source (i.e. within kms of the canyon head) in more river-fed submarine canyons.

## 3.6 Conclusions

Two source-to-sink field campaigns in Bute Inlet during the freshest of 2016 and 2018 recorded the most extensive number (N = 113) of directly monitored turbidity currents in a submarine channel. Here, we analyse the role of river discharge and tides on the generation of turbidity currents. In isolation both elevation of Homathko River discharge (the primary freshwater input to Bute Inlet) and low tides showed statistical significance as turbidity current triggering mechanisms when compared to background conditions. The relative importance of each of these triggering variables was statistically calculated using logistic regression on the timing of turbidity currents during 2018. Here, turbidity current occurrence was at least 1.8 times more likely at low tide than any other position in the cycle for a given tidal range; and for every percentile increase in Homathko River discharge, the likelihood of a turbidity current increased

by 9%. Additionally, this logistic regression model was able to calculate turbidity current probability for any given input of Homathko River discharge and water level; successfully predicting 86% of turbidity current activity during 2018. We validated our model by predicting turbidity current activity for the 2016 monitoring dataset in Bute Inlet, and at other similar sites of direct monitoring (Squamish and Fraser Rivers). Here, $>$ 84% successful hindcasts of turbidity current activity showed good predictive power for systems where sediment supply is seasonal and turbidity currents are principally triggered at low tide. We suggest that our model can be further extended to river deltas where sediment flux is either river- or tidally controlled, accounting for 87% of the global sediment flux from river deltas to the ocean, though there remains a compelling need for more direct measurements to test our predictive model at larger directly river-fed submarine canyons.

# Chapter 4

# Spatiotemporal Unsteadiness of Bottom Currents Revealed from Direct Monitoring across a Mixed Depositional System

**This chapter is an altered version of text planned for submission to**
***Nature Communications***

Lewis P. Bailey, Michael A. Clare, James E. Hunt, Elda Miramontes, Ian Kane, Ivan D. Haigh, Marco Fonnesu, Ricardo Argiolas, Giuseppe Malgesini and Regis Wallerand

LB and MC conceptualised the research question. ENI and Total provided the data for the study, including pre-processed bathymetry data. LB processed ADCP and current metre measurements, led on data analysis and visualisation (with assistance from MC and JH) and writing the original manuscript. MC, IK and EM then provided scientific input to improve the original manuscript. All co-authors provided feedback and edited the original manuscript.

Seafloor currents, driven down-slope by gravity or along-slope by thermohaline circulation, dictate the pathways, burial efficiency and the ultimate fate of particles in the deep-sea, including organic carbon and pollutants. These currents form the largest sediment accumulations on the planet and transfer orders of magnitude more sediment across the ocean than rivers on land. Recent studies suggest that 'mixed' deep-sea sedimentary systems may be the norm, wherein along- and down-slope transport processes interact and rarely act in isolation. However, our understanding of such interactions, and hence robust reconstruction of past oceanographic regimes, palaeo-climates and modern transport pathways, is hindered by a paucity of direct near-seafloor measurements. Here, using the most extensive and sustained monitoring of a deep-sea mixed

system to date, we show how seafloor currents vary in intensity and direction across tidal to seasonal timescales and how regional bottom currents can be strongly steered by subtle seafloor topography. We posit that the high spatiotemporal variability observed in the near-bed regime of bottom currents may have been significantly underestimated, underlining a need for detailed monitoring in more mixed systems worldwide.

## 4.1 Introduction

Deep-marine sediments are the ultimate sinks for organic carbon and pollutants, and form important archives of past climate and natural hazards (Llave et al., 2006; Legge et al., 2020; van der Voort et al., 2021). The mechanisms that dominate the transport and deposition of sediment in deep water, particularly on the continental slope, include: (1) episodic, down-slope gravity-driven sediment flows (e.g. turbidity currents); and (2) semi-permanent along-slope, thermohaline-driven contour currents. Episodic turbidity currents sculpt submarine canyons that can rival or exceed the scale of rivers on land (Shepard, 1972; Harris & Whiteway, 2011), while deposits at their deep-sea termini (submarine fans) form the largest sediment accumulations on Earth (Talling et al., 2013). Persistent reworking and deposition by contour currents over millions of years can form extensive (100s km long) and thick (up to kms) accumulations known as contourite drifts (Faugères & Stow, 2008; Rebesco et al., 2014). It is increasingly being recognised that these processes rarely operate in isolation, and that mixed depositional systems may be the norm; wherein down- and along-slope systems interact. These interactions are most pronounced where along-slope contour currents orthogonally intersect down-slope oriented submarine canyons or channels, either directly deflecting sediment suspended by gravity flows, or shaping the morphology of their deposits during periods when gravity flows are not operational (e.g. Mulder et al., 2008; Hernández-Molina et al., 2017; Sansom, 2018; Miramontes et al., 2019; Fonnesu et al., 2020; Fuhrmann et al., 2020, 2021; Pandolpho et al., 2021; Rodrigues et al., 2021). These dynamic interactions can modify sediment transport regimes, controlling the distribution and fate of sediments, organic carbon, nutrients, and anthropogenic particles such as microplastics (Viana et al., 2007; Maier et al., 2019b; Kane et al., 2020).

To date, it has largely been necessary to make inferences about these flow interactions based on the depositional legacy they left behind, such as the resultant channel-drift geometries and internal stratigraphic architectures, which often serve as the basis for palaeoceanographic reconstructions (Voigt et al., 2013; Rodrigues et al., 2021). However, such reconstructions can be equivocal, with competing models arising from apparently similar channel geometries and stratigraphic architecture (e.g. Rebesco et al., 2014; Sansom, 2018; Fonnesu et al., 2020; Fuhrmann et al., 2020; Miramontes et al., 2020). Uncertainty in the nature of these interactions and palaeoflow reconstructions,

primarily stems from a paucity of direct monitoring of the near-bed current regime in mixed depositional systems (McCave et al., 2017). Recent advances in deep-sea monitoring, particularly the use of acoustic Doppler current profilers (ADCPs), have catalysed a step-change in our understanding of turbidity currents; however, detailed current measurements have been only made in less than ten of the >9000 submarine canyons worldwide (e.g. Khripounoff et al., 2003; Xu et al., 2010; Harris & Whiteway, 2011; Azpiroz-Zabala et al., 2017; Sequeiros et al., 2019; Heerema et al., 2020). Perhaps more remarkable is that fewer still equivalent measurements exist of the near-bed regime of contour currents (Zhao et al., 2015), despite their globally important role in deep-sea sediment, nutrient and pollutant transfer (Rebesco et al., 2014; Kane et al., 2020). The limited extent of monitoring relates to logistical challenges posed by their deep water setting and the vast spatial extents of such depositional systems.

Recent measurements of contour currents over a ~6400 $km^2$ area offshore Argentina and Uruguay revealed significant spatial variability in bottom current direction and velocity, likely due to steering by seafloor relief velocity (Steinmann et al., 2020; Wilckens et al., 2021). However, these current measurements were opportunistically recorded by an ADCP mounted on a vessel in transit, and hence recorded at each point location for only short (5 minute) time-averaged windows, and did not truly characterise the near-bed regime. The low frequency nature (38 kHz) of the ADCP meant that current measurements could not be made closer than 150 m above the seafloor. Longer duration (two years) monitoring, using a higher frequency (75 kHz) ADCP deployed on a deep-sea mooring in the South China Sea, measured currents within tens of metres of the seafloor recording significant seasonal variations in mesoscale eddy direction and intensity that create temporally-variable sediment re-suspension and transport (Zhang et al., 2014; Zhao et al., 2015). These novel observations were only recorded at a single location, however, and it is not possible to determine how the spatial footprint of near-bed currents varies. Furthermore, these previous monitoring efforts have focused on discrete processes (e.g. gravity flows or contour currents only), and do not address interactions in mixed systems. These interactions can fundamentally modify sediment transport pathways, as revealed by two recent studies, based on (1) scaled-down laboratory modelling that simulated gravity flow-contour current interaction (Miramontes et al., 2020), and (2) an integration of subsurface geophysical, seafloor and near-bed (3 m above seafloor) monitoring of contour currents outside of canyons offshore East Africa (Fuhrmann et al., 2020). While the latter example provided field observations of the near-bed direction of contour currents, no measurements were reported in the submarine canyons; hence, the specific process interactions were necessarily inferred.

In order to fill key gaps in our understanding of deep-sea particulate transport, to calibrate numerical models, and enable robust palaeoceanographic and climatic reconstructions, there is a compelling need to acquire field-scale current measurements as close to the seafloor as possible in mixed turbidite-contourite systems to determine

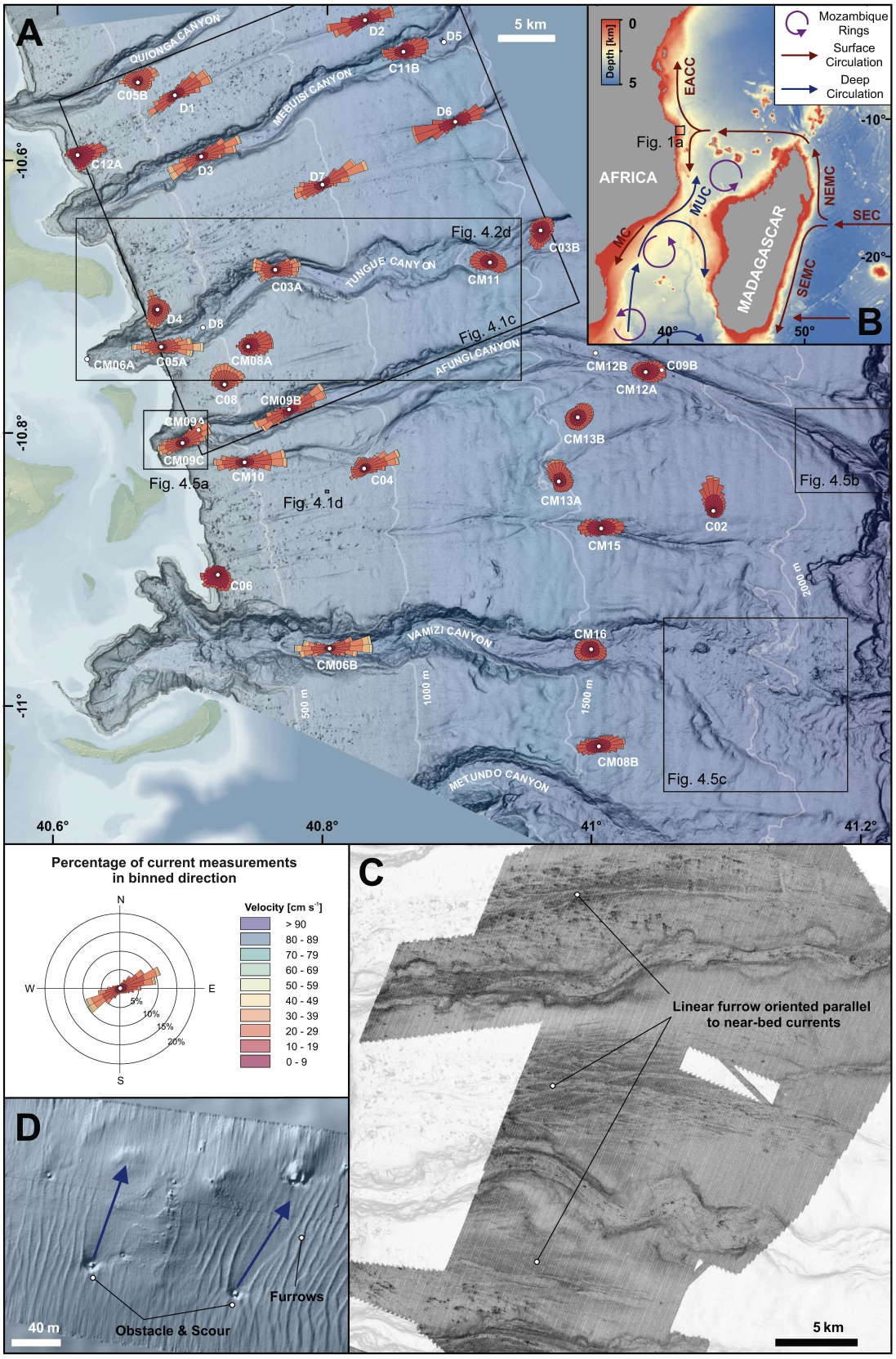


**Figure 4.1:** A) An overview of near-bed currents offshore North Mozambique, East Africa. Rose diagrams show the number of measurements in a 12° bin interval as a percentage of total

*(continued)*

**Figure 4.1:** *(cont.)* measurements from the closest to seafloor measurement from each mooring (Table 4.1). Each direction arm of the rose plot is then subdivided to show the percentage of recorded velocities in intervals of 10ms-1 as shown in the legend. Locations of Figs. 4.1c,d, 4.2 and 4.4 shown. (B) Bathymetry (GEBCO) offshore East Africa showing location of study site and regional ocean circulation patterns based on van van Aken et al. (2004) and Schott et al. (2009). MC: Mozambique Current; MUC: Mozambique Undercurrent; SEC: South Equatorial Current; NEMC: Northeast Madagascar Current; SEMC: Southeast Madagascar Current; EACC: East African Coastal Current. (C) East-west trending linear furrows from multibeam backscatter (5 m bin size) oriented parallel to seafloor currents proximal to gullies. (D) Furrows and scours at the seafloor (0.6 m bin size remotely operated vehicle multibeam) indicate the dominance of north-flowing bottom currents.

how near-bed current velocity and direction varies: (1) across large spatial areas; (2) in response to variable seafloor relief; (3) over differing timescales (e.g. tidal to seasonal). Here we address these issues based on analysis of a remarkably spatially- and temporally-extensive monitoring array that recorded near-bed currents. We integrate near-bed (to within 3 m of seafloor) current measurements made at 35 mooring locations that recorded over a four-year monitoring period, with $>$2500 km$^2$ of high-resolution seafloor multibeam bathymetry that spans a mixed submarine canyon-contourite depositional system, on the Mozambique continental slope (Fig. 4.1). We aim to use these detailed, synchronous and spatially-distributed measurements to quantify the dynamic interactions across a large mixed depositional system for the first time, and address the following questions. First, how does bottom current velocity and direction vary temporally and spatially across a large mixed system? Second, to what extent does seafloor relief influence bottom currents and over what spatial scale? Specifically, how do orthogonally-oriented bottom currents interact with submarine canyons and gullies? Third, what are the implications of the diverse interactions we observe for particulate transport and deposition in mixed systems?

## 4.2 Data and Methods

Here, we integrate new high-resolution multibeam bathymetric data acquired over a mixed turbidite-contourite system offshore Mozambique, spanning an area of 65 x 50 km, with direct measurements of near-bed currents made at 35 deep-sea mooring locations. The unusually large number of moorings and extensive seafloor surveying enables the first quantitative characterisation of near-bed currents across the diverse geomorphology of a mixed deep-sea depositional system study area, including within and adjacent to submarine canyons, within linear gullies, and unconfined areas of open slope (Fig. 4.1).

### 4.2.1 Seafloor Bathymetry

Two separate multibeam surveys covering the study site were collected in 2013 and 2014 with a Hugin 1000 autonomous underwater vehicle (AUV) using a Kongsberg EM2040 sonar with 140° swath width. Data were gridded into 5 m x 5 m bins and have a vertical resolution of approximately 0.1 m. A more focused (190 m-wide) bathymetric survey was also performed using a Remotely Operated Vehicle, with data gridded to 0.6 m x 0.6 m bins, with a vertical resolution on the order of a few centimetres (Fig. 4.1d; FUGRO, 2017). Seafloor data including bathymetric elevation (Fig. 4.1a) and backscatter (i.e. the strength of the signal reflected from the seafloor, where dark colours represent more competent and/or coarser-grained substrate; Fig. 4.1c) were provided in processed form by ENI, hence no processing of raw data was performed in this study. The bathymetric raster surface was used to generate a greyscale slope attribute map in ESRI ArcGIS that was found to best illustrate the geomorphological features. These datasets were also analysed to determine the height of canyons and gullies. These heights were measured vertically from the deepest point of the canyon or gulley (i.e. thalweg) to an inflection point on the flanking slope where the bathymetry levels out.

### 4.2.2 Moored Instruments

Table 4.1 provides detail on positioning, deployment duration and instruments on each of the moored stations. Twelve moorings comprised paired single-point current meters that measured velocity and direction at 3 and 5 m above bed (mAB; labelled C in Fig. 4.1a). Two of these moorings (C05A and C05B) also held up-looking 300 kHz ADCPs positioned 10 mAB (accounting for blanking distance data were collected from 15 mAB). The remaining 23 moorings included 600 kHz down-looking ADCPs that recorded vertical profiles either at 0.5 m resolution to within 10.5 m of the seafloor (labelled CM in Fig. 4.1a) or at 1 m resolution to 11 mAB (labelled D in Fig. 1a). Data from two of the moorings (C02 and C08 located on open-slope areas; Fig. 4.1a) were previously reported in Fuhrmann et al. (2020). ADCPs record current velocity (i.e. speed and direction) and echo intensity at different elevations ('bins') within the water column. The latter is related to scattering of the acoustic pulses generated by the ADCP, which are enhanced by sediment suspensions, and records the strength of the returned signal. Higher echo intensities generally relate to higher suspended sediment concentrations, until a concentration threshold is reached as which point the signal will be attenuated (Simmons et al., 2020). ADPC data were provided in textfile format and analysed into Matlab as follows.

First, to determine the net sense of near-bed flow at each mooring, and assess how it varies spatially across the study area, velocity data were extracted from the bin closest to seafloor (Table 4.1) and presented as rose diagrams that quantify both the speed

**Table 4.1:** Specifications and location information for the moorings and instruments deployed offshore North Mozambique.

| Mooring | Location | Water Depth [m] | Instrument | Most Proximal Data [mAB] | Most Distal Data [mAB] | Resolution [mins] | Bin Size [m] | Start | End |
|---|---|---|---|---|---|---|---|---|---|
| C02 | Open Slope | 1768 | Aanderaa Seaguard Current Meter | 3; 5 | | 10 | | 11/03/13 | 25/10/14 |
| C03A | Tungue Canyon | 1014 | Aanderaa Seaguard Current Meter | 3; 5 | | 10 | | 11/03/13 | 20/04/14 |
| C03B | Tungue Canyon | 1710 | Aanderaa Seaguard Current Meter | 3; 5 | | 10 | | 25/04/14 | 25/10/14 |
| C02 | Open Slope | 1768 | Aanderaa Seaguard Current Meter | 3; 5 | | 10 | | 11/03/13 | 25/10/14 |
| C04 | Open Slope | 993 | Aanderaa Seaguard Current Meter | 3; 5 | | 10 | | 11/03/13 | 26/10/14 |
| C05A | Tungue Canyon | 605 | Aanderaa Seaguard Current Meter | 3; 5 | | 10 | | 12/03/13 | 04/12/13 |
| | | | Upward-looking RDI 300 kHz ADCP | 15 | 111 | 10 | 2 | | |
| C05B | Open Slope | 595 | Aanderaa Seaguard Current Meter | 3; 5 | | 10 | | 05/12/13 | 25/10/14 |
| | | | Upward-looking RDI 300 kHz ADCP | 15 | 113 | 10 | 2 | | |
| C06 | Open Slope | 199 | Aanderaa Seaguard Current Meter | 3; 5 | | 10 | | 09/03/13 | 26/10/14 |
| C08 | Open Slope | 520 | Aanderaa Seaguard Current Meter | 3; 5 | | 10 | | 10/03/13 | 26/10/14 |
| C09B | Afungi Canyon | 1822 | Aanderaa Seaguard Current Meter | 3; 5 | | 10 | | 27/04/14 | 25/10/14 |
| C11B | Mebuisi Canyon | 1506 | Aanderaa Seaguard Current Meter | 3; 5 | | 10 | | 26/04/14 | 25/10/14 |
| C12A | Open Slope | 197 | Aanderaa Seaguard Current Meter | 3; 5 | | 10 | | 09/03/13 | 02/12/13 |
| C12A | Open Slope | 197 | Aanderaa Seaguard Current Meter | 3; 5 | | 10 | | 05/12/13 | 25/10/14 |
| CM06A | Tungue Canyon | 116 | Downward-looking 600 kHz ADCP | 10.5 | 21.0 | 10 | 0.5 | 23/12/11 | 26/04/12 |
| CM06B | Vamizi Canyon | 1126 | Downward-looking 600 kHz ADCP | 10.5 | 20.0 | 10 | 0.5 | 05/10/12 | 31/03/15 |
| CM08A | Open Slope | 686 | Downward-looking 600 kHz ADCP | 10.5 | 23.0 | 10 | 0.5 | 24/12/11 | 05/05/12 |
| CM08B | Open Slope | 1531 | Downward-looking 600 kHz ADCP | 10.5 | 15.0 | 10 | 0.5 | 29/09/12 | 15/01/15 |
| CM09A | Afungi Canyon | 431 | Downward-looking 600 kHz ADCP | 10.5 | 21.5 | 10 | 0.5 | 24/12/11 | 05/02/13 |
| CM09B | Afungi Canyon | 948 | Downward-looking 600 kHz ADCP | 10.5 | 20.0 | 10 | 0.5 | 10/02/13 | 10/05/13 |
| CM09C | Afungi Canyon | 449 | Downward-looking 600 kHz ADCP | 10.5 | 18.0 | 10 | 0.5 | 07/09/13 | 01/07/14 |
| CM10 | Gully | 546 | Downward-looking 600 kHz ADCP | 10.5 | 16.5 | 10 | 0.5 | 27/09/12 | 31/03/15 |
| CM11 | Tungue Canyon | 1583 | Downward-looking 600 kHz ADCP | 10.5 | 15.0 | 10 | 0.5 | 25/12/11 | 02/04/15 |
| CM12A | Afungi Canyon | 1842 | Downward-looking 600 kHz ADCP | 10.5 | 17.0 | 10 | 0.5 | 25/12/11 | 02/04/12 |
| CM12B | Afungi Canyon | 1766 | Downward-looking 600 kHz ADCP | 10.5 | 13.5 | 10 | 0.5 | 04/10/12 | 29/03/15 |
| CM13A | Open Slope | 1503 | Downward-looking 600 kHz ADCP | 10.5 | 17.0 | 10 | 0.5 | 29/09/12 | 26/06/13 |
| CM13B | Open Slope | 1521 | Downward-looking 600 kHz ADCP | 10.5 | 16.0 | 10 | 0.5 | 16/11/13 | 01/04/15 |
| CM15 | Gully | 1572 | Downward-looking 600 kHz ADCP | 10.5 | 19.0 | 10 | 0.5 | 05/02/13 | 17/01/15 |
| CM16 | Vamizi Canyon | 1811 | Downward-looking 600 kHz ADCP | 10.5 | 17.5 | 10 | 0.5 | 04/02/13 | 31/03/15 |
| D1 | Gully | 717 | Downward-looking 600 kHz ADCP | 11 | 35 | 10 | 1 | 28/07/14 | 18/04/15 |
| D2 | Gully | 1213 | Downward-looking 600 kHz ADCP | 11 | 34 | 10 | 1 | 27/07/14 | 26/04/15 |
| D3 | Mebuisi Canyon | 923 | Downward-looking 600 kHz ADCP | 11 | 36 | 10 | 1 | 21/07/14 | 18/04/15 |
| D4 | Open Slope | 249 | Downward-looking 600 kHz ADCP | 11 | 38 | 10 | 1 | 20/07/14 | 20/04/15 |
| D5 | Mebuisi Canyon | 1606 | Downward-looking 600 kHz ADCP | 11 | 30 | 10 | 1 | 26/07/14 | 15/04/15 |
| D6 | Gully | 1522 | Downward-looking 600 kHz ADCP | 11 | 28 | 10 | 1 | 27/07/14 | 14/04/15 |
| D7 | Gully | 996 | Downward-looking 600 kHz ADCP | 11 | 35 | 10 | 1 | 20/07/14 | 17/04/15 |
| D8 | Tungue Canyon | 1606 | Downward-looking 600 kHz ADCP | 11 | 34 | 10 | 1 | 21/07/14 | 20/04/15 |

and direction of near-bed currents. These were current roses were overlain on the seafloor (i.e. bathymetric) data to cross-compare the sense of direction with any geomorphological features (Fig. 4.1a). Second, time series plots were created to illustrate the temporal variability in near-bed current speed and direction (Fig. 4.2a,b), and the acoustic backscatter, which provides a proxy measure of suspended sediment concentration (Fig. 4.2c,d). Third, in order to assess temporal variations in particle transport, cumulative vector plots were created that integrate the temporal changes in current speed and velocity (4.2e). These cumulative vector plots provide insight not just into the net-sense of near-bed flow, but also how that evolves over the monitoring period. Fourth, to determine the extent to which topography influences the current regime, net current speed and direction were extracted at different elevations above the seafloor within a gulley, within a canyon, and compared with that on an area of open slope, also presented as rose diagrams (Fig. 4.3). Finally, acoustic backscatter is compared with near-bed velocity to investigate the influence of temporal variations in current speed and direction on sediment suspension.

## 4.3 Geomorphological and Oceanographic Setting

The present-day Mozambique slope lies offshore from a narrow (10-20 km) mixed carbonate-siliciclastic shelf bounded on the seaward edge by a barrier island system and a steep (up to 70°) shelf break. A sequence of east-west trending submarine canyons occurs along the continental slope, cutting into the shelf break, and incising up to 200 m vertically. The morphology of individual canyons is variable, but all terminate at or prior to intersection with the Davie Fracture Zone ~70 km offshore (Fig. 4.1a; Franke et al., 2015). The Rovuma Delta (located north of the study area) was a major depositional environment through most of the Tertiary (Salman & Abdula, 1995), however the development of the East African Rift System during the Cenozoic strongly modified continental drainage patterns (Roberts et al., 2012; Stagna et al., 2021). A series of ephemeral rivers discharge on to the shelf, but these do not directly connect to canyon heads and modern sediment supply to canyon heads is low (Maselli et al., 2020).

Ocean currents offshore Mozambique are complex and can be highly energetic. Circulation is strongly influenced by the Northeast Madagascar Current (NEMC). The NEMC diverges to the northward flowing East African Coastal Current (EACC) and the southward-bound Mozambique Current (MU; Collins et al., 2016) which forms part of the Agulhas Current system, the strongest western boundary current in the southern hemisphere (Fig. 4.1b; Lutjeharms, 2006). The deeper-water regime (>800 m water depth) is dominated by the north-flowing Mozambique Undercurrent (MUC; de Ruijter et al., 2002). The entire water column can also be affected by the formation of mesoscale (>300 km diameter) southward-bound anticyclonic eddies (MCE), due to the interaction between NEMC with Madagascar (de Ruijter et al., 2002; Schouten et al.,

2003; Collins et al., 2014; Ullgren et al., 2016). These eddies can alter the bottom current regime (Miramontes et al., 2019), and may have the potential to resuspend sediment (Zhang et al., 2014).

## 4.4 Results and Discussion

### 4.4.1 Sub-annual Variability in Bottom Current Intensity and Direction

Direct near-bed measurements on the open-slope areas show a dominance of northward directed bottom currents, typically between 0.2-0.4 $ms^{-1}$ with a maximum of 0.6 $ms^{-1}$ along shallower ($\sim$500 m water depth) sections (Fig. 4.1b). These measurements are consistent with the formation of north to northeast trending obstacle-scour features (Fig. 4.1c) and asymmetric canyon and channel cross sectional morphologies previously reported by Fuhrmann et al. (2020). However, our long-duration measurements reveal that near-bed flow is not persistent, and its intensity and direction vary temporally, sometimes reversing over periods of days to weeks. Periods of northwards flow coincide with those where near-bed currents are the fastest, resulting in a net-northwards direction of flow across the continental slope. Periods of southward-directed flow occur with lower velocities of $<$0.3 $ms^{-1}$ in shallower water ($\sim$500 m) and 0.1 $ms^{-1}$ in deeper areas ($\sim$1800 m). Near-bed flow is generally antithetic between shallow and deep water, wherein periods of northward-directed flow in shallow water ($\sim$500 m) are generally southward-directed in deeper water ($\sim$1800 m), and vice versa; however, the timing of the multiple sub-annual current reversals are also not always synchronous along the slope (Figs. 4.2a,b). The net-northward transport of near-bed water masses along the entire slope is likely related to the MUC (Figs. 4.1b; 4.2e), and we interpret the temporal and spatial variability of this regional thermohaline current to the passing of eddies. The frequency of major reversals is consistent with MCE activity (Schouten et al., 2003), which has also been shown to decrease the intensity of the MUC in the Mozambique Channel (Miramontes et al., 2019). The transient switching of near-bed current direction could easily be missed by shorter-duration monitoring, potentially leading to misinterpretation of the net-direction of the regional current. Indeed, we observe further variations on even shorter timescales, wherein the direction and intensity of bottom currents fluctuates across tidal cycles (Fig. 4.2c,d). These observations underline the value of sustained near-bed current measurements at multiple locations, and demonstrates that it is not only the velocity of contour currents that can vary across sub-annual timescales, but also the direction of flow. Contour currents are clearly far from being steady, continuous flows, and can be extremely dynamic.

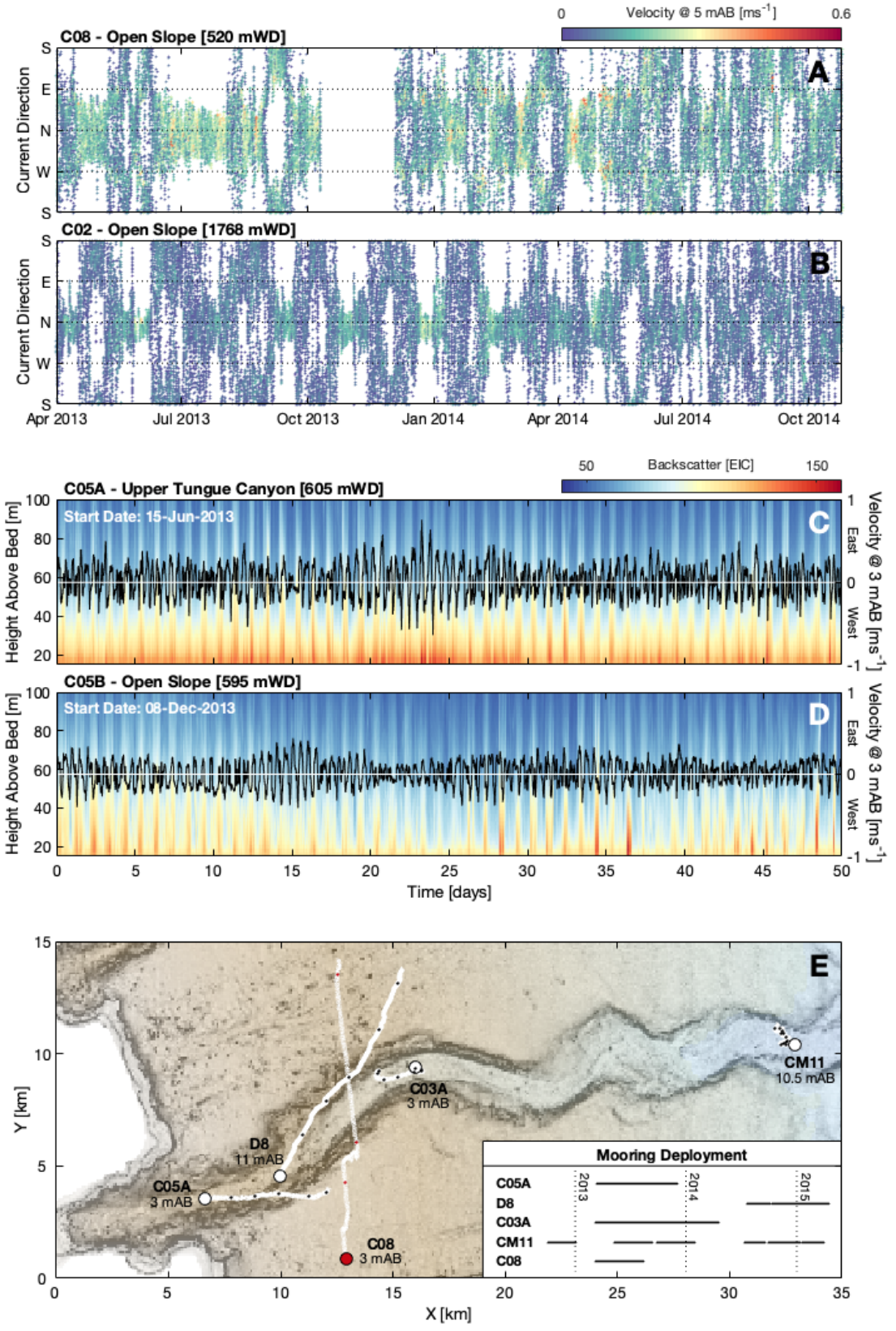


**Figure 4.2:** Time series plots to demonstrate the spatial and temporal variation in bottom current direction and velocity. Direction and velocity of near bed currents at 3 mAB at moorings (A) C08 and (B) C02 on the open slope. 50 days internal tide measurements at 3 mAB coupled

*(continued)*

**Figure 4.2:** *(cont.)* with ADCP acoustic backscatter from 15 to 100 mAB (C) within the upper sections of Tungue Canyon, C05A (D) and the open slope, C05B. NB. 50-day intervals do not correspond. (E) Cumulative vector plots compare the dominant trends of bottom currents within Tungue Canyon (C05A, D8, C03A and CM11) and the open slope (C08). Data is from closest bin to seafloor (Table 4.1). Black (Tungue Canyon) and red (open slope) points along the vector plot represent the passing of 50 days. Insert shows duration of instrument deployment; vector plots show data from all periods of monitoring.

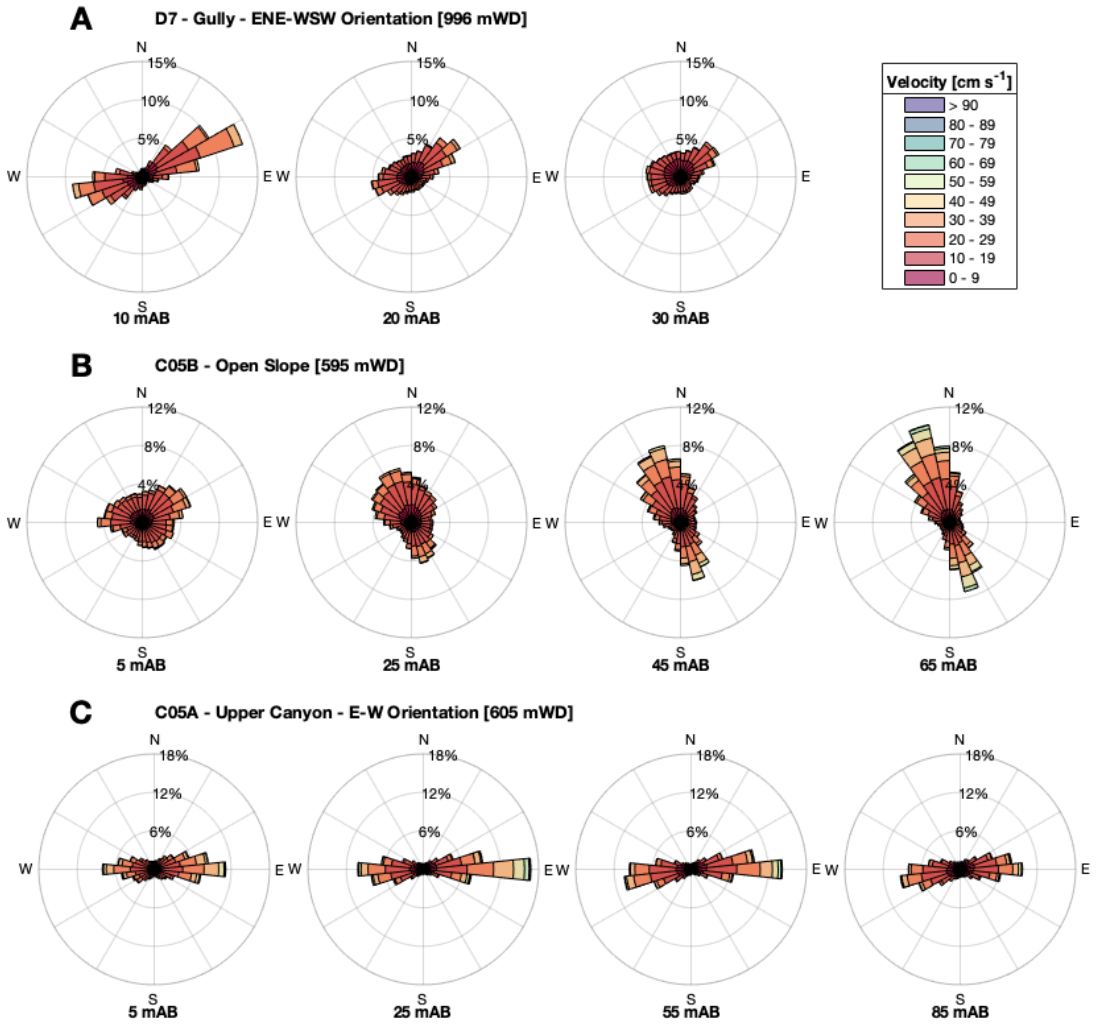


**Figure 4.3:** Rose diagrams to show variation in current velocity and direction with increasing height above the seafloor (A) in a gully, D7; (B) on the open slope ∼1 km south of Quionga Canyon, C05B, and; (C) within the upper reaches of Tungue Canyon, C05A. Measurements from C05A and C05B at 5 mAB are recorded by current meters, all other measurements acquired from ADCPs. Rose plots show the number of measurements in a 12° bin interval as a percentage of total measurements for a given height above the seafloor. Each direction arm of the rose plot is then subdivided to show the percentage of recorded velocities in intervals of 10 $ms^{-1}$.

### 4.4.2 Topographic Steering of Bottom Currents Across Multiple Scales

In contrast to open-slope areas, where near-bed currents cumulatively flow northwards in an unconfined manner, the highly variable seafloor morphology of the Mozambique

continental slope exerts a strong control on the local behaviour of bottom currents. These effects are particularly pronounced within large submarine canyons, where bottom currents are captured by the steep confining topography. Bottom currents are steered along canyon axes (approximately E-W; Figs. 4.1a; 4.2c), with their sense of direction being modulated on a tidal frequency, resulting in a semi-diurnal alternation of up- and down-canyon oriented flow. The influence of canyon morphology steering bottom currents can extend onto the adjacent open slope. For example, moorings C04 and C05B (both positioned on open slope ~1 km outside of a canyon; Fig. 4.1a) both record a dominant E-W current regime (Fig. 4.3b). This is in contrast to the other measurements on the open slope (e.g. C02, C08 and CM13A; Fig. 4.1a) where only a slight (i.e. NE-NW) deflection to the prevailing north-trending current is observed.

Near-bed current magnitude in submarine canyons shows a similar negative correlation with water depth as to that seen on the open-slope areas, despite the difference in the direction of flow. The most intense bottom currents occur within the upper reaches and heads of canyons (up to 0.84 $ms^{-1}$; Figs. 4.1; 4.2c). The net-direction of bottom currents can vary significantly within an individual canyon. For example, the shallowest two moorings within Tungue Canyon (C05A and D8; located at 605 and 746 m water depth) reveal a strongly net-down-canyon near-bed flow, whereas flow is net-up-canyon at more distal canyon reaches (C03A at 1014 and CM11 at 1583 m water depth; Fig. 4.2e). The net up-canyon displacement at the distal moorings is interpreted to relate to the focusing of internal tidal currents that creates a tidal bore directed up-canyon. We suggest that those vigorous internal tidal currents are strongly reflected back down-canyon when they hit the steep bathymetry in canyon heads, as has been observed in Monterey (Petruncio et al., 1998; Zhao et al., 2012; Hall et al., 2014; Maier et al., 2019b), Eel (Waterhouse et al., 2017) and Whittard Canyons (Hall et al., 2017). However, as with the regional bottom currents on the open-slope, it is particularly important that measurement timescales are long enough to calculate the net-direction of flow. For instance, measurements at C03A (1014 m water depth in Tungue Canyon) reveal short-lived (weeks) intervals where near-bed flow counter the net-westward-directed flow (Fig. 4.2e).

Perhaps more surprising, is the influence that much smaller topographic features can have on bottom currents. Moorings located within low relief (typically 20 m deep) gullies, appear to be similarly effective at steering bottom currents (e.g. D7; Figs. 4.1; 4.3a). The orientations of the gullies and measured near-bed currents match those of streaked seafloor accumulations of granular sediment (as interpreted from multibeam backscatter imaging, Fig. 4.1c), which indicates that these near-bed flows were capable of mobilising and (re)distributing sediments across the seafloor in a direction that is orthogonal to the regional thermohaline-driven current. The influence of topographic steering appears to relate to the scale of the relief. While bottom currents are focused and strongly

steered near-seafloor within a gulley axis, this influence becomes less pronounced further above the seafloor. A mooring (D7) within a NE-SW trending 20 m-deep gulley recorded axis-parallel currents at 10 mAB, but with the topographic influence barely recognisable at 30 mAB (Fig. 4.3a). The influence of the adjacent submarine canyon on mooring C04 and C05B is seemingly only restricted to the bottom few metres and is indiscernible by 25 mAB (Fig. 4.3b). The much greater topographic confinement provided by submarine canyons resulted in currents consistently aligning with the canyon thalweg at all elevations measured by the ADCP (i.e. from 5 m to 85 mAB; Fig. 4.3c). No measurements were made above the height of the canyon, hence it is not possible to determine at precisely what height above bed this influence is no longer felt, but based on the gulley observations, it is likely that the pronounced relief of these canyons fundamentally affects bottom current steering over at least the full height (i.e. $\sim$200 m) of these features.

### 4.4.3 Implications for Sediment Transport in Mixed Systems

Crescentic bedforms and knickpoints within Afungi Canyon and large scours in the distal reaches of Vamizi Canyon provide abundant evidence for down-canyon sediment transport by gravity flows (Figs. 4.1a; 4.4). However, no evidence of turbidity currents was provided from any of the ADCP measurements during the period of instrument deployment. This, coupled with the low present-day sediment supply (Maselli et al., 2020) indicates that these canyons are currently largely inactive with respect to gravity flows. Instead it is bottom currents that either flow parallel to the slope, or are steered by topography that dominate contemporary sediment transport. Enhanced acoustic backscatter in the water column recorded by ADCPs provides further strong evidence for the transport of suspended sediment during periods of heightened near-bed current activity (Figs. 4.2c,d; 4.5; Hill et al., 2003; Ha et al., 2011; Baeye & Fettweis, 2015; Simmons et al., 2020). Semidiurnal peaks in current velocity correlate with increases in ADCP acoustic backscatter, which is particularly notable at submarine canyon where bottom currents are most vigorous (Figs. 4.2c; 4.5), but is also observed to a lesser degree at open-slope locations (Fig. 4.2d).

A lack of constraint on the suspended sediment grain sizes means a precise inverse estimation of sediment concentration would be unreliable; however, given backscatter can be recorded down to the closest ADCP measurement point above seafloor (i.e. is not fully attenuated), we suggest that very high sediment concentrations (i.e. $\gg$1 g litre$^{1}$) are unlikely (Hill et al., 2003; Simmons et al., 2020). Bottom currents, particularly where internal tides are steered by topography, are considered to be the dominant mechanism for contemporary sediment transport, locally driving net-down-slope transfer, and are modulated on a tidal frequency (Fig. 4.2c,d). While modern sediment supplies are restricted, a stock of sediment that was deposited by past gravity currents, focused

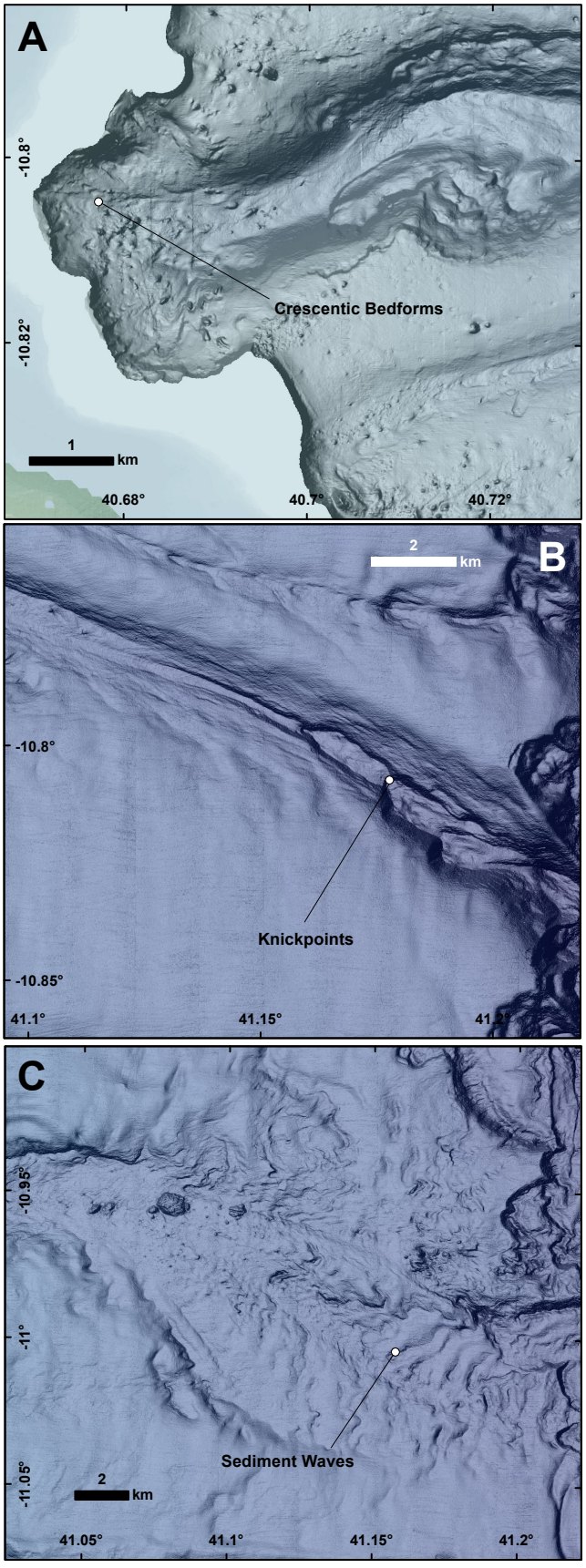


**Figure 4.4:** Morphological evidence of past turbidity current activity. (A) Crescentic bedforms and (B) knickpoints in Afungi Canyon, and (C) large scale scours and sediment wave trains in Vamizi Canyon. Locations of seafloor features shown in Fig. 4.1a.

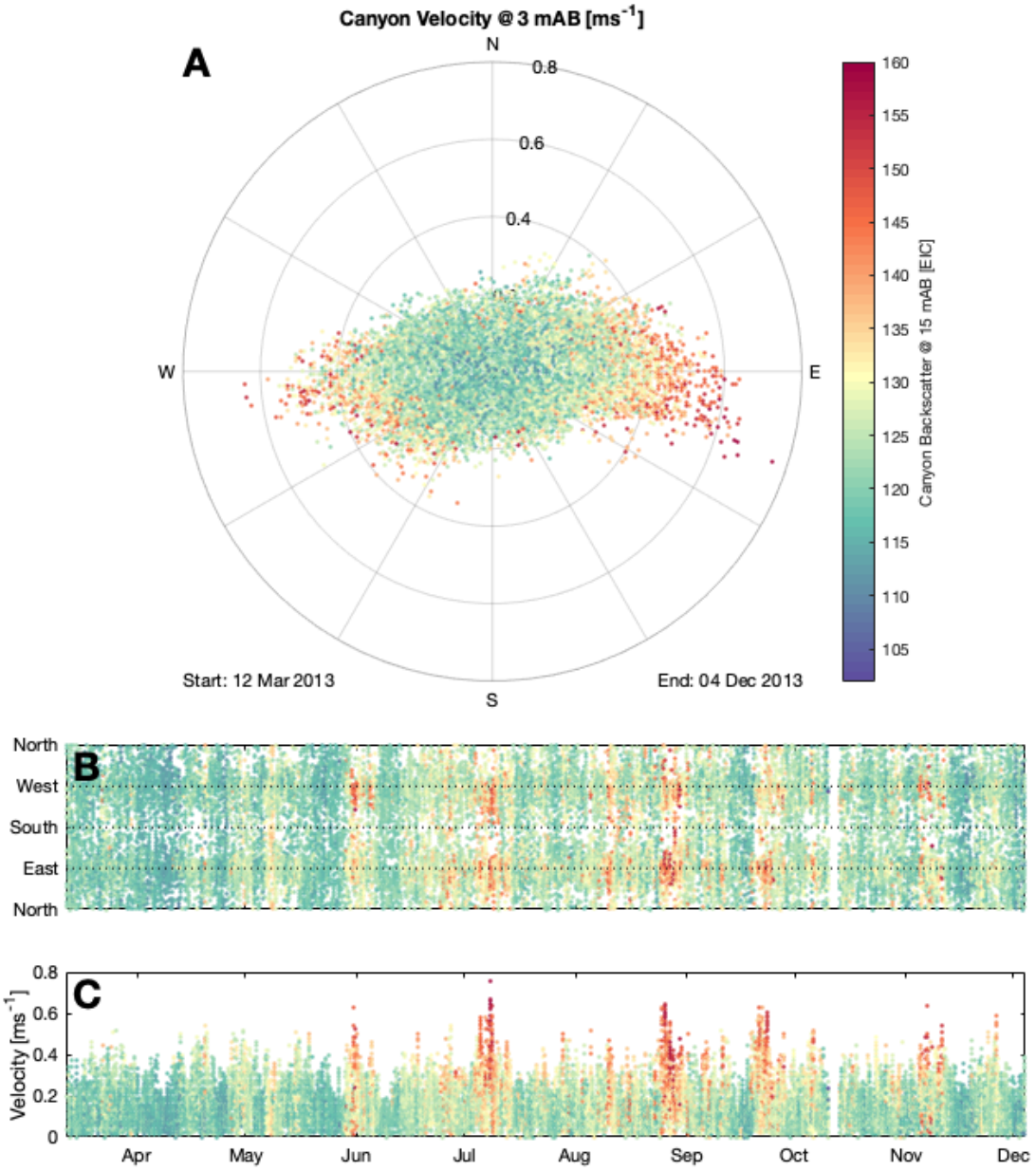


**Figure 4.5:** ADCP acoustic backscatter measurements recorded at C05A in upper Tungue Canyon. (A) Rose diagram showing the velocity and direction for each measurement from the current metre located 3 mAB. Scatter time series plots for (B) direction and (C) velocity at 3 mAB. All scatter points are coloured to the corresponding ADCP acoustic backscatter measurement recorded at 15 mAB.

within submarine canyon axes, is available for reworking and redistribution by bottom currents along canyons, linear gullies, and across the open-slope where near-bed flow intersects sufficient accumulations of mobile sediment (Fig. 4.1c; e.g. Principaud et al., 2018)

Models of mixed depositional systems have largely focused on the direct interplay between episodic gravity currents and contour currents. However, the relative infrequency of gravity currents, compared to the near-persistency of contour currents,

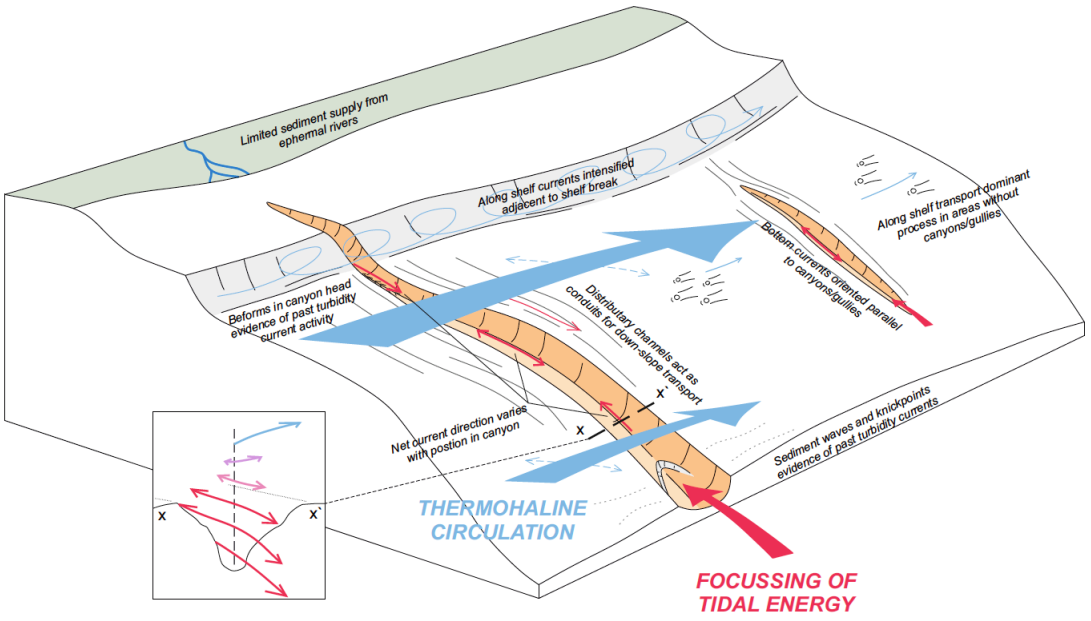


**Figure 4.6:** Conceptual diagram to show the complex near-bed current regime offshore North Mozambique. North-trending currents, following the Mozambique Undercurrent, are dominant on the open slope. However, strong topographic controls exist proximal to submarine canyons and other more local seafloor morphological features. Here focussing of internal tides generate strong currents capable of resuspending sediment providing a pathway for down-slope particle transport. Insert shows how such focussing of internal tides extends (both vertically and laterally) out of submarine canyons with tidal currents remaining aligned with canyon orientation.

means that direct interaction between these processes (e.g. Miramontes et al., 2020) may be relatively rare in most mixed systems (e.g. Fuhrmann et al., 2021). Instead, it is the interaction between contour currents and the gravity current-created topography and deposits that is likely to be more common (i.e. 'passive' interaction sensu Fuhrmann et al., 2021). Based on a lack of asymmetrically-reworked deposits, Fuhrmann et al. (2021) suggested that the reworking influence of contour currents does not extend to the base of highly confined channels. Here, we show that it is not that the currents do not reach the canyon or channel base, but instead that such confining topography fundamentally steers bottom currents, creating canyon or channel-parallel flow (Fig. 4.6). The resultant deposits, which will likely comprise reworked turbidites, may be indiscernible from those emplaced by gravity currents, therefore complicating the calculation of turbidite recurrence intervals or paleoseismicity in the ancient and recent record. It has long been recognised that bottom currents may be steered by regional to local topography, but observations of such interactions have been missing until now (Faugères & Stow, 2008; Rebesco et al., 2014). The bed-proximal topographic steering observed with high frequency ADCPs is missing from previous observational studies that used lower frequency, long-range ADCPs, which could not image closer than 10s to 100s of metres within seafloor, and also from numerical models that incorporate low-resolution bathymetry and that do not fully extend to the seafloor (Zhang et al., 2014;

Zhao et al., 2015; Steinmann et al., 2020; Wilckens et al., 2021). We posit that the role of topographically-steered bottom currents, which can exceed 1 $ms^{-1}$ near-bed in many submarine canyons (Shepard, 1976; Petruncio et al., 1998; Lee et al., 2009; Hall & Carter, 2011; Martín et al., 2011; Shanmugam, 2013; Aslam et al., 2018; Maier et al., 2019b), may have been dramatically underestimated in many mixed turbidity-contour current systems, and that future direct monitoring is needed to unravel both direct and passive interactions.

## 4.5 Conclusions

Using an unprecedented collection of monitoring datasets that capture the near-bed regime of bottom currents across a mixed depositional system for the first time, we have shown how the intensity and direction of contour currents can vary across tidal and seasonal timescales, and the often-extreme influence of seafloor topography in steering currents. Robust determination of the net-transport direction of bottom currents was only possible through sustained and high frequency measurements at multiple locations that recorded close to the seafloor. No direct interactions between gravity currents and contour currents were observed, due to the inactivity of gravity flows during the period of study, yet the interaction between deposits from past gravity currents and the regional bottom currents are profound. The wide variability in behaviour observed across 35 mooring locations underlines the challenges that remain in characterising bottom currents even when direct measurements are available, particularly as such a monitoring campaign is unprecedented. Near-bed seafloor processes are clearly more complex and dynamic than has been presumed. We hope our new observations motivate future, sustained near-bed monitoring efforts elsewhere to fill the many gaps in our understanding of these globally-important deep-sea transport systems and the dynamic distribution and accumulation of sediment, carbon and pollutants.

# Chapter 5

# Conclusions

## 5.1 Overview

Using novel direct monitoring data, this thesis focused on determining the frequency and timing of turbidity currents and other sediment transport events in and adjacent to submarine canyons, and assessing to what extent the mechanisms that initiate, precondition and trigger these sediment transport events relate to their magnitude (i.e. velocity and runout). To understand the multiple processes of sediment transport that occur within submarine canyons and channels, detailed geophysical monitoring datasets were analysed; specifically using ADCPs for precise measurements of transport event timing in three physiographically-diverse settings. These included: (1) The oceanographically-fed Monterey Canyon, offshore California; (2) a river-fed submarine channel in Bute Inlet fjord, British Columbia; and (3) the sediment starved northern Mozambique continental slope.

## 5.2 Response to Research Questions

This section outlines the main conclusions to each of the key research questions outlined in Chapter 1.

**Question 1: What is the controlling factor in turbidity current activity and timing – system preconditioning or external triggers? (Chapter 2)**

The thesis first focused on identifying the factors that control turbidity current activity. Previous studies have commonly assumed that turbidity currents are caused by

major external events, such as storms, river floods or major earthquakes (Table 2.1; and references therein). However, testing turbidity current triggers requires measuring the timing of turbidity currents and potential triggers with precision, and only in rare cases can deposits be dated at sufficiently high resolution to directly isolate such external triggers. Additionally, while there has been a growing trend to direct turbidity current monitoring using ADCPs throughout the past decade, previous studies using ADCPs have either collected data at low temporal resolution, or involved instruments located far away from where flows originate. Moreover, monitoring instruments were typically deployed for a few months, missing parts of annual or longer cycles. This ensures that the controls on turbidity currents activity remain poorly tested (Table 2.1).

Chapter 2 presented some of the most detailed direct flow measurements to date, which allow the timing of turbidity currents to be precisely constrained in Monterey Canyon, offshore California as well as the environmental conditions that may trigger them. The primary conclusion of this chapter was that no consistent trigger was observed for the fourteen flows that were recorded in Monterey Canyon, but turbidity currents were more frequent in the winter storm season. During the winter, heightened wave energy increases sediment transport to the canyon head and similar volumes of sediment were estimated to enter the canyon head between flows. A single powerful (up to 4.8 $ms^{-1}$ and $>$52 km runout) event was observed outside the winter, when sediment supply rate is reduced. However, the total sediment volume entering the canyon head was approximately four times higher than the mean between winter events. Chapter 2 therefore proposed that turbidity current activity is better related to sediment supply and slope preconditioning rather than individual triggers.

Chapter 2 then combined insights from Monterey Canyon and other sites of direct monitoring (the Squamish Delta, British Columbia and the Congo Canyon, offshore Angola) to produce a model for preconditioning and triggering of turbidity currents via slope failure, in locations of sustained sediment accumulation such as canyon heads and river deltas. In this model, rapid or sustained sediment supply alone can produce elevated pore pressures, which may persist, thereby predisposing slopes to fail for hours to months (or potentially even longer in muddy systems) after initial sediment deposition. Small perturbations in antecedent conditions resulting in local pore pressure variation then become capable triggers, demonstrating that major external events such as earthquakes, storms or river floods are not a prerequisite for turbidity current activity.

A shortcoming of this study, and other monitoring studies of turbidity currents is a lack of detailed monitoring of how shallow subsurface conditions evolve as sediment is supplied; in particular the monitoring of pore pressures. Efforts have been made in a small number of settings where submarine landslides are known to have occurred, to use in-situ geotechnical instrumentation to monitor the evolution of near-seafloor pore pressures that can be enhanced by sediment accumulation, generation of biogenic

gas, perturbation by seismic or wave loading, tidal effects, or the offshore infiltration of meteoric ground water (Bennett, 1977; Okusa, 1985; Chillarige et al., 1997; Christian et al., 1997; Sultan et al., 2010, 2020; Stegmann et al., 2011). However, while these geotechnical monitoring studies have been able to document transient changes in pore pressures, including generation of values in excess of hydrostatic conditions, no measurements have been made coincident with the inception of a turbidity current. As such, future research should focus on understanding and measuring the pore pressure regime in submarine canyons head or at river deltas and relating these measurements to the timing of submarine landslides and subsequent generation of a turbidity current. One potential method to measure the pore pressure regime prior to slope failure would be to install piezometers (that measure pore pressure) within the head of a turbidity current system. The river-fed fjords in British Columbia (e.g. Bute Inlet and Howe Sound) would provide an ideal test site for such a method. Firstly, the deltas here are easily accessible at low tide to for instrument burial, and secondly the locations of slope failures are better constrained when compared to a submarine canyon head, therefore increasing the likelihood of an instrument recording a failure.

**Question 2: How do preconditioning and triggering mechanisms combine to enhance turbidity current activity? (Chapter 3)**

Chapter 2 demonstrated that the common driver of turbidity current activity is enhanced sediment supply; either sudden and rapid, or sustained over a longer period of time. Such elevations in sediment supply to submarine canyon and channel heads are often highly predictable; for example, during peaks in a river flood hydrograph, or when long-shore sediment transport is elevated during storm seasons. Therefore, on an annual cycle, periods of enhanced turbidity current activity may be similarly predictable. To build on this, Chapter 3 used a novel multivariate statistical approach to combine preconditioning and triggering factors to predict the likelihood of turbidity current occurrence for given environmental conditions. Unlike Monterey Canyon, where numerous potential triggering mechanisms exist, the mechanisms for turbidity current generation are better constrained offshore from river deltas such as at Bute Inlet, where turbidity current generation has previously been shown to relate to river discharge and low tides.

Two source-to-sink field campaigns (Spring and Summer freshets of 2016 and 2018) in the river-fed Bute Inlet recorded the most extensive number (N = 113) of directly monitored turbidity currents in a submarine channel to date. Chapter 3 analysed the role of river discharge and tides on the generation of turbidity currents. In isolation, both elevation of Homathko River discharge (the primary freshwater input to Bute Inlet) and low tides showed statistical significance as turbidity current triggering mechanisms when compared to background conditions. The relative importance of each of these triggering variables was statistically calculated using logistic regression on the timing of turbidity currents during 2018. Here, turbidity current occurrence was at least 1.8

times more likely at low tide than any other position in the cycle for a given tidal range; and for every percentile increase in Homathko River discharge, the likelihood of a turbidity current increased by 9%. Additionally, this logistic regression model was able to calculate turbidity current probability for any given input of Homathko River discharge and water level; successfully predicting 86% of turbidity current activity during 2018. The model was validated by predicting turbidity current activity for the 2016 monitoring dataset in Bute Inlet, and at other similar sites of direct monitoring (Squamish and Fraser Rivers). Here, >84% successful hindcasts of turbidity current activity showed good predictive power for systems where sediment supply is seasonal and turbidity currents are principally triggered at low tide.

The logistic model built using direct turbidity current modelling in Bute Inlet provides a framework that can be tested by future studies. We suggest that our model can be further extended to river deltas where sediment flux is either river- or tidally controlled, accounting for 87% of the global sediment flux from river deltas to the ocean, although there remains a compelling need for more direct measurements to test our predictive model at larger directly river-fed submarine canyons. Recent monitoring in the Congo Canyon has shown turbidity current recurrence correlates with spring tide intervals (Talling et al., 2021). Applying the logistic model to Congo River discharge and water level would be an ideal step to further develop the logistic model, but some key questions are open. For example, the Congo River is almost always in flood (due to its exceptionally large catchment area), so to what extent does this alter the relative importance of river discharge and water level as triggering variables? Furthermore, will the river discharge normalisation in the current version of the logistic model be applicable to a flood hydrograph without the extreme seasonality observed in the Homathko River? The Congo Canyon as a future test site will also allow an investigation into supply of sediment through longshore transport or oceanographic turbidity current triggers. Here, the incorporation of a wave parameter will quantify the relative importance of oceanographic processes to both river discharge and tidal. A number of other key aspects will need to be validated before the model can be more widely applied. For instance, it remains unclear how well the predictive model may hold for river systems that interact with oceanographic processes (e.g. littoral cells) where they flow out into the open ocean, rather than into a confined fjord, or in settings where tides, or indeed rivers play a smaller role in turbidity current initiation. There is therefore a compelling case to quantify littoral transport to systems rather than estimates based on wave energy (as in Chapter 2). This thesis also did not cover the generation of turbidity currents within freshwater lakes and whether flows can be predicted in this setting remains an open question. Here, hyperpycnal flows are common due to the ambient density of freshwater, and tides are not active for turbidity current triggering (e.g. Lambert & Giovanoli, 1988; Crookshanks & Gilbert, 2008). As monitoring is becoming more common, there will be opportunities to test these different controlling factors, and how these factors control long runout (i.e. 1:100, or more, events). To resolve these questions, it will

be important that high temporal resolution data are acquired, the timing of turbidity currents is made close to their source, and that the other processes are well constrained (e.g. simultaneous detailed monitoring of along shelf currents, river discharge or any other potential variable linked to turbidity current generation).

**Question 3: What controls sediment transport in submarine canyons during sustained periods of turbidity current inactivity? (Chapter 4)**

Chapters 2 and 3 focus on the roles of turbidity currents in submarine canyons and channels. However, in some settings, near-bed currents can also shape seafloor morphology during periods when turbidity currents are not operational. Chapter 4 investigates a direct monitoring dataset from the sediment starved North Mozambique continental slope, where turbidity currents are rare, to understand how near-bed currents can control and modify sediment transport regimes.

Using an unprecedented collection of monitoring datasets that capture the near-bed regime of bottom currents across a mixed depositional system for the first time, Chapter 4 shows how the intensity and direction of contour currents can vary across tidal and seasonal timescales, and the often-extreme influence of seafloor topography in steering near-bed currents. Robust determination of the net-transport direction of bottom currents was only possible through sustained and high frequency measurements at multiple locations that recorded close to the seafloor. No direct interactions between gravity currents and contour currents were observed, due to the inactivity of gravity flows during the period of study, yet the interaction between deposits from past gravity currents and the regional bottom currents are profound. The wide variability in behaviour observed across 35 mooring locations underlines the challenges that remain in characterising bottom currents even when direct measurements are available, particularly as such a monitoring campaign is unprecedented. Near-bed seafloor processes are clearly more complex and dynamic than has been presumed and capable of transporting sediment and associated matter through submarine canyons even when turbidity currents are not active.

A key finding from Chapter 4 was that confining topography (e.g. submarine canyons or gullies) fundamentally steers bottom currents, creating canyon or channel-parallel flow. The resultant deposits, which likely comprise reworked turbidites, may be indiscernible from those emplaced by gravity currents. Chapter 4 does not quantify sediment transport, and an open step for the future may be to calculate shear stress on the seafloor offshore North Mozambique to develop our understanding of near-bed sediment dynamics. Future work should also attempt to identify the velocity structure of internal canyon resuspensions coupled with coring efforts to analyses their deposits. The Whittard Canyon, offshore Ireland would make an ideal test site. Here, strong $>1$ $ms^{-1}$ internal tidal currents have previously been recorded along with of frequent (up to 6 annually) turbidity currents (Hall et al., 2017; Aslam et al., 2018). The occurrence

of both sediment transport mechanisms allows for a direct comparison between the deposits from near-bed currents and how they differ from turbidites. Such an understanding is key for the calculation of turbidite recurrence intervals or paleoseismicity in the ancient and recent record.

## 5.3 Future Research Directions

### 5.3.1 Continued Direct Monitoring

A host of recent successful ADCP deployments have led to continuously new insights sediment transport mechanisms in submarine canyons and channels (e.g. Chapters 2; 3; 4; Xu et al., 2004; Liu et al., 2012; Khripounoff et al., 2012; Hughes Clarke, 2016; Clare et al., 2016; Azpiroz-Zabala et al., 2017; Paull et al., 2018; Hage et al., 2019; Normandeau et al., 2020). Such a success should stimulate future field campaigns either to continue monitoring either in previously monitored systems to build long-term records of turbidity current activity, or in new settings to add to our knowledge of the global continuum (or test if a continuum exists) of sediment transport in submarine canyons and channels. To date, there has been a bias to monitor in systems where turbidity current activity is perceived to be high. However, even at sites of very low or no turbidity current activity (e.g. Normandeau et al., 2020) sediment transport is still active. More monitoring is needed in contourite and mixed turbidite-contourite systems. Contourite research is still in its infancy compared to turbidity currents (Rebesco et al., 2014) and as Chapter 4 demonstrates the interplay between submarine canyons and near-bed currents is complex. Where turbidity currents frequently (i.e. 10s per year) interact with near-bed currents will further complicate sediment transport and therefore represent a key setting for the focus of future direct field monitoring campaigns.

The use of multiple moorings along the flow paths of turbidity currents should also drive future research to understand the factors that control flow magnitude (i.e. velocity, runout and sediment concentration). Source to sink measurements of turbidity currents has the disadvantage of being high risk (turbidity currents have the ability to damage or wash away expensive instruments), require expensive ship-time, and can only record for short ($\sim$months) periods. However, emerging technology and methods means turbidity currents are becoming easier and cheaper to monitor. Developing and testing new monitoring equipment (e.g. passive hydrophones and seismometer networks that can be placed out of the path of damaging flows; Clare et al., 2017, 2020) should also be a focus of future work to enable measurements in some of the largest ($>$1000s of km) submarine canyons.

There is a compelling need to monitor at the source of turbidity current initiation, either within the head of submarine canyons, at the river mouth where direct river-canyon

head connection exists or along the shelf between. The evolution of geotechnical conditions such as pore pressures is yet to be quantified. Furthermore, previous studies have lacked monitoring of sediment loading, accumulation, or changes in slope gradient from high resolution repeat mapping. Unlike a river plume-initiated turbidity current (e.g. Hage et al., 2019), a landslide-initiated flow has yet to by directly monitored. Future targeted deployments similar to that of Hughes Clarke (2016) and Hage et al. (2019) to capture such a flow will develop our understanding of how and when submarine landslides occur and how the subsequent turbidity current differs to that of a plume-triggered event.

### 5.3.2 Understanding the Role of Climate Change on the Frequency, Magnitude and Timing of Turbidity Currents

Long-term changes to climate over thousands to millions of years are thought to impart a strong control the recurrence intervals of submarine landslides and turbidity currents (Weaver et al., 1992; Romans et al., 2009; Covault & Graham, 2010; Tappin, 2010). But what impacts will shorter, contemporary changes in warming climate have on the flux of sediment and associated particles to the deep-sea? Will a warming climate increase the frequency and magnitude of powerful turbidity currents? While past rapid warming periods over geological history have not necessarily altered submarine landslide and turbidity current recurrence (e.g. Urlaub et al., 2013), it is likely that modern warming will alter source-to-sink sediment pathways (e.g. Syvitski, 2003). Furthermore, a trend towards more frequent river floods (e.g. Milly et al., 2002) and a proportional increase in hurricane strength (e.g. Holland & Bruyère, 2014) may elevate the potential of turbidity current triggering. However, any changes are unlikely to be universal worldwide, as the effects of climate change can be complex. For instance, tropical cyclones may become more powerful, but their paths appear to be shifting poleward under global warming (Studholme et al., 2021). Therefore some areas will experience tropical cyclones that previously have not, while others will experience less impact that before. Understanding the potential changes to turbidity current frequency, regardless of trigger, is critical for geohazard assessments.

Chapters 2 and 3 demonstrate that sediment supply is the common driver in turbidity current activity across different physiographic settings. Turbidity currents can be anticipated during the winter in Monterey Canyon, when increased wave energy delivers greater quantities of sediment to the canyon head; while in Bute Inlet turbidity currents occur during the summer following enhanced glacial-melt and fluvial transport. Mechanisms of sediment supply are susceptible to change in a future warming climate. For example, where turbidity currents are generated at the deltas of glacial-fed rivers, such as Bute Inlet, unseasonably warm weather may lead to early onset of melting, reducing peak river discharge but lengthening the season where turbidity currents would

be expected. Additionally, the frequency of extreme rainfall will likely increase in a warming climate. Here, pulses in rainfall-induced river discharge will alter the volume of sediment arriving at the onset of glacial melt.

Long-term monitoring of turbidity current activity is key to identifying the change in flow frequency and predicting further changes with future climate warming. Sites such as Bute Inlet and Howe Sound, both of which are fed by glacial-melt rivers provide ideal test sites, where several years of monitoring already exist for comparison and mechanisms of turbidity current generation are well constrained. Future test sites should also focus on locations susceptible to extreme weather, to assess how this will impact turbidity current activity and geohazard potential. The directly river-fed Gaoping Canyon, offshore Taiwan, is one example of a potential test site where tropical cyclones pass through the region annually. Understanding the mechanism of turbidity current triggering in the Gaoping Canyon, and the relative importance of triggering variables (i.e. Gaoping River discharge, storm waves and tides) will facilitate future modelling and prediction of possible impacts of short-term climate change.

### 5.3.3 Long-term Changes in Turbidity Current Frequency, Magnitude and Timing following Extreme Events

If sediment supply is the driver of turbidity current occurrence what happens if a system supply of sediment rapidly changes? Over an annual cycle Chapters 2 and 3 demonstrate that changes in sediment supply result in a 'switch on' of turbidity current activity. But the impact of an extreme change in sediment delivery is unknown. Recently, a glacial outburst flood (GLOF) occurred in 2020 resulting in a turbidity current running through the entire length and beyond ($>$ 60 km) the submarine channel in Bute Inlet. The turbidity of the river flowing into Bute Inlet remains elevated at the time of thesis submission and it has been suggested that such events may result in long lasting (decades) increases in sediment delivery (Giesbrecht et al., 2021; Tilston et al., 2021; Piret et al., 2022).

Such an event presents a rare opportunity to study the long-term impacts on turbidity current activity following a dramatic change in sediment supply. As outlined in Chapter 3, Bute Inlet has previously been a site of extremely detailed time series surveys between 2008 and 2020, with ADCP deployments during 2016 and 2018. Future instrument deployment in Bute Inlet therefore represents a unique research opportunity with the evolution of the submarine canyon and turbidity current activity already well documented for use as a pre-event baseline for comparison. As such, continued monitoring here should aim to answer the following key research questions: (1) What effect does a rapid increase in sediment supply have on turbidity current frequency – is a single powerful turbidity current generated immediately or does the sediment stock change turbidity current frequency over months, years or decades timescales?

In the case of Bute Inlet, will turbidity currents now occur outside of the freshet, or will the period of turbidity current 'switch on' be extended? Or, will turbidity current frequency just increase during the freshet? Answering this will help our understanding between preconditioning and triggering factors (i.e. in Bute Inlet is elevated river discharge important as a trigger or can turbidity currents initiate without an obvious triggering mechanism as discussed in Chapter 2 in Monterey Canyon). (2) Will an increase in sediment supply lead to greater magnitude (i.e. runout and sediment concentration) turbidity currents? The initial turbidity current ran through and beyond the entire submarine channel. Understanding the volume of sediment transported to the depositional lobe is key to understanding the rate of sediment and organic carbon burial. (3) How long will turbidity current activity in Bute Inlet need to revert back to levels observed pre-GLOF? Extreme sediment input following GLOFs represents one mechanism of rapid sediment supply, and such events similar to that observed in Bute Inlet will likely become more frequent in our warming climate. For example, the global glacier lake volume has increased by almost 50% over the past 30 years due to global warming (Shugar et al., 2020). Understanding the long-term changes in turbidity current frequency, timing and magnitude following extreme increases in sediment supply is therefore critical for future geohazard assessments of strategic seafloor infrastructure.

## 5.4 Concluding Remarks

This thesis presented and analysed direct monitoring datasets to better understand how sediment transport is initiated and varies between different submarine canyon and channel systems. Using novel statistical and quantitative analysis it has been shown for the first time that:

- Major external triggers such as earthquakes, storms or river floods are not a prerequisite for turbidity current activity, instead turbidity currents in Monterey Canyon were triggered by subtle changes in antecedent conditions, such as the onset of a minor storm.
- Sediment supply is the common driver of turbidity current activity in different physiographic settings. Where sediment supply is seasonal (during a storm season when wave energy and littoral transport is elevated or during peaks in a river flood hydrograph) windows of enhanced turbidity current activity can be anticipated.
- Preconditioning and triggering factors combine to increase the likelihood of turbidity current occurrence. Where preconditioning and triggering variables can be quantified the probability of a turbidity current can be statistically predicted.
- Near-bed seafloor processes are more complex and dynamic than has been presumed and capable of transporting sediment and associated matter through submarine canyons even when turbidity currents are not active.

# Appendix A

# What Determines the Downstream Evolution of Turbidity Currents?

Analysing the role of internal tides as a turbidity current triggering mechanism in Monterey Canyon (Chapter 2) contributed to the investigation of the downsteam evolution of turbidity currents by Heerema et al. (2020).

**This is a reproduction of text published in**
***Earth and Planetary Science Letters***

Catharina J. Heerema, Peter J. Talling, Matthieu J. B. Cartigny, Charles K. Paull, Lewis P. Bailey, Stephen M. Simmons, Daniel R. Parsons, Michael A. Clare, Roberto Gwiazda, Krystal Anderson, Katherine L. Maier, Jingping P. Xu, Esther J. Sumner, Kurt J. Rosenberger, Jenny Gales, Mary McGann, Lionel Carter, Edward Pope and the Monterey Coordinated Canyon Experiment (CCE) Team (2020). What Determines the Downstream Evolution of Turbidity Currents? Earth and Planetary Science Letters, 532, 116023. DOI: 10.1016/j.epsl.2019.116023

Seabed sediment flows called turbidity currents form some of the largest sediment accumulations, deepest canyons and longest channel systems on Earth. Only rivers transport comparable sediment volumes over such large areas; but there are far fewer measurements from turbidity currents, ensuring they are much more poorly understood. Turbidity currents differ fundamentally from rivers, as turbidity currents are driven by the sediment that they suspend. Fast turbidity currents can pick up sediment, and self-accelerate (ignite); whilst slow flows deposit sediment and dissipate. Self-acceleration cannot continue indefinitely, and flows might reach a near-uniform state (autosuspension). Here we show how turbidity currents evolve using the first detailed measurements from multiple locations along their pathway, which come from

Monterey Canyon offshore California. All flows initially ignite. Typically, initially-faster flows then achieve near-uniform velocities (autosuspension), whilst slower flows dissipate. Fractional increases in initial velocity favour much longer runout, and a new model explains this bifurcating behaviour. However, the only flow during less-stormy summer months is anomalous as it self-accelerated, which is perhaps due to erosion of surficial-mud layer mid-canyon. Turbidity current evolution is therefore highly sensitive to both initial velocities and seabed character.

## A.1 Introduction

Seafloor sediment density flows (called turbidity currents) are the dominant global mechanism for transporting sediment from the continental shelf to the deep sea. These flows play a crucial role in global organic carbon burial and geochemical cycles (Galy et al., 2007), and supply of nutrients to deep-sea ecosystems (Canals et al., 2006). Only rivers transport sediment over comparable areas, although one turbidity current can carry more sediment than the annual flux from all the world's rivers combined (Talling et al., 2013). Powerful turbidity currents can badly damage seafloor infrastructure, including oil and gas pipelines, and telecommunication cable networks. The latter carry over 95% of global data traffic (Carter et al., 2014), forming the backbone of the internet and financial markets. Turbidity current deposits host valuable oil and gas reserves, and form thick sequences of ancient rocks that record Earth's history (Nilsen et al., 2007). The downstream evolution of velocities and runout lengths controls how sediment is dispersed, the resulting deposit character and shape, and hazards to seafloor infrastructure. It is thus important to understand how turbidity currents work, especially what controls their runout, and changes in flow velocity with distance.

Turbidity currents differ profoundly from terrestrial rivers; unlike rivers they are driven by the weight of sediment they carry, and this sediment can be entrained or deposited onto the seafloor along turbidity current pathways. Previous work suggested that exchange of sediment with the seabed may lead to positive feed- backs, such that turbidity current behaviour is inherently unstable and diverges (Fig. A.1; Bagnold, 1962; Parker, 1982). These studies proposed that flows which erode sediment become denser, and thus accelerate, causing increased erosion, and further acceleration (Fig. A.1a). This process is called ignition, and it may play a pivotal role in producing powerful and long runout flows. Conversely, flows that deposit sediment may decelerate, leading to further deposition ('dissipation'; Fig. A.1b). Such positive feedbacks may produce thresholds in behaviour that depend on small differences in initial flow state. It has also been proposed that flows could achieve a near-uniform state in which erosion is balanced by sediment deposition, termed autosuspension (Fig. A.1c, d; Pantin, 1979). Here, turbulence within the flow is strong enough to keep particles in suspension, and counteracts their settling velocity (Parker, 1982). However, unlike ignition, there is no

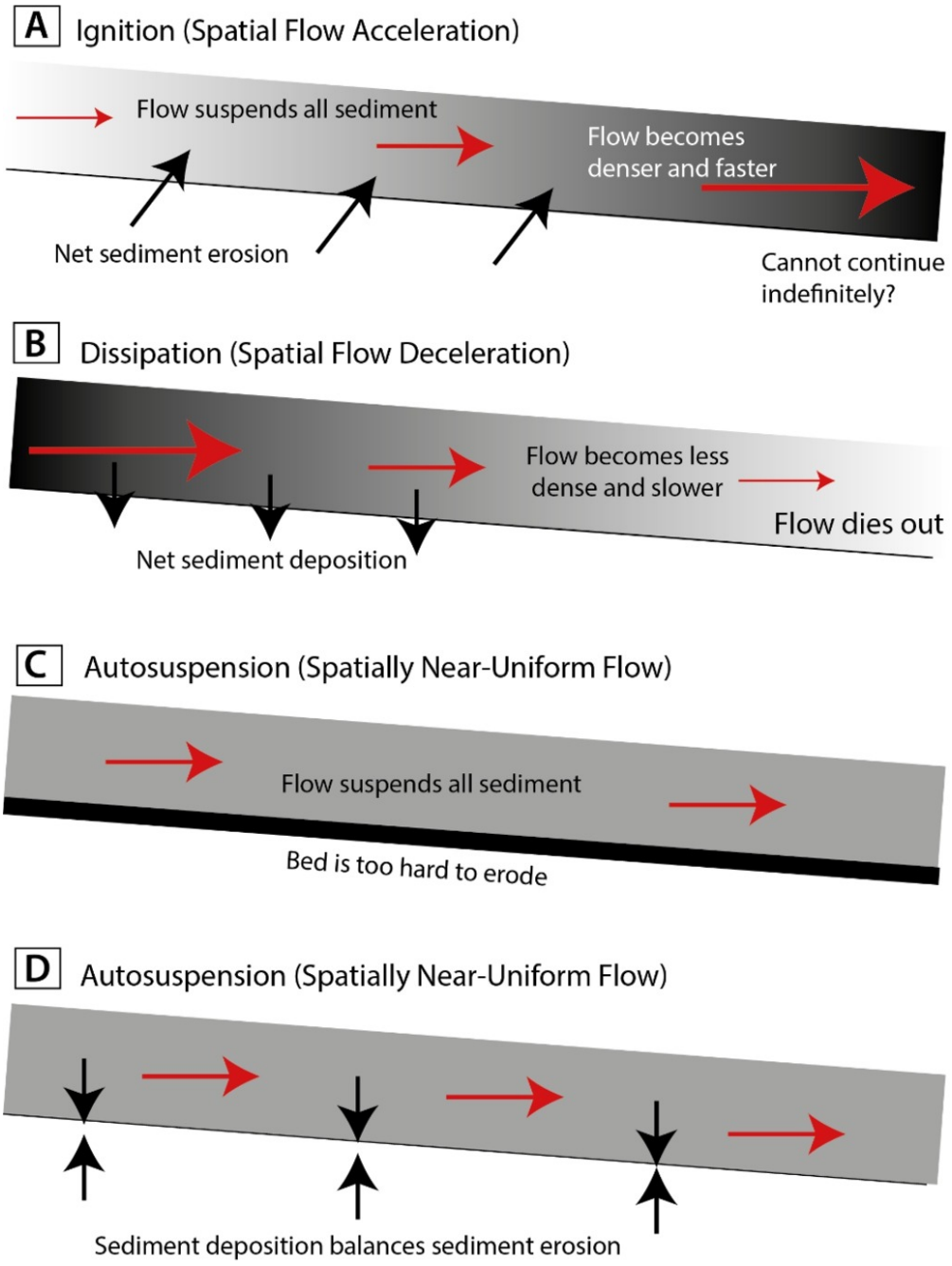


**Figure A.1:** Ignition, dissipation and autosuspension of turbidity currents. (A) Ignition is caused by net sediment erosion that increases flow density, causing increased velocities. This positive feedback cannot continue indefinitely, as elevated sediment concentrations eventually damp turbulence, shield the bed from erosion, or increase friction. (B) Dissipation is caused by sediment deposition, which leads to spatial decreases in flow density, and thus velocity. This negative feedback causes the flow to eventually die out. (C and D) Autosuspension comprises a situation in which flow density remains constant, and flow velocities are constant spatially. (C) Flow may be powerful enough to suspend all of the sediment it carries, but the substrate is too hard to erode. Alternatively, localised areas of erosion and deposition may also balance each other out, leading to no net change in suspended sediment. (D) Sediment deposition may be balanced by an equal amount of substrate erosion. Models for autosuspension in (C) and (D) assume flow is dilute and fully turbulent. We subsequently present an alternative model for autosuspension (Fig. 7), where flow is driven by a dense near-bed layer.

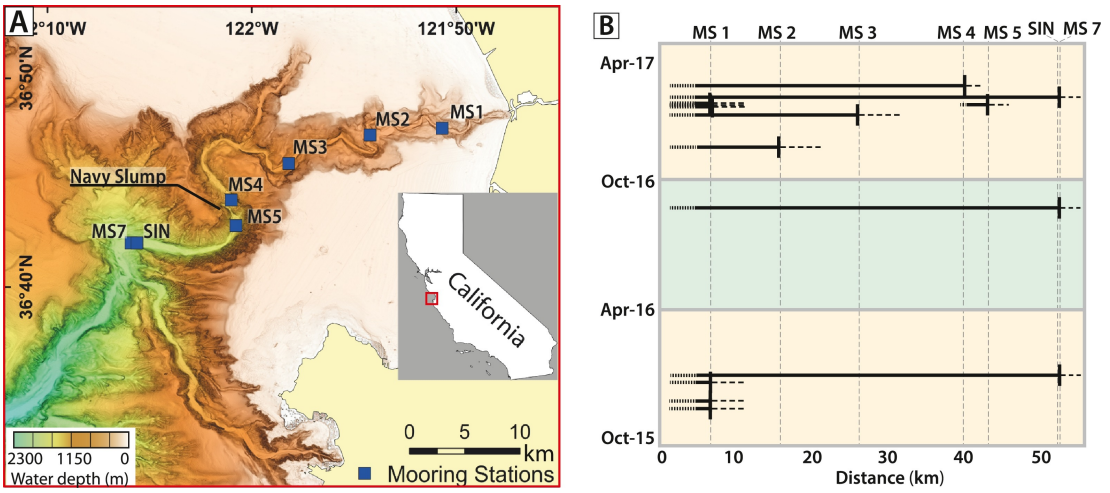


**Figure A.2:** Location, runout distances and velocities of turbidity currents in Monterey Canyon. (A) Bathymetry map of Monterey Canyon showing location of moorings in this study (MS1 to MS7, SIN), and Navy Slump. (B) Timing and runout distance of turbidity currents in Monterey Canyon between October 2015 and April 2017. Horizontal lines show 13 events registered by ADCPs. The green and yellow boxes show the 6-month deployment periods. Locations of moorings (MS1 to MS7, SIN) are indicated. The exact point where flows terminate between moorings is uncertain.

net gain of sediment from the bed, as the bed is too hard to erode (Fig. A.1c), or sediment erosion balances sediment deposition during autosuspension (Fig. A.1d). Flows that balance erosion and deposition will tend towards spatially uniform velocities, assuming that seabed gradient and flow width do not change markedly. Self-acceleration due to ignition is unlikely to continue indefinitely: increased sediment concentrations will eventually damp the turbulence that keeps sediment aloft (Baas et al., 2009) and shield the bed from rapid erosion, or increase frictional drag and thus reduce flow velocities. However, there is considerable debate over what happens after ignition ceases (Fig. A.1a). Do the flows reach a state of autosuspension; and if so, what do autosuspending flows look like? In particular, do flows develop a dense near-bed layer that drives the event (as proposed by e.g. Winterwerp, 2006), or remain an entirely dilute and fully turbulent suspension (e.g. Cantero et al., 2012)?

Turbidity currents are notoriously difficult to monitor in action, due to their location, episodic occurrence, and ability to damage instruments in their path (Inman et al., 1976; Talling et al., 2013). Consequently, there are very few direct measurements from oceanic turbidity currents, ensuring fundamental theories on how turbidity currents work are poorly tested. In particular, ignition and autosuspension have been difficult to reproduce in laboratory experiments (Southard & Mackintosh, 1981). This may be because most laboratory experiments are relatively slow moving, compared to full-scale oceanic flows, and thus have limited ability to erode their substrate, or fully support sediment with realistic grain sizes. Experimental flows thus tend to dissipate. Sequeiros et al. (2009, 2018) successfully produced self-accelerating turbidity currents in relatively slow moving ($<$20 cm s$^{-1}$) laboratory experiments with low density particles,

but they did not reproduce fully realistic processes of seabed erosion. However, new technologies have recently led to major advances in monitoring of active turbidity currents (Hughes Clarke, 2016). This includes acoustic Doppler current profilers (ADCPs) that measure velocity profiles to within a few meters of the seafloor (Xu et al., 2010). Here we use ADCP and other sensor data to observe spatial patterns of flow ignition, dissipation, and auto- suspension in unprecedented detail; and to study how flows work in general.

This study analyses the most detailed (7 locations at sub-minute intervals) field measurements yet from oceanic turbidity currents, which include the fastest (up to 7.2 $ms^{-1}$) flows captured via moored instruments. These measurements come from the upper 52 km of Monterey Canyon, offshore California (Fig. A.2a Paull et al., 2018). Previous direct monitoring of turbidity currents has typically involved measurements at a relatively small number ($\leq 3$) of locations along their pathway, which provides limited information on how flows behave (Khripounoff et al., 2009; Liu et al., 2012; Azpiroz-Zabala et al., 2017). By having measurements in seven locations along a turbidity current pathway we are able to determine how flows evolve. Here we focus on changes in the average flow front velocities between measurement locations (termed transit velocities), maximum internal velocities, as well as duration of flow velocities in each event (as measured by ADCPs).

### A.1.1 Aims

The first aim is to document changes in turbidity current velocity and runout distance, and hence flow behaviour. What is the observed pattern of ignition, autosuspension and dissipation; and do multiple flows show a consistent pattern of behaviour? The second aim is to understand what causes these patterns of flow behaviour. In particular, we consider how two factors (initial velocity and substrate erodibility) affect flow behaviour, and how near-uniform flow (autosuspension) may follow ignition. Our third aim is to determine if broadly similar flow behaviour is seen elsewhere, although suitable field data are sparse. Our fourth aim is to compare these field observations to most widely accepted theories for ignition and autosuspension. To what extent do these new field data provide a test of past theories? Finally, we develop a new generalised model for how turbidity currents operate in submarine canyons floored by loose-sand, which better explains these novel field observations.

#### A.1.1.1 Terminology

*Turbidity current* is used here as a general term for all types of submarine sediment density flow. *Dense flow* signifies sediment concentrations that are high enough to damp

turbulence significantly, such that turbulence is no longer the main support mechanism, whilst *dilute flow* is fully turbulent. There is no single threshold value for sediment concentration at which turbulence is strongly damped, as this depends on multiple factors including flow velocity, sediment mineralogy and grainsize. But dilute flows typically have sediment concentrations of $\ll$1%, whilst dense flows might often contain $>$10% sediment by volume. *Diverging* behaviour denotes how small changes in initial flow velocity are linked to large changes in subsequent runout. It does not imply that flow behaviour is bimodal, and intermediate runout lengths can still occur.

## A.2 Materials and Methods

The Coordinated Canyon Experiment (CCE) monitored the upper 52 km of Monterey Canyon (California, USA) to water depths of 1850 m, for 18 months from 2015 to 2017 (Fig. A.2; Paull et al., 2018). Sand is primarily delivered to the canyon head via longshore drift, with little river input (Paull et al., 2005). The entire canyon-channel system extends for over 300 km, but flows that runout for over 60 km, to a water depth of 2,850 m, only occur every few hundred years (Stevens et al., 2014). Flows are confined, and experience a constant seafloor gradient and width in the upper part of Monterey Canyon (Fig. A.3). The upper Monterey Canyon, up to 2100 m water depth, has a sinuosity of 1.9 (Paull et al., 2011). The canyon briefly narrows at a constriction between 1300 and 1400 m water depth, called the Navy Slump (Figs. A.2, A.3; Paull et al., 2011). This study uses data recorded by ADCPs along the canyon thalweg (Fig. A.2), which were part of a larger instrumental array (Paull et al., 2018).

### A.2.1 ADCP Measurements

ADCPs documented velocity profiles through the turbidity currents (Fig. A.3), although they are typically unable to make measurements within a few meters of the bed. The shallowest five mooring stations (MS1 to 5), and deepest mooring station (MS7), had downward-looking 300 kHz ADCPs located approximately 65 m above the bed seafloor (Paull et al., 2018). ADCPs on these moorings recorded velocity at 30 second intervals. A Seafloor Instrument Node (SIN) was located on the seafloor between MS5 and MS7, which contained three separate upward-looking ADCPs recording at 10 second intervals, using acoustic sources with three different frequencies (300, 600, 1200 kHz). No reliable ADCP measurements of current velocity are available from the shallowest mooring (MS1) for some flows, as this mooring broke loose on January 15, 2016 (Paull et al., 2018).

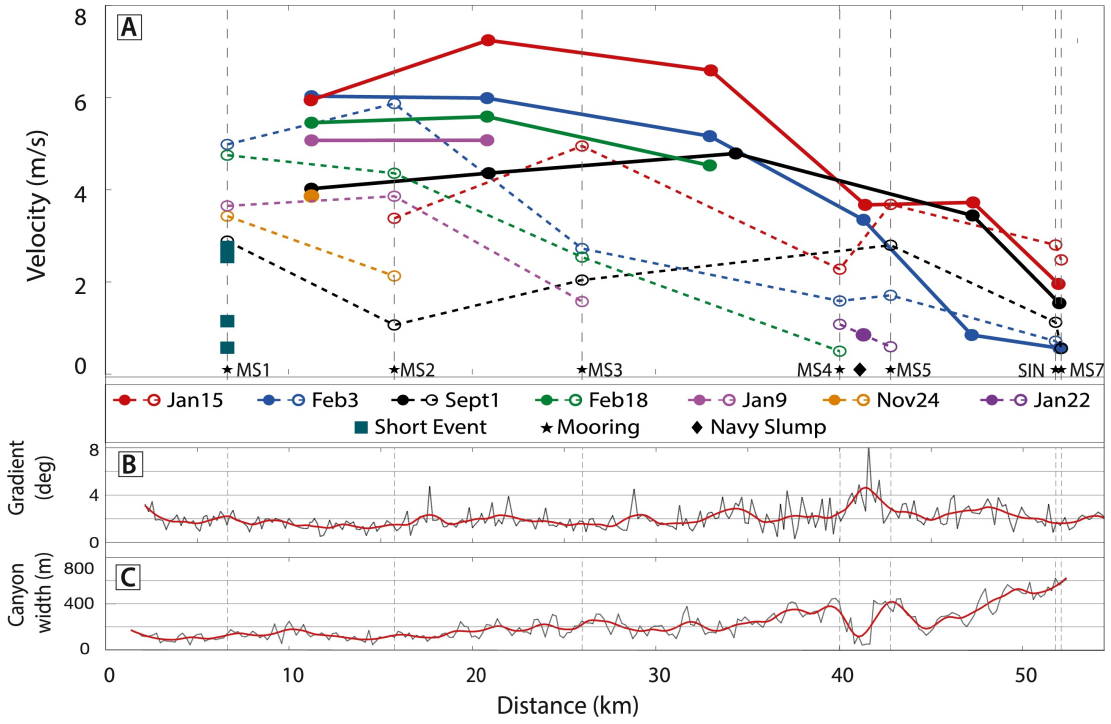


**Figure A.3:** Velocities of turbidity currents in Monterey Canyon and properties of the thalweg. (A) Changes in flow velocity with distance along Monterey Canyon's thalweg. Solid dots and solid lines show frontal velocities between moorings. Open symbols and dotted lines show maximum internal velocity measured at each mooring by an ADCP, including for some flows that only reached the first mooring (solid squares). (B) Changes in thalweg gradient. (C) Changes in axial channel width, defined by the width of mapped bedforms.

### A.2.2 Maximum Flow Velocity Measured by ADCPs

Determining the maximum reliable velocity measured by the ADCP is not straightforward. The arrival of an event is accompanied by mooring tilt and high near-bed sediment concentrations, influencing the ability of ADCPs to accurately record velocities (Paull et al., 2018). Side-lobe interference may compromise some ADCP measurements within 1-3 m of the seabed (Teledyne RD Instruments, 2011), although this depends on the relative strength of backscatter from side-lobe areas and sediment in the flow. We thus adopted a consistent procedure for calculating maximum ADCP-measured velocities, which excludes the 20 highest values during an event. The overall trend of internal velocities remains the same, and therefore our ADCP data processing does not change this paper's main conclusions.

### A.2.3 Transit Velocities and Runout Distance Flow

As frontal or maximum velocities only tell part of how flow is evolving, and changes in velocity structure, the duration of a fast-moving flow is also quantified and presented (Table A.1). This duration, determined for three different velocity thresholds, provides an additional indication of how flows may lengthen or stretch over time.

**Table A.1:** Flow duration (to nearest minute) for each mooring station and event. For each event, a threshold flow velocity was set to determine the duration of the flow at each mooring. The ADCP data was displayed using contour lines corresponding to each threshold, allowing for determination of flow duration at every mooring. Left hand columns denote flow velocity threshold $\geq$1 ms$^{-1}$. Middle columns denote flow velocity threshold $\geq$2 ms$^{-1}$. The right-hand column denotes flow velocity threshold $\geq$3 ms$^{-1}$. Where no flow duration is given, there was no ADCP measurement (January 15, MS1, and September 1, MS4). A duration of 0 min indicates the flow is no longer measured at the specified threshold velocity at that mooring.

| Flow Threshold | $\geq$1 ms$^{-1}$ | | | | | | | $\geq$2 ms$^{-1}$ | | | | | | | $\geq$3 ms$^{-1}$ | | | | | | |
|---|---|---|---|---|---|---|---|---|---|---|---|---|---|---|---|---|---|---|---|---|---|
| Mooring | MS1 | MS2 | MS3 | MS4 | MS5 | SIN | MS7 | MS1 | MS2 | MS3 | MS4 | MS5 | SIN | MS7 | MS1 | MS2 | MS3 | MS4 | MS5 | SIN | MS7 |
| Distance [km] | 6.7 | 16 | 26 | 40 | 43 | 51.8 | 52 | 6.7 | 16 | 26 | 40 | 43 | 51.8 | 52 | 6.7 | 16 | 26 | 40 | 43 | 51.8 | 52 |
| Jan-15 | | 87 | 141 | 182 | 213 | 112 | 89 | | 10 | 59 | 23 | 41 | 37 | 22 | | 9 | 30 | 0 | 25 | 1 | 0 |
| Sep-01 | 20 | 4 | 73 | | 22 | 45 | 0 | 1 | 1 | 7 | 0 | 11 | 0 | 0 | 1 | 0 | 0 | 0 | 3 | 0 | 0 |
| Feb-03 | 48 | 74 | 73 | 67 | 65 | 0 | 0 | 28 | 17 | 26 | 0 | 4 | 0 | 0 | 16 | 15 | 3 | 0 | 0 | 0 | 0 |
| Feb-18 | 34 | 26 | 70 | 0 | | | | 15 | 12 | 16 | | | | | 8 | 8 | 2 | | | | |
| Jan-09 | 35 | 23 | 43 | | | | | 19 | 11 | 0 | | | | | 11 | 8 | 0 | | | | |
| Nov-24 | 33 | 15 | | | | | | 12 | 4 | | | | | | 9 | 1 | | | | | |
| Jan-21 | 31 | | | | | | | 10 | | | | | | | 2 | | | | | | |
| Jan-20 | 25 | | | | | | | 7 | | | | | | | 3 | | | | | | |
| Dec-01 | 16 | | | | | | | 7 | | | | | | | 3 | | | | | | |
| Jan-23 | 9 | | | | | | | 0 | | | | | | | 0 | | | | | | |
| Jan-06 | 7 | | | | | | | 1 | | | | | | | 0 | | | | | | |
| Dec-11 | 3 | | | | | | | 0 | | | | | | | 0 | | | | | | |
| Jan-20 | | | | 37 | 0 | | | | | | | 0 | 0 | | | | | 0 | 0 | | |

### A.2.4 Duration of Powerful Flow Measured by ADCP

Flow arrival times at the 6 ADCP moorings and SIN were used to measure transit velocities, which are average front velocities across distances between 0.5 km and 15 km (Fig. A.3a). Arrival times are based on 30 second (or 10 second for SIN) recording interval of the ADCPs, corrected for clock drift. Distances between sensors were measured along the canyon thalweg, based on a 15 m bathymetric grid. It is assumed that flows principally followed the thalweg (Fig. A.2a).

### A.2.5 Canyon Topography

Seafloor gradient is determined along a midline through the canyon thalweg (Fig. A.3b), using an average of 10 grid-cells, each of which has a length of 15 m. Canyon width is defined using the area of active bedforms (Paull et al., 2018), and measured every 200 m down the canyon. The canyon floor is delimited by steep canyon walls with slopes of $\sim$10 to 45°.

### A.2.6 Grain Size

Sediment traps were mounted at 10 meters above the seafloor on moorings. They were tilted and brought closer to the bed by the initial powerful stages of some flows. Grain sizes in sediment traps from the upper canyon (MS1, MS2, and MS3) were used for most events. For the September 1st event, MS3 and MS4 are used, as the event ignited farther down in the canyon. Laser particle grain size measurements were taken every 1-5 cm from traps. Discs released automatically into the traps at 8-day intervals provided time markers.

## A.3 Results

The entire sensor array in Monterey Canyon recorded 15 flows (Paull et al., 2018). Here we consider only the 13 flows measured using the moored ADCP array (Fig. A.2b), as we rely on ADCP measurements. Twelve of these 13 ADCP-measured flows started in the upper canyon at water depths of $< 300$ m. Flows were measured first by ADCPs at Mooring Station (MS) 1, located 6.7 km from the canyon head (Figs. A.2a and A.3a). Many flows then rapidly dissipated, including six flows that died out entirely before MS2, which is 9 km downstream of MS1 (Fig. A.3a). Of the seven flows measured at multiple moorings, three flows terminated within the sensor array. One event occurred only in the mid-canyon, between MS4 and MS5. Three further flows swept through the entire sensor array, running out for over 50 km from the canyon head, although

they had very different velocities and durations at the final sensor site (Figs. A.3a and 4). Most (12 of 13) flows were initiated during the winter months (Fig. A.2b), during which time storm waves are most pronounced and are thought to be important for flow initiation (Paull et al., 2018). Only one event occurred in the summer months. This event on September 1st 2016 did not coincide with large wave heights, a river flood, or earthquake; suggesting another, as yet poorly understood, trigger (Paull et al., 2018).

Transit velocities are available for the seven flows that reached multiple moorings (Fig. A.3a). The transit velocities between the first two moorings (MS1 and MS2) have broadly similar values of between 4 and 6 $ms^{-1}$. The runout length of these flows varied greatly, with large increases in runout length correlating with only slightly faster initial frontal velocity (Fig. A.3a). However, one event recorded during the CCE experiment showed a different trend, and it was the only event occurring outside the winter months, on September 1st (Fig. A.1b). This event started with an initial comparatively low initial frontal velocity between MS1 and MS2 of $\sim$4 $ms^{-1}$, identical to the frontal velocity of the November 24th event (Fig. A.2c; Paull et al., 2018). However, the November 24th event failed to reach MS3; whilst the September 1st event accelerated between MS3 and MS5, and reached the end of the instrument array (Fig. A.3a).

The maximum ADCP velocities measured within flows occurred within the first 10 minutes of the flow front arrival. These internal velocities show a broadly similar pattern to the transit velocities (Fig. A.3a). Flows with slower maximum ADCP-measured velocities at the first mooring tended to die out abruptly in the upper canyon, whilst events with faster ADCP-measured velocities ran out for much longer distances (Fig. A.3a). Note that ADCP measurements define six shorter runout events that are only recorded at one mooring, and thus lack transit velocity data.

Flow behaviour is only partly captured by transit and maximum ADCP measured velocities. For example, modest increases in transit velocity are often associated with more prolonged periods of powerful flow (Fig. A.4; Table A.1). As a powerful flow is more efficient in entraining substrate, the duration of powerful flow is important for ignition or autosuspension. Flows tend to stretch, as the frontal part of the flow runs ahead from the slower moving body and tail (Fig. A.4; Azpiroz-Zabala et al., 2017). Overall, long runout events occurring in winter tended to significantly stretch, such that they extended for almost the entire length of the instrument array. Shorter winter events, based on data from the shorter winter event on November 24th, are initially $\sim$10 km in length as the event arrives at MS2, but die out in the upper-canyon. The long runout summer event was initially weak, but became much more prolonged and faster mid-canyon, as well as increasing its transit velocity; before dissipating rapidly between MS5 and MS7 (Fig. A.4). Most flows started with a flow front thickness $< 10$ m. The long run-out events in winter developed thicknesses $> 30$ m (Fig. A.4; Paull et al., 2018).

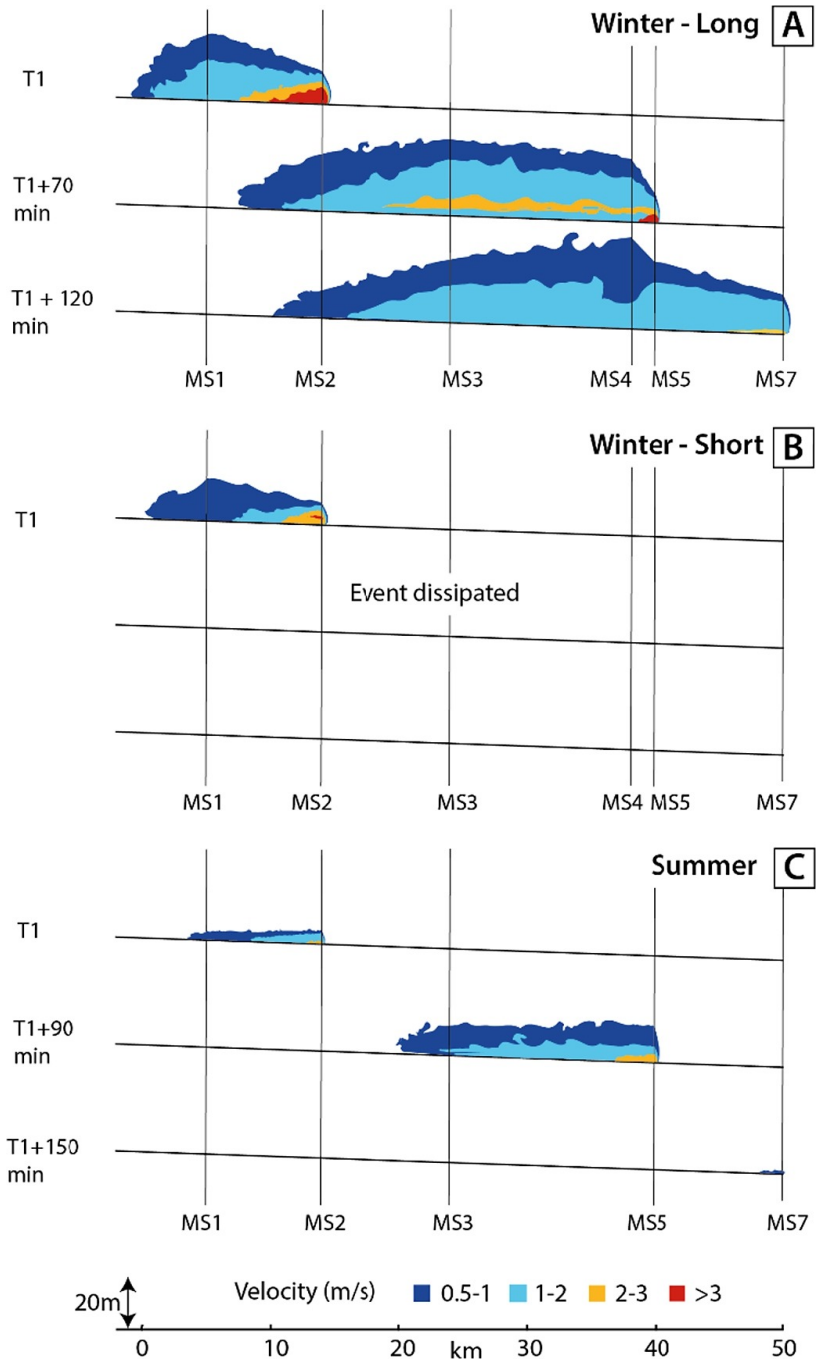


**Figure A.4:** Turbidity current structure at consecutive snap-shots in time, showing changes in flow-length, internal velocity-structure, and flow-thickness. Flow velocities between moorings are inferred, as are velocities in the lower 3-4 m of the flow (due to ADCP side-lobe interference). (A) Long run-out flow, which is initially fast, based primarily on the January 15th event. The MS1 mooring was dragged down-canyon during the January 15th event. Thus, ADCP-data from the February 3rd event are used for MS1 in T1 snapshot, and it is unknown if the 15th January flow was present at MS1 during the T1+70 min snapshot. (B) Shorter runout flow that was initially powerful, but then dissipated rapidly, based on November 24th event. This event carried an 800 kg object at $\geq$4 ms$^{-1}$, for $\sim$1 km in the upper canyon (Paull et al., 2018). (C) Example of an initially-weak turbidity current on September 1st, which then accelerated markedly in the mid-canyon, and dissipated rapidly between MS5 and MS7. This is the only event that occurred during summer months (Fig. A.2b).

## A.4 Discussion

### A.4.1 Is there a Consistent Pattern of Behaviour for Turbidity Currents?

Eleven of the twelve flows show a broadly consistent pattern of runout behaviour, which can be based on the initial transit velocity between the first two moorings, and the maximum ADCP- measured velocities at the first mooring (Fig. A.3a). Flows with the fastest initial velocities tend to run out further. However, small changes in initial transit velocities, or maximum ADCP-measured velocities, lead to much larger changes in runout distance and sub- sequent flow velocity. Runout distances are thus highly sensitive to initial velocities, leading to diverging flow behaviour (Fig. A.3a). All flows initially accelerate, and the initially fastest flows have near-uniform transit velocities for several tens of kilometres and can stretch up to 35 km in length (Fig. A.4). Flows with only mum ADCP-measured velocities, die out mid-canyon. The six slow-fractionally slower ($\sim$0.5 ms$^{-1}$) initial transit velocities, or maximum ADCP-measured velocities, die out mid-canyon. The six slowest moving flows at MS1 terminate rapidly before reaching MS2 (Fig. A.3a). These flows that die out in the upper or mid-canyon are initially powerful, and can sometimes carry heavy (800 kg) objects, or move moorings down-canyon, at velocities of $\geq$4 ms$^{-1}$, but their power does not persist for several kilometres. Only the fastest flows at the first mooring maintain their velocity for longer distances, and lengthen significantly. The single exception to this general pattern of behaviour (Figs. A.2c and A.3) occurred on September 1st 2016. This flow's transit velocity and maximum ADCP-measured velocity increased in the mid-canyon (Fig. A.3a), and the duration of powerful flow lengthened markedly (Fig. A.4).

These field data thus provide new insights into where and how flows ignite, dissipate or autosuspend. A notable observation is that the four most powerful flows at MS1 have near-uniform transit velocities for $\sim$20-35 km, from MS1 to MS3; and near-uniform maximum internal (ADCP-measured) velocities from MS1 to MS2 (Fig. A.3a). This suggests that an initial phase of acceleration (ignition) is followed by near-uniform flow velocities (autosuspension), at least near the flow front. Transit velocities are averages over substantial distances, and internal (ADCP-measured) velocities come from a few specific locations. Thus, it is possible that flow velocities show greater localized variability than depicted in Fig. A.3a. However, available field data indicate near-uniform transit velocities (autosuspension) over substantial distances.

### A.4.2 What Factors Control Turbidity Current Behaviour?

We now seek to understand what controls these patterns of flow behaviour. Twelve flows accelerated rapidly from rest within the upper 6.7 km of the canyon, reaching velocities of at least 3 to 6 ms$^{-1}$ at MS1 (Fig. A.2). These turbidity currents were most

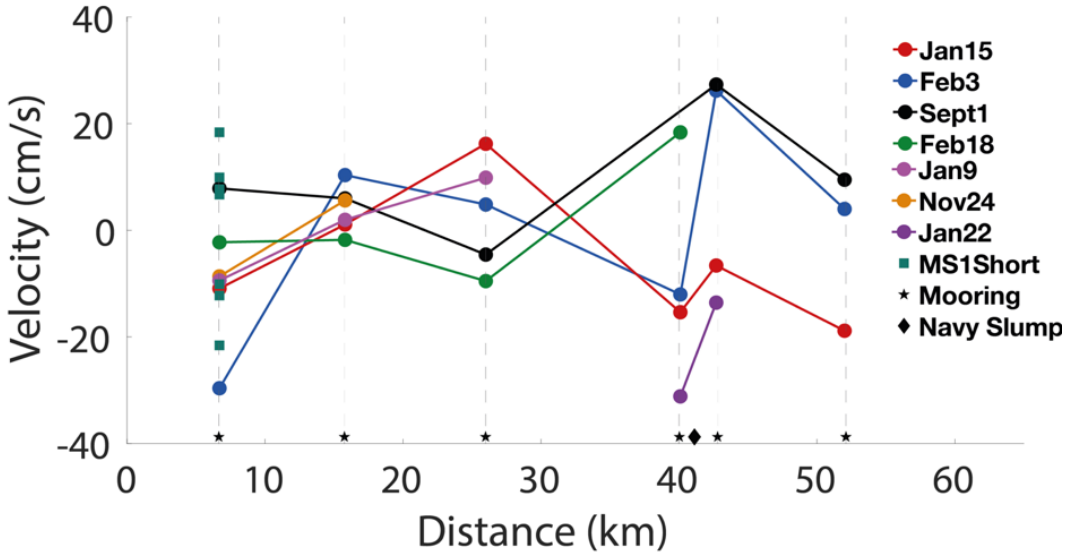


**Figure A.5:** Variation in the velocity of internal tides in Monterey Canyon during turbidity current events. Negative values show flow direction down-canyon. The tidal velocities are based on ten-minute averages of ADCP measurements immediately before flow arrival. The key for events corresponds to that in Fig A.2c, which plots changes in frontal and internal (ADCP measured) velocities for the same events. Frontal and maximum internal flow velocities are consistently much higher than these tidal velocities, suggesting that internal tides had limited effects of on flow ignition or dissipation.

likely generated by seabed failure, typically during storm events, as sediment plumes from rivers are weak or absent (Paull et al., 2018). An initial phase of acceleration will partly result from gravitational acceleration of the failed mass, but it may also indicate that flow eroded the seabed and self-accelerated (ignited). However, the relative importance of simple gravitational acceleration of an initial failure, and ignitive self-acceleration via subsequent seabed erosion, is uncertain due to a lack of repeat bathymetric surveys with high enough frequency upstream of MS1.

Beyond MS1, small ($<$0.5-1 ms$^{-1}$) increases in initial transit or maximum ADCP-measured velocities are associated with profound differences in subsequent flow behaviour (Figs. A.2c and A.3). We thus infer that initial velocities in the upper canyon determine later flow behaviour. Flows with only fractionally higher initial transit velocities, or maximum internal ADCP-measured velocities, tend to run out for much greater distances (Fig. A.3a; Table A.1). This strongly diverging flow behaviour is not due to changes in seafloor gradient or canyon width, as canyon axial channel width ($\sim$200 m) and gradient ($\sim$2°) are relatively uniform from MS1 to MS3 (Fig. A.2d, e), and all of these flows experienced similar changes in canyon slope and width. However, the axial channel widens significantly beyond MS3 (from $\sim$200 to $\sim$600 m), which may explain why most flows consistently decelerate beyond MS3 and MS4 (Fig. A.3).

The September 1st event is anomalous, as it was initially slow moving but its transit velocity then increased mid-canyon (Fig. A.3a), and the duration of powerful flow velocities increased (Fig. A.4; Table A.1). This acceleration is not related to steepening or

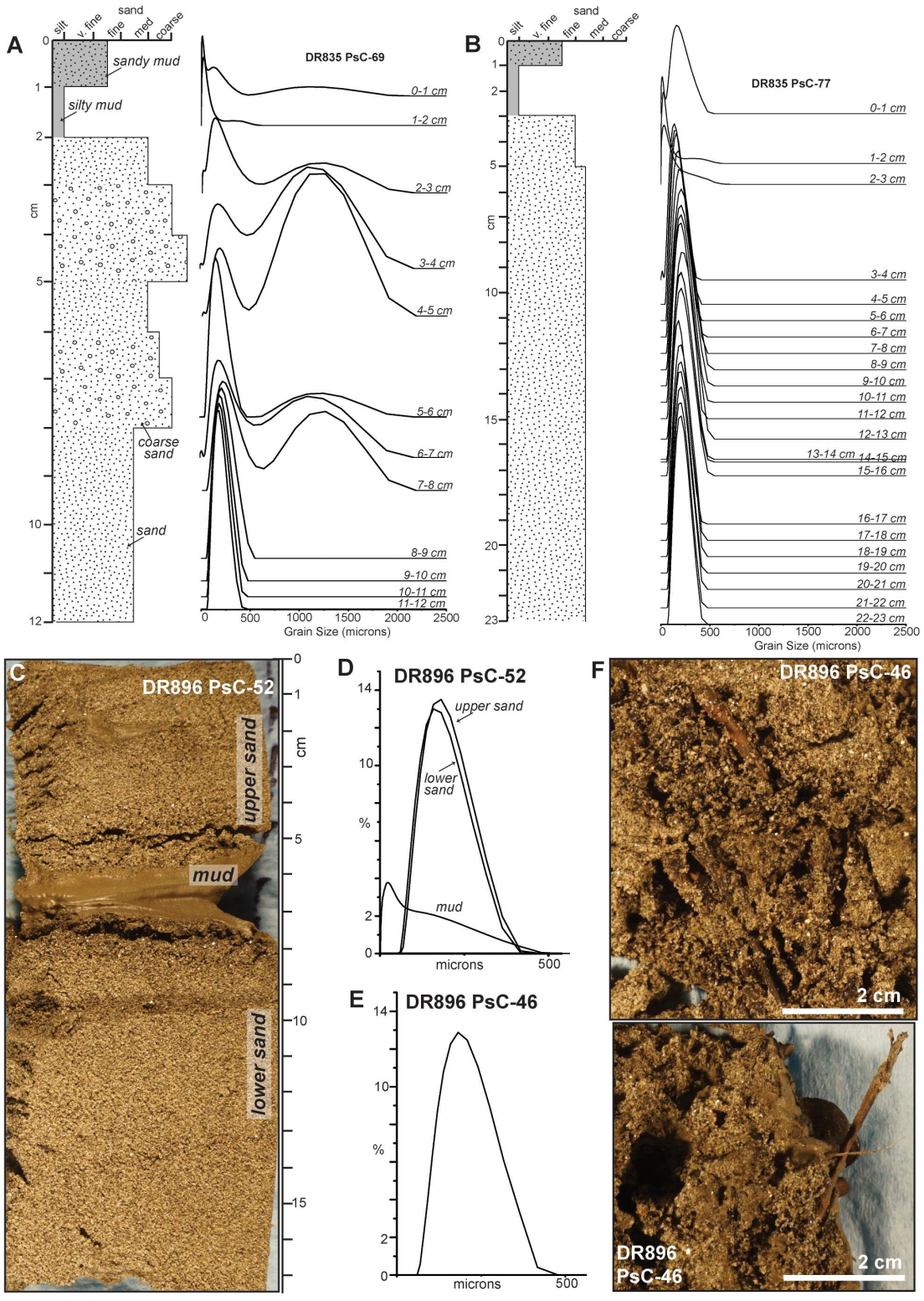


**Figure A.6:** Remotely operated vehicle (ROV) pushcore samples acquired near MS7. (A,B) Pushcores acquired in April 2016, following the January 15, 2016 event, shown as schematic log (left) and grain-size distributions (right). Stratigraphy and coarse grain size populations differ between these two closely spaced pushcores (57 m apart). (C–F) Pushcores acquired in October 2016, after the September 1, 2016 event, shown as photographs and grain-size distributions. Woody plant material in sand is highlighted in (F). From Maier et al. (2019a).

narrowing of the canyon, and cannot be explained by a 'tail wind' from internal tides (Fig. A.5). This flow was also the only event to occur in summer (Fig. A.2b). One hypothesis is that self-acceleration of the September 1st event resulted from entrainment of a surficial-mud layer, deposited during less-stormy summer months. Surficial-mud layers that are 1-12 cm thick occur in the nearby La Jolla Canyon (Paull et al., 2013), whilst mud layers in cores from MS7 in Monterey Canyon are 1-3 cm thick, with modal grain sizes of ∼50-80 µm (Fig. A.6; Maier et al., 2019a). However, it is not clear whether surficial-mud layers are better developed during summer months, as information from repeat coring during different seasons is lacking. Moreover, strong (50-80 cm $s^{-1}$) internal tides in Monterey Canyon rework canyon floor mud throughout the year (Maier et al., 2019a). An alternative hypothesis for mid-canyon ignition of the September 1st event is triggering of a local substrate failure, forming a knickpoint. Such knickpoints are observed in several places on the canyon floor, and they have been termed 'master head scarps' in past work (Paull et al., 2010). However, we also lack suitably detailed time-lapse seabed surveys from the mid- canyon to determine whether a local knickpoint failure occurred.

### A.4.3 Do Submarine Flows in other Locations Show Similar Behaviour?

Having determined that there is a consistent pattern of flow behaviour in Monterey Canyon, albeit with one exception, we now seek to understand if similar behaviour occurs elsewhere, and is thus of more general importance. There are few other locations worldwide where the transit or internal velocities of oceanic turbidity currents have been measured at more than 4 locations along the flow pathway. Indeed, we are aware of only 3 such datasets (Fig. A.7).

One of these field datasets comes from cable breaks along Gaoping Canyon, offshore Taiwan, which (unlike Monterey Canyon) is fed by a major river mouth (Fig. A.7b; Gavey et al., 2017). Seabed gradients along Gaoping Canyon (0.3-1.0°; Gavey et al., 2017) are somewhat lower than Monterey Canyon (1.6-2.3°; Fig. A.7; Paull et al., 2018). Transit velocities in Gaoping Canyon are nearly constant for ∼100 km, suggesting that the turbidity currents reach a near-uniform equilibrium state. This pattern of uniform flow front velocities (autosuspension) is thus not specific to Monterey Canyon, and it may persist over even longer distances.

A second data set comes from a turbidity current that broke submarine cables offshore from the Grand Banks, Newfoundland, in 1929 (Heezen & Ewing, 1952; Piper et al., 1988). The turbidity current resulted from extensive but thin (average 5 m) failures on the continental slope, with ∼185 $km^3$ of sediment deposited on the Sohm Abyssal Plain (Piper & Aksu, 1987; Piper et al., 1988). These failures progressively entrained seawater and evolved into debris flows, and then turbidity currents ((Piper et al., 1999). Flow was confined initially within multiple valleys for the first ∼500 km of the pathway (Hughes

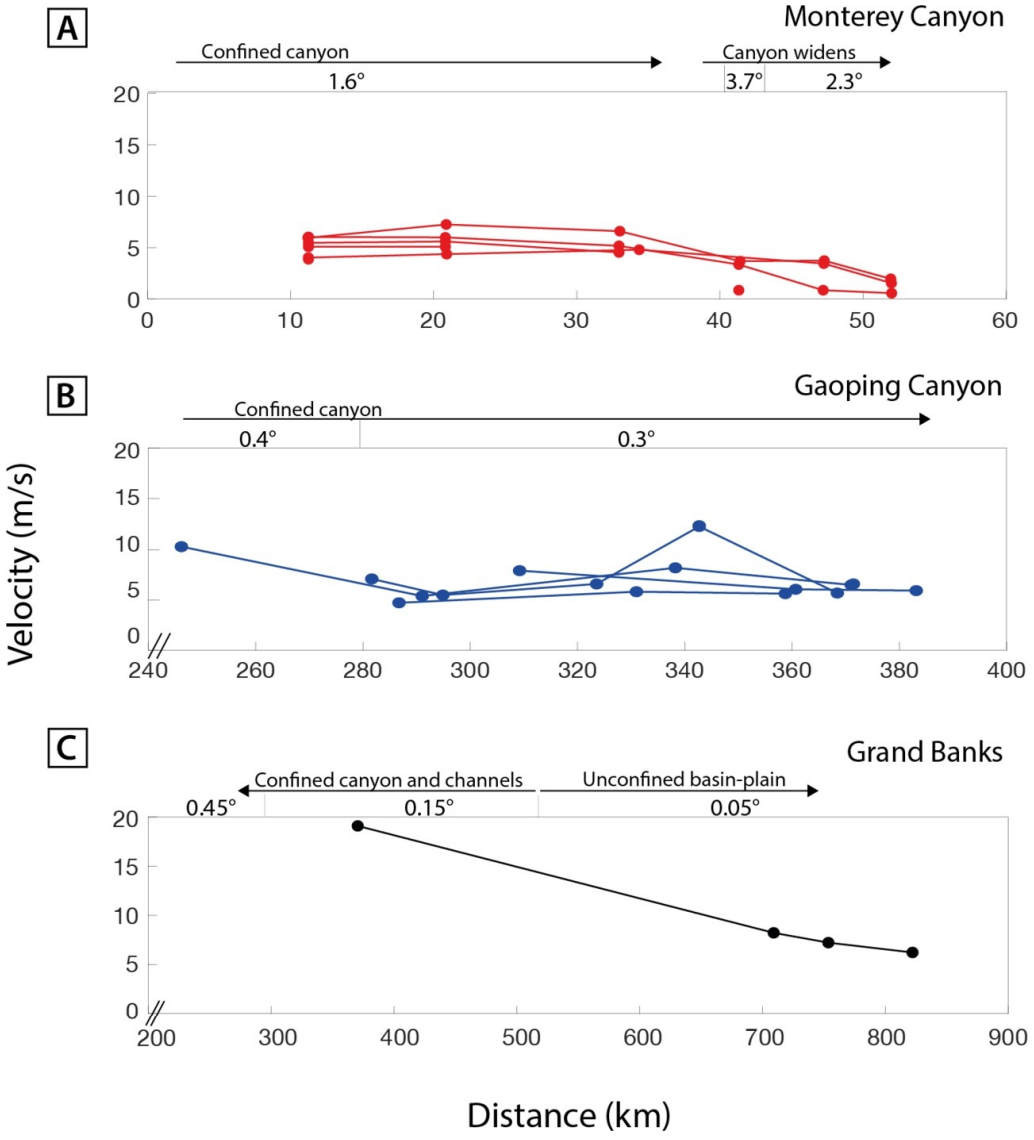


**Figure A.7:** Changes in frontal velocities of turbidity currents over distance. Variations in seabed gradient and flow confinement are also shown. (A) Frontal velocities of flows in Monterey Canyon. Fig. A.3 shows detailed changes in seabed gradient and channel floor width. (B) Frontal velocities of flows confined within Gaoping Canyon, offshore Taiwan, based on cable breaks (Gavey et al., 2017). Average seabed gradients are shown, but detailed surveys of canyon width are currently lacking. (C) Frontal velocities of the Grand Banks turbidity current in 1929, offshore Newfoundland, based on cable breaks (Heezen & Ewing, 1952; Hughes Clarke, 1988; Piper et al., 1999). Distance is from the initial earthquake epicentre, although coincident cable breaks occurred over a wider area. The initial part of this flow was confined by submarine fan-valleys, but was unconfined during its later stages, as it spread across a basin plain (Piper et al., 1999). Detailed data on the seafloor gradient over the entire length of the event are lacking, and are based on Stevenson et al. (2018) and Piper & Hundert (2002).

Clarke et al., 1990), where it reached a transit velocity of 19 $ms^{-1}$ on a gradient of $\sim$0.5° (Hughes Clarke, 1988). This initial phase of the flow eroded the seabed, and may have ignited; although this is not demonstrated by flow velocities from cable breaks. Transit velocities then decreased to 6.2 $ms^{-1}$ on gradients of $\sim$0.15 to 0.05°, as flow became poorly confined, and spread to become several hundred kilometres wide (Fig.

A.7c; Heezen & Ewing, 1952; Hughes Clarke, 1988; Hughes Clarke et al., 1990; Piper & Hundert, 2002). Its transit velocity continuously decreased with distance during these later stages, showing how reduction in confinement can control flow behaviour, leading to dissipation.

### A.4.4 Comparison of Field Data to Previous Theory of Autosuspension and Ignition

We now compare our new field observations to previous influential theory that predicts when a submarine turbidity current will autosuspend or ignite (Bagnold, 1962; Pantin, 1979; Parker, 1982; Parker et al., 1986). It is important to understand whether these unusually detailed field observations can provide a robust test of such theories.

#### A.4.4.1 Initial Energy-Balance Theory

Initial work (Bagnold, 1962; Pantin, 1979; Parker, 1982) formulated a theory for whether turbidity currents autosuspend or ignite that is based on energy losses and gains by the flow. It was assumed that movement of sediment down-slope results in loss of potential energy, whilst energy is expended by processes that keep sediment grains aloft. When energy gains equal or exceed energy losses, the flow can carry all of the sediment it suspends. Then, if the flow can also erode loose sediment from the bed, it ignites (Fig. A.1). However, if no erodible material is available, the flow auto- suspends. Alternatively, if energy losses exceed energy gains, then some of the suspended sediment will settle out, and the flow will eventually dissipate.

Equation A.1 and Fig. A.8 result from this initial energy-balance theory ((Bagnold, 1962; Pantin, 1979; Parker, 1982), as previously depicted by (Sequeiros et al., 2009). Fig. A.8 predicts the threshold frontal velocity ($u_h$) for ignition, as a function of sediment settling velocity ($w_s$) and seafloor gradient ($\beta$). The threshold constant for ignition to occur ($\varepsilon$), varies between different authors. Bagnold (1962) and Parker (1982) assume that potential energy gain must at least equal or exceed energy losses ($\varepsilon \leq 1$). In contrast, Pantin (1979) assumes that only a small fraction ($\varepsilon \leq 0.01$) of potential energy gain will be available to keep sediment aloft, with most potential energy being dissipated in other ways.

$$\frac{w_s cos\beta}{u_h sin\beta} \leq \varepsilon \begin{cases} \varepsilon = 0.01 & \text{(Pantin, 1979)} \\ \varepsilon = 1 & \text{(Parker, 1982)} \\ \varepsilon = cos\beta & \text{(Bagnold, 1962)} \end{cases} \tag{A.1}$$

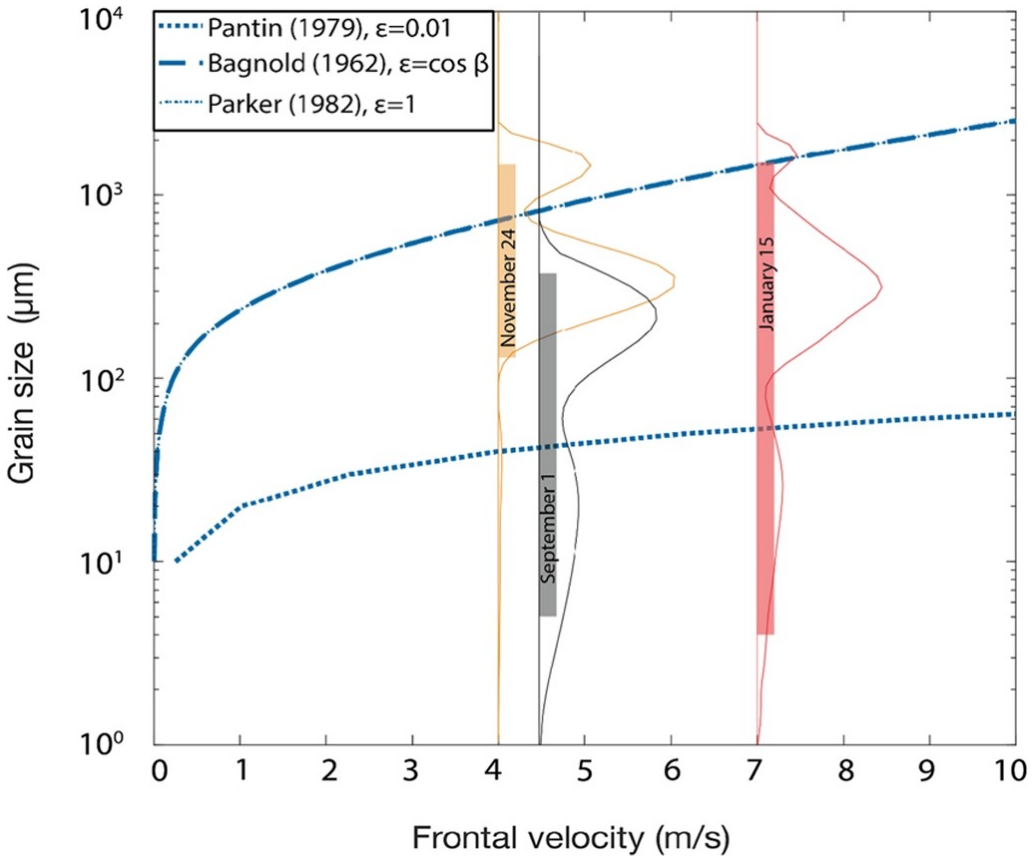


**Figure A.8:** Comparison of field measurements in Monterey Canyon to past energy-balance theory for autosuspension, following Sequeiros et al. (2009). It shows the threshold flow velocity predicted by three past theories, for a given grain-size and seabed gradient, above which flows carry all suspended sediment (i.e. autosuspend). If seabed sediment is available for erosion, the flow will also ignite. Blue lines show the different threshold constants ($\varepsilon$ in Equation A.1) used by different authors, assuming a seabed gradient of 2°. Autosuspension occurs below the lines. Note that results for the threshold constant of Bagnold (1962) coincide with those of Parker (1982) for the case of Monterey Canyon. Grain-size distributions for three events (November 24th, September, 1st, and January 15th) in Monterey Canyon, based on sediment traps located 10 m above the bed. The grain-size distributions shown here are averages for each event in sediment traps from the upper canyon where flows are assumed to ignite. The coloured boxes show the 10th percentile ($D_{10}$) and 90th percentile ($D_{90}$) of the coarsest grain-size samples in traps from each event.

As we use the flow front velocity ($u_h$), we only consider whether ignition or autosuspension occurs near the flow front. As noted by past authors (Bagnold, 1962; Pantin, 1979; Parker, 1982; Sequeiros et al., 2009), Equation A.1 is a necessary condition for ignition, but it is not a sufficient condition for ignition; indeed it is rather conservative (Parker et al., 1986). Suitable sediment must also be available for erosion and incorporation into the flow. This might not be the case, for example, if the flow was moving over hard bedrock.

Measurements from Monterey Canyon can be combined with Equation A.1 to compare observed and predicted flow velocities associated with ignition (Fig. A.8). We use a seabed gradient of 2° (Fig. A.1e; Paull et al., 2018), and sediment traps on moorings for

grainsize distributions for three separate turbidity currents. The sediment trap closest to the location of ignition in that flow is used (Fig. A.1c), together with the coarsest subsample from each flow deposit in that trap. These traps were initially suspended 10 m above the bed, but they were sometimes dragged closer to the bed during the first few minutes of flow (Paull et al., 2018). The method of Ferguson & Church (2004) is used to estimate settling velocities for individual grains, which assumes that flow is dilute. Settling velocities could become hindered at higher sediment concentrations.

Fig. A.8 shows transit (average frontal) velocities needed for ignition for the grain sizes captured by traps in the Monterey Canyon flows, for different values of $\varepsilon$ that have been proposed previously. There is reasonable agreement between our field observations with the approach of both Parker (1982), and Bagnold (1962). Where flows ignited in Monterey Canyon, grain sizes observed in sediment traps mainly lie within the field of ignition (Fig. A.8). There is poorer agreement with Pantin (1979), suggesting that potential energy losses do not need to be 100 times greater than energy losses o keep sediment aloft, and thus for ignition to occur.

#### A.4.4.2 Subsequent More Complex Turbulence Energy-Balance Theory

The simple energy-balance approach summarized by Equation (Fig. A.1; Bagnold, 1962; Pantin, 1979; Parker, 1982) sets out a necessary condition for autosuspension or ignition. However, flows that fulfil Equation A.1 need not ignite, as other conditions are also important. For example, sediment exchange with the seabed will strongly influence flow density and thus velocity (Parker et al., 1986; Traer et al., 2012), whilst entrainment of surrounding water will cause momentum to be lost (Parker et al., 1986).

Parker et al. (1986) therefore subsequently developed a more advanced and complete theory. This theory initially comprised three layer-averaged equations based on budgets of fluid (water) mass, sediment mass and momentum within the flow (Parker et al., 1986). A fourth layer-averaged equation was then based on budgets of turbulent kinetic energy within the flow, including turbulence production at the upper and lower flow boundary, dissipation of turbulence due to viscosity, and work done by turbulence against vertical density gradients (Parker et al., 1986). This approach led to a more complex criterion for ignition (equation 16 of Parker et al., 1986). This criterion involves layer-averaged sediment concentration, flow velocity and thickness, sediment settling velocity, bed shear velocity, and rates of sediment and water entrainment (Parker et al., 1986). This more advanced but complex criterion for ignition implicitly assumes that sediment is mainly supported by fluid turbulence. It would not apply to denser sediment flows in which turbulence is strongly damped, and where other processes become important for sediment support, such as support via grain-to-grain collisions, or excess pore pressure.

### A.4.5 Why Past Autosuspension and Ignition Theory is Difficult to Test

Although unprecedented in their detail, our field observations from Monterey Canyon provide a rather weak test of the initial simpler energy-balance theory (Bagnold, 1962; Pantin, 1979; Parker, 1982), and they are unable to test the more complex turbulent energy-balance (Parker et al., 1986) theory, for three key reasons.

First, both types of theory involve a single sediment settling velocity, and thus require that a representative grain size is chosen. However, turbidity currents in Monterey Canyon contain a wide range of grain sizes (Fig. A.8), as is often the case for turbidity currents elsewhere. Thus, there is an issue of which representative grain size to choose from this wide distribution (Fig. A.8). There are also major issues related to measurement of grain size in the field via sediment traps, as traps only sample grain size at a single height, and traps may be less effective at capturing finer grains than coarser grains.

Second, in the case of theory based on turbulent kinetic energy budgets (Parker et al., 1986), we lack sufficiently precise measurements of key parameters needed by this theory, most notably layer-averaged sediment concentrations, but also rates of sediment and water entrainment.

Finally, and most importantly, some key assumption that underpin past theories may not hold. For example, Parker et al. (1986) theory based on turbulent kinetic energy budgets assumes that flow is dilute, such that turbulence is always the main support mechanism. Field evidence suggests that some turbidity currents in Monterey Canyon are driven by dense near-bed layers with high ($>$10% by volume) sediment concentrations (Fig. A.8; Paull et al., 2018). These dense layers are needed to explain the fast ($\geq$4 $ms^{-1}$) movement of very heavy (up to 800 kg) objects for several kilometres (Paull et al., 2018). It is unlikely that entirely dilute flows could carry such heavy objects, at high velocities, for such distances; the heavy objects are instead entombed in a dense near-bed layer (Paull et al., 2018). Turbulence is damped strongly in such dense near-bed layers, and settling will be hindered (Winterwerp, 2006). Other sediment support mechanisms become important, such as grain collisions or excess pore pressures that partly carry the sediment load. The more advanced ignition theory (Parker et al., 1986) would thus be unable to capture the behaviour of flows in Monterey Canyon with dense near-bed layers.

### A.4.6 New Travelling Wave Model

We now outline a new conceptual model for how initially fast-moving turbidity currents operate in confined settings, underlain by loose sand, based on our field observations. Following Paull et al. (2018), this model includes dense near-bed layers that

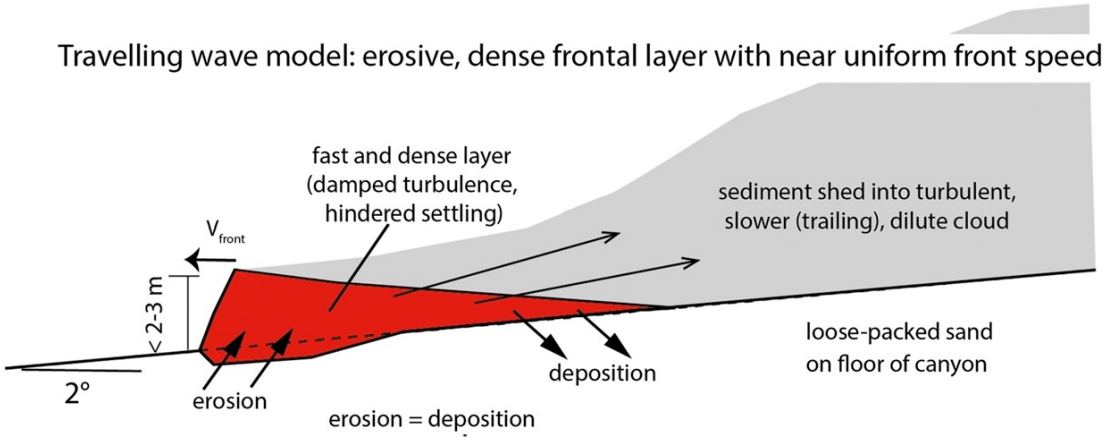


**Figure A.9:** New travelling wave model for turbidity current behaviour in loose-sand submarine canyons, in which flows contain a fast and dense near-bed layer at their front, as proposed by Paull et al. (2018). Erosion at the front of this dense near-bed layer is balanced by sediment deposition from its rear, leading to uniform transit velocity and autosuspension. Sediment is shed backwards to form a trailing sediment cloud that is dilute and fully turbulent, which lengthens over time.

drive the flow, in which turbulence is not the main support mechanism. The model thus better fits detailed field observations from Monterey Canyon. A new model is needed because past theory for ignition and autosuspension (Parker et al., 1986) was not formulated to include dense near-bed layers. The new model differs from past work (e.g Paull et al., 2018), as it explains how flows that initially ignite may then autosuspend, as they reach a uniform transit velocity.

We propose that during initial ignition, and the following near-equilibrium (autosuspension) phase, a fast and dense near-bed layer exists at the flow front, which drives the overall event, similar to Fig. A.9 ((Winterwerp, 2006). This dense near-bed layer near the flow front maintains an approximately uniform frontal velocity, as erosion of the bed near its front, is balanced by deposition at its rear (Fig. A.9). Thus, although the dense layer is locally either erosive or depositional at a single location, erosion and deposition are balanced over the whole of the layer, such that the dense layer velocity is near-uniform. This leads to autosuspension (Fig. A.9). We envisage that sediment concentrations in the dense layer (10-30%) are those attributed by Winterwerp et al. (1992) to hyperconcentrated flow, which is capable of forming the crescentic shaped bedforms seen along the floor of Monterey Canyon (Winterwerp et al., 1992; Paull et al., 2018). It has been suggested that liquefied flows of sand could only travel for short distances (Lowe, 1976) on steep slopes (>3°) due to rapid dissipation of excess pore fluid pressures and basal sedimentation. However, addition of small fractions of cohesive mud, as seen in Monterey Canyon (Maier et al., 2019a), increase the time taken for excess pore pressure to dissipate by orders of magnitude and hinders settling (Iverson et al., 2010), thus greatly increasing runout of partly-liquefied flow. Sediment from the dense layer is shed backwards into a dilute and fully turbulent sediment cloud. This trailing

cloud increases in length (stretches) as the dense flow front runs ahead of the trailing body (Figs. A.3 and A.8; Azpiroz-Zabala et al., 2017).

We term this new model the 'travelling wave model', and it is broadly comparable to behaviour seen in laboratory experiments involving dense, dry granular avalanches (Pouliquen & Forterre, 2002; Mangeney et al., 2007). A key feature of these experiments is that the dry avalanches that are fast enough can erode their underlying substrate, in their case loose sand. These dry granular avalanche experiments show two types of behaviour (Pouliquen & Forterre, 2002; Mangeney et al., 2007). Slower moving avalanches dissipate, as they fail to erode and entrain their substrate. However, sufficiently fast moving dry granular avalanches erode, and form a travelling wave with near-uniform frontal transit velocities (Pouliquen & Forterre, 2002; Mangeney et al., 2007; Edwards & Gray, 2015). Erosion of sand from near the front of the travelling wave is balanced by deposition from its rear (Fig. A.9). The avalanche thus contains a substantial fraction of locally eroded material. The transit velocity of this travelling wave is strongly determined by the thickness of the frontal avalanche, as in the dry granular experiments (Pouliquen & Forterre, 2002; Mangeney et al., 2007). Frontal thickness determines the down-slope driving force near the front, at least for near-uniform gradients and flow densities. The flow thickness in turn depends on the depth of eroded material, and thus on rates of frontal erosion (Pouliquen & Forterre, 2002; Mangeney et al., 2007). Turbidity currents will differ in key regards from these dry granular avalanches that occur on far steeper ($> 30°$) gradients. For example, erosion of water-saturated canyon floor sediment, such as via abrupt loading and liquefaction, may allow turbidity currents to erode on much lower ($< 2°$) gradients than dry granular avalanches. Settling velocities will be much greater in air, and turbidity currents can also comprise trailing dilute suspensions. However, we draw a first-order analogy with the ability of faster moving dry granular avalanches that exceed a threshold and erode their substrate, whilst depositing from their rear, and thus maintain dense flow with near-uniform transit velocity.

This new travelling wave model also needs to account for crescent shaped bedforms that are abundant along the floor of Monterey Canyon (Paull et al., 2018), and many other sandy submarine canyons (Symons et al., 2016), which have been linked to instabilities (termed cyclic steps) in supercritical flows (Hughes Clarke, 2016). Bedforms in Monterey Canyon have amplitudes of 1 to 3 m, and wavelengths of 20 to 80 m (Paull et al., 2018). As discussed in more detail by Paull et al. (2018), tracking of extremely heavy (800 kg) objects showed that they experienced repeated vertical oscillations of 1-3 m, as they were carried down Monterey Canyon at velocities of $\sim$4 $ms^{-1}$. Bedforms were thus most likely continuously present, and must have been at least partly formed by the dense travelling wave. This is consistent with field observations and laboratory experiments showing that cyclic steps and up-slope migrating bedforms can form beneath supercritical flows with very high (20-40% volume) sediment concentrations

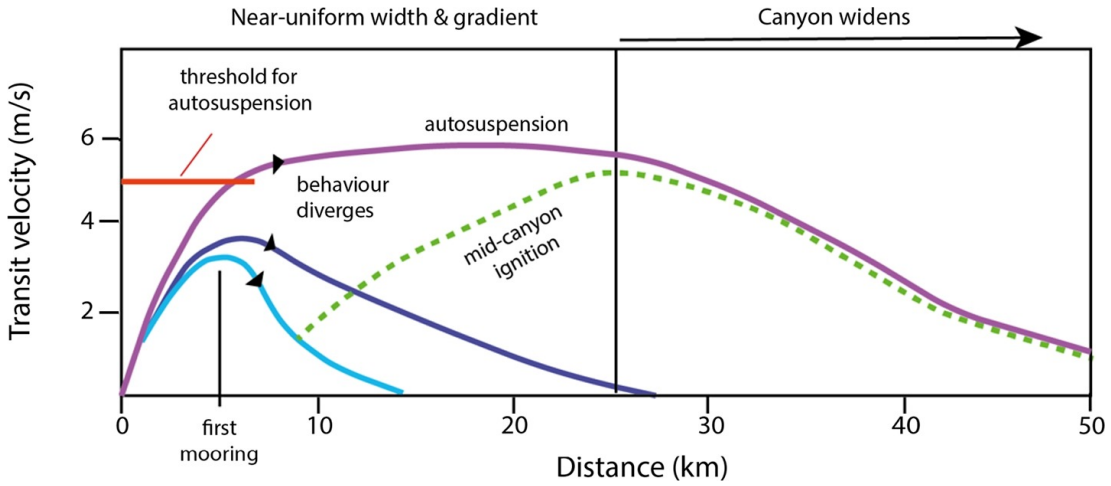


**Figure A.10:** Summarising model for turbidity current behaviour in submarine canyons underlain by loose sand. Patterns of flow behaviour, based on frontal transit velocities that are simplified from Fig. A.3a. Small increases in transit velocity at the first mooring are associated with major differences in subsequent flow velocities and runout distance, causing divergence in flow behaviour (purple, dark blue and light blue lines). However, flows can sometimes self-accelerate and ignite within the mid-canyon (green dotted line), due to changes in substrate strength and erodibility. There is a threshold initial transit velocity (red line) above which flows can autosuspend (purple line).

(Winterwerp et al., 1990, 1992) as well as dilute supercritical flows (Kostic & Parker, 2006; Covault et al., 2017).

Future work is now needed to test this new travelling wave model, such as via direct measurements of sediment concentration in turbidity currents, or by determining the importance of locally derived or far-travelled sediment in near-bed layers.

## A.5 Conclusions

Here we analyse the most detailed measurements yet from within seafloor turbidity currents, showing how their transit and maximum measured internal velocities vary with distance. Overall, we observed that small ($<$ 0.5-1 ms$^{-1}$) increases in average transit velocities are associated with large differences in subsequent runout (Fig. A.10). Fractional increases in initial velocities may lead to flows with near-uniform velocities associated with autosuspension, enabling much longer runout. Flows with only slightly lower initial velocities die out in upper or mid-canyon. Patterns of transit and internal velocities with distance thus diverge markedly (Fig. A.10).

However, one flow in Monterey Canyon is an exception to this general pattern, as it self-accelerated mid-canyon (Fig. A.10, dotted green line). It is also the only flow that occurred during less-stormy summer months. Erosion of a weak surficial-mud layer with underlying fine sand, is likely to also favour self-acceleration. Turbidity current

behaviour may therefore be highly sensitive to both initial transit velocities and substrate character.

Our observations show that initial self-acceleration (ignition) can be followed by a phase of near-uniform transit velocities (autosuspension), at least for initially faster flow events (Fig. A.10). Previous models have proposed that autosuspension may follow on from ignition, as erodible bed material runs out. But this is not the case in Monterey Canyon, as loose sand is available along the canyon floor. Instead, we propose that flows are driven by thin and dense, frontal, near-bed layers (which we call a travelling wave; Fig. A.9). Faster moving travelling waves can reach an autosuspending state, as frontal erosion balances deposition from their rear, so that near-uniform frontal flow thicknesses and thus velocities are maintained. These dense travelling waves shed a slower moving dilute sediment cloud, which lengthens as the flow runs out. But this dilute cloud does not drive the flow, and changes in its sediment concentration are thus less important. This travelling wave model itself needs further testing, including via direct measurements of near-bed sediment concentrations, but it is consistent with movement of very heavy objects at high velocity near the flow front (Paull et al., 2018).

# Bibliography

Amblas, D., Ceramicola, S., Gerber, T. P., Canals, M., Chiocci, F. L., Dowdeswell, J. A., Harris, P. T., Huvenne, V. A., Lai, S. Y., Lastras, G., et al. (2018). Submarine canyons and gullies. In *Submarine Geomorphology*, (pp. 251–272). Springer.

Amblas, D., Urgeles, R., Canals, M., Calafat, A. M., Rebesco, M., Camerlenghi, A., Estrada, F., De Batist, M., & Hughes-Clarke, J. E. (2006). Relationship between continental rise development and palaeo-ice sheet dynamics, northern antarctic peninsula pacific margin. *Quaternary Science Reviews*, *25*(9-10), 933–944.

Arjona-Camas, M., Puig, P., Palanques, A., Emelianov, M., & Durán, R. (2019). Evidence of trawling-induced resuspension events in the generation of nepheloid layers in the foix submarine canyon (nw mediterranean). *Journal of Marine Systems*, *196*, 86–96.

Aslam, T., Hall, R. A., & Dye, S. R. (2018). Internal tides in a dendritic submarine canyon. *Progress in Oceanography*, *169*, 20–32.

Ayranci, K., Lintern, D. G., Hill, P. R., & Dashtgard, S. E. (2012). Tide-supported gravity flows on the upper delta front, fraser river delta, canada. *Marine Geology*, *326*, 166–170.

Azpiroz-Zabala, M., Cartigny, M. J., Talling, P. J., Parsons, D. R., Sumner, E. J., Clare, M. A., Simmons, S. M., Cooper, C., & Pope, E. L. (2017). Newly recognized turbidity current structure can explain prolonged flushing of submarine canyons. *Science advances*, *3*(10), e1700200.

Baas, J. H., Best, J. L., Peakall, J., & Wang, M. (2009). A phase diagram for turbulent, transitional, and laminar clay suspension flows. *Journal of Sedimentary Research*, *79*(4), 162–183.

Baeye, M., & Fettweis, M. (2015). In situ observations of suspended particulate matter plumes at an offshore wind farm, southern north sea. *Geo-Marine Letters*, *35*(4), 247–255.

Bagnold, R. A. (1954). Experiments on a gravity-free dispersion of large solid spheres in a newtonian fluid under shear. *Proceedings of the Royal Society of London. Series A. Mathematical and Physical Sciences*, *225*(1160), 49–63.

Bagnold, R. A. (1962). Auto-suspension of transported sediment; turbidity currents. *Proceedings of the Royal Society of London. Series A. Mathematical and Physical Sciences*, *265*(1322), 315–319.

Bailey, L. P., Clare, M. A., Rosenberger, K. J., Cartigny, M. J., Talling, P. J., Paull, C. K., Gwiazda, R., Parsons, D. R., Simmons, S. M., Xu, J., et al. (2021). Preconditioning by sediment accumulation can produce powerful turbidity currents without major external triggers. *Earth and Planetary Science Letters*, *562*, 116845.

Baines, P. G. (1982). On internal tide generation models. *Deep Sea Research Part A. Oceanographic Research Papers*, *29*(3), 307–338.

Bamber, D. (1975). The area above the ordinal dominance graph and the area below the receiver operating characteristic graph. *Journal of mathematical psychology*, *12*(4), 387–415.

Bea, R. G., Wright, S. G., Sircar, P., & Niedoroda, A. W. (1983). Wave-induced slides in south pass block 70, mississippi delta. *Journal of Geotechnical Engineering*, *109*(4), 619–644.

Bell Jr, T. (1975). Topographically generated internal waves in the open ocean. *Journal of Geophysical Research*, *80*(3), 320–327.

Bennett, R. H. (1977). Pore-water pressure measurements: Mississippi delta submarine sediments. *Marine Georesources & Geotechnology*, *2*(1-4), 177–189.

Bennett, R. H., & Faris, J. R. (1979). Ambient and dynamic pore pressures in fine-grained submarine sediments: Mississippi delta. *Applied Ocean Research*, *1*(3), 115–123.

Bornhold, B. D., Ren, P., & Prior, D. B. (1994). High-frequency turbidity currents in british columbia fjords. *Geo-Marine Letters*, *14*(4), 238–243.

Brackenridge, R. E., Hernández-Molina, F., Stow, D., & Llave, E. (2013). A pliocene mixed contourite–turbidite system offshore the algarve margin, gulf of cadiz: seismic response, margin evolution and reservoir implications. *Marine and Petroleum Geology*, *46*, 36–50.

Camerlenghi, A., Rebesco, M., & Pudsey, C. (1997). High resolution terrigenous sedimentary record of a sediment drift on the antarctic peninsula pacific margin (initial results of the 'SEDANO' program). *The Antarctic Region: Geological Evolution and Processes*, (pp. 705–710).

Canals, M., Danovaro, R., Heussner, S., Lykousis, V., Puig, P., Trincardi, F., Calafat, A. M., de Madron, X. D., Palanques, A., & Sanchez-Vidal, A. (2009). Cascades in mediterranean submarine grand canyons. *Oceanography*, *22*(1), 26–43.

Canals, M., Puig, P., De Madron, X. D., Heussner, S., Palanques, A., & Fabres, J. (2006). Flushing submarine canyons. *Nature*, *444*(7117), 354–357.

Cantero, M. I., Cantelli, A., Pirmez, C., Balachandar, S., Mohrig, D., Hickson, T. A., Yeh, T.-h., Naruse, H., & Parker, G. (2012). Emplacement of massive turbidites linked to extinction of turbulence in turbidity currents. *Nature Geoscience*, *5*(1), 42–45.

Caplan-Auerbach, J., Dziak, R., Bohnenstiehl, D., Chadwick, W., & Lau, T.-K. (2014). Hydroacoustic investigation of submarine landslides at west mata volcano, lau basin. *Geophysical Research Letters*, *41*(16), 5927–5934.

Carson, B., Baker, E., Hickey, B., Nittrouer, C., DeMaster, D., Thorbjarnarson, K., & Snyder, G. (1986). Modern sediment dispersal and accumulation in quinault submarine canyon—a summary. *Marine Geology*, *71*(1-2), 1–13.

Carter, L., Burnett, D., Drew, S., Marle, G., Hagadorn, L., Bartlett-McNeil, D., & Irvine, N. (2009). *Submarine cables and the oceans: connecting the world*. 31. UNEP/Earthprint.

Carter, L., Gavey, R., Talling, P. J., & Liu, J. T. (2014). Insights into submarine geohazards from breaks in subsea telecommunication cables. *Oceanography*, *27*(2), 58–67.

Carter, L., Milliman, J. D., Talling, P. J., Gavey, R., & Wynn, R. B. (2012). Near-synchronous and delayed initiation of long run-out submarine sediment flows from a record-breaking river flood, offshore Taiwan. *Geophysical Research Letters*, *39*(12), 6–10.

Casagrande, J., & Watson, F. (2003). *Hydrology and Water Quality of the Carmel and Salinas Lagoons, Monterey Bay, California: 2002/2003*. Central Coast Watershed Studies Report No. WI-2003-14 to the Monterey County Water Resources Agency Board.

Cattaneo, A., Babonneau, N., Ratzov, G., Dan-Unterseh, G., Yelles, K., Bracène, R., Mercier De Lepinay, B., Boudiaf, A., & Déverchère, J. (2012). Searching for the seafloor signature of the 21 may 2003 boumerdès earthquake offshore central algeria. *Natural Hazards and Earth System Sciences*, *12*(7), 2159–2172.

Chamberlain, T. K. (1964). Mass transport of sediment in the heads of scripps submarine canyon, california. *Papers in marine geology, Shepard commemorative volume: New York, Macmillan Company*, (pp. 42–64).

Chillarige, A., Morgenstern, N., Robertson, P., & Christian, H. (1997). Seabed instability due to flow liquefaction in the fraser river delta. *Canadian Geotechnical Journal*, *34*(4), 520–533.

Christian, H., Woeller, D., Robertson, P., & Courtney, R. (1997). Site investigations to evaluate flow liquefaction slides at sand heads, fraser river delta. *Canadian Geotechnical Journal*, *34*(3), 384–397.

Clare, M., Lintern, D. G., Rosenberger, K., Clarke, J. E. H., Paull, C., Gwiazda, R., Cartigny, M. J., Talling, P. J., Perara, D., Xu, J., et al. (2020). Lessons learned from the monitoring of turbidity currents and guidance for future platform designs. *Geological Society, London, Special Publications*, *500*(1), 605–634.

Clare, M. A., Hughes Clarke, J. E., Talling, P. J., Cartigny, M. J., & Pratomo, D. G. (2016). Preconditioning and triggering of offshore slope failures and turbidity currents revealed by most detailed monitoring yet at a fjord-head delta. *Earth and Planetary Science Letters*, *450*, 208–220.

Clare, M. A., Vardy, M. E., Cartigny, M. J., Talling, P. J., Himsworth, M. D., Dix, J. K., Harris, J. M., Whitehouse, R. J., & Belal, M. (2017). Direct monitoring of active geohazards: Emerging geophysical tools for deep-water assessments. *Near Surface Geophysics*, *15*(4), 427–444.

Collins, C., Hermes, J., & Reason, C. (2014). Mesoscale activity in the comoros basin from satellite altimetry and a high-resolution ocean circulation model. *Journal of Geophysical Research: Oceans*, *119*(8), 4745–4760.

Collins, C., Hermes, J., Roman, R., & Reason, C. (2016). First dedicated hydrographic survey of the c omoros b asin. *Journal of Geophysical Research: Oceans*, *121*(2), 1291–1305.

Conway, K. W., Barrie, J. V., Picard, K., & Bornhold, B. D. (2012). Submarine channel evolution: active channels in fjords, british columbia, canada. *Geo-Marine Letters*, *32*(4), 301–312.

Cooper, C. K., Wood, J., & Andrieux, O. (2013). Turbidity current measurements in the congo canyon. In *Offshore Technology Conference*. OnePetro.

Covault, J. A., & Graham, S. A. (2010). Submarine fans at all sea-level stands: Tectono-morphologic and climatic controls on terrigenous sediment delivery to the deep sea. *Geology*, *38*(10), 939–942.

Covault, J. A., Kostic, S., Paull, C. K., Sylvester, Z., & Fildani, A. (2017). Cyclic steps and related supercritical bedforms: building blocks of deep-water depositional systems, western north america. *Marine Geology*, *393*, 4–20.

Crookshanks, S., & Gilbert, R. (2008). Continuous, diurnally fluctuating turbidity currents in kluane lake, yukon territory. *Canadian Journal of Earth Sciences*, *45*(10), 1123–1138.

Dai, M., Yin, Z., Meng, F., Liu, Q., & Cai, W.-J. (2012). Spatial distribution of riverine doc inputs to the ocean: an updated global synthesis. *Current Opinion in Environmental Sustainability*, *4*(2), 170–178.

Dalrymple, R. A., & Dean, R. G. (1991). *Water wave mechanics for engineers and scientists*, vol. 2. World Scientific Publishing Company.

Davies, J. S., Howell, K. L., Stewart, H. A., Guinan, J., & Golding, N. (2014). Defining biological assemblages (biotopes) of conservation interest in the submarine canyons of the south west approaches (offshore united kingdom) for use in marine habitat mapping. *Deep Sea Research Part II: Topical Studies in Oceanography*, *104*, 208–229.

de Bettignies, F., Dauby, P., Thomas, F., Gobet, A., Delage, L., Bohner, O., Loisel, S., & Davoult, D. (2020). Degradation dynamics and processes associated with the accumulation of laminaria hyperborea (phaeophyceae) kelp fragments: an in situ experimental approach. *Journal of Phycology*, *56*(6), 1481–1492.

de Ruijter, W. P., Ridderinkhof, H., Lutjeharms, J. R., Schouten, M. W., & Veth, C. (2002). Observations of the flow in the mozambique channel. *Geophysical Research Letters*, *29*(10), 140–1.

de Stigter, H. C., Boer, W., de Jesus Mendes, P. A., Jesus, C. C., Thomsen, L., van den Bergh, G. D., & van Weering, T. C. (2007). Recent sediment transport and deposition in the nazaré canyon, portuguese continental margin. *Marine Geology*, *246*(2-4), 144–164.

de Stigter, H. C., Jesus, C. C., Boer, W., Richter, T. O., Costa, A., & van Weering, T. C. (2011). Recent sediment transport and deposition in the lisbon–setúbal and cascais submarine canyons, portuguese continental margin. *Deep Sea Research Part II: Topical Studies in Oceanography*, *58*(23-24), 2321–2344.

Delaney, J., & Kelley, D. (2015). Next-generation science in the ocean basins: Expanding the oceanographer's toolbox utilizing submarine electro-optical sensor networks. In *Seafloor Observatories*, (pp. 465–502). Springer.

Dengler, A., Wilde, P., Noda, E., & Normark, W. (1984). Turbidity currents generated by hurricane iwa. *Geo-Marine Letters*, *4*(1), 5–11.

Domencich, T. A., & McFadden, D. (1975). Urban travel demand-a behavioral analysis. Tech. rep.

Ducea, M., House, M. A., & Kidder, S. (2003). Late cenozoic denudation and uplift rates in the santa lucia mountains, california. *Geology*, *31*(2), 139–142.

Dugan, B., & Sheahan, T. C. (2012). Offshore sediment overpressures of passive margins: Mechanisms, measurement, and models. *Reviews of Geophysics*, *50*(3), 1–20.

Dupre, W. R. (1990). Quaternary geology of the monterey bay region, california.

Edwards, A., & Gray, J. (2015). Erosion–deposition waves in shallow granular free-surface flows. *Journal of Fluid Mechanics*, *762*, 35–67.

Eggenhuisen, J. T., Cartigny, M. J., & de Leeuw, J. (2017). Physical theory for near-bed turbulent particle suspension capacity. *Earth Surface Dynamics*, *5*(2), 269–281.

Eidam, E., Ogston, A., & Nittrouer, C. (2019). Formation and removal of a coastal flood deposit. *Journal of Geophysical Research: Oceans*, *124*(2), 1045–1062.

Eidam, E., Ogston, A., Nittrouer, C., & Warrick, J. (2016). Tidally dominated sediment dispersal offshore of a small mountainous river: Elwha river, washington state. *Continental Shelf Research*, *116*, 136–148.

Eittreim, S. L., Xu, J., Noble, M., & Edwards, B. D. (2002). Towards a sediment budget for the santa cruz shelf. *Marine Geology*, *181*(1-3), 235–248.

Farnsworth, K. L., & Warrick, J. A. (2007). Sources, dispersal, and fate of fine sediment supplied to coastal california. Tech. rep., US Geological Survey.

Farrow, G. E., Syvitski, J. P., & Tunnicliffe, V. (1983). Suspended particulate loading on the macrobenthos in a highly turbid fjord: Knight inlet, british columbia. *Canadian Journal of Fisheries and Aquatic Sciences*, *40*(S1), s273–s288.

Faugères, J.-C., & Stow, D. (2008). Contourite drifts: nature, evolution and controls. *Developments in sedimentology*, *60*, 257–288.

Felix, M., & Peakall, J. (2006). Transformation of debris flows into turbidity currents: mechanisms inferred from laboratory experiments. *Sedimentology*, *53*(1), 107–123.

Ferguson, R., & Church, M. (2004). A simple universal equation for grain settling velocity. *Journal of sedimentary Research*, *74*(6), 933–937.

Fildani, A., & Normark, W. R. (2004). Late quaternary evolution of channel and lobe complexes of monterey fan. *Marine Geology*, *206*(1-4), 199–223.

Fildani, A., Normark, W. R., Kostic, S., & Parker, G. (2006). Channel formation by flow stripping: Large-scale scour features along the monterey east channel and their relation to sediment waves. *Sedimentology*, *53*(6), 1265–1287.

Fleckenstein, J. H., Niswonger, R. G., & Fogg, G. E. (2006). River-aquifer interactions, geologic heterogeneity, and low-flow management. *Groundwater*, *44*(6), 837–852.

Flemings, P., Long, H., Dugan, B., Germaine, J., John, C., Behrmann, J., Sawyer, D., Franke, C., et al. (2008). Pore pressure penetrometers document high overpressure near the seafloor where multiple submarine landslides have occured on the continental slope, offshore louisiana, gulf of mexico. *Earth and Planetary Science Letters*, *269*(3-4), 309–325.

Fonnesu, M., Palermo, D., Galbiati, M., Marchesini, M., Bonamini, E., & Bendias, D. (2020). A new world-class deep-water play-type, deposited by the syndepositional interaction of turbidity flows and bottom currents: The giant eocene coral field in northern mozambique. *Marine and Petroleum Geology*, *111*, 179–201.

Fox, J. (1997). *Applied regression analysis, linear models, and related methods.*. Sage Publications, Inc.

Franke, D., Jokat, W., Ladage, S., Stollhofen, H., Klimke, J., Lutz, R., Mahanjane, E. S., Ehrhardt, A., & Schreckenberger, B. (2015). The offshore east african rift system: Structural framework at the toe of a juvenile rift. *Tectonics*, *34*(10), 2086–2104.

FUGRO (2017). Integrated Report, Rev.3, Document Number 440200BRRS01016. Tech. rep.

Fuhrmann, A., Kane, I., Clare, M., Ferguson, R., Schomacker, E., Bonamini, E., & Contreras, F. (2020). Hybrid turbidite-drift channel complexes: An integrated multiscale model. *Geology*, *48*(6), 562–568.

Fuhrmann, A., Kane, I. A., Schomacker, E., Clare, M. A., & Pontén, A. (2021). Bottom current modification of turbidite lobe complexes. *Frontiers in Earth Science*, (p. 1152).

Gales, J. A., Talling, P. J., Cartigny, M. J., Hughes Clarke, J., Lintern, G., Stacey, C., & Clare, M. A. (2019). What controls submarine channel development and the morphology of deltas entering deep-water fjords? *Earth Surface Processes and Landforms*, *44*(2), 535–551.

Galy, V., France-Lanord, C., Beyssac, O., Faure, P., Kudrass, H., & Palhol, F. (2007). Efficient organic carbon burial in the Bengal fan sustained by the Himalayan erosional system. *Nature*, *450*(7168), 407–410.

Garfield, N., Rago, T. A., Schnebele, K. J., & Collins, C. A. (1994). Evidence of a turbidity current in monterey submarine canyon associated with the 1989 loma prieta earthquake. *Continental Shelf Research*, *14*(6), 673–686.

Gatter, R., Clare, M., Kuhlmann, J., & Huhn, K. (2021). Characterisation of weak layers, physical controls on their global distribution and their role in submarine landslide formation. *Earth-Science Reviews*, (p. 103845).

Gavey, R., Carter, L., Liu, J. T., Talling, P. J., Hsu, R., Pope, E., & Evans, G. (2017). Frequent sediment density flows during 2006 to 2015, triggered by competing

seismic and weather events: Observations from subsea cable breaks off southern Taiwan. *Marine Geology*, *384*, 147–158.

Giesbrecht, I., Tank, S., Del Bel Belluz, J., & Jackson, J. (2021). Sustained impact of a glacial lake outburst flood on winter turbidity regimes across the land-ocean aquatic continuum. In *EGU General Assembly Conference Abstracts*, (pp. EGU21–16594).

Goldfinger, C. (2011). Submarine Paleoseismology Based on Turbidite Records. *Annual Review of Marine Science*, *3*(1), 35–66.

Gordon, R., & Marshall, N. (1976). Submarine canyons: Internal wave traps? *Geophysical Research Letters*, *3*(10), 622–624.

Gray, A. B., Pasternack, G. B., Watson, E. B., Warrick, J. A., & Goñi, M. A. (2015). Effects of antecedent hydrologic conditions, time dependence, and climate cycles on the suspended sediment load of the salinas river, california. *Journal of Hydrology*, *525*, 632–649.

Greene, H., Maher, N., & Paull, C. (2002). Physiography of the monterey bay national marine sanctuary and implications about continental margin development. *Marine Geology*, *181*(1-3), 55–82.

Greene, H. G. (1990). Regional tectonics and structural evolution of the monterey bay region, central california.

Greene, H. G., & Hicks, K. R. (1990). Ascension–monterey canyon system: history and development.

Griffiths, G., & Flatt, D. (1987). A self-contained acoustic doppler current profiler—design and operation. In *Fifth International Conference on Electronics for Ocean Technology*, (pp. 41–47).

Grützner, J., Hillenbrand, C.-D., & Rebesco, M. (2005). Terrigenous flux and biogenic silica deposition at the antarctic continental rise during the late miocene to early pliocene: implications for ice sheet stability and sea ice coverage. *Global and Planetary Change*, *45*(1-3), 131–149.

Grützner, J., Rebesco, M., Cooper, A. K., Forsberg, C. F., Kryc, K. A., & Wefer, G. (2003). Evidence for orbitally controlled size variations of the east antarctic ice sheet during the late miocene. *Geology*, *31*(9), 777–780.

Guiastrennec-Faugas, L., Gillet, H., Jacinto, R. S., Dennielou, B., Hanquiez, V., Schmidt, S., Simplet, L., & Rousset, A. (2020). Upstream migrating knickpoints and related sedimentary processes in a submarine canyon from a rare 20-year morphobathymetric time-lapse (capbreton submarine canyon, bay of biscay, france). *Marine Geology*, *423*, 106143.

Guiastrennec-Faugas, L., Gillet, H., Silva Jacinto, R., Dennielou, B., Tkaczuk, G., Simplet, L., & Sabine, S. (2019). Time-laspe morphobathymetry and interface cores faced with 490 days adcp measurements in an active canyon (capbreton canyon, bay of biscay). In *AGU Fall Meeting Abstracts*, vol. 2019, (pp. OS31A–03).

Ha, H., Maa, J.-Y., Park, K., & Kim, Y. (2011). Estimation of high-resolution sediment concentration profiles in bottom boundary layer using pulse-coherent acoustic doppler current profilers. *Marine Geology*, *279*(1-4), 199–209.

Hage, S., Cartigny, M. J., Sumner, E. J., Clare, M. A., Hughes Clarke, J. E., Talling, P. J., Lintern, D. G., Simmons, S. M., Silva Jacinto, R., Vellinga, A. J., Allin, J. R., Azpiroz-Zabala, M., Gales, J. A., Hizzett, J. L., Hunt, J. E., Mozzato, A., Parsons, D. R., Pope, E. L., Stacey, C. D., Symons, W. O., Vardy, M. E., & Watts, C. (2019). Direct Monitoring Reveals Initiation of Turbidity Currents From Extremely Dilute River Plumes. *Geophysical Research Letters*, (pp. 310–320).

Hage, S., Galy, V., Cartigny, M., Acikalin, S., Clare, M., Gröcke, D., Hilton, R., Hunt, J., Lintern, D., McGhee, C., et al. (2020). Efficient preservation of young terrestrial organic carbon in sandy turbidity-current deposits. *Geology*, *48*(9), 882–887.

Hall, R. A., Alford, M. H., Carter, G. S., Gregg, M. C., Lien, R.-C., Wain, D. J., & Zhao, Z. (2014). Transition from partly standing to progressive internal tides in monterey submarine canyon. *Deep Sea Research Part II: Topical Studies in Oceanography*, *104*, 164–173.

Hall, R. A., Aslam, T., & Huvenne, V. A. (2017). Partly standing internal tides in a dendritic submarine canyon observed by an ocean glider. *Deep Sea Research Part I: Oceanographic Research Papers*, *126*, 73–84.

Hall, R. A., & Carter, G. S. (2011). Internal tides in monterey submarine canyon. *Journal of Physical Oceanography*, *41*(1), 186–204.

Hanley, J. A., & McNeil, B. J. (1982). The meaning and use of the area under a receiver operating characteristic (roc) curve. *Radiology*, *143*(1), 29–36.

Harris, P. T. (2012). 6 - seafloor geomorphology—coast, shelf, and abyss. In P. T. Harris, & E. K. Baker (Eds.) *Seafloor Geomorphology as Benthic Habitat*, (pp. 109–155). London: Elsevier.

Harris, P. T., & Whiteway, T. (2011). Global distribution of large submarine canyons: Geomorphic differences between active and passive continental margins. *Marine Geology*, *285*(1-4), 69–86.

Harrold, C., Light, K., & Lisin, S. (1998). Organic enrichment of submarine-canyon and continental-shelf benthic communities by macroalgal drift imported from nearshore kelp forests. *Limnology and Oceanography*, *43*(4), 669–678.

Hay, A. E. (1987). Turbidity currents and submarine channel formation in rupert inlet, british columbia: 1. surge observations. *Journal of Geophysical Research: Oceans*, *92*(C3), 2875–2881.

Heerema, C. (2021). *Evolution of Turbidity Currents: New insights from direct field measurements*. Ph.D. thesis, Durham University.

Heerema, C. J., Talling, P. J., Cartigny, M. J., Paull, C. K., Bailey, L., Simmons, S. M., Parsons, D. R., Clare, M. A., Gwiazda, R., Lundsten, E., et al. (2020). What determines the downstream evolution of turbidity currents? *Earth and Planetary Science Letters*, *532*, 116023.

Heezen, B. C., Ewing, M., & Johnson, G. L. (1966). The gulf of corinth floor. In *Deep Sea Research and Oceanographic Abstracts*, vol. 13, (pp. 381–411). Elsevier.

Heezen, B. C., & Ewing, W. M. (1952). Turbidity currents and submarine slumps, and the 1929 Grand Banks (Newfoundland) earthquake. *American Journal of Science*, *250*(12), 849–873.

Heezen, B. C., Johnson, G. L., & Hollister, C. D. (1969). The northwest atlantic mid-ocean canyon. *Canadian Journal of Earth Sciences*, *6*(6), 1441–1453.

Heezen, B. C., Menzies, R., Schneider, E., Ewing, W. M., & Granelli, N. C. (1964). Congo Submarine Canyon. *AAPG Bulletin*, *48*(7), 1126–1149.

Heijnen, M. S., Clare, M. A., Cartigny, M. J., Talling, P. J., Hage, S., Lintern, D. G., Stacey, C., Parsons, D. R., Simmons, S. M., Chen, Y., et al. (2020). Rapidly-migrating and internally-generated knickpoints can control submarine channel evolution. *Nature communications*, *11*(1), 1–15.

Hernández-Molina, F. J., Larter, R. D., & Maldonado, A. (2017). Neogene to quaternary stratigraphic evolution of the antarctic peninsula, pacific margin offshore of adelaide island: transitions from a non-glacial, through glacially-influenced to a fully glacial state. *Global and Planetary Change*, *156*, 80–111.

Hessler, A. M., & Fildani, A. (2019). Deep-sea fans: tapping into earth's changing landscapes. *Journal of Sedimentary Research*, *89*(11), 1171–1179.

Hickin, E. J. (1989). Contemporary squamish river sediment flux to howe sound, british columbia. *Canadian Journal of Earth Sciences*, *26*(10), 1953–1963.

Hill, D., Jones, S., & Prandle, D. (2003). Derivation of sediment resuspension rates from acoustic backscatter time-series in tidal waters. *Continental Shelf Research*, *23*(1), 19–40.

Hill, P. R., & Lintern, D. G. (2021). Sedimentary processes at the mouth of a tidally-influenced delta: New insights from submarine observatory measurements, fraser delta, canada. *Sedimentology*, *68*(6), 2649–2670.

Hizzett, J. L., Hughes Clarke, J. E., Sumner, E. J., Cartigny, M., Talling, P., & Clare, M. (2018). Which triggers produce the most erosive, frequent, and longest runout turbidity currents on deltas? *Geophysical Research Letters*, *45*(2), 855–863.

Holland, G., & Bruyère, C. L. (2014). Recent intense hurricane response to global climate change. *Climate Dynamics*, *42*(3), 617–627.

Holland, R. (1976). Landforms of british columbia: a physiographic outline. *British Columbia Dept Mines Petrol Res Bull*.

Hosmer Jr, D. W., Lemeshow, S., & Sturdivant, R. X. (2013). *Applied logistic regression*, vol. 398. John Wiley & Sons.

Hotchkiss, F. S., & Wunsch, C. (1982). Internal waves in hudson canyon with possible geological implications. *Deep Sea Research Part A. Oceanographic Research Papers*, *29*(4), 415–442.

Howarth, J. D., Orpin, A. R., Kaneko, Y., Strachan, L. J., Nodder, S. D., Mountjoy, J. J., Barnes, P. M., Bostock, H. C., Holden, C., Jones, K., et al. (2021). Calibrating the marine turbidite palaeoseismometer using the 2016 kaikōura earthquake. *Nature Geoscience*, *14*(3), 161–167.

Hsu, S.-K., Kuo, J., Lo, C.-L., Tsai, C.-H., Doo, W.-B., Ku, C.-Y., & Sibuet, J.-C. (2008). Turbidity Currents, Submarine Landslides and the 2006 Pingtung Earthquake off SW Taiwan. *Terrestrial, Atmospheric and Oceanic Sciences*, *19*(6), 767.

Huang, Z., Nichol, S. L., Harris, P. T., & Caley, M. J. (2014). Classification of submarine canyons of the australian continental margin. *Marine Geology*, *357*, 362–383.

Hughes Clarke, J., Brucker, S., Muggah, J., Hamilton, T., Cartwright, D., Church, I., & Kuus, P. (2012). Temporal progression and spatial extent of mass wasting events on the squamish prodelta slope. In *Landslides and engineered slopes: Protecting society through improved understanding*, (pp. 1091–1096). Citeseer.

Hughes Clarke, J. E. (1988). *The geological record of the 1929" Grand Banks" earthquake and its relevance to deep-sea clastic sedimentation*. National Library of Canada.

Hughes Clarke, J. E. (2016). First wide-angle view of channelized turbidity currents links migrating cyclic steps to flow characteristics. *Nature communications*, *7*(1), 1–13.

Hughes Clarke, J. E., Marques, C. R. V., & Pratomo, D. (2014). Imaging active mass-wasting and sediment flows on a fjord delta, squamish, british columbia. In S. Krastel, J.-H. Behrmann, D. Völker, M. Stipp, C. Berndt, R. Urgeles, J. Chaytor, K. Huhn, M. Strasser, & C. B. Harbitz (Eds.) *Submarine Mass Movements and Their Consequences: 6th International Symposium*, (pp. 249–260). Cham: Springer International Publishing.

Hughes Clarke, J. E., Shor, A. N., Piper, D. J., & Mayer, L. A. (1990). Large-scale current-induced erosion and deposition in the path of the 1929 grand banks turbidity current. *Sedimentology*, *37*(4), 613–629.

Huvenne, V. A., Tyler, P. A., Masson, D. G., Fisher, E. H., Hauton, C., Huehnerbach, V., Le Bas, T. P., & Wolff, G. A. (2011). A picture on the wall: innovative mapping reveals cold-water coral refuge in submarine canyon. *PloS one*, *6*(12), e28755.

Iatrou, M., Ferentinos, G., Papatheodorou, G., Piper, D. J., & Tripsanas, E. (2007). Anthropogenic turbidity current deposits in a seismically active graben, the gulf of corinth, greece: a useful tool for studying turbidity current transport processes. In *Submarine Mass Movements and Their Consequences*, (pp. 149–157). Springer.

Ikehara, K., Irino, T., Usami, K., Jenkins, R., Omura, A., & Ashi, J. (2014). Possible submarine tsunami deposits on the outer shelf of sendai bay, japan resulting from the 2011 earthquake and tsunami off the pacific coast of tohoku. *Marine Geology*, *358*, 120–127.

Inman, D. L., Nordstrom, C. E., & Flick, R. E. (1976). Currents in Submarine Canyons: An Air-Sea-Land Interaction. *Annual Review of Fluid Mechanics*, *8*(1), 275–310.

Ivanov, V., Shapiro, G., Huthnance, J., Aleynik, D., & Golovin, P. (2004). Cascades of dense water around the world ocean. *Progress in oceanography*, *60*(1), 47–98.

Iverson, R. M. (2005). Debris-flow mechanics. In *Debris-flow hazards and related phenomena*, (pp. 105–134). Springer.

Iverson, R. M., Logan, M., LaHusen, R. G., & Berti, M. (2010). The perfect debris flow? aggregated results from 28 large-scale experiments. *Journal of Geophysical Research: Earth Surface*, *115*(F3).

Johnson, K. S., Paull, C. K., Barry, J. P., & Chavez, F. P. (2001). A decadal record of underflows from a coastal river into the deep sea. *Geology*, *29*(11), 1019–1022.

Kane, I. A., & Clare, M. A. (2019). Dispersion, accumulation, and the ultimate fate of microplastics in deep-marine environments: A review and future directions. *Frontiers in earth science*, *7*, 80.

Kane, I. A., Clare, M. A., Miramontes, E., Wogelius, R., Rothwell, J. J., Garreau, P., & Pohl, F. (2020). Seafloor microplastic hotspots controlled by deep-sea circulation. *Science*, *368*(6495), 1140–1145.

Kawagucci, S., Miwa, T., Lindsay, D. J., Ogura, E., Yamamoto, H., Nishibayashi, K., Yokooka, H., Nishi, S., Takahashi, A., & Lee, S. (2020). Deep-sea water displacement from a turbidity current induced by the super typhoon hagibis. *PeerJ*, *8*, e10429.

Khripounoff, A., Crassous, P., Bue, N. L., Dennielou, B., & Jacinto, R. S. (2012). Different types of sediment gravity flows detected in the var submarine canyon (northwestern mediterranean sea). *Progress in Oceanography*, *106*, 138–153.

Khripounoff, A., Vangriesheim, A., Babonneau, N., Crassous, P., Dennielou, B., & Savoye, B. (2003). Direct observation of intense turbidity current activity in the zaire submarine valley at 4000 m water depth. *Marine Geology*, *194*(3-4), 151–158.

Khripounoff, A., Vangriesheim, A., Crassous, P., & Etoubleau, J. (2009). High frequency of sediment gravity flow events in the Var submarine canyon (Mediterranean Sea). *Marine Geology*, *263*(1-4), 1–6.

Killworth, P. D. (1983). Deep convection in the world ocean. *Reviews of Geophysics*, *21*(1), 1–26.

Komar, P. D., & Inman, D. L. (1970). Longshore sand transport on beaches. *Journal of geophysical research*, *75*(30), 5914–5927.

Kostic, S., & Parker, G. (2006). The response of turbidity currents to a canyon–fan transition: internal hydraulic jumps and depositional signatures. *Journal of Hydraulic Research*, *44*(5), 631–653.

Krause, D. C., White, W. C., PIPER, D. J. W., & Heezen, B. C. (1970). Turbidity currents and cable breaks in the western new britain trench. *Geological Society of America Bulletin*, *81*(7), 2153–2160.

Laberg, J., & Camerlenghi, A. (2008). The significance of contourites for submarine slope stability. *Developments in sedimentology*, *60*, 537–556.

Lambert, A., & Giovanoli, F. (1988). Records of riverbome turbidity currents and indications of slope failures in the rhone delta of lake geneva. *Limnology and Oceanography*, *33*(3), 458–468.

Lebreton, L. C., Van Der Zwet, J., Damsteeg, J.-W., Slat, B., Andrady, A., & Reisser, J. (2017). River plastic emissions to the world's oceans. *Nature communications*, *8*(1), 1–10.

Lee, H., Galy, V., Feng, X., Ponton, C., Galy, A., France-Lanord, C., & Feakins, S. J. (2019). Sustained wood burial in the bengal fan over the last 19 my. *Proceedings of the National Academy of Sciences*, *116*(45), 22518–22525.

Lee, H. J., Chough, S., & Yoon, S. (1996). Slope-stability change from late pleistocene to holocene in the ulleung basin, east sea (japan sea). *Sedimentary Geology*, *104*(1-4), 39–51.

Lee, I.-H., Wang, Y.-H., Liu, J. T., Chuang, W.-S., & Xu, J. (2009). Internal tidal currents in the gaoping (kaoping) submarine canyon. *Journal of Marine Systems*, *76*(4), 397–404.

Legge, O., Johnson, M., Hicks, N., Jickells, T., Diesing, M., Aldridge, J., Andrews, J., Artioli, Y., Bakker, D. C., Burrows, M. T., et al. (2020). Carbon on the northwest european shelf: Contemporary budget and future influences. *Frontiers in Marine Science*, *7*, 143.

Lemeshow, S., & Hosmer Jr, D. W. (1982). A review of goodness of fit statistics for use in the development of logistic regression models. *American journal of epidemiology*, *115*(1), 92–106.

Lintern, D. G., & Hill, P. R. (2010). An underwater laboratory at the fraser river delta. *Eos, Transactions American Geophysical Union*, *91*(38), 333–334.

Lintern, D. G., Hill, P. R., & Stacey, C. (2016). Powerful unconfined turbidity current captured by cabled observatory on the fraser river delta slope, british columbia, canada. *Sedimentology*, *63*(5), 1041–1064.

Lintern, D. G., Mosher, D. C., & Scherwath, M. (2019). Advancing from subaqueous mass movement case studies to providing advice and mitigation.

Liu, J. T., Kao, S.-J., Huh, C.-A., & Hung, C.-C. (2013). Gravity flows associated with flood events and carbon burial: Taiwan as instructional source area. *Annual Review of Marine Science*, *5*, 47–68.

Liu, J. T., Wang, Y. H., Lee, I.-H., & Hsu, R. T. (2010). Quantifying tidal signatures of the benthic nepheloid layer in gaoping submarine canyon in southern taiwan. *Marine Geology*, *271*(1-2), 119–130.

Liu, J. T., Wang, Y.-H., Yang, R. J., Hsu, R. T., Kao, S.-J., Lin, H.-L., & Kuo, F. H. (2012). Cyclone-induced hyperpycnal turbidity currents in a submarine canyon. *Journal of Geophysical Research: Oceans*, *117*(C4).

Llave, E., Schönfeld, J., Hernández-Molina, F., Mulder, T., Somoza, L., Del Río, V. D., & Sánchez-Almazo, I. (2006). High-resolution stratigraphy of the mediterranean outflow contourite system in the gulf of cadiz during the late pleistocene: the impact of heinrich events. *Marine Geology*, *227*(3-4), 241–262.

Locat, J., Leroueil, S., Locat, A., & Lee, H. (2014). Weak layers: their definition and classification from a geotechnical perspective. In *Submarine mass movements and their consequences*, (pp. 3–12). Springer.

Louviere, J. J., Hensher, D. A., & Swait, J. D. (2000). *Stated choice methods: analysis and applications*. Cambridge university press.

Lowe, D. R. (1976). Subaqueous liquefied and fluidized sediment flows and their deposits. *Sedimentology*, *23*(3), 285–308.

Lucchi, R., Rebesco, M., Caburlotto, A., Colizza, E., & Fontolan, G. (2002a). Sedimentary processes and glacial cycles on the sediment drifts of the antarctic peninsula pacific margin: preliminary results of sedano-ii project.

Lucchi, R. G., Rebesco, M., Camerlenghi, A., Busetti, M., Tomadin, L., Villa, G., Persico, D., Morigi, C., Bonci, M., & Giorgetti, G. (2002b). Mid-late pleistocene glacimarine sedimentary processes of a high-latitude, deep-sea sediment drift (antarctic peninsula pacific margin). *Marine Geology*, *189*(3-4), 343–370.

Lutjeharms, J. R. (2006). *The agulhas current*, vol. 329. Springer.

Maier, K. L., Gales, J. A., Paull, C. K., Rosenberger, K., Talling, P. J., Simmons, S. M., Gwiazda, R., McGann, M., Cartigny, M. J., Lundsten, E., et al. (2019a). Linking direct measurements of turbidity currents to submarine canyon-floor deposits. *Frontiers in Earth Science*, *7*, 144.

Maier, K. L., Rosenberger, K. J., Paull, C. K., Gwiazda, R., Gales, J., Lorenson, T., Barry, J. P., Talling, P. J., McGann, M., Xu, J., et al. (2019b). Sediment and organic carbon transport and deposition driven by internal tides along monterey canyon, offshore california. *Deep Sea Research Part I: Oceanographic Research Papers*, *153*, 103108.

Major, J. J., & Iverson, R. M. (1999). Debris-flow deposition: Effects of pore-fluid pressure and friction concentrated at flow margins. *Geological Society of America Bulletin*, *111*(10), 1424–1434.

Mangeney, A., Tsimring, L., Volfson, D., Aranson, I. S., & Bouchut, F. (2007). Avalanche mobility induced by the presence of an erodible bed and associated entrainment. *Geophysical Research Letters*, *34*(22).

Maria, A., Carey, S., Sigurdsson, H., Kincaid, C., & Helgadóttir, G. (2000). Source and dispersal of jokulhlaup sediments discharged to the sea following the 1996 vatnajokull eruption. *Geological Society of America Bulletin*, *112*(10), 1507–1521.

Martín, J., Palanques, A., Vitorino, J., Oliveira, A., & de Stigter, H. C. (2011). Near-bottom particulate matter dynamics in the Nazaré submarine canyon under calm and stormy conditions. *Deep-Sea Research Part II: Topical Studies in Oceanography*, *58*(23-24), 2388–2400.

Martín, J., Puig, P., Palanques, A., Masqué, P., & García-Orellana, J. (2008). Effect of commercial trawling on the deep sedimentation in a mediterranean submarine canyon. *Marine Geology*, *252*(3-4), 150–155.

Maselli, V., Kroon, D., Iacopini, D., Wade, B. S., Pearson, P. N., & De Haas, H. (2020). Impact of the east african rift system on the routing of the deep-water drainage network offshore tanzania, western indian ocean. *Basin Research*, *32*(5), 789–803.

Masson, D. G., Wynn, R. B., & Talling, P. J. (2010). Large Landslides on Passive Continental Margins: Processes, Hypotheses and Outstanding Questions. *Submarine Mass Movements and Their Consequences*, *28*, 153–165.

Mastbergen, D., van den Ham, G., Cartigny, M., Koelewijn, A., de Kleine, M., Clare, M., Hizzett, J., Azpiroz, M., & Vellinga, A. (2016). Multiple flow slide experiment in the westerschelde estuary, the netherlands. In *Submarine Mass Movements and Their Consequences*, (pp. 241–249). Springer.

Mastbergen, D. R., & Van den Berg, J. H. (2003). Breaching in fine sands and the generation of sustained turbidity currents in submarine canyons. *Sedimentology*, *50*(4), 625–637.

McCave, I. N., Thornalley, D., & Hall, I. R. (2017). Relation of sortable silt grain-size to deep-sea current speeds: Calibration of the 'mud current meter'. *Deep Sea Research Part I: Oceanographic Research Papers*, *127*, 1–12.

McFadden, D. (1974). The measurement of urban travel demand. *Journal of public economics*, *3*(4), 303–328.

McGregor, B., Stubblefield, W. L., Ryan, W. B., & Twichell, D. C. (1982). Wilmington submarine canyon: a marine fluvial-like system. *Geology*, *10*(1), 27–30.

Milliman, J. D., & Meade, R. H. (1983). World-wide delivery of river sediment to the oceans. *The Journal of Geology*, *91*(1), 1–21.

Milliman, J. D., & Syvitski, J. P. (1992). Geomorphic/tectonic control of sediment discharge to the ocean: the importance of small mountainous rivers. *The journal of Geology*, *100*(5), 525–544.

Milly, P. C. D., Wetherald, R. T., Dunne, K., & Delworth, T. L. (2002). Increasing risk of great floods in a changing climate. *Nature*, *415*(6871), 514–517.

Miramontes, E., Eggenhuisen, J. T., Jacinto, R. S., Poneti, G., Pohl, F., Normandeau, A., Campbell, D. C., & Hernández-Molina, F. J. (2020). Channel-levee evolution in combined contour current–turbidity current flows from flume-tank experiments. *Geology*, *48*(4), 353–357.

Miramontes, E., Penven, P., Fierens, R., Droz, L., Toucanne, S., Jorry, S. J., Jouet, G., Pastor, L., Jacinto, R. S., Gaillot, A., et al. (2019). The influence of bottom currents on the zambezi valley morphology (mozambique channel, sw indian ocean): In situ current observations and hydrodynamic modelling. *Marine Geology*, *410*, 42–55.

Mitchell, N. C. (2005). Interpreting long-profiles of canyons in the usa atlantic continental slope. *Marine Geology*, *214*(1-3), 75–99.

Mitchell, N. C. (2006). Morphologies of knickpoints in submarine canyons. *Geological Society of America Bulletin*, *118*(5-6), 589–605.

Mordecai, G., Tyler, P. A., Masson, D. G., & Huvenne, V. A. (2011). Litter in submarine canyons off the west coast of Portugal. *Deep-Sea Research Part II: Topical Studies in Oceanography*, *58*(23-24), 2489–2496.

Mountjoy, J. J., Howarth, J. D., Orpin, A. R., Barnes, P. M., Bowden, D. A., Rowden, A. A., Schimel, A. C., Holden, C., Horgan, H. J., Nodder, S. D., Patton, J. R., Lamarche, G., Gerstenberger, M., Micallef, A., Pallentin, A., & Kane, T. (2018). Earthquakes drive large-scale submarine canyon development and sediment supply to deep-ocean basins. *Science Advances*, *4*(3).

Mulder, T., Faugères, J.-C., & Gonthier, E. (2008). Mixed turbidite–contourite systems. *Developments in sedimentology*, *60*, 435–456.

Mulder, T., Migeon, S., Savoye, B., & Faugères, J.-C. (2001). Inversely graded turbidite sequences in the deep Mediterranean: a record of deposits from flood-generated turbidity currents? *Geo-Marine Letters*, *21*(2), 86–93.

Mulder, T., Savoye, B., & Syvitski, J. (1997). Numerical modelling of a mid-sized gravity flow: the 1979 nice turbidity current (dynamics, processes, sediment budget and seafloor impact). *Sedimentology*, *44*(2), 305–326.

Mulder, T., Syvitski, J. P., Migeon, S., Faugères, J.-C., & Savoye, B. (2003). Marine hyperpycnal flows: initiation, behavior and related deposits. a review. *Marine and Petroleum Geology*, *20*(6-8), 861–882.

Mulder, T., & Syvitski, J. P. M. (1995). Turbidity Currents Generated at River Mouths during Exceptional Discharges to the World Oceans. *The Journal of Geology*, *103*(3), 285–299.

Nagel, D. K., Mullins, H. T., & Greene, H. G. (1986). Ascension submarine canyon, california—evolution of a multi-head canyon system along a strike-slip continental margin. *Marine Geology*, *73*(3-4), 285–310.

Nieminski, N., Paull, C. K., Wolfson-Schwehr, M., & Caress, D. W. (2019). Matching individual turbidites to instrumentally measured sediment gravity flow events in monterey canyon, offshore california. In *AGU Fall Meeting Abstracts*, vol. 2019, (pp. OS32A–03).

Nienhuis, J. H., Ashton, A. D., Edmonds, D. A., Hoitink, A., Kettner, A. J., Rowland, J. C., & Törnqvist, T. E. (2020). Global-scale human impact on delta morphology has led to net land area gain. *Nature*, *577*(7791), 514–518.

Nilsen, T. H., Shew, R. D., Steffens, G. S., & Studlick, J. R. (2007). Front matter: Atlas of deep-water outcrops: Aapg studies in geology 56.

Nittrouer, C. A., & Wright, L. D. (1994). Transport of particles across continental shelves. *Reviews of Geophysics*, *32*(1), 85–113.

Normandeau, A., Bourgault, D., Neumeier, U., Lajeunesse, P., St-Onge, G., Gostiaux, L., & Chavanne, C. (2020). Storm-induced turbidity currents on a sediment-starved shelf: Insight from direct monitoring and repeat seabed mapping of upslope migrating bedforms. *Sedimentology*, *67*(2), 1045–1068.

Normark, W. (1970). Channel piracy on monterey deep-sea fan. In *Deep Sea Research and Oceanographic Abstracts*, vol. 17, (pp. 837–846). Elsevier.

Normark, W. R. (1989). Observed parameters for turbidity-current flow in channels, reserve fan, lake superior. *Journal of Sedimentary Research*, *59*(3), 423–431.

Normark, W. R., Carlson, P. R., Chan, M., & Archer, A. (2003). Giant submarine canyons: Is size any clue to their importance in the rock record? *Special Papers-Geological Society of America*, (pp. 175–190).

Normark, W. R., & Hess, G. R. (1980). Quaternary growth patterns of california submarine fans.

Ogston, A. S., Drexler, T. M., & Puig, P. (2008). Sediment delivery, resuspension, and transport in two contrasting canyon environments in the southwest gulf of lions. *Continental Shelf Research*, *28*(15), 2000–2016.

Okey, T. A. (1997). Sediment flushing observations, earthquake slumping, and benthic community changes in monterey canyon head. *Continental Shelf Research*, *17*(8), 877–897.

Okusa, S. (1985). Measurements of wave-induced pore pressure in submarine sediments under various marine conditions. *Marine Georesources & Geotechnology*, *6*(2), 119–144.

Özener, P. T., Özaydın, K., & Berilgen, M. M. (2009). Investigation of liquefaction and pore water pressure development in layered sands. *Bulletin of Earthquake Engineering*, *7*(1), 199–219.

Page, B. M., Coleman, R. G., & Thompson, G. A. (1998). Late cenozoic tectonics of the central and southern coast ranges of california. *Geological Society of America Bulletin*, *110*(7), 846–876.

Palanques, A., Guillén, J., Puig, P., & de Madron, X. D. (2008). Storm-driven shelf-to-canyon suspended sediment transport at the southwestern gulf of lions. *Continental Shelf Research*, *28*(15), 1947–1956.

Palanques, A., Martín, J., Puig, P., Guillén, J., Company, J., & Sardà, F. (2006). Evidence of sediment gravity flows induced by trawling in the palamós (fonera) submarine canyon (northwestern mediterranean). *Deep Sea Research Part I: Oceanographic Research Papers*, *53*(2), 201–214.

Palanques, A., Puig, P., Guillén, J., Durrieu de Madron, X., Latasa, M., Scharek, R., & Martín, J. (2011). Effects of storm events on the shelf-to-basin sediment transport in the southwestern end of the gulf of lions (northwestern mediterranean). *Natural Hazards and Earth System Sciences*, *11*(3), 843–850.

Pandolpho, B. T., da Fontoura Klein, A. H., Dutra, I., Mahiques, M. M., Viana, A. R., Bueno, G. V., Machado, A. A., Camargo, Y. L., Hercos, C. M., Lima, Y., et al. (2021). Seismic record of a cyclic turbidite-contourite system in the northern campos basin, se brazil. *Marine Geology*, *434*, 106422.

Pantin, H. (1979). Interaction between velocity and effective density in turbidity flow: phase-plane analysis, with criteria for autosuspension. *Marine Geology*, *31*(1-2), 59–99.

Paradis, S., Puig, P., Masqué, P., Juan-Díaz, X., Martín, J., & Palanques, A. (2017). Bottom-trawling along submarine canyons impacts deep sedimentary regimes. *Scientific reports*, *7*(1), 1–12.

Parker, G. (1982). Conditions for the ignition of catastrophically erosive turbidity currents. *Marine Geology*, *46*(3-4), 307–327.

Parker, G., Fukushima, Y., & Pantin, H. M. (1986). Self-accelerating turbidity currents. *Journal of Fluid Mechanics*, *171*, 145–181.

Parsons, J. D., Bush, J. W., & Syvitski, J. P. (2001). Hyperpycnal plume formation from riverine outflows with small sediment concentrations. *Sedimentology*, *48*(2), 465–478.

Patsch, K., & Griggs, G. B. (2006). *Littoral cells, sand budgets, and beaches: understanding California's shoreline*. Institute of Marine Sciences, University of California, Santa Cruz.

Paull, C., Caress, D., Lundsten, E., Gwiazda, R., Anderson, K., McGann, M., Conrad, J., Edwards, B., & Sumner, E. (2013). Anatomy of the la jolla submarine canyon system; offshore southern california. *Marine Geology*, *335*, 16–34.

Paull, C., Mitts, P., Ussler I I I, W., Keaten, R., & Greene, H. (2005). Trail of sand in upper Monterey Canyon: Offshore California. *Bulletin Of The Geological Society Of America*, *117*(41921), 1134.

Paull, C., Ussler, W., Greene, H., Keaten, R., Mitts, P., & Barry, J. (2003). Caught in the act: the 20 december 2001 gravity flow event in monterey canyon. *Geo-Marine Letters*, *22*(4), 227–232.

Paull, C. K., Caress, D. W., Ussler III, W., Lundsten, E., & Meiner-Johnson, M. (2011). High-resolution bathymetry of the axial channels within monterey and soquel submarine canyons, offshore central california. *Geosphere*, *7*(5), 1077–1101.

Paull, C. K., Talling, P. J., Maier, K. L., Parsons, D., Xu, J., Caress, D. W., Gwiazda, R., Lundsten, E. M., Anderson, K., Barry, J. P., Chaffey, M., O'Reilly, T., Rosenberger, K. J., Gales, J. A., Kieft, B., McGann, M., Simmons, S. M., McCann, M., Sumner, E. J., Clare, M. A., & Cartigny, M. J. (2018). Powerful turbidity currents driven by dense basal layers. *Nature Communications*, *9*(1), 1–9.

Paull, C. K., Ussler III, W., Caress, D. W., Lundsten, E., Covault, J. A., Maier, K. L., Xu, J., & Augenstein, S. (2010). Origins of large crescent-shaped bedforms within the axial channel of Monterey Canyon, offshore California. *Geosphere*, *6*(6), 755–774.

Peng, C.-Y. J., Lee, K. L., & Ingersoll, G. M. (2002). An introduction to logistic regression analysis and reporting. *The journal of educational research*, *96*(1), 3–14.

Petruncio, E. T., Rosenfeld, L. K., & Paduan, J. D. (1998). Observations of the internal tide in monterey canyon. *Journal of Physical Oceanography*, *28*(10), 1873–1903.

Pierdomenico, M., Casalbore, D., & Chiocci, F. L. (2019). Massive benthic litter funnelled to deep sea by flash-flood generated hyperpycnal flows. *Scientific reports*, *9*(1), 1–10.

Piper, D. J., & Aksu, A. E. (1987). The source and origin of the 1929 grand banks turbidity current inferred from sediment budgets. *Geo-Marine Letters*, *7*(4), 177–182.

Piper, D. J., Cochonat, P., & Morrison, M. L. (1999). The sequence of events around the epicentre of the 1929 Grand Banks earthquake: initiation of debris flows and turbidity current inferred from sidescan sonar. *Sedimentology*, *46*(1), 79–97.

Piper, D. J., & Hundert, T. (2002). Provenance of distal sohm abyssal plain sediments: history of supply from the wisconsinan glaciation in eastern canada. *Geo-Marine Letters*, *22*(2), 75–85.

Piper, D. J., & Normark, W. R. (2009). Processes that initiate turbidity currents and their influence on turbidites: a marine geology perspective. *Journal of Sedimentary Research*, *79*(6), 347–362.

Piper, D. J., & Savoye, B. (1993). Processes of late quaternary turbidity current flow and deposition on the var deep-sea fan, north-west mediterranean sea. *Sedimentology*, *40*(3), 557–582.

Piper, D. J., Shor, A. N., & Hughes Clarke, J. E. (1988). The 1929 grand banks earthquake, slump and turbidity current.

Piret, L., Bertrand, S., Nguyen, N., Hawkings, J., Rodrigo, C., & Wadham, J. (2022). Long-lasting impacts of a 20th century glacial lake outburst flood on a patagonian fjord-river system (pascua river). *Geomorphology*, *399*, 108080.

Pohl, F., Eggenhuisen, J. T., Kane, I. A., & Clare, M. A. (2020). Transport and burial of microplastics in deep-marine sediments by turbidity currents. *Environmental science & technology*, *54*(7), 4180–4189.

Pope, E., Talling, P., Urlaub, M., Hunt, J., Clare, M., & Challenor, P. (2015). Are large submarine landslides temporally random or do uncertainties in available age constraints make it impossible to tell? *Marine Geology*, *369*, 19–33.

Pope, E. L., Talling, P. J., & Carter, L. (2017a). Which earthquakes trigger damaging submarine mass movements: Insights from a global record of submarine cable breaks? *Marine Geology*, *384*, 131–146.

Pope, E. L., Talling, P. J., Carter, L., Clare, M. A., & Hunt, J. E. (2017b). Damaging sediment density flows triggered by tropical cyclones. *Earth and Planetary Science Letters*, *458*, 161–169.

Pouliquen, O., & Forterre, Y. (2002). Friction law for dense granular flows: application to the motion of a mass down a rough inclined plane. *Journal of fluid mechanics*, *453*, 133–151.

Principaud, M., Mulder, T., Hanquiez, V., Ducassou, E., Eberli, G. P., Chabaud, L., & Borgomano, J. (2018). Recent morphology and sedimentary processes along the western slope of great bahama bank (bahamas). *Sedimentology*, *65*(6), 2088–2116.

Prior, D. B., & Bornhold, B. D. (1989). Submarine sedimentation on a developing holocene fan delta. *Sedimentology*, *36*(6), 1053–1076.

Prior, D. B., Bornhold, B. D., & Johns, M. W. (1986). Active sand transport along a fjord-bottom channel, bute inlet, british columbia. *Geology*, *14*(7), 581–584.

Prior, D. B., Bornhold, B. D., Wiseman, W. J., & Lowe, D. R. (1987). Turbidity current activity in a british columbia fjord. *Science*, *237*(4820), 1330–1333.

Prior, D. B., Wiseman, W. J., & Gilbert, R. (1981). Submarine slope processes on a fan delta, howe sound, british columbia. *Geo-Marine Letters*, *1*(2), 85–90.

Puig, P., Canals, M., Company, J. B., Martín, J., Amblas, D., Lastras, G., Palanques, A., & Calafat, A. M. (2012). Ploughing the deep sea floor. *Nature*, *489*(7415), 286–289. URL http://www.nature.com/articles/nature11410

Puig, P., Greenan, B. J., Li, M. Z., Prescott, R. H., & Piper, D. J. (2013a). Sediment transport processes at the head of Halibut Canyon, eastern Canada margin: An interplay between internal tides and dense shelf-water cascading. *Marine Geology*, *341*, 14–28.

Puig, P., Ogston, A. S., Mullenbach, B. L., Nittrouer, C. A., Parsons, J. D., & Sternberg, R. W. (2004). Storm-induced sediment gravity flows at the head of the Eel

submarine canyon, northern California margin. *Journal of Geophysical Research: Oceans*, *109*(C3), 1–10.

Puig, P., Palanques, A., & Martín, J. (2013b). Contemporary sediment-transport processes in submarine canyons. *Annual review of marine science*, *6*, 53–77.

Puig, P., Palanques, A., Orange, D., Lastras, G., & Canals, M. (2008). Dense shelf water cascades and sedimentary furrow formation in the cap de creus canyon, northwestern mediterranean sea. *Continental Shelf Research*, *28*(15), 2017–2030.

Rao, J. S., & Liu, H. (2017). Discordancy partitioning for validating potentially inconsistent pharmacogenomic studies. *Scientific reports*, *7*(1), 1–12.

Rebesco, M., Hernández-Molina, F. J., Van Rooij, D., & Wåhlin, A. (2014). Contourites and associated sediments controlled by deep-water circulation processes: State-of-the-art and future considerations. *Marine Geology*, *352*, 111–154.

Roberts, E. M., Stevens, N., O'Connor, P. M., Dirks, P., Gottfried, M. D., Clyde, W., Armstrong, R., Kemp, A., & Hemming, S. (2012). Initiation of the western branch of the east african rift coeval with the eastern branch. *Nature Geoscience*, *5*(4), 289–294.

Rodrigues, S., Hernández-Molina, F., & Kirby, A. (2021). A late cretaceous mixed (turbidite-contourite) system along the argentine margin: Paleoceanographic and conceptual implications. *Marine and Petroleum Geology*, *123*, 104768.

Romans, B. W., Normark, W. R., McGann, M. M., Covault, J. A., & Graham, S. A. (2009). Coarse-grained sediment delivery and distribution in the holocene santa monica basin, california: implications for evaluating source-to-sink flux at millennial time scales. *Geological Society of America Bulletin*, *121*(9-10), 1394–1408.

Rosenberger, K. J., Storlazzi, C. D., & Cheriton, O. M. (2016). Variability of the internal tide on the southern monterey bay continental shelf and associated bottom boundary layer sediment transport. *Continental Shelf Research*, *120*, 68–81.

Sagnotti, L., Macri, P., Camerlenghi, A., & Rebesco, M. (2001). Environmental magnetism of antarctic late pleistocene sediments and interhemispheric correlation of climatic events. *Earth and Planetary Science Letters*, *192*(1), 65–80.

Salman, G., & Abdula, I. (1995). Development of the mozambique and ruvuma sedimentary basins, offshore mozambique. *Sedimentary Geology*, *96*(1-2), 7–41.

Sansom, P. (2018). Hybrid turbidite–contourite systems of the tanzanian margin. *Petroleum Geoscience*, *24*(3), 258–276.

Schlacher, T. A., Schlacher-Hoenlinger, M. A., Williams, A., Althaus, F., Hooper, J. N., & Kloser, R. (2007). Richness and distribution of sponge megabenthos in continental margin canyons off southeastern australia. *Marine Ecology Progress Series*, *340*, 73–88.

Schott, F. A., Xie, S.-P., & McCreary Jr, J. P. (2009). Indian ocean circulation and climate variability. *Reviews of Geophysics*, *47*(1).

Schouten, M. W., de Ruijter, W. P., Van Leeuwen, P. J., & Ridderinkhof, H. (2003). Eddies and variability in the mozambique channel. *Deep Sea Research Part II: Topical Studies in Oceanography*, *50*(12-13), 1987–2003.

Seed, H. B., & Rahman, M. (1978). Wave-induced pore pressure in relation to ocean floor stability of cohesionless soils. *Marine Georesources & Geotechnology*, *3*(2), 123–150.

Sequeiros, O. E., Mosquera, R., & Pedocchi, F. (2018). Internal structure of a self-accelerating turbidity current. *Journal of Geophysical Research: Oceans*, *123*(9), 6260–6276.

Sequeiros, O. E., Naruse, H., Endo, N., Garcia, M. H., & Parker, G. (2009). Experimental study on self-accelerating turbidity currents. *Journal of Geophysical Research: Oceans*, *114*(C5).

Sequeiros, O. E., Pittaluga, M. B., Frascati, A., Pirmez, C., Masson, D. G., Weaver, P., Crosby, A. R., Lazzaro, G., Botter, G., & Rimmer, J. G. (2019). How typhoons trigger turbidity currents in submarine canyons. *Scientific reports*, *9*(1), 1–15.

Shanmugam, G. (2000). 50 years of the turbidite paradigm (1950s—1990s): deep-water processes and facies models—a critical perspective. *Marine and petroleum Geology*, *17*(2), 285–342.

Shanmugam, G. (2013). New perspectives on deep-water sandstones: Implications. *Petroleum Exploration and Development*, *40*(3), 316–324.

Shepard, F. P. (1972). Submarine canyons. *Earth-Science Reviews*, *8*(1), 1–12.

Shepard, F. P. (1976). Tidal components of currents in submarine canyons. *The Journal of Geology*, *84*(3), 343–350.

Shepard, F. P. (1981). Submarine canyons: multiple causes and long-time persistence. *AAPG bulletin*, *65*(6), 1062–1077.

Shugar, D. H., Burr, A., Haritashya, U. K., Kargel, J. S., Watson, C. S., Kennedy, M. C., Bevington, A. R., Betts, R. A., Harrison, S., & Strattman, K. (2020). Rapid worldwide growth of glacial lakes since 1990. *Nature Climate Change*, *10*(10), 939–945.

Simmons, S., Azpiroz-Zabala, M., Cartigny, M., Clare, M., Cooper, C., Parsons, D., Pope, E., Sumner, E., & Talling, P. (2020). Novel acoustic method provides first detailed measurements of sediment concentration structure within submarine turbidity currents. *Journal of Geophysical Research: Oceans*, *125*(5), e2019JC015904.

Smith, D. P., Kvitek, R., Iampietro, P. J., & Wong, K. (2007). Twenty-nine months of geomorphic change in upper monterey canyon (2002–2005). *Marine Geology*, *236*(1-2), 79–94.

Smith, D. P., Ruiz, G., Kvitek, R., & Iampietro, P. J. (2005). Semiannual patterns of erosion and deposition in upper monterey canyon from serial multibeam bathymetry. *GSA Bulletin*, *117*(9-10), 1123–1133.

Southard, J. B., & Mackintosh, M. E. (1981). Experimental test of autosuspension. *Earth Surface Processes and Landforms*, *6*(2), 103–111.

Stagna, M. D., Maselli, V., Grujic, D., Reynolds, P., Reynolds, D., Iacopini, D., Richards, B., Underhill, J. R., & Kroon, D. (2021). Structural controls on slope evolution and sediment dispersal pathways along the northern tanzania continental margin, western indian ocean. *Marine Geology*, (p. 106662).

Stanford, J. D., Hemingway, R., Rohling, E. J., Challenor, P. G., Medina-Elizalde, M., & Lester, A. J. (2011). Sea-level probability for the last deglaciation: A statistical analysis of far-field records. *Global and Planetary Change*, *79*(3-4), 193–203.

Stegmann, S., Sultan, N., Kopf, A., Apprioual, R., & Pelleau, P. (2011). Hydrogeology and its effect on slope stability along the coastal aquifer of nice, france. *Marine Geology*, *280*(1-4), 168–181.

Steinmann, L., Baques, M., Wenau, S., Schwenk, T., Spiess, V., Piola, A. R., Bozzano, G., Violante, R., & Kasten, S. (2020). Discovery of a giant cold-water coral mound province along the northern argentine margin and its link to the regional contourite depositional system and oceanographic setting. *Marine Geology*, *427*, 106223.

Stevens, T., Paull, C. K., Ussler, W. I., McGann, M., Buylaert, J.-P., & Lundsten, E. (2014). The timing of sediment transport down monterey submarine canyon, offshore california. *GSA Bulletin*, *126*(1-2), 103–121.

Stevenson, C. J., Feldens, P., Georgiopoulou, A., Schönke, M., Krastel, S., Piper, D. J., Lindhorst, K., & Mosher, D. (2018). Reconstructing the sediment concentration of a giant submarine gravity flow. *Nature communications*, *9*(1), 1–7.

Stow, D., Hernández-Molina, F., Llave, E., Bruno, M., García, M., del Rio, V. D., Somoza, L., & Brackenridge, R. (2013). The cadiz contourite channel: Sandy contourites, bedforms and dynamic current interaction. *Marine Geology*, *343*, 99–114.

Straub, K. M., Jerolmack, D. J., Mohrig, D., & Rothman, D. H. (2007). Channel network scaling laws in submarine basins. *Geophysical Research Letters*, *34*(12).

Studholme, J., Fedorov, A. V., Gulev, S. K., Emanuel, K., & Hodges, K. (2021). Poleward expansion of tropical cyclone latitudes in warming climates. *Nature Geoscience*, (pp. 1–15).

Sultan, N., Cochonat, P., Canals, M., Cattaneo, A., Dennielou, B., Haflidason, H., Laberg, J., Long, D., Mienert, J., Trincardi, F., et al. (2004). Triggering mechanisms of slope instability processes and sediment failures on continental margins: a geotechnical approach. *Marine Geology*, *213*(1-4), 291–321.

Sultan, N., Garziglia, S., Bompais, X., Woerther, P., Witt, C., Kopf, A., & Migeon, S. (2020). Transient groundwater flow through a coastal confined aquifer and its impact on nearshore submarine slope instability. *Journal of Geophysical Research: Earth Surface*, *125*(9), e2020JF005654.

Sultan, N., Savoye, B., Jouet, G., Leynaud, D., Cochonat, P., Henry, P., Stegmann, S., & Kopf, A. (2010). Investigation of a possible submarine landslide at the var delta front (nice continental slope, southeast france). *Canadian Geotechnical Journal*, *47*(4), 486–496.

Sumner, E., & Paull, C. K. (2014). Swept away by a turbidity current in mendocino submarine canyon, california. *Geophysical Research Letters*, *41*(21), 7611–7618.

Sumner, E. J., Siti, M. I., McNeill, L. C., Talling, P. J., Henstock, T. J., Wynn, R. B., Djajadihardja, Y. S., & Permana, H. (2013). Can turbidites be used to reconstruct a paleoearthquake record for the central sumatran margin? *Geology*, *41*(7), 763–766.

Syahnur, Y., Jaya, K. A., & Ariseputra, I. P. (2015). Geomatics best practices in saka indonesia pangkah limited (case study: Ujung pangkah pipeline integrity).

Symons, W. O., Sumner, E. J., Paull, C. K., Cartigny, M. J., Xu, J., Maier, K. L., Lorenson, T. D., & Talling, P. J. (2017). A new model for turbidity current behavior based on integration of flow monitoring and precision coring in a submarine canyon. *Geology*, *45*(4), 367–370.

Symons, W. O., Sumner, E. J., Talling, P. J., Cartigny, M. J., & Clare, M. A. (2016). Large-scale sediment waves and scours on the modern seafloor and their implications for the prevalence of supercritical flows. *Marine Geology*, *371*, 130–148.

Syvitski, J. P. (2003). Supply and flux of sediment along hydrological pathways: research for the 21st century. *Global and Planetary Change*, *39*(1-2), 1–11.

Syvitski, J. P., & Farrow, G. E. (1983). Structures and processes in bayhead deltas: Knight and bute inlet, british columbia. *Sedimentary geology*, *36*(2-4), 217–244.

Talling, P., Baker, M., Pope, E., Cula, C., Cartigny, M., Faria, R., Clare, M., Simmons, S., Silva Jacinto, R., Heijnen, M., et al. (2021). Novel sensor array helps to understand submarine cable faults off west africa. *EarthArXiv*.

Talling, P., Clare, M., Urlaub, M., Pope, E., Hunt, J., & Watt, S. (2014). Large Submarine Landslides on Continental Slopes: Geohazards, Methane Release, and Climate Change. *Oceanography*, *27*(2), 32–45.

Talling, P., Wynn, R., Masson, D., Frenz, M., Cronin, B., Schiebel, R., Akhmetzhanov, A., Dallmeier-Tiessen, S., Benetti, S., Weaver, P., et al. (2007). Onset of submarine debris flow deposition far from original giant landslide. *Nature*, *450*(7169), 541–544.

Talling, P. J. (2014). On the triggers, resulting flow types and frequencies of subaqueous sediment density flows in different settings. *Marine Geology*, *352*, 155–182.

Talling, P. J., Allin, J., Armitage, D. A., Arnott, R. W., Cartigny, M. J., Clare, M. A., Felletti, F., Covault, J. A., Girardclos, S., Hansen, E., et al. (2015). Key future directions for research on turbidity currents and their deposits. *Journal of Sedimentary Research*, *85*(2), 153–169.

Talling, P. J., Masson, D. G., Sumner, E. J., & Malgesini, G. (2012). Subaqueous sediment density flows: Depositional processes and deposit types. *Sedimentology*, *59*(7), 1937–2003.

Talling, P. J., Paull, C. K., & Piper, D. J. (2013). How are subaqueous sediment density flows triggered, what is their internal structure and how does it evolve? direct observations from monitoring of active flows. *Earth-Science Reviews*, *125*, 244–287.

Tappin, D. (2010). Submarine mass failures as tsunami sources: their climate control. *Philosophical Transactions of the Royal Society A: Mathematical, Physical and Engineering Sciences*, *368*(1919), 2417–2434.

Teledyne RD Instruments (2011). Acoustic doppler current profiler principles of operation: A practical primer. *Teledyne RDI*, (p. 1).

Thornton, E. B. (2016). Temporal and spatial variations in sand budgets with application to southern monterey bay, california. *Marine Geology*, *382*, 56–67.

Tilston, M., Shugar, D. H., Clare, M., Heijnen, M., Acikalin, S., Cartigny, M., Talling, P., Parsons, D., Lintern, G., Stacey, C., et al. (2021). Effects of extreme events on the morphology of submarine channels: the case of the elliot hazard cascade. In *EGU General Assembly Conference Abstracts*, (pp. EGU21–16595).

Traer, M., Hilley, G., Fildani, A., & McHargue, T. (2012). The sensitivity of turbidity currents to mass and momentum exchanges between these underflows and their surroundings. *Journal of Geophysical Research: Earth Surface*, *117*(F1).

Tubau, X., Canals, M., Lastras, G., Rayo, X., Rivera, J., & Amblas, D. (2015). Marine litter on the floor of deep submarine canyons of the northwestern mediterranean sea: the role of hydrodynamic processes. *Progress in Oceanography*, *134*, 379–403.

Twichell, D. C., & Roberts, D. G. (1982). Morphology, distribution, and development of submarine canyons on the united states atlantic continental slope between hudson arid baltimore canyons. *Geology*, *10*(8), 408–412.

Ullgren, J. E., André, E., Gammelsrød, T., & Hoguane, A. M. (2016). Observations of strong ocean current events offshore pemba, northern mozambique. *Journal of Operational Oceanography*, *9*(1), 55–66.

Urlaub, M., Talling, P. J., & Masson, D. G. (2013). Timing and frequency of large submarine landslides: implications for understanding triggers and future geohazard. *Quaternary Science Reviews*, *72*, 63–82.

van Aken, H. M., Ridderinkhof, H., & de Ruijter, W. P. (2004). North atlantic deep water in the south-western indian ocean. *Deep Sea Research Part I: Oceanographic Research Papers*, *51*(6), 755–776.

van den Beld, I. M., Guillaumont, B., Menot, L., Bayle, C., Arnaud-Haond, S., & Bourillet, J.-F. (2017). Marine litter in submarine canyons of the bay of biscay. *Deep Sea Research Part II: Topical Studies in Oceanography*, *145*, 142–152.

Van den Berg, J. H., Van Gelder, A., & Mastbergen, D. R. (2002). The importance of breaching as a mechanism of subaqueous slope failure in fine sand. *Sedimentology*, *49*(1), 81–95.

van der Voort, T. S., Blattmann, T. M., Usman, M., Montluçon, D., Loeffler, T., Tavagna, M. L., Gruber, N., & Eglinton, T. I. (2021). Mosaic (modern ocean sediment archive and inventory of carbon): a (radio) carbon-centric database for seafloor surficial sediments. *Earth System Science Data*, *13*(5), 2135–2146.

Van Weering, T., & Van Iperen, J. (1984). Fine-grained sediments of the zaire deep-sea fan, southern atlantic ocean. *Geological Society, London, Special Publications*, *15*(1), 95–113.

Vangriesheim, A., Khripounoff, A., & Crassous, P. (2009). Turbidity events observed in situ along the congo submarine channel. *Deep Sea Research Part II: Topical Studies in Oceanography*, *56*(23), 2208–2222.

Vanoudheusden, E., Sultan, N., & Cochonat, P. (2004). Mechanical behaviour of unsaturated marine sediments: experimental and theoretical approaches. *Marine geology*, *213*(1-4), 323–342.

Vendettuoli, D., Clare, M., Clarke, J. H., Vellinga, A., Hizzet, J., Hage, S., Cartigny, M., Talling, P., Waltham, D., Hubbard, S., et al. (2019). Daily bathymetric surveys document how stratigraphy is built and its extreme incompleteness in submarine channels. *Earth and Planetary Science Letters*, *515*, 231–247.

Viana, A., Almeida, W., Nunes, M., & Bulhões, E. (2007). The economic importance of contourites. *Geological Society, London, Special Publications*, *276*(1), 1–23.

Villa, G., Persico, D., Bonci, M. C., Lucchi, R. G., Morigi, C., & Rebesco, M. (2003). Biostratigraphic characterization and quaternary microfossil palaeoecology in

sediment drifts west of the antarctic peninsula–implications for cyclic glacial–interglacial deposition. *Palaeogeography, Palaeoclimatology, Palaeoecology*, *198*(1-2), 237–263.

Voigt, I., Henrich, R., Preu, B. M., Piola, A. R., Hanebuth, T. J., Schwenk, T., & Chiessi, C. M. (2013). A submarine canyon as a climate archive—interaction of the antarctic intermediate water with the mar del plata canyon (southwest atlantic). *Marine Geology*, *341*, 46–57.

Völker, D., Scholz, F., & Geersen, J. (2011). Analysis of submarine landsliding in the rupture area of the 27 february 2010 maule earthquake, central chile. *Marine Geology*, *288*(1-4), 79–89.

Waelbroeck, C., Labeyrie, L., Michel, E., Duplessy, J.-C., Mcmanus, J. F., Lambeck, K., Balbon, E., & Labracherie, M. (2002). Sea-level and deep water temperature changes derived from benthic foraminifera isotopic records. *Quaternary science reviews*, *21*(1-3), 295–305.

Wang, Z., Xu, J., Talling, P. J., Cartigny, M. J., Simmons, S. M., Gwiazda, R., Paull, C. K., Maier, K. L., & Parsons, D. R. (2020). Direct evidence of a high-concentration basal layer in a submarine turbidity current. *Deep Sea Research Part I: Oceanographic Research Papers*, *161*, 103300.

Waterhouse, A. F., Mackinnon, J. A., Musgrave, R. C., Kelly, S. M., Pickering, A., & Nash, J. (2017). Internal tide convergence and mixing in a submarine canyon. *Journal of Physical Oceanography*, *47*(2), 303–322.

Watson, F., Anderson, T., Casagrande, J., Kozlowski, D., Newman, W., Hager, J., D.P., S., & Curry, R. (2003). *Hydrology and Water Quality of the Carmel and Salinas Lagoons, Monterey Bay, California: 2002/2003*. Salinas Valley Sediment Sources. Central Coast Watershed Studies Report No. WI-2002-10 to the California Central Coast Water Quality Control Board.

Weaver, P., Rothwell, R., Ebbing, J., Gunn, D., & Hunter, P. (1992). Correlation, frequency of emplacement and source directions of megaturbidites on the madeira abyssal plain. *Marine Geology*, *109*(1-2), 1–20.

Wilckens, H., Miramontes, E., Schwenk, T., Artana, C., Zhang, W., Piola, A. R., Baques, M., Provost, C., Hernández-Molina, F. J., Felgendreher, M., et al. (2021). The erosive power of the malvinas current: Influence of bottom currents on morpho-sedimentary features along the northern argentine margin (sw atlantic ocean). *Marine Geology*, *439*, 106539.

Willis, C. M., & Griggs, G. B. (2003). Reductions in fluvial sediment discharge by coastal dams in california and implications for beach sustainability. *The Journal of Geology*, *111*(2), 167–182.

Winterwerp, J. (2006). Stratification effects by fine suspended sediment at low, medium, and very high concentrations. *Journal of Geophysical Research: Oceans*, *111*(C5).

Winterwerp, J. C., Bakker, W. T., Mastbergen, D. R., & van Rossum, H. (1992). Hyperconcentrated sand-water mixture flows over erodible bed. *Journal of Hydraulic Engineering*, *118*(11), 1508–1525.

Winterwerp, J. C., de Groot, M. B., Mastbergen, D. R., & Verwoert, H. (1990). Hyperconcentrated sand-water mixture flows over a flat bed. *Journal of Hydraulic Engineering*, *116*(1), 36–54.

Wright, L. (1977). Sediment transport and deposition at river mouths: a synthesis. *Geological Society of America Bulletin*, *88*(6), 857–868.

Wright, S., & Rathje, E. (2003). Triggering mechanisms of slope instability and their relationship to earthquakes and tsunamis. *Pure and Applied Geophysics*, *160*(10), 1865–1877.

Xu, J. (2011). Measuring currents in submarine canyons: Technological and scientific progress in the past 30 years. *Geosphere*, *7*(4), 868–876.

Xu, J., Barry, J. P., & Paull, C. K. (2013). Small-scale turbidity currents in a big submarine canyon. *Geology*, *41*(2), 143–146.

Xu, J., Noble, M., Eittreim, S. L., Rosenfeld, L. K., Schwing, F. B., & Pilskaln, C. H. (2002). Distribution and transport of suspended particulate matter in monterey canyon, california. *Marine Geology*, *181*(1-3), 215–234.

Xu, J., Noble, M., & Rosenfeld, L. K. (2004). In-situ measurements of velocity structure within turbidity currents. *Geophysical research letters*, *31*(9).

Xu, J., Sequeiros, O. E., & Noble, M. A. (2014). Sediment concentrations, flow conditions, and downstream evolution of two turbidity currents, monterey canyon, usa. *Deep Sea Research Part I: Oceanographic Research Papers*, *89*, 11–34.

Xu, J., Swarzenski, P. W., Noble, M., & Li, A.-C. (2010). Event-driven sediment flux in hueneme and mugu submarine canyons, southern california. *Marine Geology*, *269*(1-2), 74–88.

Yoklavich, M. M., Greene, H. G., Cailliet, G. M., Sullivan, D. E., Lea, R. N., & Love, M. S. (2000). Habitat associations of deep-water rockfishes in a submarine canyon: an example of a natural refuge. *Fishery Bulletin*, *98*(3), 625–625.

Zeng, J., Lowe, D. R., Prior, D. B., WISEMAN JR, W. J., & Bornhold, B. D. (1991). Flow properties of turbidity currents in bute inlet, british columbia. *Sedimentology*, *38*(6), 975–996.

Zhan, Z., Cantono, M., Kamalov, V., Mecozzi, A., Müller, R., Yin, S., & Castellanos, J. C. (2021). Optical polarization–based seismic and water wave sensing on transoceanic cables. *Science*, *371*(6532), 931–936.

Zhang, Y., Liu, Z., Zhao, Y., Colin, C., Zhang, X., Wang, M., Zhao, S., & Kneller, B. (2018). Long-term in situ observations on typhoon-triggered turbidity currents in the deep sea. *Geology*, *46*(8), 675–678.

Zhang, Y., Liu, Z., Zhao, Y., Wang, W., Li, J., & Xu, J. (2014). Mesoscale eddies transport deep-sea sediments. *Scientific reports*, *4*(1), 1–7.

Zhao, Y., Liu, Z., Zhang, Y., Li, J., Wang, M., Wang, W., & Xu, J. (2015). In situ observation of contour currents in the northern south china sea: Applications for deepwater sediment transport. *Earth and Planetary Science Letters*, *430*, 477–485.

Zhao, Z., Alford, M. H., Lien, R.-C., Gregg, M. C., & Carter, G. S. (2012). Internal tides and mixing in a submarine canyon with time-varying stratification. *Journal of physical oceanography*, *42*(12), 2121–2142.

Zhong, G., & Peng, X. (2021). Transport and accumulation of plastic litter in submarine canyons—the role of gravity flows. *Geology*, *49*(5), 581–586.